Development of Resonant Tunnelling Diode Terahertz Emitter

Kristof Jan Philip Jacobs

University of Sheffield

Department of Electrical and Electronic Engineering

Thesis submitted to the University of Sheffield for the degree of Doctor of Philosophy

May 2015

Dedicated to

my family

Abstract

This thesis reports on the development of high current density InGaAs/AlAs/InP resonant tunnelling diodes (RTDs) grown by metal-organic vapour phase epitaxy (MOVPE) for terahertz (THz) applications. A wide variety of characterisation techniques are employed to investigate the material properties and quality on the wafer level allowing future device and growth optimisation.

An optical characterisation technique based on photoluminescence (PL) spectroscopy is developed to non-destructively map the doping and structural composition of the RTD on the wafer level. A new non-destructive optical characterisation technique to resolve the absolute energy level position of the first electron state of RTDs through low temperature PL spectroscopy is also reported. The absolute energy levels are resolved by a combination of type-I and type-II quantum well (QW) recombination, allowing an investigation into important scattering mechanisms affecting device performance, and monitor the QW alloy content and thickness non-destructively. Details of the growth process and the characterisation techniques are discussed.

A new fabrication technique based on conventional i-line photolithography for micron scale high current density RTD devices is also developed with accurate control over the final device area (and hence characteristics). This is achieved by measuring the V-I characteristic of the RTD during the fabrication process, which has not been previously possible. This was made possible by guiding the emitter current through the full RTD structure by a large second contact electrode on the collector side and using an air-bridge contact to the collector. Important information about the RTD performance is extracted by using this method. Temperature dependent V-I characterisation is also carried out to investigate the valley current of the RTD. Details of the design, fabrication, and characterisation of a room temperature operating THz emitter in the 300 GHz band are reported.

Acknowledgements

I gratefully acknowledge the support of all my colleagues and friends. I would like to thank the following individuals in particular.I would like to thank all my colleagues at the semiconductor lasers research group for making my time as a PhD researcher memorable. Thank you: Pavlo, Omar, Kris, Xiao, Jon, Nasser, Razvan, Little Dave, Negin, Majid, Hifsa, Richard, Hongchi, Luke, Brett, Avan, Noura, Amilia, Siming, Wei, Alex, Soroush, and Ozaki-sensei.

Many thanks go to Dr Sarma, Prof. Cockburn, Dr Revin, and Prof Wada for stimulating discussions on mutual research interests. Thanks go to the Ossila team for the interesting R&D projects which I could work on during my MSc and PhD. Thanks go to Kojima-sensei for interesting discussions, great time in the Old House, and lending me his THz detector to characterise my THz emitters. Special thanks go to Ben Stevens for growth and being my second supervisor, David Childs for advice on characterisation, Ken Kennedy and Saurabh Kumar for advice on device fabrication, and particularly to my supervisor Richard Hogg for always believing in me and his invaluable supervision.

It was also a great honour to collaborate with Ohnishi-san and Mukai-san of Rohm Semiconductor, Japan, on this highly technological project. I gratefully acknowledge financial support from the Engineering and Physical Sciences Research Council (EPSRC) for my studentship to undertake research into terahertz technology. Final thanks are to my family and Aneta for their continuous support throughout my University career.

Publications

[1] K.J.P. Jacobs, B.J. Stevens, T. Mukai, D. Ohnishi, R.A. Hogg, "Non-Destructive Mapping of Doping and Structural Composition of MOVPE-grown High Current Density Resonant Tunnelling Diodes through Photoluminescence Spectroscopy", Journal of Crystal Growth, 418, 102, (2015)

[2] K.J.P. Jacobs, B.J. Stevens, O. Wada, T. Mukai, D. Ohnishi, R.A. Hogg. "Accurate Mesa Area Control of High Current Density Resonant Tunnelling Diodes for THz Applications". To be submitted to Applied Physics Express for publication

[3] K.J.P. Jacobs, B.J. Stevens, T. Mukai, D. Ohnishi, R.A. Hogg, "Absolute Energy Levels of Resonant Tunnelling Diodes Resolved by Photoluminescence Spectroscopy". To be submitted to Applied Physics Letters for publication

Conferences & Invited Seminars

[1] K.J.P. Jacobs, B.J. Stevens, T. Mukai, D. Ohnishi, R.A. Hogg "Non-destructive Wafer Level Mapping of Doping Concentrations of High Speed Resonant Tunnelling Diodes for Terahertz Applications", 18th European Molecular Beam Epitaxy workshop (EUROMBE2015), Canazei, Italy, March (2015)

[2] K.J.P. Jacobs, B.J. Stevens, T. Mukai, D. Ohnishi, R.A. Hogg, "Non-destructive Mapping of Doping and Structural Composition of High Current Density Resonant Tunnelling Diodes Grown by Metal-Organic Vapour Phase Epitaxy Through Photoluminescence Spectroscopy", 46th International Conference on Solid State Devices and Materials (SSDM2014), Tsukuba, Japan, September (2014)

[3] K.J.P. Jacobs, B.J. Stevens, T. Mukai, D. Ohnishi, R.A. Hogg, "Non-destructive Mapping of Doping and Structural Composition of High Current Density Resonant Tunnelling Diodes Grown by MOVPE Through Photoluminescence Spectroscopy", Invited Seminar at the Graduate School of

Engineering, Department of Electrical and Electronic Engineering, Kobe University, Japan, September (2014)

[4] K.J.P. Jacobs, B.J. Stevens, T. Mukai, D. Ohnishi, R.A. Hogg, "Non-Destructive Mapping of Doping Concentrations in High Current Density Resonant Tunnelling Diodes", UK Semiconductor Conference, University of Sheffield, UK, July (2014)

[5] K.J.P. Jacobs, B.J. Stevens, T. Mukai, D. Ohnishi, R.A. Hogg, "Photoluminescence Spectroscopy of High Current Density Resonant Tunnelling Diodes Grown by Metal-Organic Vapour Phase Epitaxy", Sixth International Conference on Optical, Optoelectronic and Photonic Materials and Applications (ICOOPMA2014), University of Leeds, UK, July (2014)

[6] K.J.P. Jacobs, B.J. Stevens, T. Mukai, D. Ohnishi, R.A. Hogg, "Photoluminescence Characterisation of High Current Density Resonant Tunnelling Diodes", UK Semiconductor Conference, University of Sheffield, UK, July (2013)

Contents

Chapter 1

Introduction

1.1 Historical Perspective

In 1958, a Japanese PhD research student at Tokyo Tsushin Kogyo (now known as Sony Corporation) named Leo Esaki reported at the International Conference on Solid State Physics in Brussels on a new diode which exhibited "negative resistance" [1]. The diode which he invented was named the Esaki or tunnel diode after the quantum-mechanical tunnelling effect which the device exploits. He received in 1973 (in conjunction with Giaever and Josephson) the Nobel Prize in physics for his pioneering work in electron tunnelling in semiconducting materials [2]. Electron tunnelling through potential barriers occurs due to the quantum mechanical wave nature of particles, an effect forbidden in classical physics. Fig. 1.1 schematically illustrates the principle.

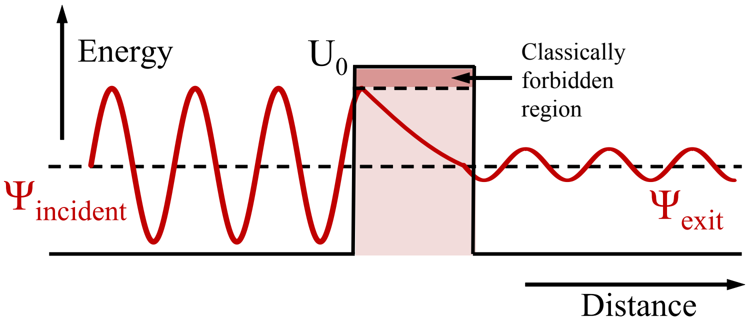

Figure 1.1: Rectangular potential barrier and particle wave function

As the wavefunction of the particle is required to be continuous at the barrier, while satisfying the Schrodinger equation in the form of Eq. 1.1, there is a finite probability that a particle will tunnel through the potential barrier U_0.

$$\frac{-\hbar^2}{2m}\frac{\partial^2\Psi(x)}{\partial x^2} = (E - U_0)\Psi(x) \tag{1.1}$$

As the wavefunction exhibits an exponential decay inside the barrier, the probability of finding the particle on the other side of the barrier is both dependent on the width and the confinement potential of the barrier. Esaki's original tunnel diode was made out of a high impurity level germanium p-n junction with a very thin depletion region where the valence band of the p-type material and the conduction band of the n-type material nearly overlapped. Fig. 1.2 schematically shows the operation principle of the diode exhibiting "negative resistance".

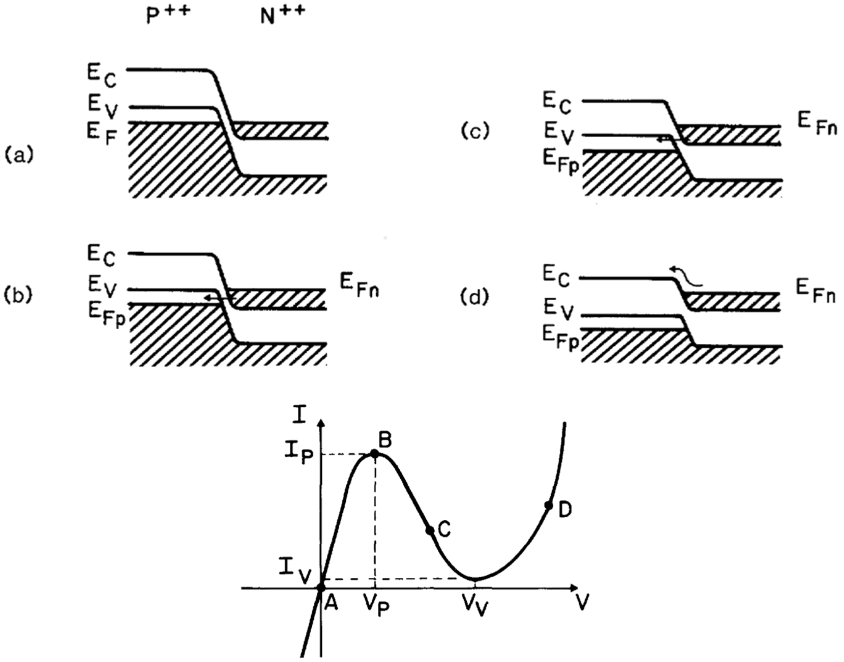

Figure 1.2: Energy band diagram of a tunnel diode at points A, B, C, and D on the V-I characteristic. Adapted from [3]

For a reverse bias and low forward bias below the peak voltage, Vp, a current flows between the n and p-type sides of the diode. As the depletion width is very thin (typically between 20 to 50 angstroms) at the p-n junction due to the high doping concentrations (typically n $>10^{19}$cm^{-3}), electrons can tunnel through the barrier between the conduction band states of the n^+ material and the valence band states of the p^+ material. When the bias is increased beyond Vp, the tunnelling current drops rapidly as the bands between both sides become misaligned and there is an absence of states in the forbidden region between the conduction and valence bands. A further increase in forward bias beyond the valley voltage, Vv, results into conduction of carriers through diffusion as a normal p-n diode.

Due to the negative differential resistance region in the V-I characteristic, this device was commonly used for microwave communications, radar, high frequency amplifier, logic circuits, and oscillator applications, as early transistors did not operate well at frequencies of several GHz [4] [5]. The conduction mechanism of the tunnel diode relies on quantum mechanical tunnelling, which is much faster than the drift and diffusion conduction mechanisms from conventional diodes and transistors [69]. From a practical perspective, this early device suffered from being a two terminal device which made it hard to use in control circuits, and did not offer any advantages as price was concerned, compared to the transistor. The tunnel diode was later still used in some special applications, but never really received large-scale use [7].

In 1973, Tsu and Esaki reported on a new tunnelling phenomenon in a superlattice, by investigating the electrical transport properties of a superlattice. They predicted that the computed resonances in the transmission coefficient of the superlattice can be observed in the electrical domain, such as in the form of a V-I characteristic [8]. Later in 1974, Chang, Tsu, and Esaki successfully demonstrated a device based on their previous theoretical work, known today as the resonant tunnelling diode (RTD) [9]. Resonant tunnelling of electrons was observed in a double-barrier heterostructure with a thin GaAs layer sandwiched between two AlGaAs barriers. For a GaAs layer of only 50 angstroms, which is smaller than the carrier thermal de Broglie wavelength ($\sim$ 250 A for electrons in GaAs at room temperature), discrete energy levels were created in the well which led to a negative differential resistance characteristic. This result demonstrated the real potential of molecular beam epitaxy (MBE) as electronic structures could be tailored on the nm level with extremely smooth films and interfaces for a specific device application by controlling the wavefunction of carriers [10].

In 1983, Sollner *et al.* reported on tunnelling experiments with the observation of negative differential conductance at terahertz frequencies. This stimulated renewed interest in the device for terahertz applications [11]. The RTD is more suitable than the Esaki diode for high frequency applications as the device capacitance, a limiting factor for high frequency performance, can be engineered depending on the structural parameters of the device. Parasitic capacitance limits the high-frequency performance of the RTD as high frequency displacement currents are shunted across the RTD, thereby effectively reducing the impedance of the RTD. The capacitance of the Esaki diode is typically high as the depletion layer thickness is very thin due to the high doping levels which are required to make the semiconductor degenerate. This capacitance limits the high frequency performance of the Esaki diode, due to the charging effect of the RC time constant. The RC time constant is typically dominated by the contact resistance and the device depletion capacitance. A typical Ge tunnel diode (50 μm (L) x 50 μm (W) x 10 μm (H)) has a bulk resistance of 1 ohm and a junction capacitance of 2.7 pF. For a time constant of 2.7 ps, the high frequency capability of this device is limited to 37 GHz ($f_{\text{limit}} = 1/(10RC)$) [12].

1.2 Basic Principle of Resonant Tunnelling Diode

The double barrier resonant tunnelling diode (DBRTD) typically consists of an undoped quantum well (QW) sandwiched between two undoped potential barriers surrounded by doped emitter and collector layers. AlGaAs/GaAs has been a very popular material system for DBRTDs due to excellent lattice matching of AlGaAs to a GaAs substrate. As the DBRTD is an open quantum system, quasi-bound electronic states are formed within the QW. Carriers tunnel through these resonant states from the emitter to the collector. This principle is schematically illustrated in Fig. 1.3.

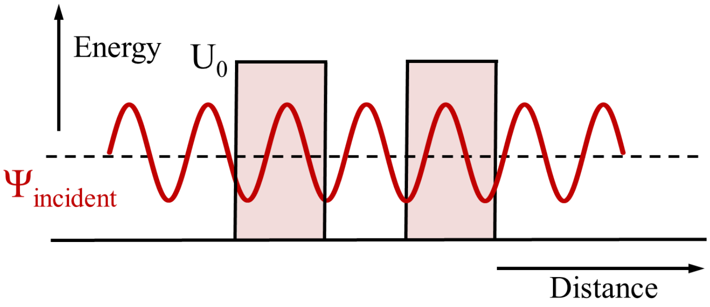

Figure 1.3: Electron wave resonance in a double barrier heterostructure

The electron wave resonance of a resonant tunnelling diode is similar to optical transmission in a Fabry-Perot etalon. The transmission probability function is unity for a symmetrical system, and is less than unity for an asymmetric system. For an asymmetric system, the reflections are not compensated inside the resonator which prevents the wave to build to the required level for unity transmission. Asymmetry can be introduced to the system by making one barrier thicker and/or by changing the confining potential of the barrier, or by applying an external bias to the structure. Resonant tunnelling occurs when the energy of the electrons in the emitter coincides with a quasi-bound state energy level. By applying an external bias to the structure, the alignment of the emitter can be swept along the quasi-bound states of the QW. Current flows as electrons tunnel through the structure and are swept out of the collector layer by the applied electric field once they tunnel out of the barrier on the collector side.

Fig. 1.4 shows (a) the Fermi sphere of electrons in the 3D emitter region at zero temperature, (b) the schematic energy-band diagram of the RTD, and (c) the corresponding V-I characteristic. The electrons in the 3D emitter lie within the Fermi sphere with a radius of k_F. The tunnelling increases when the resonant energy level passes through the Fermi sphere. The tunnelling current drops rapidly when the resonant energy level drops below the conduction band of the emitter as no electron states are present within the band-gap. The reduction in current leads to the creation of the negative differential resistance (NDR).

An important figure of merit is the peak to valley current ratio (PVCR), which is the ratio between the on and off resonance current.

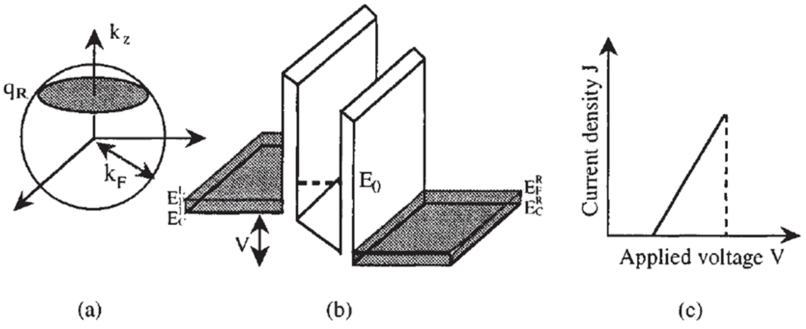

Figure 1.4: (a) Fermi sphere of electrons in the emitter (b) schematic energy-band diagram of the RTD (c) corresponding V-I characteristic. Adapted from Mizuta & Tanoue [13]

A large PVCR maximises the dynamic range of the device. The valley current can often be associated with thermionic emission through higher resonant states or above the barrier, scattering by phonons, impurities, and interface roughness, tunnelling via impurity states in the barriers, and tunnelling via X and L states [13].

1.3 Summary of Previous Work

In 1983, Sollner *et al.* demonstrated that charge transport in a RTD can be very fast with experiments at 2.5 THz for a GaAs/AlGaAs based RTD [11]. The intrinsic response time of the device was measured experimentally by investigating the difference in the V-I performance at direct current (DC) and high frequency. To produce alternating current (AC) signals across the double-barrier structure, an optically pumped methanol laser operating at 2.5 THz was matched to the tungsten whisker antenna of a corner reflector antenna mount, where the RTD was bonded to [14].

Fig. 1.5 (a) schematically illustrates the corner reflector antenna mount which was used to supply DC and AC signals to the DBRTD. Fig. 1.5(b) shows the measured V-I characteristics up to 2.5 THz.

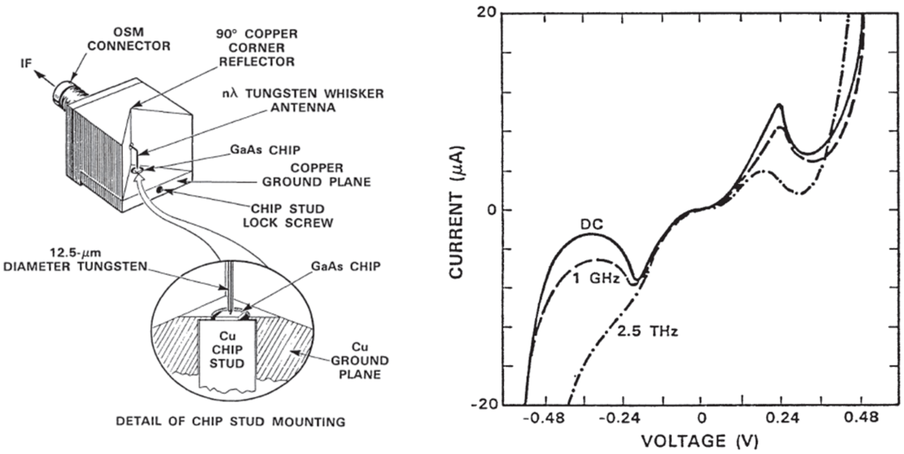

Figure 1.5: (a) Corner reflector antenna mount used in the experiments to supply DC bias and AC signals to the RTD (b) V-I curves taken up to 2.5 THz. Adapted from [14]

Sollner *et al.* found that the V-I curve at 2.5 THz was different in the NDR region from the DC curve as the negative differential resistance disappeared in one direction. This was taken as evidence that the charge transit time for this device was in the order of 60 fs, which was in good agreement with theoretical modelling.

Oscillations were demonstrated for the first time from double barrier resonant tunneling structures by Sollner *et al.* in 1984, with a maximum observed oscillation frequency of 18 GHz at 200 K with an output power of 50 μW [15]. Since that time, several attempts have been made to construct practical devices at millimeter and submillimeter wavelengths. Waveguide and planar technology have both been implemented for the realisation of RTD oscillators. In early work, the implementation of the RTD in a waveguide oscillator was mainly limited by the inductance of the whisker used to connect the device in the circuit. Fig. 1.6 shows an example of a waveguide oscillator developed by Brown *et al.* in 1992 where a semiconfocal open-cavity resonator was used to stabilise a RTD waveguide oscillator at frequencies near 100 GHz [16]. Planar technology has become more popular due to recent advancements in the semiconductor manufacturing technology allowing feedback and antenna elements to be placed very near to the active area to reduce losses.

In 1991, Brown *et al.* obtained oscillation frequencies up to 712 GHz using DBRTDs at room temperature using the InAs/AlSb material system, with the RTD devices mounted in a rectangular waveguide resonator. The measured power density at 360 GHz was 90 Wcm^{-2}.

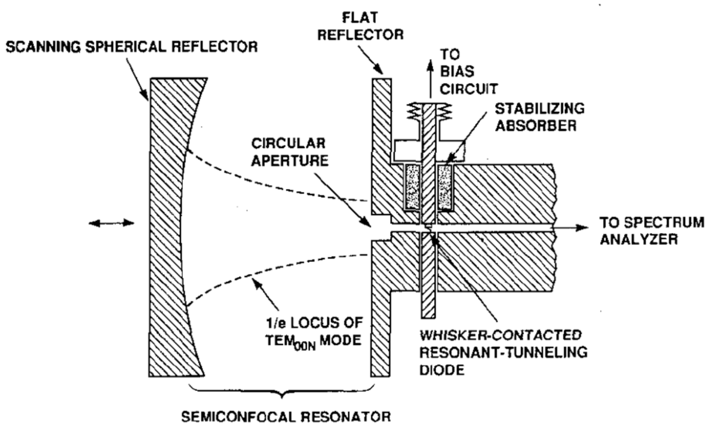

Figure 1.6: Schematic cross-sectional diagram of a quasi-optical RTD oscillator for operation in the 100 GHz region. Adapted from [16]

The InAs/AlSb material system offers three main advantages over the GaAs/AlAs material system for high speed RTDs [17]. The first advantage is that the electron effective mass of InAs is smaller than for GaAs, which does not only increase the confinement energy, but also causes the electrons to drift much more rapidly across a depletion layer. The maximum oscillation frequency increases due to the reduction in depletion layer transit time [18]. Secondly, using InAs instead of GaAs lowers the total series resistance, as nearly ideal ohmic contacts can be formed to InAs with the Fermi level being pinned in the conduction band, which reduces the RC time constant and consequently increases the maximum frequency of operation [19]. The third advantage is that the InAs/AlSb band structure has a staggered type-II band offset at the Γ point, compared to the type-I offset in a GaAs/AlAs structure, which leads to a higher current density for a given barrier thickness as the attenuation coefficient of an electron tunnelling through an AlSb barrier is smaller than it would at the same energy in the AlAs barrier. The smaller attenuation coefficient due to the band offset causes the electrons to tunnel through the barriers close to the valence-band edge of AlSb [20][21][22]. A high current density leads to a reduced RC time constant of the RTD, as required for high speed operation.

It has also been found that GaAs/AlAs DBRTDs do not offer very good PVCRs for peak current densities greater than 10^5 Acm^{-2}. A maximum PVCR of 3.0 was reported for a GaAs/AlAs DBRTD with a Jpeak of 1.2×10^5Acm^{-2} [23]. Techniques have been implemented to improve the PVCR of GaAs based DBRTDs, which include using as $In_xGa_{1-x}As$ layer as a pre-well by lowering the space charge barrier for the injected electrons [25] [24] on the emitter side or as quantum well material [26], and AlGaAs "chair barriers" outside the AlAs barriers of the DB structure to improve the PVCR to 6.3 at room temperature [27]. Noteworthy is that triple barrier resonant tunnelling structures (TBRTS) also offer better PVCRs as the first quantum well in the structure acts as an energy filter for the electrons to tunnel through the second quantum well [28]. Oscillations up to 420 GHz were demonstrated in GaAs/AlAs resonant tunneling diodes with a PVCR of only 1.5 at room temperature [18].

The InGaAs/AlAs/InP material has become very popular today as this material system can offer a very high PVCR and ΔJ (ΔJ = Jpeak - Jvalley) [29][30][31][32][33]. A PVCR of 30 was reported in 1988 for a RTD with a pseudomorphic InAs subwell and AlAs barriers [34]. The InAs subwell permitted a thinner well while still maintaining a low resonance energy, providing a large interval between resonant levels, and greatly reducing alloy scattering compared to a InGaAs well. Of note is that AlAs is often preferred in this material system above ternary InAlAs barriers due to low alloy-related scattering. However, the requirement is that the barrier thickness is small enough (<3 nm) to ensure that the AlAs material is pseudomorphically grown to the $In_{0.53}Ga_{0.47}As$ for a low misfit dislocations density [35].

In 1994, Smith *et al.* proposed a technique with the top ohmic contact in a GaAs/AlAs RTD replaced by a Schottky contact, and the device downscaled to submicron dimensions to reduce the parasitic resistance and consequently increase the maximum frequency of operation of GaAs/AlAs based devices [36]. A f_{MAX} of 900 GHz was determined from measured DC and microwave parameters. Later in 1995, the same research group estimated a maximum frequency of oscillation 2.2 THz for similar Schottky-collector resonant tunnel diodes (SRTDs) using the AlAs/InGaAs/InP material system [37]. A 64-element oscillator array was demonstrated, shown in Fig. 1.7(a) which oscillated coherently at 650 GHz, while a 16-element array at 290 GHz produced an output power of 28 μW [38]. To minimise the DC power consumption in the bias stabilisation circuit, they implemented a Schottky diode behaving as a non-linear resistor [39][40]. Further, a Si lens, shown in Fig.1.7(b) was used to couple the power from the oscillator array from the substrate into free-space, and to ensure coherent oscillation of all 64 array elements. Electron beam lithography was used to fabricate these RTDs with 0.1 micron T-shaped air-bridged Schottky collectors [41].

During the same period, Orihashi *et al.* from Tokyo Tech. reported in 1995 on one THz harmonic oscillation for a InGaAs/AlAs RTD integrated with a slot antenna [42]. Fig. 1.8 schematically shows the THz emitter. This device was fabricated using e-beam lithography (EBL) and metal-insulator-metal (MIM) reflectors were integrated for the slot antenna. Fundamental and third-harmonic frequencies of 342 GHz and 1.02 THz were reported. The maximum output power at these frequencies was 23 μW and 0.6 μW, respectively.

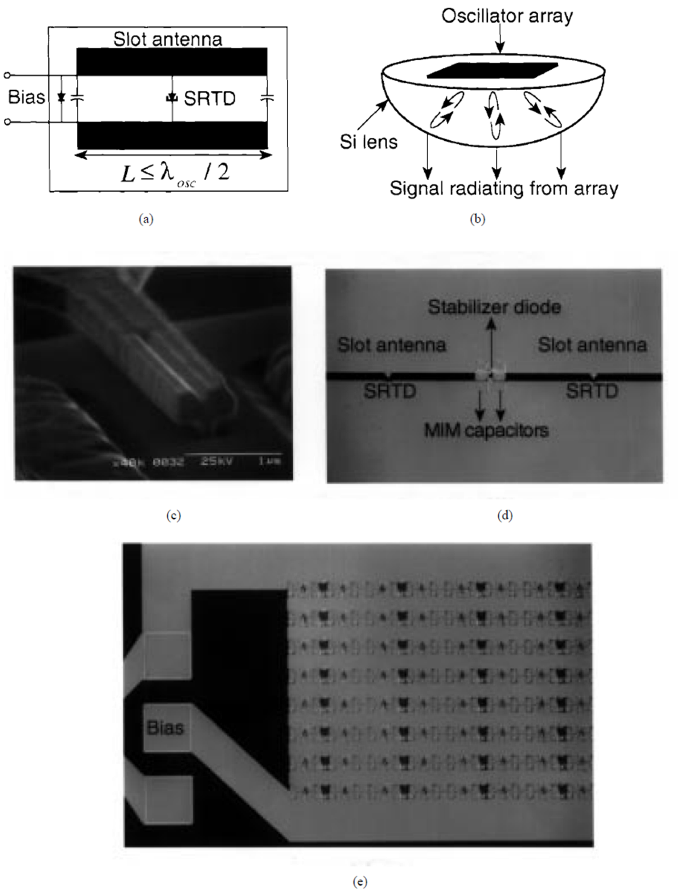

Figure 1.7: THz emitter developed at University of California, Santa Barbara (UCSB) (a) circuit schematic of a SRTD oscillator (b) quasi-optical oscillator array on a silicon lens which formed a resonant cavity (c) SEM photograph of a 0.1 μm contact stripe InGaAs SRTD (d) section of the oscillator array (e) monolithic 64-element oscillator array with slot-antenna coupled SRTDs. Adapted from [38]

A sheet resistor of bismuth was deposited parallel to the RTD on the outside of the antenna to suppress low-frequency (2 to 3 GHz) parasitic oscillations from the external bias circuit. Fundamental oscillation frequencies of 831 GHz, 1.04 THz, and 1.45 THz were later reported by the same research group in 2009 [43], 2010 [44], and 2014 [80], respectively. To achieve a fundamental oscillation at 831 GHz, Suzuki *et al.* from Tokyo Tech. optimised the collector spacer layer thickness to 20 nm and reduced the mesa area to less than 1 μm^2 to minimise the parasitic capacitance of the RTD. The device had an ultra-high peak current density of 18 mA/μm^2 and a PVCR of 2.

To further increase the oscillation frequency to 1.04 THz, Suzuki *et al.* introduced a graded emitter and thin barriers in the DBRTD to reduce the transit time in the collector depletion region and the resonant tunnelling time, respectively. An output power of 7 μW was achieved at 1.04 THz with a peak current density of 24 mA/μm^2 for the MOVPE grown RTD [30][46].

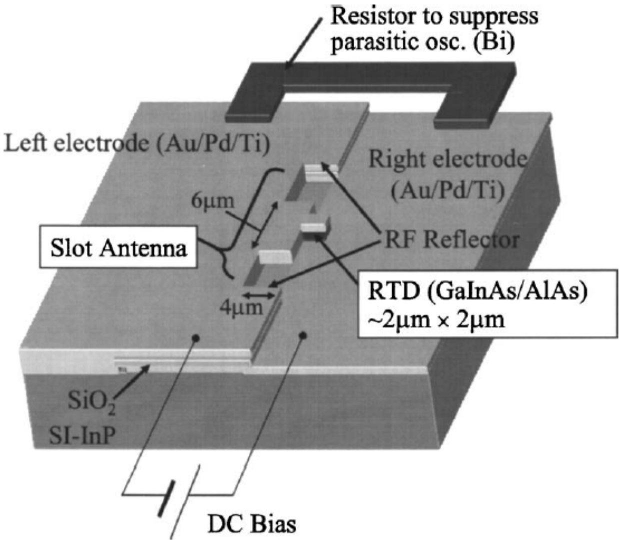

Figure 1.8: THz emitter using a RTD oscillator integrated with a slot antenna, developed at Tokyo Tech., Japan. Adapted from [42]

Fig.1.9 (a) schematically illustrates the effect of the graded emitter on the band structure. The three step graded emitter reduces the transit time in the collector depletion region by suppressing the transition between the Γ and L bands as the resonant level align in the quantum well at a lower bias. Another technique previously applied by the group to reduce the electric field in the collection region was spike doping the collector region. With this technique, schematically illustrated in Fig. 1.9(b), the oscillation frequency was increased to 898 GHz [47].

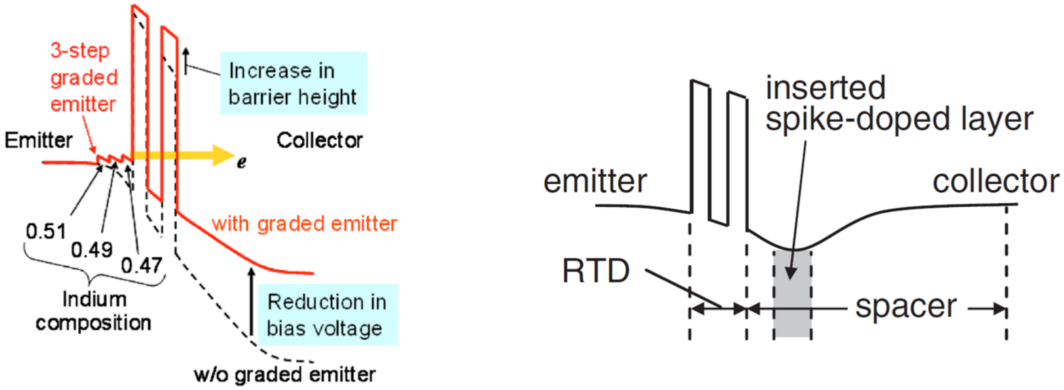

(a) (b)

Figure 1.9: Schematic conduction-band profile of RTD (a) with (solid line) and without (dashed line) graded emitter, adapted from [44] (b) Spike doping in the collector spacer layer, adapted from [47]

In 2011, Feiginov *et al.* at TU Darmstadt, reported on a RTD oscillator operating at a fundamental frequency of 1111 GHz with a RTD mesa area of 0.35 μm^2 and a peak current density of 14 mA/μm^2. A planar Vivaldi antenna on a dielectric membrane was used to extract the radiation from the resonator [48]. In this configuration, the antenna emitted the radiation in the plane of the membrane which mechanically held the emitting antenna and resonator together. Fig. 1.10 shows an image of the emitter.

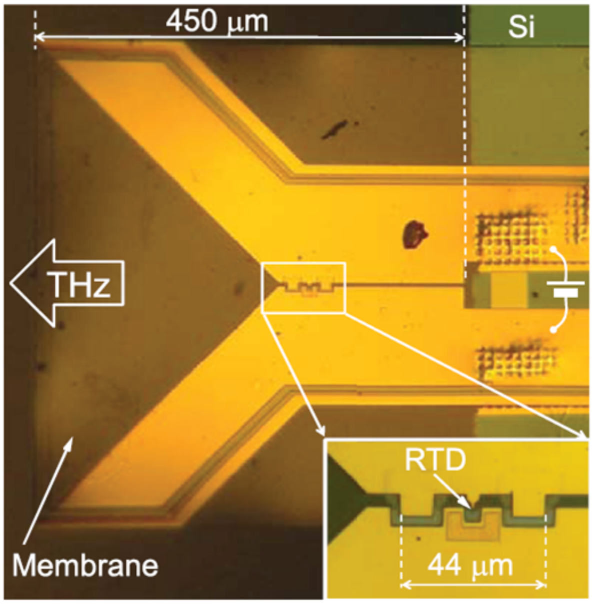

Figure 1.10: THz emitter developed at TU Darmstadt operating at 1111 GHz. Adapted from [48]

Tokyo Tech. demonstrated fundamental oscillation at 1.31 THz in 2012 with an output power of 10 μW through optimisation of the well width and barrier thickness to further reduce the tunnelling time through the DBRTD. This was achieved with a RTD mesa area of 0.33 μm^2 and a thin quantum well of 3.9 nm and potential barriers of 1.0 nm [49]. A fundamental oscillation frequency of 1.42 THz with an output power of $\sim$ 1 μW was reported in 2014 by the same group through further optimisation of the collector spacer thickness [50]. The optimum spacer thickness was 12 nm, due to the trade-off between the transit time in the collector depletion region and the parasitic device capacitance. Most recently, they reported on an oscillation frequency of 1.55 THz through optimisation of the antenna length to 16 μm [81]. The aforementioned results are primarily based on slot antenna resonators mounted on a Si lens.

In 2013, Koyama *et al.* from Canon, Japan, observed oscillations at 1.02 to 1.4 THz using RTD based oscillators integrated with patch antennas without a Si lens to couple the radiation from the chip into the atmosphere [52]. This was achieved with InGaAs/InAlAs triple-barrier RTDs exhibiting a peak current density of 2.8 mA/μm^2. Fig. 1.11(a) schematically shows the THz emitter. The requirement of the Si lens to couple the radiation out of the substrate was eliminated by using a square patch antenna for surface emission. Another technique to eliminate the bulky Si lens was developed by Tokyo Tech., based on a square patch antenna fabricated on a 7 μm thick BCB layer stacked on the RTD with slot resonator [53]. This technique is shown schematically in Fig. 1.11 (b). A 4:1 ratio between the power in the upward and substrate direction was reported.

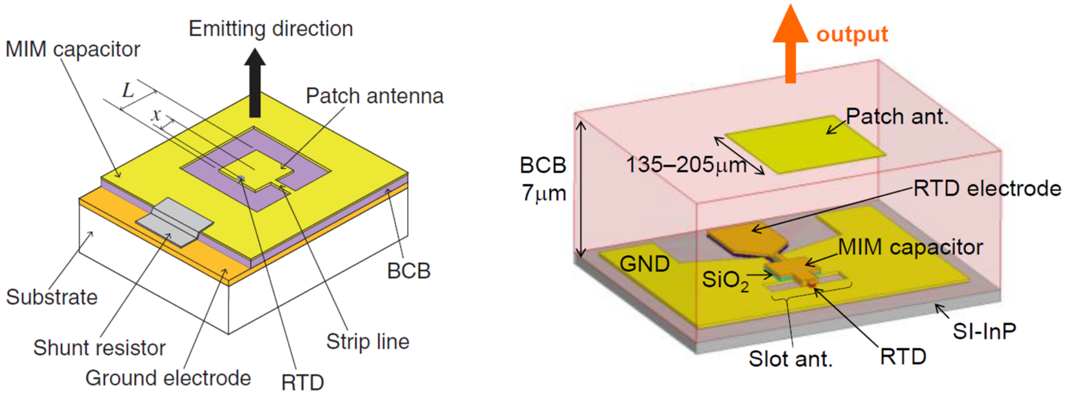

Figure 1.11: (a) RTD-based oscillator with an integrated square patch antenna developed at Canon inc., Japan. Adapted from [52] (b) RTD oscillator integrated with patch antenna developed at Tokyo Tech., Japan. The patch antenna is located directly above the slot antenna. Adapted from [53]

Since the early 1990s, several techniques have also been introduced to increase the output power of the oscillator through improved resonator and RTD design, including offset slot antennas and oscillator arrays. Maximum power transfer occurs from the RTD to the antenna when the radiation conductance of the antenna is equal to half the negative differential conductance of the RTD (assuming the antenna loss is negligible). The maximum extractable output power from a tunnel diode is determined by the current and voltage spans (ΔI and ΔV)in the NDR region, which is approximately equal to (3/16) $\Delta V \Delta I$, for a cubic polynomial fit to the I-V characteristic [54][55][56]. Due to the capacitance of the RTD, the oscillation frequency of the RTD is often far below the peak conductance of the antenna, which results in a small radiation conductance. One solution was proposed by Prof. Asada at Tokyo Tech. in 2006 based on an offset slot antenna structure, where the position of the RTD is shifted within the slot antenna [62]. With this technique, the radiation conductance and oscillation frequency can be independently determined by the lengths of the short and long parts of the slot, respectively. This technique was later successfully demonstrated [58][59][60]. In 2013, Suzuki *et al.* demonstrated a high output power oscillation of $\sim$ 400 μW at 530

- 590 GHz using a single oscillator with an offset slot antenna [60]. Since Reddy *et al.* demonstrated coherent oscillation in 1997 with an oscillator array [38] several attempts were carried out to increase the output power by using similar techniques [61][62][63][64][65][66]. Combined output powers of 610, 270, and 180 μW at 620, 770, and 810 GHz were obtained with a two-element array in 2013 [60]. Suzuki *et al.* expects output powers of 10 and 1 mW at 500 GHz and 1 THz, respectively, with more than five to ten elements [60].

1.4 Terahertz Sources and Applications

This section gives a brief overview of the recent technological advances in terahertz source technology, and gives an introduction into the emerging applications of terahertz radiation. Fig. 1.12 shows a diagram of the electromagnetic spectrum. The terahertz band spans the region of the electromagnetic spectrum between the microwaves and the infrared light, typically between 100 GHz and 30 THz.

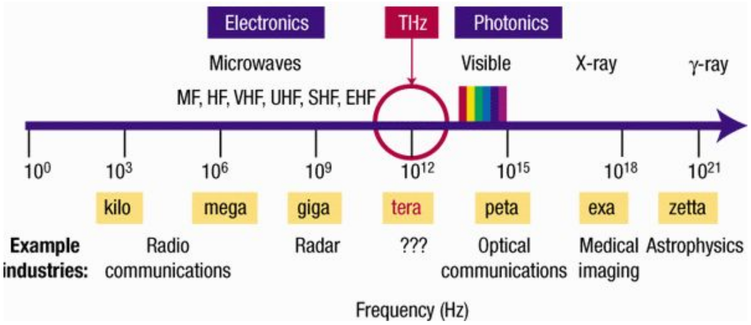

Figure 1.12: Electromagnetic wave spectrum (adapted from http://thznetwork.net)

Due to the technological challenges to develop efficient emitters in the THz region, this band of frequencies is also known as the terahertz gap [67].

Optical and electronic devices have been developed to operate in the THz range, but often suffer from a low output power [68]. Fig. 1.13 shows a diagram of output power (as of year 2007) of the THz sources as a function of frequency. As shown in Fig. 1.13, the high and low frequency ends of the THz spectrum are covered by the optical and solid-state electronic devices, respectively. The major factor which limits the operating frequency of the solid-state electronic devices is the carrier transit-time [69]. The optical devices are challenged by the requirement of low energy band-to-band transitions to extend towards longer emission wavelengths. Recent optical THz devices, denoted by ovals in Fig. 1.13, include the P-type Ge laser [70], THz quantum cascade laser (QCL) [71][72][73], THz wave parametric amplifier [74][75], and the uni-travelling

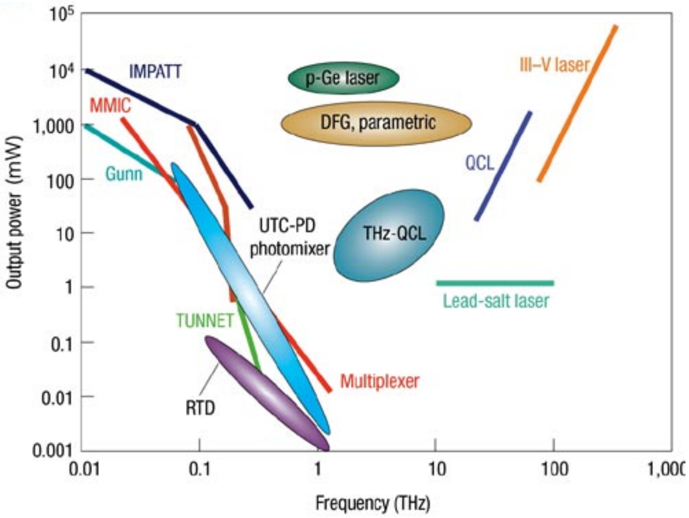

Figure 1.13: THz emission output power as a function of frequency. The ovals denote recent THz sources (adapted from [68])

carrier photodiode (UTC-PD) [76]. Amongst the electronic devices, the RTD is known to be a very promising candidate for the realisation of compact, coherent, and room temperature operating THz emitters. Transistors have also been studied intensively on the electron device side [77][78][79]. To date, the RTD is recognised as the fastest electronic device with a fundamental oscillation at 1.55 THz being reported by Suzuki *et al.* in 2014 [80] [81].

Applications of THz waves include ultra-broadband wireless communications [82], spectroscopic sensing and imaging [68][83], and high-resolution radar [84]. Many non-conducting materials (e.g. paper, leather, plastic, soft biological tissue) are semi-transparent to THz waves and have “THz fingerprints”, which allows for imaging, identification, and analysis of materials. There is currently a growing interest in the applications of THz radiation for active security imaging and pharmaceutical and industrial process monitoring. An example, terahertz time domain spectroscopy (TDS) is used in the semiconductor industry to evaluate the properties of semiconductor wafers, including mobility and conductivity [68]. Furthermore, as THz radiation is non-ionising, unlike X-rays, this radiation is very attractive for biomedical applications (e.g. cancer detection) as the relatively low photon energy of the THz wave does not cause damage to biological soft tissue. It is also well known that the spectral region between 0.1-30 THz can offer ultra-fast wireless communications [89]. A more in-depth discussion about the future of THz communications is given in the following section. For the development of these emerging applications, there is a big drive for the realisation of compact, low cost, and room temperature operating THz sources. An electronics based approach is essential for low cost and/or consumer applications.

1.5 Terahertz Communications

For over the last three decades, wireless data rates have been following Edholm's Law, doubling roughly every 18 months. Future data rates of tens of Gbit/s are therefore expected [90]. Higher carrier frequencies are required for these data rates as the channel capacity is limited by the bandwidth. Shannon's channel capacity formula is given by Eq. 1.2

$$C = B \log_2 \left(1 + \frac{S}{N}\right) \tag{1.2}$$

where C is the channel capacity, B the bandwidth, and S/N the signal-to-noise ratio. THz communication systems will be used in the future to transmit very high data rates over short distances to establish local wireless connections to high speed fiber-optical networks [91]. For future wireless data communications, Britz proposed a so called Triple-Stack Nanocellular Architecture which uses existing cellular and wi-fi infrastructure for low bandwidth traffic in combination with the high bandwidth THz "super channel" for short distance high data traffic [92]. At the moment, the lower frequency band of 275 - 3000 GHz has not been allocated yet for specific uses, and offers very high wireless data which match the current bandwidths of fibre optic communications [93].

Demonstration of THz communication has been extensively carried out [85][86][87][88]. In 2011, Mukai *et al.* demonstrated wireless data transmission at 1.5 Gbit/s in the 300 GHz band using a RTD coupled to an antenna with simple amplitude shift keying (ASK) modulation [94]. In 2012, Ishigaki *et al.* demonstrated wireless data transmission using ASK modulation with RTDs oscillating at 542 GHz with bit error rates (BERs) of $2\text{x}10^{-8}$ and $3\text{x}10^{-5}$ for data rates of 2 and 3 Gbit/s, respectively [86]. At these frequencies, the wavelength is small enough to allow on-chip integration of the antenna. However, at 300 GHz, the maximum omni-directional quarter wavelength antenna size is 250 µm, which results in a small collecting area [92]. In addition to the small collection area of the THz antenna, the atmospheric propagation loss at THz frequencies is high, due to the strong absorption by oxygen and water vapour molecules [95]. As a result, significant antenna gain will be required for applications beyond one meter. Due to the high directionality of high gain antennas, maintaining link alignment between the transmitter and receiver will also become more challenging for long distance data transmission. Some sort of dynamic beam shaping/steering technology will be required in the future [96]. The use of highly directional antennas will inevitably lead to efficient reuse of the spectrum for point-to-multipoint applications and enable high density wireless networks.

1.6 Gaps in Knowledge

1.6.1 Optical Characterisation of High Current Density Resonant Tunnelling Diode

The QW perfection and uniformity, and doping uniformity of the emitter and collector layers of the RTD over the full wafer are important parameters. High peak and low valley currents are required, with low device variability and high yield in volume manufacture, to make RTD based THz emitters commercially viable. Standard non-destructive wafer characterisation techniques provide limited information about these parameters.

To date, the optical properties of high current density RTDs are relatively unexplored. In this work, conflicting assertions in the literature are clarified about unambiguous identification of the photoluminescence (PL) emission from high current density RTD structures. Furthermore, a new PL mapping has been developed to allow important information about doping level and uniformity, ternary alloy composition and uniformity, and uniformity of quantum well thickness to be deduced with a high spatial uniformity in a non-destructive test. The observed non-uniformity is further analysed by X-Ray diffraction to confirm details of the growth process. The use of the Moss-Burstein shift to measure the doping concentration, and map the uniformity of doping for a particular epitaxy tool is also new. A new non-destructive optical characterisation technique to resolve the absolute energy level position of the first electron state of RTDs through low temperature PL spectroscopy is also reported. The absolute energy levels of MOVPE grown InGaAs/AlAs/InP based RTD structures are resolved by a combination of type-I and type-II QW recombination, which allows an investigation into important scattering mechanisms affecting device performance, and monitor the QW alloy content and thickness non-destructively.

1.6.2 Terahertz Resonant Tunnelling Diode Emitter Fabricated Through I-line Photolithography

Electron-beam lithography (EBL) is typically applied for the realisation of micron and submicron scale terahertz RTDs. Eliminating EBL in the fabrication stage is desirable from a manufacturing perspective, as patterning a full wafer with EBL can be time consuming and costly due to the serial nature of the process.

In this work, a novel fabrication method of micron scale, high current density RTDs is developed based on air-bridge technology, standard i-line photolithography, and wet chemical etching.

The method is not only simple and manufacturable, but also provides accurate control over the final device area (and hence characteristics) by measuring the V-I characteristic of the RTD during the fabrication process. This technique allows ultra-fine control of the final device area and characteristics. Accurate control of the final device area is not only important from a manufacturing standpoint to minimise the device variability in volume manufacture, but also with regard to impedance matching the RTD to the antenna for maximum power extraction. The requirement for a second contact metallisation to the emitter layer is also eliminated by guiding the emitter current through the full RTD structure by a second contact electrode on the collector side, simplifying the overall device fabrication process. There appears to be no report about such a technique in the literature.

Furthermore, the V-I characteristics of high current density RTDs for THz applications have primarily been reported in the literature for measurements at room temperature. In this work, temperature dependent V-I characterisation was carried out from 20 K - 300 K to investigate the temperature dependent device performance. Using the newly developed techniques, terahertz emission at 350 GHz is demonstrated by integration of the RTD and a slot antenna.

1.7 Outline of Thesis

This thesis covers the development work of InGaAs/AlAs/InP high current density RTDs grown by MOVPE for THz applications. Chapter 1 covers a historical perspective, the basic principle of double barrier RTDs, a summary of previous work, and the application of RTDs to THz emission, including THz communications. Chapter 2 covers optical spectroscopy of InGaAs. Photoluminescence is investigated as a function of doping concentration to enable non-destructive mapping of doping concentrations of the contact and the collector/emitter layers on the wafer level. The PL results are compared with electrochemical capacitance-voltage (eCV) and secondary ion mass spectrometry (SIMS) data. Chapter 3 investigates PL spectroscopy of high current density RTDs. PL is investigated for doped and undoped structures, and for structures with varying well widths. The experimental results are compared with modelling results. Low temperature PL mapping is used to investigate the ternary alloy composition and uniformity, and uniformity of quantum well thickness of the RTD. The details of the growth process are further explored by high resolution X-Ray diffractometry (HR-XRD). Chapter 4 describes the design of the THz emitter with the RTD and monolithical integration of the antenna on an InP substrate. The design considerations of the emitter are discussed including metal-insulator-metal (MIM) structure design, slot antenna design, bias stabilisation, and output coupling of the THz radiation. Chapter 5 describes the fabrication process of the RTD based THz emitter. This chapter also covers the development work of the air-bridge structure, low resistance ohmic contacts, and MIM structure. Chapter 6 covers device characterisation of the RTD based THz emitter. The dependence of the electrical V-I characteristics on mesa area and temperature is investigated. THz emission is demonstrated in the 300 GHz band. Chapter 7 provides a summary of this thesis and details future work.

References

[1] Esaki, L., Solid State Physics in Electronics and Telecommunications, Proceedings of the International Conference on Solid State Physics, Brussels, 1958 (Desirant, M. and Michels, J. L., ed.), Vol. 1, Semiconductors, Part I, Academic Press (1960) p. 514.

[2] Esaki, Leo. "Long Journey into Tunneling," Nobel lecture, 12 December, 1973, published in Reviews of Modern Physics, Vol. 46 (1974), p. 237 also in Nobel Lectures, Physics 1971-1980, Editor Stig Lundqvist (World Scientific Publishing Co., 1992).

[3] Swartz, R., "Technology commentary - In perspective: The tunnel diode," Solid-State Circuits Conference. Digest of Technical Papers. 1986 IEEE International , vol.XXIX, no., pp.277,280, 19-21 Feb. 1986

[4] G. E.-Tunnel Diode Manual, First Edition G. E. Semiconductor Products Dept. Mar. 1961

[5] Thompson, P., "The place of the tunnel diode in solid-state circuits," Solid-State Circuits Conference. Digest of Technical Papers. 1962 IEEE International , vol.V, no., pp.66,67, 14-16 Feb. 1962

[6] S. M. Sze & Kwok K. NG, Tunnel Devices, in Physics of Semiconductor Devices, 3rd ed. New York: Wiley, 2007, pp. 417-465.

[7] Dr. Charles W. Mueller, an oral history conducted in 1975 by Mark Heyer and Al Pinsky, IEEE History Center, Hoboken, NJ, USA.

[8] R. Tsu and L. Esaki, "Tunneling in a Finite Superlattice," Appl. Phys. Lett., 22, No. 11, pp. 562564, 1973.

[9] L. L. Chang, L. Esaki, R. Tsu, "Resonant Tunneling in Semiconductor Double Barriers" Appl. Phys. Lett. 24, 593 (1974)

[10] H. Sakaki: Proc. Int. Symp. Foundation of Quantum Mechanics, Phys. Soc. J., p. 94 (1984)

[11] T. C. L. G. Sollner, W. D. Goodhue, P. E. Tannenwald, C. D. Parker, D. O. Peck, “Resonant tunneling through quantum wells at frequencies up to 2.5 THz”, Appl. Phys. Lett. 43, 588 (1983)

[12] K. K. N. Chang, “Parametric and Tunnel Diodes,” Prentice-Hall, Englewood Cliffs, New Jersey, 1964.

[13] Mizuta H and Tanoue T, The Physics and Applications of Resonant Tunneling Diodes (Cambridge: Cambridge University Press), 1995.

[14] Capasso, Federico. Physics of quantum electron devices. Berlin ; New York : Springer-Verlag, 1990.

[15]] T. C. L. G. Sollner, P. E. Tannenwald, D. D. Peck, and W. D. Goodhue, “Quantum Well Oscillators”, Appl. Phys. Lett., Vol. 45, No. 12, pp. 13191321, 1984.

[16] E. R. Brown, C. D. Parker, K. M. Molvar, and K. D. Stephan, “A quasioptically stabilized resonant tunnelling diode oscillator for the millimetre and submillimetre-wave regions,” IEEE Transactions on Microwave Theory and Techniques, vol. 40, no. 5, pp. 846-850, May 1992.

[17] Brown, E.R.; Soderstrom, J.R.; Parker, C.D.; Mahoney, L.J.; Molvar, K.M.; McGill, T.C., “Oscillations up to 712 GHz in InAs/AlSb resonanttunneling diodes,” Applied Physics Letters , vol.58, no.20, pp.2291,2293, May 1991

[18] E. R. Brown, T. C. L. G. Sollner, C. D. Parker, W. D. Goodhue, and C. L. Chen, “Oscillations up to 420 GHz in GaAs/AlAs resonant tunneling diodes,” Appl. Physics Lett., vol. 55, no. 23, pp. 1777-1719, 1989.

[19] C. A. Mead and W. G. Spitzer, “Fermi Level Position at Metal-Semiconductor Interfaces”, Phys. Rev., 134, A713 (1964).

[20] J. R. Soderstrom, E. R. Brown, C. D. Parker, L. J. Mahoney, J. Y. Yao, T. G. Andersson, and T. C. McGill, “Growth and characterization of high current density, high-speed InAs/AlSb resonant tunneling diodes”, Applied Physics Letters 58, 275 (1991)

[21] J. R. Soderstrom, E. T. Yu, M. K. Jackson, Y. Rajakarunanayake, and T. C. McGill, “Two-band modeling of narrow band gap and interband tunneling devices”, Journal of Applied Physics 68, 1372 (1990)

[22] G. Bastard, “Theoretical investigations of superlattice band structure in the envelope-function approximation”, Phys. Rev. B 25, 7584 (1982)

[23] E. Ozbay and David M. Bloom, “110 GHz monolithic resonant tunneling diode trigger circuit”, IEEE Electron Device Lett., vol. 12, pp.480 -482 (1991)

[24] Riechert, H.; Bernklau, D.; Reithmaier, J.-P.; Schnell, R.D., “High performance resonant tunnelling structures on GaAs substrates,” Electronics Letters , vol.26, no.5, pp.340,342 (1990)

[25] K.L. Lear, W.S. Lee, and J.S. Harris, “Experimental Dependence of Resonant Tunnel Diode Current on Accumulation Layer Band Profiles,” IEEE Trans. Electron Devices 36, 2619 (1989).

[26] H.M. Yoo, S.M. Goodnick, and J.R. Arthur, “Influence of spacer layer thickness on the current-voltage characteristics of AlGaAs/GaAs and AlGaAs/InGaAs resonant tunneling diodes”, Appl. Phys. Lea. 56, 84 (1990).

[27] V.K. Reddy, AJ. Tsao, and D.P. Neikirk,“ High peak-to-valley current ratio AlGaAs/AlAs/GaAs double barrier resonant tunnelling diodes”, Electron. Let. 26, 1742 (1990).

[28] T. Nakagawa, H. Inamoto, T. Kojima and K. Ohta, “Observation of resonant tunneling in AlGaAs/GaAs triple barrier diodes”, Appl. Phys. Lett., 49, 73 (1986)

[29] T. P. E. Broekaert and C. G. Fonstad: IEDM Tech. Dig., 1989, p. 559.

[30] H. Sugiyama, H. Yokoyama, A. Teranishi, S. Suzuki, and M. Asada, “Extremely High Peak Current Density of over 1 x 106 A/cm2 in InP-based InGaAs/AlAs Resonant Tunneling Diodes Grown by Metal-organic Vapor-phase Epitaxy”, Jpn. J. Appl. Phys., Vol. 49, 051201, 2010.

[31] T. P. E. Broekaert and C. G. Fonstad: J. Appl. Phys. 68 (1990) 4310.

[32] H. Sugiyama, H. Matsuzaki, Y. Oda, H. Yokoyama, T. Enoki, and T. Kobayashi: Jpn. J. Appl. Phys. 44 (2005) 7314.

[33] J. Osaka and H. Matsuzaki: Jpn. J. Appl. Phys. 40 (2001) 3114.

[34] Tom P. E. Broekaert, Wai Lee, and Clifton G. Fonstad, “Pseudomorphic In0.53Ga0.47As/AlAs/InAs resonant tunneling diodes with peak-to-valley current ratios of 30 at room temperature”, Applied Physics Letters 53, 1545 (1988)

[35] Elliott R. Brown ; C. D. Parker ; Arthur R. Calawa ; M. J. Manfra ; T. C. L. G. Sollner ; Chang L. Chen ; Stella W. Pang ; K. M. Molvar; “High-speed resonant-tunneling diodes made

from the In0.53Ga0.47As/AlAs material system". Proc. SPIE 1288, High-Speed Electronics and Device Scaling, 122 (August 1, 1990)

[36] Smith, R.P.; Alien, S.T.; Reddy, M.; Martin, S.C.; Liu, J.; Muller, R.E.; Rodwell, M.J.W., "0.1 μm Schottky-collector AlAs/GaAs resonant tunneling diodes", Electron Device Letters, IEEE , vol.15, no.8, pp.295,297, Aug. 1994

[37] M. Reddy, M J. Mondry, M. J. W. Rodwell, S. C. Martin, R. E. Muller, R. P. Smith, D. H. Chow, and J. N. Schulman, "Fabrication and dc, microwave characteristics of submicron Schottky-collector AlAs/In0.53Ga0.47As/InP resonant tunneling diodes", Journal of Applied Physics 77, 4819 (1995)

[38] Reddy, M.; Martin, S.C.; Molnar, A.C.; Muller, R.E.; Smith, R.P.; Siegel, P.H.; Mondry, M.J.; Rodwell, M.J.W.; Kroemer, H.; Allen, S.J., Jr., "Monolithic Schottky-collector resonant tunnel diode oscillator arrays to 650 GHz," Electron Device Letters, IEEE , vol.18, no.5, pp.218,221, May 1997

[39] M. Reddy, R. Y. Yu, H. Kroemer, M. J. W. Rodwell, S. C. Martin, R. E. Muler, et al, "Bias stabilisation for resonant tunnel diode oscillators," IEEE Microwave and Guided Wave Letters, vol. 5, no.7, pp.219-221, July 1995.

[40] J. T. Wallmark and A. H. Dansky, "Nonlinear biasing resistors for microwave tunnel-diode oscillators," IEEE Transactions on Microwave Theory and Techniques, vol.11, pp.260-262, July 1963.

[41] R. E. Muller, S. C. Martin, R. P. Smith, S. T. Allen, M. Reddy, U. Bhattacharya, and M. J. W. Rodwell, "Electron-beam lithography for the fabrication of air-bridged, submicron Schottky-collectors," J. Vac. Sci. Technol. B , vol. 12, no. 6, pp. 36683672, Nov./Dec. 1994

[42] N. Orihashi, S. Suzuki, and M. Asada, "One THz harmonic oscillation of resonant tunneling diodes", Applied Physics Letters 87, 233501 (2005)

[43] S. Suzuki, A. Teranishi, K. Hinata, M. Asada, H. Sugiyama, and H. Yokoyama, "Fundamental Oscillation of up to 831 GHz in GaInAs/AlAs Resonant Tunneling Diode", Appl. Phys. Exp., vol. 2, 054501, 2009.

[44] S. Suzuki, M. Asada, A. Teranishi, H. Sugiyama, and H. Yokoyama, "Fundamental oscillation of resonant tunneling diodes above 1 THz at room temperature," Appl. Phys. Lett., vol. 97, 242102(1-3), 2010.

[45] S. Suzuki & M. Asada, 46st International Conference on Solid State Devices and Materials, Tsukuba, 2014

[46] H. Sugiyama, A. Teranishi, S. Suzuki, and M. Asada, "Structural and electrical transport properties of MOVPE-grown pseudomorphic AlAs/InGaAs/InAs resonant tunneling diodes on InP substrates“, Jpn. J. Appl. Phys. vol. 53, 031202(1-6), 2014.

[47] S. Suzuki, K. Sawada, A. Teranishi, M. Asada, H. Sugiyama, and H. Yokoyama, "Fundamental Oscillations at $\sim$ 900 GHz with Low Bias Voltages in RTDs with Spike-doped Structures," Electronics Lett., Vol. 46, pp. 10061007, 2010.

[48] Michael Feiginov, Cezary Sydlo, Oleg Cojocari, and Peter Meissner,"Resonant-tunnelling-diode oscillators operating at frequencies above 1.1 THz", Applied Physics Letters 99, 233506 (2011)

[49] H. Kanaya, H. Shibayama, R. Sogabe, S. Suzuki, and M. Asada, "Fundamental Oscillation up to 1.31 THz in Resonant Tunneling Diodes with Thin Well and Barriers", Appl. Phys. Express, vol. 5, 124101, Nov. 2012.

[50] H. Kanaya , R. Sogabe , T. Maekawa , S. Suzuki , M. Asada . Kanaya, H., Sogabe, R., Maekawa, T., Suzuki, S., Asada, M.: "Fundamental oscillation up to 1.42 THz in resonant tunneling diodes by optimized collector spacer thickness", J. Infrared, Millim. Terahertz Waves, 2014, 35, pp. 425431

[51] Maekawa, T.; Kanaya, H.; Suzuki, S.; Asada, M., "Frequency increase in terahertz oscillation of resonant tunnelling diode up to 1.55 THz by reduced slot-antenna length," Electronics Letters , vol.50, no.17, pp.1214,1216, Aug. 14 2014

[52] Koyama,Y., Sekiguchi,R., and Ouch,T., "Oscillations up to 1.40 THz from Resonant-Tunneling-Diode-Based Oscillators with Integrated Patch Antennas", Appl. Phys. Express 6 064102 (2013)

[53] Okada, K.; Suzuki, S.; Asada, M., "Resonant-tunneling-diodeterahertz oscillator integrated with slot-coupled patch antenna," Indium Phosphide and Related Materials (IPRM), 26th International Conference on , vol., no., pp.1,2, 11-15 May 2014

[54] Kim, C.S.; Brandli, A., "High-Frequency High-Power Operation of Tunnel Diodes," Circuit Theory, IRE Transactions on , vol.8, no.4, pp.416,425, Dec 1961

[55] Trambarulo, R., “Some X-band microwave Esaki-diode circuits,” Solid-State Circuits Conference. Digest of Technical Papers. 1961 IEEE International , vol.IV, no., pp.18,19, 15-17 Feb. 1961

[56] M. Asada, S. Suzuki, and N. Kishimoto, “Resonant Tunneling Diodes for Sub-Terahertz and Terahertz Oscillators”, Jpn. J. Appl. Phys., vol.47, pp.4375-4384, 2008.

[57] S. Suzuki and M. Asada, “Proposal of Resonant Tunneling Diode Oscillators with Offset-Fed Slot Antennas in Terahertz and Sub-Terahertz Range”, Jpn. J. Appl. Phys. Vol. 46, No. 1, pp. 119-121 (2007).

[58] M. Shiraishi, H. Shibayama, K. Ishigaki, S. Suzuki, M. Asada, H. Sugiyama, and H. Yokoyama, “High Output Power ($\sim$ 400 μW) Oscillators at around 550GHz Using Resonant Tunneling Diodes with Graded Emitter and Thin Barriers”, Appl. Phys. Express, vol. 4, 064101, 2011.

[59] K. Hinata, M. Shiraishi, S. Suzuki, M. Asada, H. Sugiyama, and H. Yokoyama, “Sub-Terahertz Resonant Tunneling Diode Oscillators with High Output Power ($\sim$ 200 μW) Using Offset-Fed Slot Antenna and High Current Density”, Appl. Phys. Express vol.3, 014001, 2010.

[60] S. Suzuki, M. Shiraishi, H. Shibayama, and M. Asada, “High-Power Operation of Terahertz Oscillators with Resonant Tunneling Diodes Using Impedance-Matched Antennas and Array Configuration”, IEEE J. Selected Topics Quantum Electron., vol. 19, no. 1, 8500108, Feb. 2013.

[61] S. Suzuki, N. Orihashi, and M. Asada, “Mutual injection locking between sub-THz oscillating resonant tunneling diodes,” Jpn. J. Appl. Phys., vol. 44, no. 48, pp. L1439L1441, 2005.

[62] S. Suzuki and M. Asada, “Coherent power combination in highly integrated resonant tunneling diode oscillators with slot antennas,” Jpn. J. Appl. Phys., vol. 46, no. 46, pp. L1108L1110, 2007.

[63] S. Suzuki, K. Urayama, and M. Asada, “Coherent power combination in multi-element subterahertz resonant tunneling diode oscillators coupled with metalinsulatormetal stub structure,” Appl. Phys. Exp., vol. 1, pp. 093001-1093001-3, 2008.

[64] M. Asada and S. Suzuki, “Theoretical analysis of coupled oscillator array using resonant tunneling diodes in subterahertz and terahertz range,” J. Appl. Phys., vol. 103, pp. 124514-1124514-9, 2008.

[65] T. Fujii, H. Mazaki, F. Takei, J. Bae, M. Narihiro, T. Noda, H. Sakaki, and K. Mizuno, "Coherent power combining of millimeter wave resonant tunneling diodes in a quasi-optical resonator," in Proc. IEEE MTT-S Int. Microwave Symp., WE3F-28, Jun. 1996, pp. 919922.

[66] H. I. Cantu andW. S. Trunscott, "Injection-locking and power combining with double barrier resonant tunnelling diodes," Electron. Lett., vol. 37, no. 20, pp. 12641265, Sep. 2001.

[67] T. Nagatsuma "Generating millimeter and terahertz waves", IEEE Microw. Mag., vol. 10, p.64 , 2009.

[68] M. Tonouchi "Cutting-edge terahertz technology", Nature Photon., vol. 1, pp.97 - 105 , 2007.

[69] S. M. Sze & Kwok K. NG, "Tunnel Devices," in Physics of Semiconductor Devices, 3rd ed. New York: Wiley, 2007, pp. 417-465.

[70] Bergner, Andreas; Heugen, Udo; Brundermann, Erik; Schwaab, Gerhard; Havenith, Martina; Chamberlin, Danielle R.; Haller, E.E., "New p-Ge THz laser spectrometer for the study of solutions: THz absorption spectroscopy of water," Review of Scientific Instruments , vol.76, no.6, pp.063110,063110-5, Jun 2005

[71] Khler, R., Tredicucci, A., Beltram, F., Beere, H.E., Linfeld, E.H., Davies, A.G., Ritchie, D.A., Iotti, R.C., and Rossi, F.: "Terahertz semiconductor-heterostructure laser", Nature, 2002, 417, pp. 156159

[72] Williams, B.S.: "Terahertz quantum-cascade lasers", Nat. Photonics, 2007, 1, pp. 517525, doi:10.1038/nphoton.2007.166

[73] Fathololoumi, S., Dupont, E., Chan, C.W.I., Wasilewski, Z.R., Laframboise, S.R., Ban, D., Mtys, A., Jirauschek, C., Hu, Q., and Liu, H.C.: "Terahertz quantum cascade lasers operating up to 200 K with optimized oscillator strength and improved injection tunneling", Opt. Express, 2012, 20, (4), pp. 38663876

[74] Kawase,K.,Shikata,J., Ito,H.,"Terahertz wave parametric source", J. Phys. D: Appl. Phys. 35 R1 (2002)

[75] Cook,D.J & Hochstrasser, R.M. "Intense terahertz pulses by four-wave rectification in air". Opt. Lett. 25,1210-1212 (2000).

[76] Ito, H., Nakajima, F., Furuta, T. & Ishibashi, T. “Continuous THz-wave generation using antenna-integrated uni-travelling-carrier photodiodes”. Semicond. Sci. Technol. 20, S191-S198 (2005)

[77] Samoska, L.A.: “An overview of solid-state integrated circuit amplifiers in the submillimeter-wave and THz regime”, IEEE Trans. Terahertz Sci. Technol., 2011, 1, (1), pp. 924, doi:10.1109/TTHZ.2011.2159558

[78] Seo, M., Urteaga, M., Hacker, J., Young, A., Griffith, Z., Jain, V., Pierson, R., Rowell, P., Skalare, A., Peralta, A., Lin, R., Pukala, D., and Rodwell, M.: ’InP HBT IC technology for terahertz frequencies: fundamental oscillators up to 0.57 THz’, IEEE J. Solid-State Circuits, 2011, 46, (10), pp. 22032214, doi:10.1109/JSSC.2011.2163213

[79] Momeni, O., and Afshari, E.: ’High power terahertz and millimeterwave oscillator design: a systematic approach’, IEEE J. Solid-State Circuits, 2011, 46, (3), pp. 583597, doi:10.1109/JSSC.2011.2104553

[80] S. Suzuki & M. Asada, 46st International Conference on Solid State Devices and Materials, Tsukuba, 2014

[81] Maekawa, T.; Kanaya, H.; Suzuki, S.; Asada, M., “Frequency increase in terahertz oscillation of resonant tunnelling diode up to 1.55 THz by reduced slot-antenna length,” Electronics Letters , vol.50, no.17, pp.1214,1216, Aug. 14 2014

[82] T. Kleine-Ostmann and T. Nagatsuma “A review on terahertz communications research”, J. Infrared, Millim. Terahertz Waves, vol. 32, pp.143 -171, 2011

[83] T. Nagatsuma, H. Nishii, and T. Ikeo, “Terahertz imaging based on optical coherence tomography [Invited],” Photon. Res. 2, B64-B69 (2014).

[84] K. B. Cooper , R. J. Dengler , N. Llombart , A. Talukdera , A. V. Panangadana , C. S. Peay and P. H. Siegel “Fast, high-resolution terahertz radar imaging at 25 meters”, Proc. SPIE, vol. 7671, 2010

[85] Asada, M.; Suzuki, S., “Compact THz oscillators with resonant tunneling diodes and application to high-capacity wireless communications,” Applied Electromagnetics and Communications (ICECom), 2013 21st International Conference on , vol., no., pp.1,5, 14-16 Oct. 2013

[86] K. Ishigaki , M. Shiraishi , S. Suzuki , M. Asada , N. Nishiyama and S. Arai "Direct intensity modulation and wireless data transmission characteristics of terahertz-oscillating resonant tunnelling diodes", Electron. Lett., vol. 48, no. 10, pp.582 -583 2012

[87] Ikeda, Y., Kitagawa, S., Okada, K., Suzuki, S., Asada, M., Direct intensity modulation of resonant-tunneling-diode terahertz oscillator up to $\sim$ 30 GHz, IEICE Electronics Express Vol. 12 (2015) No. 3 pp. 20141161

[88] S. Koenig, D. Lopez-Diaz,J. Antes,F. Boes,R., Henneberger,A. Leuther,A. Tessmann,R. Schmogrow,D. Hillerkuss,R. Palmer, T. Zwick,C. Koos, W. Freude,O. Ambacher, J. Leuthold & I. Kallfass, "Wireless sub-THz communication system with high data rate", Nature Photonics 7, 977981 (2013)

[89] H. Song and T. Nagatsuma "Present and future of terahertz communications", IEEE Trans. TeraHz. Sci. Technol., vol. 1, no. 1, pp.256 -263, 2011

[90] S. Cherry "Edholm's law of bandwidth", IEEE Spectrum, vol. 41, no. 7, pp.58 -60, 2004

[91] Handbook of Terahertz Technology for Imaging, Sensing and Communications. Edited by D. Saeedkia, Woodhead Publishing Ltd. 2013.

[92] D. Britz, "Evolution of Extreme Personal Bandwidth and Local Area Triple-Stack Terahertz Wireless Networks", IEEE 802.15-15-10-0150-00-0thz, March 2010.

[93] J. Wells "Faster than fiber: The future of multi-G/s wireless", IEEE Microw. Mag., vol. 10, no. 3, pp.104 -112, 2009

[94] T. Mukai, M. Kawamura, T. Takada, T. Nagatsuma, Tech. Dig. Optical Terahertz Science and Technology Meeting, MF42, Santa Barbara, 2011

[95] Y. Yang, A. Shutler, and D. Grischkowsky, "Measurement of the transmission of the atmosphere from 0.2 to 2 THz," Opt. Express 19, 8830-8838 (2011).

[96] D. Britz, Terahertz Wireless Communications: New Radio Architectures to Meet Exponential Data Growth?, Beyond 4G & LTE-Advanced, Newark, NJ, AT&T,2011

Chapter 2

Optical Spectroscopy of InGaAs

2.1 Introduction

The doping uniformity of the emitter/collector and contact layers of the RTD over the wafer is an important parameter. High peak and low valley currents, and low resistance ohmic contacts are required to maximise the output power of the RTD. Thin potential barriers, and a high doping density are used in the emitter/collector to the increase of incident electron density to achieve a high tunnelling current density. The tunnelling current density is known to be very sensitive to the doping concentration in the emitter as the current density almost doubles for a twofold increase in the emitter doping concentration [35]. A RTD with a high peak current density allows for a reduction in device area, which in turn minimises the parasitic capacitance of the device, as required for high speed operation. Low resistance ohmic contacts are also therefore required, not only to minimise the excess voltage drop of the device which could lead to dc-bistability, but also to minimise the RC time constant. A uniform doping concentration over the wafer is important in volume manufacture to minimise device variability and optimise yield.

This chapter covers photoluminescence spectroscopy of n-type InGaAs. Photoluminescence is measured as a function of doping concentration for InGaAs test-layers at low temperatures and correlated to secondary-ion mass spectroscopy (SIMS) and electrochemical capacitance-voltage (eCV) profiling, to allow a non-destructive measurement of the absolute doping concentration of n-doped InGaAs. This enables non-destructive wafer level mapping of doping concentrations of the collector/emitter and contact layers of the RTD. The rapid non-destructive characterisation and wafer mapping of these structures promises a route to future growth optimisation of the RTD structures.

2.2 Layer Structure and Sample Preparation

InGaAs test layers with varying doping concentrations were grown to measure photoluminescence as a function of doping concentration. These test layers were grown with a staircase-like doping profile (increasing with growth direction), which could later easily be selectively etched off by eCV profiling. This material was grown as part of a doping calibration procedure of the MOVPE reactor. The epitaxial growth was carried out by Dr. B.J. Stevens and consisted of a 100 nm undoped InP buffer layer, followed by five successive 200 nm n-doped $In_{0.53}Ga_{0.47}As$ layers with disilane flows of 20, 50, 150, 300 & 600 sccm, respectively. Fig. 2.1(a) schematically shows the layer structure of the test-structure. The n-doped InGaAs layers are grown on a single 2″ wafer to ensure identical growth conditions for each layer. To investigate the doping uniformity of the contact and emitter/collector layers of the RTD structure, two 2″ test wafers were grown with a single 200 nm n^+ lattice matched InGaAs layer for Si_2H_6 flows of 700 sccm and 55 sccm, for doping concentrations of $2x10^{19}cm^{-3}$ and $3x10^{18}cm^{-3}$, respectively. Fig. 2.1(b) and 2.1(c) schematically show the layer structures used to investigate the doping uniformity of the contact and emitter/collector layers, respectively.

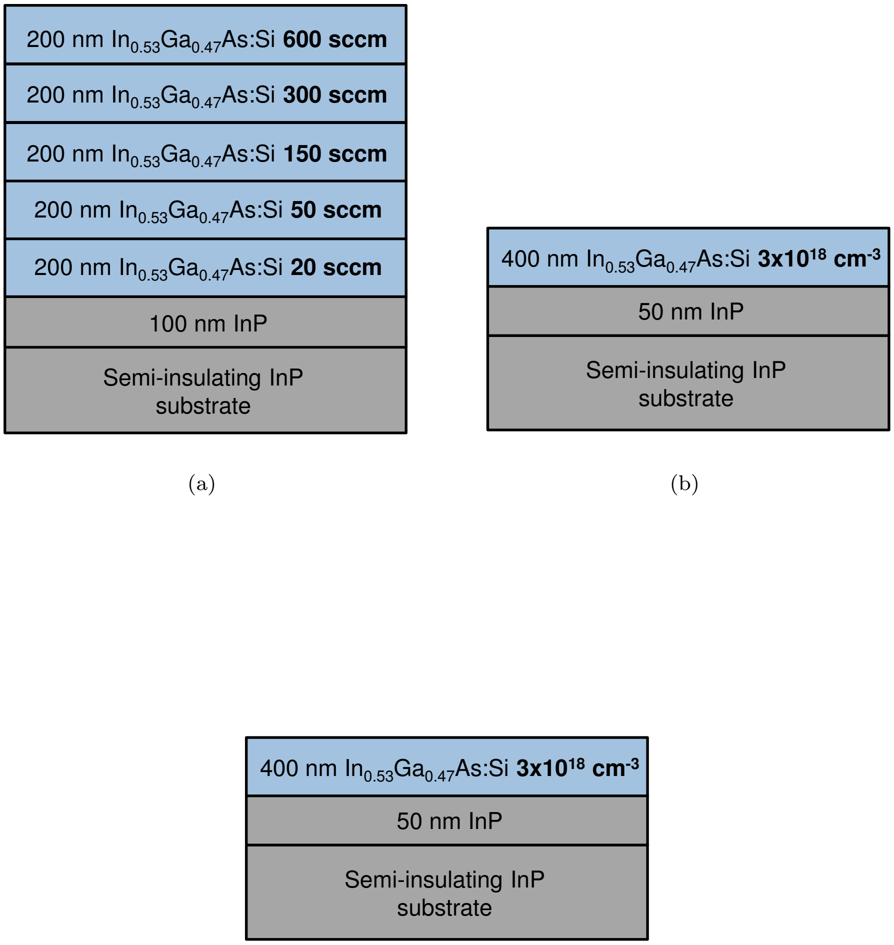

(a) (b)

(c)

Figure 2.1: Schematic of (a) n^+ InGaAs test-structure (b)(c) doping uniformity test-structures with doping concentrations equivalent to the contact and emitter/collector layers of the RTD structure, respectively.

The structural quality of the epitaxy was evaluated by HR-XRD. Fig. 2.2 shows an omega-2theta HR-XRD scan measured on the test-structure shown in Fig.2.1 (a). A negative lattice mismatch of 2.92x10^{-2}°is measured between the InGaAs and the InP substrate diffraction peaks. The signal from the InP substrate is much stronger than the InGaAs layers as the substrate is thicker (350 µm) than the InGaAs layers (1 µm in total). A 2.92x10^{-2}°compressive strain corresponds to an alloy composition of $In_{0.54}Ga_{0.46}As$, indicating good lattice matching to the InP substrate and pseudomorphic growth. This was confirmed by differential interference contrast (DIC) microscopy, as no obvious signs of lattice relaxation were observed.

Rohm Semiconductor carried out the SIMS measurements as part of the doping calibration procedure of the MOVPE reactor.

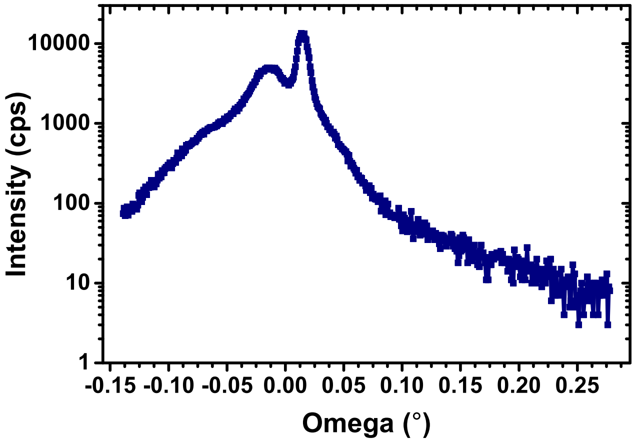

Figure 2.2: HR-XRD omega-2theta scan of the layer structure shown in Fig. 2.1(a)

The doping calibration was performed at a growth temperature of 660 °C. The surface temperature was measured with a Laytec EpiTT pyrometer and the thermocouple setpoint to achieve this was set to 595 °C. Fig. 2.3 shows the measured SIMS profile of silicon (Si) incorporation, and oxygen (O), carbon (C), and hydrogen (H) contamination within the sample, respectively.

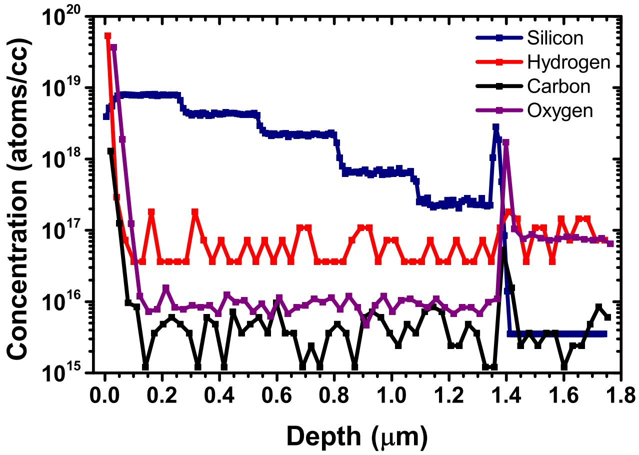

Figure 2.3: Silicon, hydrogen, carbon, and oxygen concentrations as a function of depth of the InGaAs test-structure shown in Fig. 2.1(a). SIMS was carried by out Rohm Semiconductor.

The required Si staircase doping profile is observed in Fig. 2.3. Carbon, hydrogen, and oxygen impurity concentrations of 3x10^{15} atoms/cm^3, 1x10^{16} atoms/cm^3, and 6x10^{16} atoms/cm^3, respectively, are measured which were close to the detection limit of the instrument. Fig. 2.4 shows the measured silicon concentration by SIMS as a function of disilane (Si_2H_6) flow.

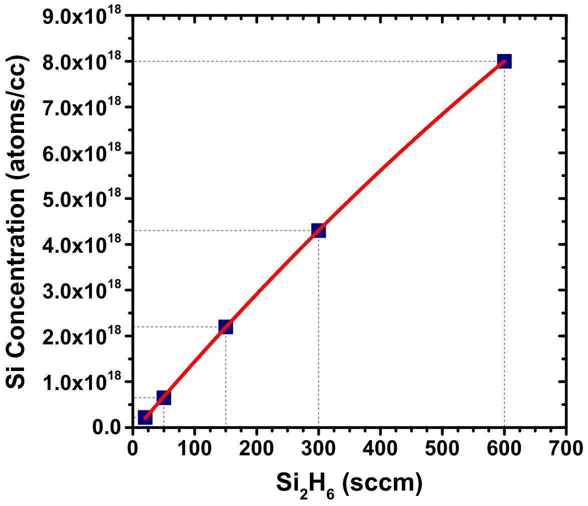

Figure 2.4: Silicon concentration as a function of disilane (Si_2H_6) flow.

A slightly sub-linear concentration increase with increasing Si_2H_6 flow is measured, indicating a lower doping incorporation efficiency for higher Si_2H_6 flows. The measured relation between the Si concentration and disilane flow was used to calibrate the doping profile of the RTD structure.

Optical access was required to each layer of the structure for the PL measurements. This was achieved by eCV profiling through the test-structure. A CVP21 eCV profiler from WEP was used to measure the free-carrier concentration and carrier diffusion throughout the InGaAs test-structure. The eCV profiling technique uses an electrolyte-semiconductor Schottky contact to create a depletion region, a region empty of conducting electrons (for n-type material), but contains ionised donors and electrically active defects [1]. This depletion region has an associated capacitance which is dependent on the free-carrier concentration. Information of the doping and electrically active defect densities is extracted by measuring this capacitance. A 0.1 M tiron based solution was used as the electrolyte. To ensure uniform electrochemical etching at the transition from high-to-low doped layer, voltage etching in electric breakdown mode was applied. In this mode, the profiler preferentially etches the InGaAs surface with the highest doping concentration as the Zener or avalanche breakdown voltage is lower for Schottky barriers with thin depletion widths. A uniform etch is important, as the capacitance of the interface between the electrolyte and semiconductor is highly dependent on the doping concentration and the total interfacial area. Fig. 2.5 shows the measured capacitance density as a function of etch depth for all four etches at 300 K. The insets on the figure represent images of the etched craters, taken with a DIC microscope. The measured capacitances, between successive etches, decreases as a function of etch depth, as expected, as the depletion width of the "Schottky" barrier scales inversely to the doping concentration. Faraday's law of electrolysis is used to calculate the depth etched from the total charge transferred by integrating the etch current (note: this calculation is automatically carried out by the eCV profiler)[1]. A transition from a measured high-to-low free-carrier concentration is observed for the first three etches (A, B, C) for integer multiples of ~ 200 nm. For etch D, the lower transition occurs at a depth of ~ 1 μm, 200 nm more than expected.

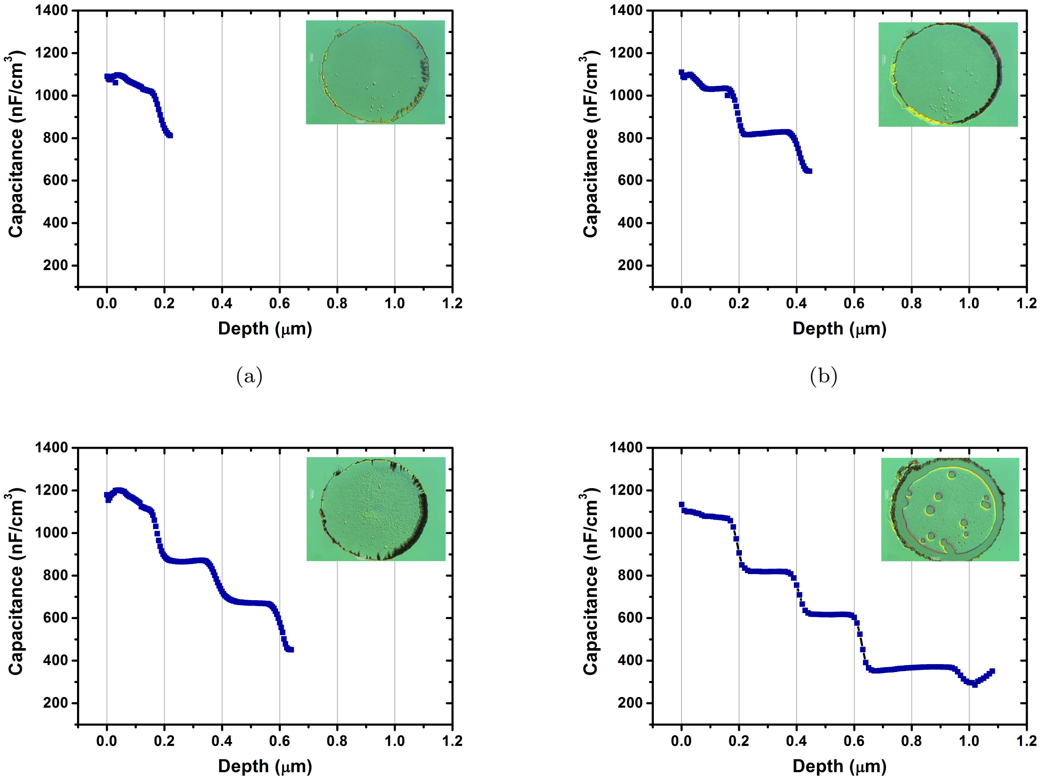

(a) (b)

(c) (d)

Figure 2.5: Capacitance density (nF/cm^2) as a function of etch depth (μm) for (a) ~ 200 nm (b) ~ 400 nm (c) ~ 600 nm (d) ~ 800 nm etch depths, as measured by eCV profiling. The insets show images of 1 mm^2 etched craters taken with a Nomarski DIC microscope.

Fig. 2.6 shows the free-carrier concentration deduced from the capacitance measurements as a function of depth for all four etches. The eCV profiler calculates the free-carrier density, from the data shown in Fig. 2.5, as a function of depth through Eq. 2.1 and Eq. 2.2

$$N = \frac{C^3}{e\epsilon}\frac{\partial V}{\partial C} \tag{2.1}$$

$$X_{dep.} = \frac{\epsilon}{C} \tag{2.2}$$

where N is the free-carrier density, C the capacitance, V the voltage, e the electric charge, ϵ the electric permittivity, and $Xdep.$ the depletion depth. The insets of Fig. 2.6 represent images of the etched craters. Fig. 2.6(d) includes a SIMS profile plot of the same sample.

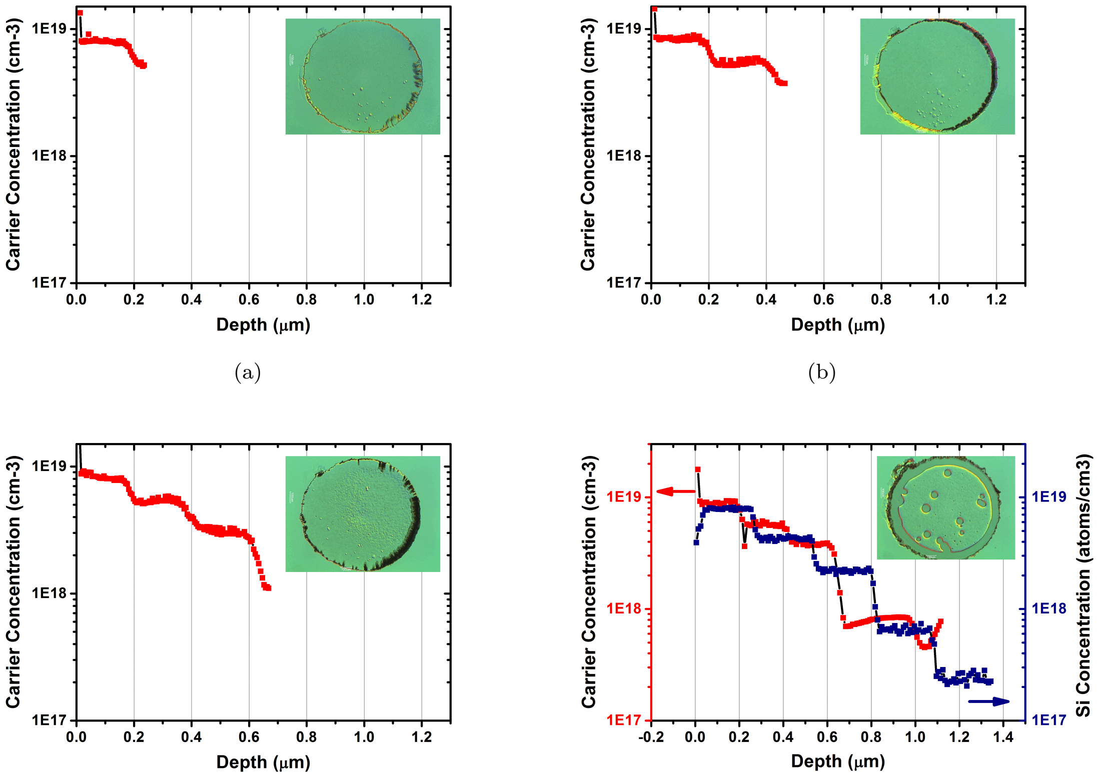

(a) (b)

(c) (d)

Figure 2.6: Free carrier concentration (cm^{-3}) as a function of depth (μm) for (a) ~ 200 nm (b) ~ 400 nm (c) ~ 600 nm (d) ~ 800 nm etch depths. The insets show images of 1 mm^2 etched craters taken with a Nomarski DIC microscope. (d) shows both the free-carrier concentration and silicon dopant concentration measured with eCV and SIMS, respectively.

For the highest doped n$^+$ InGaAs layer, a good correlation is measured between the silicon dopant concentration and free-carrier concentration by SIMS and eCV, respectively, with essentially 100 % of incorporated dopants releasing a charge carrier at room temperature, as expected for n-type materials. Fig. 2.7 shows SIMS and eCV, extracted from Fig.2.6(d), as a function of Si_2H_6 flow. A logarithmic fit is applied to the data to show the strong linear relation between the doping/free-carrier concentration and disilane flow (plotted on a logarithmic scale).

Fig. 2.8(a) shows the measured free-carrier concentration as a function of SIMS, and (b) the measured difference between both measurement techniques. For the deepest (lowest) doped layer,

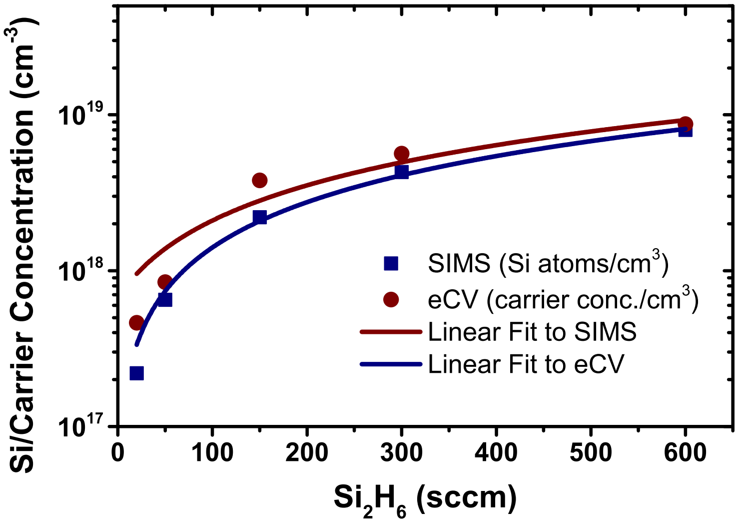

Figure 2.7: Silicon and free-carrier concentration as a function of Si_2H_6 flow measured by SIMS and eCV, respectively.

a 100 % difference is observed between SIMS and eCV. The cause of the measured difference is not yet clear, but is possibly due to non-optimal etching conditions resulting in an increase in area for an apparent increase in free-carrier concentration, the influence of the highly doped crater sidewall on the measurements, and non-uniform etching, as observed for the deeper, lower doped layers as shown on inset images of Fig. 2.6. For accurate eCV measurements, the step layer sequence should have been reversed to avoid issues with the highly doped sidewall. However, for PL studies in order to minimise PL emission from deeper layers, a sequence with reducing doping concentration with increasing etch depth is optimal.

eCV profiling does not only measure the free-carrier concentration, but also the electron diffusion within the n-doped InGaAs layers. In Fig. 2.6, sloped transition regions between doped layers are observed due to the majority carrier screening effect [2]. The free-carrier concentration is smeared out for abrupt spatial changes in impurity concentration.

This screening length is known as the Debye length, and is defined by Eq. 2.3

$$Ld = \sqrt{\frac{\epsilon kT}{e^2 N}} \tag{2.3}$$

where Ld is the Debye length, k the Boltzmann constant, T the temperature, e the electric charge, and N the free-carrier density. Fig. 2.9 shows the calculated Debye length as a function of free-carrier concentration, through Eq. 2.3, for temperatures from 10-300 K. As shown in Fig. 2.9, the

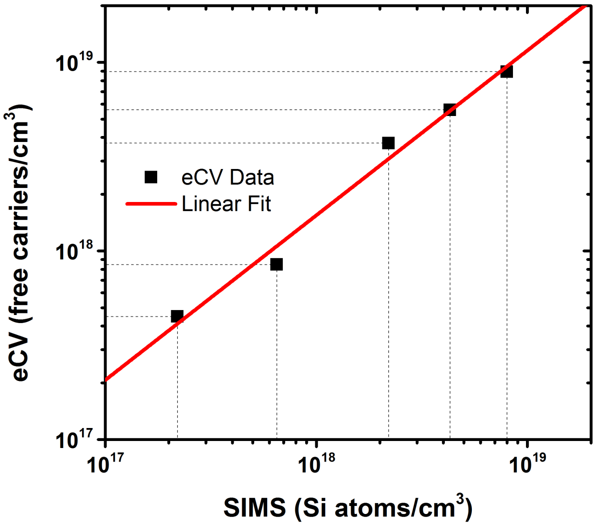

(a)

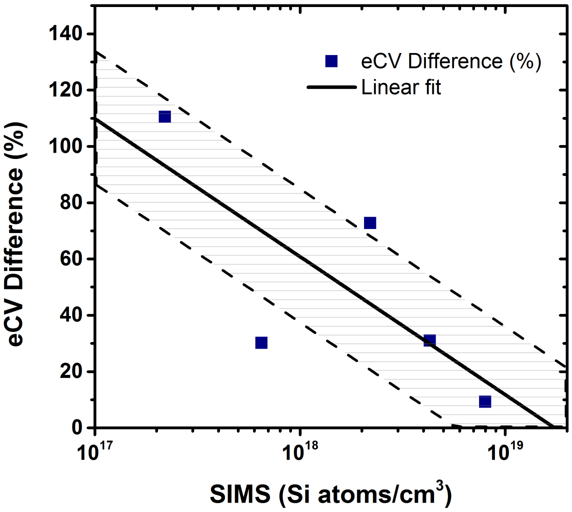

(b)

Figure 2.8: (a) Measured free-carrier concentration as a function of SIMS (b) measured error in free-carrier concentration as a function silicon incorporation. Linear least square fits are applied to the data. The dashed lines indicate a one-standard deviation confidence limit to the fit.

Debye length increases as a function of temperature. This indicates that the doping distribution in the InGaAs test-structure can be resolved with greater accuracy by cooling the sample down. Low temperature profiling is achievable with CV profiling, but becomes impractical for eCV profiling, due to freezing of the electrolyte. Screening lengths of 46 nm, 62 nm, 70 nm, and 156 nm are calculated for free-carrier concentrations of 9.0x10^{18} cm^{-3}, 5.5x10^{18} cm^{-3}, 4.0x10^{18} cm^{-3}, 8.0x10^{17}

cm^{-3}, respectively, for InGaAs with a relative permittivity of 13.9 at 300 K. Good agreement between theory and experimental data is observed. A screening length of 156 nm for the transition region between the 2x10^{17} cm^{-3} and 6x10^{17} cm^{-3} silicon doped layers is not observed. This is attributed to non-uniform etching, as the inset image of the etched crater shown on Fig. 2.6(d) indicates. The etch craters were subsequently cleaved out, bonded with indium to a ceramic tile, and attached to the cryostat's cold finger for temperature dependent PL measurements. All samples were placed on a single ceramic tile to ensure thermal matching.

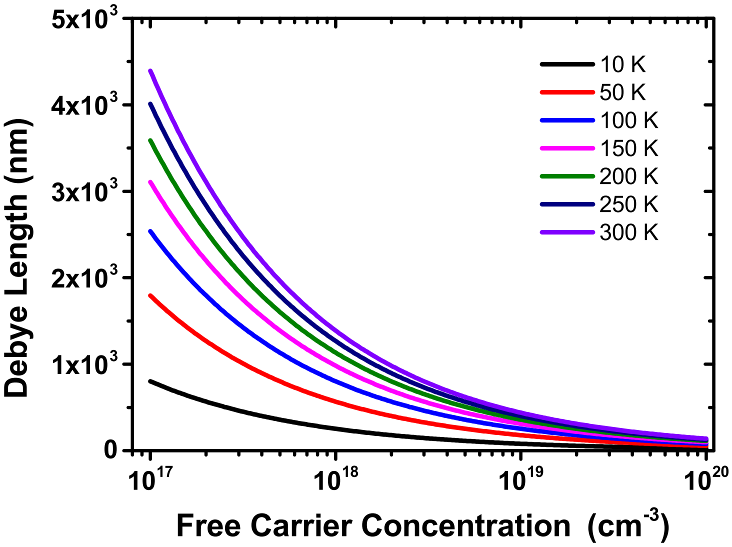

Figure 2.9: Debye length as a function of free carrier concentration in InGaAs for temperatures from 10-300 K.

2.3 Low Temperature Photoluminescence Spectroscopy

The PL experiments were performed in a closed-cycle helium cryostat over a temperature range between 15-300 K. Fig. 2.10 shows a photograph of the low temperature PL mapping tool which was built for this work. A LabVIEW user interface program was written to control the automated X-Y stage and collect and process the spectral data.

A Nd:YVO$_4$ laser at 532 nm was used for optical excitation, pulsed at 20 Hz by an optical chopper. Neutral density filters were installed for excitation density dependent measurements. Laser excitation at a wavelength of 532 nm was selected to minimise the penetration depth of the optical light in InGaAs. The penetration depth is defined as the depth at which 1/e (i.e. 37 %) of the total incident light is transmitted [3]. The photon density as a function of distance is governed by the

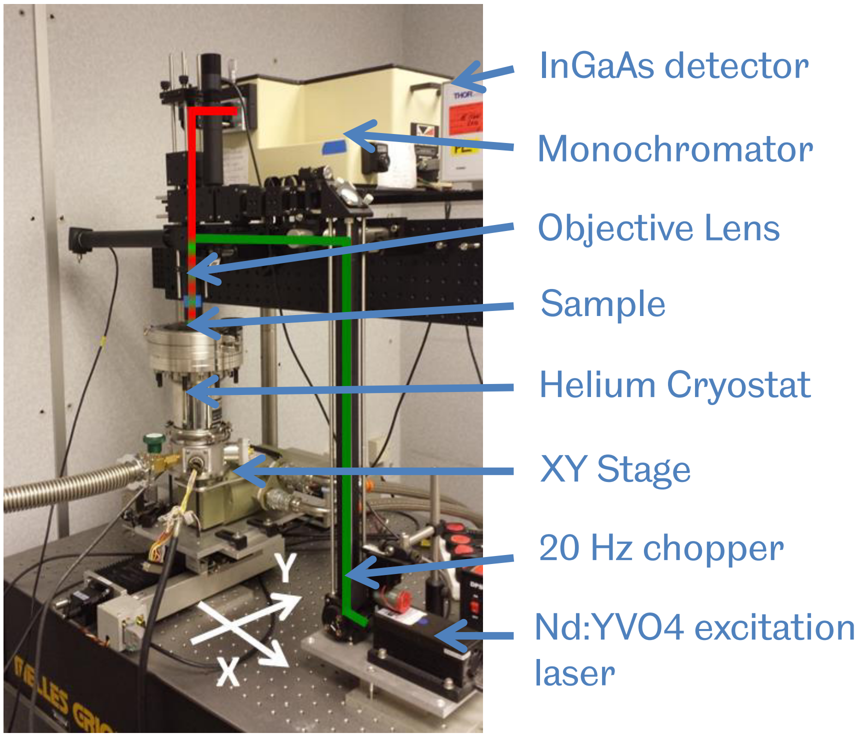

Figure 2.10: Low temperature PL mapping tool

Beer-Lambert law of absorption through Eq 2.4.

$$P = P_i(1 - R)(1 - e^{-\alpha x}) \tag{2.4}$$

where P is the transmitted power, Pi the incident power, R the Fresnel reflection, α the absorption length, and X the distance. The absorption length is given by Eq. 2.5.

$$\alpha = \frac{4\pi v k}{c} \tag{2.5}$$

where v is the photon frequency, k the extinction coefficient, and c the speed of light. At 300 K, the penetration depth of the optical excitation at 532 nm is approximately 60 nm for undoped InGaAs [4], therefore little influence on the PL signal from underlying InGaAs layers is expected. Noteworthy is that the penetration depth is larger at lower temperatures due to the increased electronic band-gap energy. The PL measurements were performed with an excitation power of $\sim$ 15 mW focused to a spot of $\sim$ 75 µm in diameter. A small excitation spot was favourable to minimise

PL emission from outside the eCV-etched crater ($\sim$ 1 mm in diameter). The PL spectra are shown uncorrected as the spectral response of the InGaAs detector did not vary by more than 20 % over the full region of interest (0.75 - 1.0 eV). The measurements were performed at low temperatures as the measured PL signal was very weak at room temperature, most likely due to the decrease in bulk non-radiative recombination lifetime, increase in surface recombination velocity, and the reduced sensitivity of an extended InGaAs detector as required for room temperature detection. Fig. 2.11(a) shows low temperature PL spectra at 15 K from the InGaAs layer structure of Fig. 2.1(a). The silicon dopant concentrations measured by SIMS are shown in the legend and are defined in units of cm^3. As no PL emission was measurable from the Fe doped InP substrate, the spectra shown in Fig. 2.11(a) are assigned to the epitaxial InGaAs layers. A common emission feature at 796 meV is observed at all PL locations, as well as a broad emission extending to shorter wavelengths. The band-gap energy of lattice matched InGaAs was previously measured by PL by various groups, with reported values ranging between 801 to 822 meV at T$\sim$ 0 K and 725 to 749 meV at T = 300 K [5][6][7][8][9]. Goetz *et al.* measured a temperature band-gap energy of 811 meV of lattice matched InGaAs at 2 K from the exciton emission-line position [7]. Following Eq. 2.6 derived by Goetz *et al.*,where x is defined as the gallium concentration, a low temperature band-gap energy of 0.803 eV is assigned to undoped In$_{0.54}$Ga$_{0.46}$As.

$$E_g(x)|_{2K} = 0.4105 + 0.6337x + 0.475x^2 \tag{2.6}$$

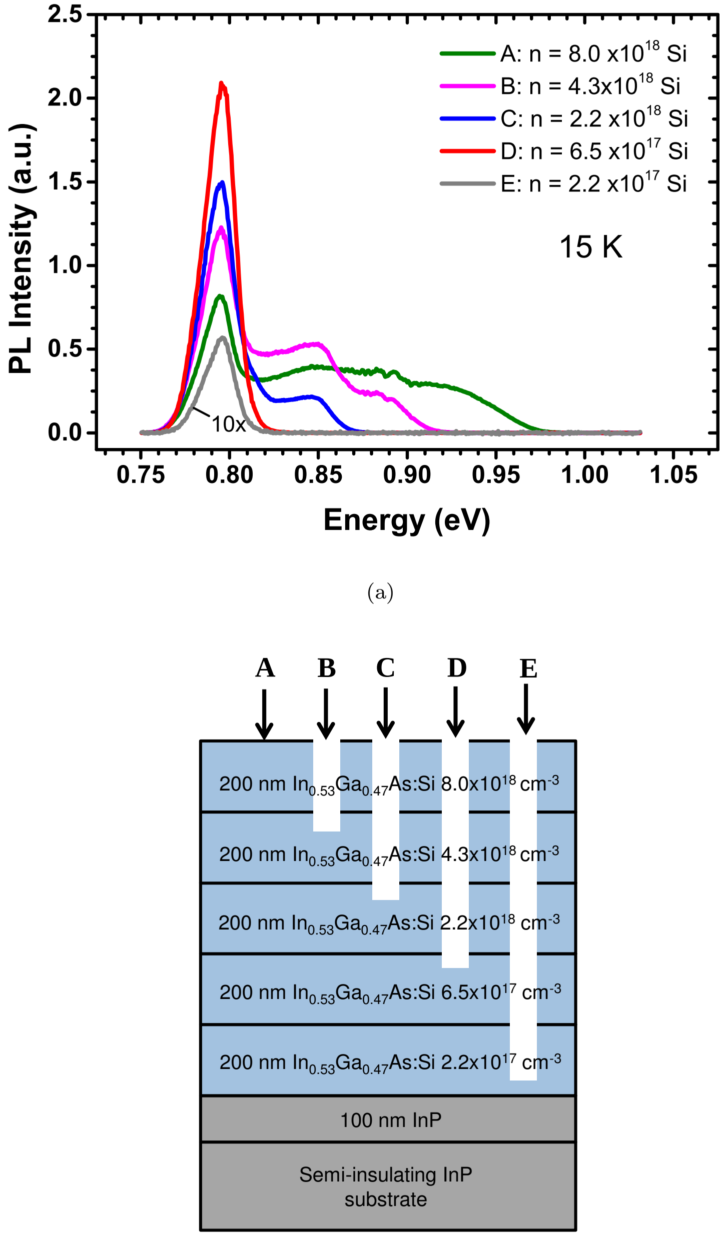

(a)

(b)

Figure 2.11: (a) Low temperature PL spectra at 15 K measured on the as-grown surface, A, and etch craters B,C,D, and E for the InGaAs layer structure shown in (b). The legend represents the doping concentration measured by SIMS.

The measured PL emission at 796 meV, as observed in Fig. 2.11(a), with a full width at half maximum (FWHM) of $\sim$ 21 meV is attributed to emission from the InGaAs crystal, which is in good agreement with the reported value by Goetz *et al.*. The measured linewidth of $\sim$ 20 meV at 796 meV is broader than the typical 1-3 meV excitonic linewidth for undoped In$_{0.53}$Ga$_{0.47}$As[10][11].

The effect of high impurity concentrations on the absorption and emission spectra of heavily doped p-type and n-type GaAs has previously been theoretically and experimentally investigated by a number of workers [12][13][14]. It is known that the PL spectra shifts to higher energies for n-type GaAs, while a shift to lower energies than the undoped band-gap is observed for p-type GaAs. For n-type GaAs, the shift to higher energies is associated with the Moss-Burstein (MB) effect overruling the band-gap narrowing effect, whereas the opposite occurs for p-type GaAs, due to the difference in electron and heavy hole effective masses of GaAs. The MB effect is known as a shift in optical band-gap with increasing carrier density, with the optical band-gap being defined as the energy separation between the top of the valence band and the unoccupied energy states in the conduction band. This effect results from the Pauli Exclusion Principle, with the Fermi level located in the conduction/valence band, for n-type/p-type material, and fundamental transitions to already filled states being forbidden. This leads to an up-shift as the interband absorption moves to a higher energy. The MB effect was first observed in n-doped InSb [15]. The MB shift is more pronounced for n-type material than p-type material due to the lower density of states. Another effect which reduces the optical band-gap is band-gap narrowing, caused by carrier impurity ions interaction and by many-body effects resulting from the spin-spin interaction and Coulomb repulsive interaction between free carriers [12] [16]. For highly doped GaAs, the spectral linewidth broadens due to the broadening in donor/acceptor density of states, and the lineshape resembles a Fermi-Dirac distribution rather than a Boltzmann distribution for the higher doping concentrations (n=1.25x10^{20} cm^{-3} for p-type GaAs , [17]). When the donor/acceptor impurity band becomes broad, it starts to overlap with the conduction/valence band and carriers become free. This transition from the localised to a delocalised state is known as the Mott transition and occurs when the distance between impurities becomes comparable to the Bohr radius [18]. For n-type InGaAs, this criterion is met for doping concentrations greater than 1.0x10^{17} cm^{-3}, from Eq.2.7

$$N_{crit} = (\frac{3}{4\pi a_B^*})^3 \tag{2.7}$$

where N_{crit} is the critical impurity density, and a_B^* the effective Bohr radius. The effective Bohr radius is given by Eq. 2.8

$$a_B^* = \frac{m_0 \varepsilon_r}{\mu} a_H \tag{2.8}$$

where m_0 the electron rest mass, ε_r the relative permittivity, μ the reduced electron-hole mass, and a_H the Bohr radius of the hydrogen atom (a_H = 5.29x10^{-11} m [3]). A reduced electron-hole mass of 0.026 m$_0$ is calculated for electron and hole masses of 0.043 m$_0$ and 0.145 m$_0$ [19], respectively.

From Eq. 2.7 & 2.8, a Bohr radius of 21.8 nm and a critical impurity density of 1.31x10^{17} cm^{-3} are calculated for InGaAs. Due to the low effective mass and associated high curvature of the electronic bands, the critical impurity density is low for materials with a small band-gap, including InGaAs. From these calculations, it follows that the Mott criterion is met for the layer structure in Fig. 2.1(a). Fig. 2.12 shows the measured PL peak intensity of the emission line at 796 meV for PL locations A-E.

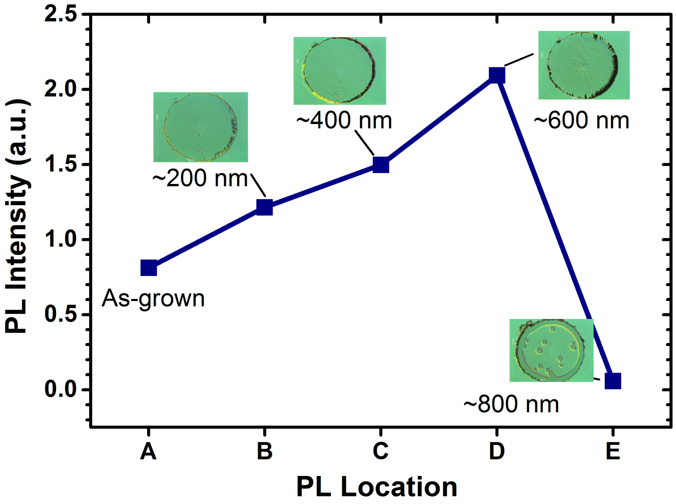

Figure 2.12: Low temperature PL peak intensity at 796 meV for PL locations A-E for the InGaAs layer test-stucture (Fig.2.1(a))

An increase in PL intensity is measured at 796 meV for PL locations A-D, suggesting that the emission originates from the lowest doped InGaAs layer with n = 2.2x10^{17} cm^{-3}. However, a weak PL emission is measured at PL location "E". A possible explanation to this observation is the presence of very little InGaAs material for the deepest etch crater. This is in line with Fig. 2.6(d) which shows that the etch quality decreased for the deeper etches, and Fig. 2.5(d) suggesting that a total of ~ 1 μm was etched instead of the required 800 nm to expose the lowest doped InGaAs layer.

Excitation dependent measurements were carried out to further investigate low temperature PL spectroscopy of the n-doped InGaAs. Fig. 2.13. shows power dependent PL spectra measured at 15 K for the PL locations A-E. These measurements were carried out with excitation powers between 20 μW and 20 mW focused to a spot of ~ 75 μm in diameter. At low excitation densities, the emission line at 797 meV shows a strong asymmetrical emission lineshape with a smooth and steep slope on the low energy and high-energy sides, respectively.

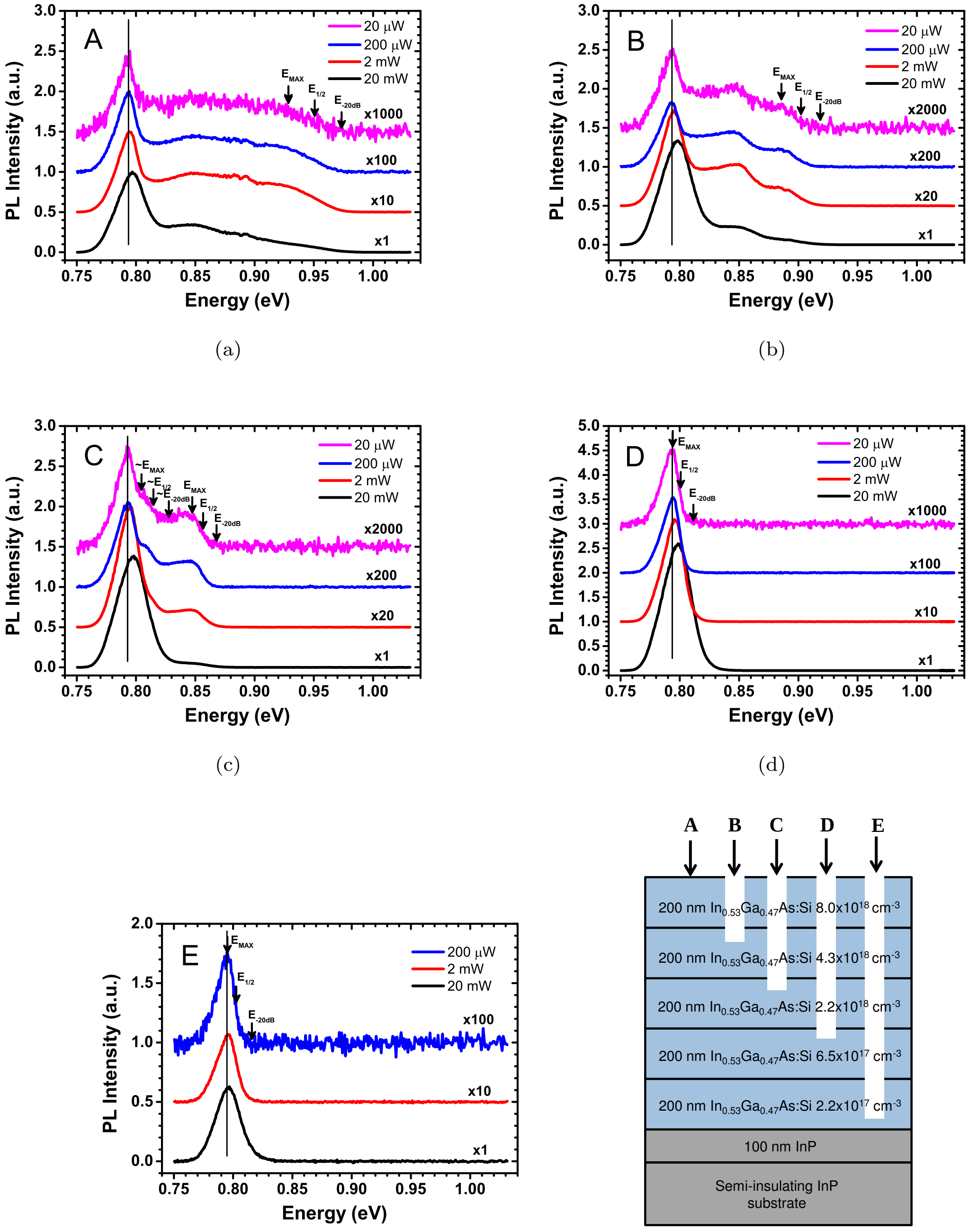

(a) (b) (c) (d) (e) (f)

Figure 2.13: Power dependent PL spectra at 15 K for PL locations A-E. The excitation power for each spectrum is shown in the legend. The arrows represent the energies at maximum intensity ($\mathrm{E}_{\mathrm{MAX}}$), half intensity ($\mathrm{E}_{1/2}$), and at -20dB ($\mathrm{E}_{\text{-20dB}}$) at the high energy tails of the spectra, for the emission originating from the surface layers of the etched craters. The value of $\mathrm{E}_{\mathrm{MAX}}$ in (a) is an estimated value as assigning the peak energy for this layer proved to be difficult due to the broad PL emission. The spectra are displaced vertically for clarity. The black vertical lines guide the eye to show the displacement of the PL peak as a function of excitation density.

Similar lineshape observations have been made for n-GaAs [20], n-type InP [21], and n-InAs [22]. The asymmetrical lineshape is a strong indication of indirect (without k-selection) band-to-band (B-B) or band-to-acceptor (B-A) transitions. Indirect transitions can occur for higher doping concentrations as the k-selection rule is relaxed due to the potential fluctuations which destroy the translation symmetry of the crystal [23][24][25][12][21]. Non vertical transitions are therefore possible as an electron can recombine with a hole regardless of the wave vector. Fig. 2.14 shows the proposed transition mechanism after Sheng *et al.* for highly n-doped GaAs [24].

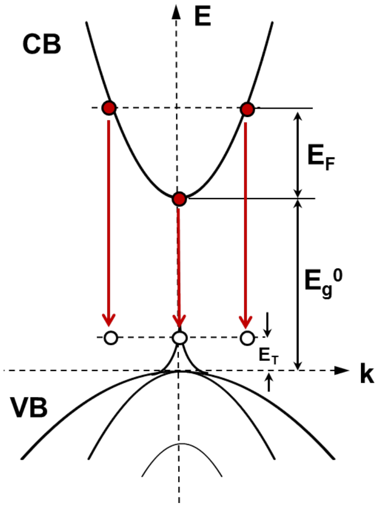

Figure 2.14: Schematic energy diagram of radiative transitions in highly n-doped GaAs. E_{g0}, E_f, and E_T, are defined as the nominal band-gap energy, Fermi energy, and the energy of the photoexcited holes in the density-of-states tail, respectively.

Sheng *et al.* have also shown that the density-of-states tail increases with increasing carrier concentration which causes the band tail to overlap with the broadened impurity acceptor levels [24]. The localised states in the band-tail due to inhomogeneous impurity distribution and potential fluctuations in heavily doped semiconductors can be treated as acceptor-like centres distributed above the top of the valence band as proposed by Levanyuk and Osipov [29]. This effect occurs for carbon acceptors in GaAs (Ea = 26.4 meV) for an electron concentration greater than $1\text{x}10^{18}\text{cm}^{-3}$. The dominant spontaneous recombination in low temperature PL spectra of heavily doped n-GaAs for doping concentrations between $1\text{x}10^{18}\text{cm}^{-3}$ and $1\text{x}10^{19}\text{cm}^{-3}$ has been assigned by Sheng *et al.* to a recombination between free electrons in the conduction band and localised holes in the deeper tail states, acting as acceptor-like states. The measured broad emission shifting towards higher energies with doping concentration in Fig. 2.11(a) is strong evidence of the MB effect. Of note is that the MB energy shift is more pronounced for semiconductors with a low effective mass, as the curvature of the bands is high and the density of states (DOS) is low. The MB energy shift was considered theoretically using a parabolic band approximation for an effective electron mass of 0.043 m_0 for InGaAs, with m_0 being defined as the electron rest mass [19]. Band-tailing and the band-gap narrowing effect are included in the approximation, but non-parabolic effects are not considered. The band-to-band optical band-gap for n-doped material without wave vector conservation is given by Eq. 2.9

$$E_{gopt} = E_{g0} + E_f - E_{bgn} - E_t \tag{2.9}$$

where E_{gopt} is the optical band-gap, E_{g0} the nominal band-gap, E_f the Fermi energy, E_{bgn} the effective band-gap narrowing, and E_t the energy shrinkage due to band tailing. The Fermi energy relative to the bottom of the conduction band for an ideal parabolic conduction band was computed using Eq. 2.10

$$E_f = \frac{\hbar^2 k_f^2}{2m_e^*} = \frac{\hbar^2}{2m_e^*}(3\pi^2 n)^{2/3} \tag{2.10}$$

where E_f is the Fermi energy, $\hbar$ the reduced Planck's constant, k_f the wave vector, m_e^* the electron effective mass, and n the free-electron concentration. The band-gap narrowing effect, E_{bgn}, due to electron-electron interaction, is approximated to $\Delta E^{(e-e)}$ =2.03x10^{-8} $n^{1/3}$ eV, with n being defined as the free-carrier concentration [26]. The energy gap shrinkage due to band tailing is included in the model as the photogenerated holes are localized at low excitation conditions in a narrow energy region of the deeper tail states at an energy position E_t [27]. The energy, E_t, is approximated to 2.5 times the root-mean-square of the potential fluctuation V_{rms} as defined by Eq. 2.11

$$V_{rms} = \frac{e^2}{4\pi\epsilon}[2\pi(N_D^+ + N_A^-)L]^{1/2} \tag{2.11}$$

where e is the electron charge, ϵ the electric permittivity, N_D^+ and N_A^- the concentration of ionized donors and acceptors, and L the screening length [23]. The sum of N_D^+ and N_A^- is approximately equal to n, and the screening length, L, is given by Eq. 2.12

$$L = (\frac{a}{2})(n \times a^3)^{-1/6} \tag{2.12}$$

where n is the free-carrier concentration, and a the effective Bohr radius. Fig. 2.15 shows the modelled optical band-gap of $In_{0.54}Ga_{0.46}As$ for doping concentrations between 1x10^{17} cm^{-3} and 3x10^{19} cm^{-3}, as well as the experimental data. The solid line represents the optical band-gap without band-tailing and band-gap narrowing effects included, which is given by the sum of the nominal band-gap and the Fermi energy in the conduction band. The blue and red dashed lines represent the optical band-gap with band-gap narrowing included, and a combination of band-gap narrowing and band-tailing effects, respectively. The triangular symbols represent the experimental data. For the quantitative analysis of the MB shift, the experimental optical band-gap is typically determined as the energy at the maximum of the spectrum [22]. Of note is that theoretical works have shown that the effective optical band-gap energy is at the energy were I_E/I_{EMAX} is at ~ 0.9 and ~ 0.6 for indirect band-to band (B-B) and band-to-acceptor (B-A) processes, respectively [22] [24]. The experimental values at E_{MAX} are plotted in the low excitation density regime to minimise the quasi-Fermi level shift due to band-filling. A small blue-shift of less than 10 meV is observed with increasing power density in Fig. 2.13, which is most likely attributed to a shift in the quasi-Fermi level as a low density of states in the band-tail states of highly doped material is expected. Good agreement is observed in Fig. 2.15 between theoretical modelling and experimental data, and work previously reported by Munoz *et al.* [26] and Fedoryshyn *et al.* [28]. From theoretical modelling, it follows that the band-tailing effect is the dominant optical band-gap reduction effect at higher doping concentrations assuming a parabolic band approximation. The observed deviation at the highest carrier density in Fig. 2.15 from the theoretical curve is most likely attributed to the non-parabolic band-structure of InGaAs at higher energies. The non-parabolic nature of the electronic band-structure of InGaAs tends to increase the effective mass of electrons at higher energies and consequently increases the density of states.

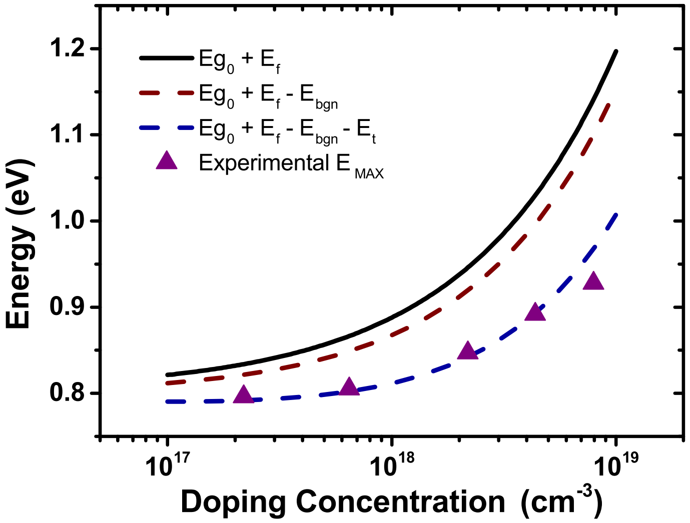

Figure 2.15: Theoretical and experimental optical band-gap as a function of doping concentration for the n^+ InGaAs test-structure. The solid and dashed lines represent the theoretical curves with and without the inclusion of the band-gap narrowing and band-tailing effects. The triangles represent the experimentally measured energy at maximum PL intensity (E_{MAX}).

2.4 Wafer Level n^{+} InGaAs Uniformity

The measured relation between doping concentration and optical band-gap from SIMS and PL, allows for a non-destructive measurement of the absolute doping concentration of n-doped InGaAs. This technique was used to non-destructively determine the absolute doping concentration uniformity of the emitter/collector and contact layers of the RTD structure using the n^{+} InGaAs test-structures, shown in Fig. 2.1 (b) and (c). These test-structures are duplicates of the contact layers (n=2x10^{19} cm^{-3} Si doped) and emitter/collector layers (n=3x10^{18} cm^{-3} Si doped) of the RTD structure, respectively.

HR-XRD was carried out to quantify any residual strain of the epitaxial InGaAs layers on InP. Tensile strains of 23x10^{-4} and 1.4x10^{-4} were measured for the contact layer and emitter/collector layer, which correspond to $In_{0.529}Ga_{0.471}As$ and $In_{0.511}Ga_{0.489}As$, respectively. eCV was performed to measure the doping concentration (approximately) in these layers, as no SIMS data was available at the time for these test-structures. Fig. 2.16 shows the measured free-carrier concentration as a function of depth, up to 70 nm, for both structures. Free-carrier concentrations of 1.3x10^{19}cm^{-3} and 3.9x10^{18}cm^{-3} are measured for the contact and emitter/collector layers, respectively. From Fig. 2.16, the corresponding doping concentrations for both layers are estimated from the measured free-carrier concentrations to be within 10 % for the contact layer and 40 % for the emitter/collector layer.

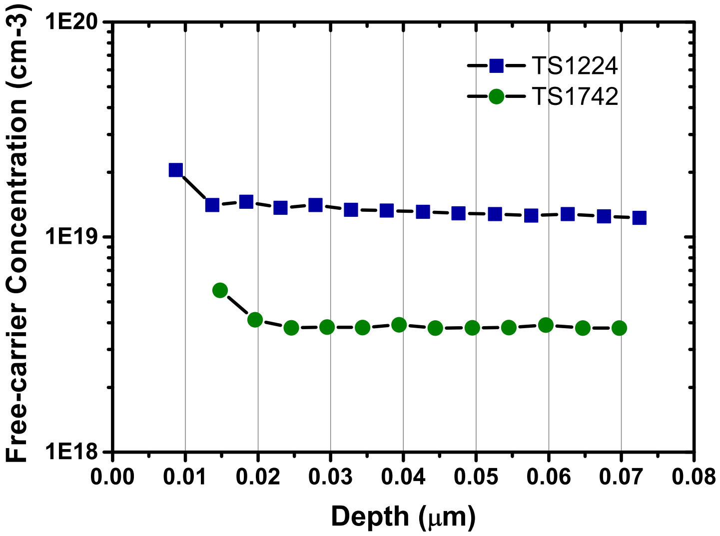

Figure 2.16: Free-carrier concentration (cm^{-3}) of the contact layer (TS1224) and emitter/collector layer (TS1742) as a function of depth (μm).

Low temperature PL spectroscopy was subsequently carried out at 15 K of both structures. Fig. 2.17 shows the measured PL spectra of both structures as a function of energy. The arrows represent the energies at maximum intensity (E_{MAX}), half intensity ($E_{1/2}$), and -20dB (E_{-20dB}) at the high energy tails of the spectra. The legend represents the measured free-carrier concentration of both wafers.

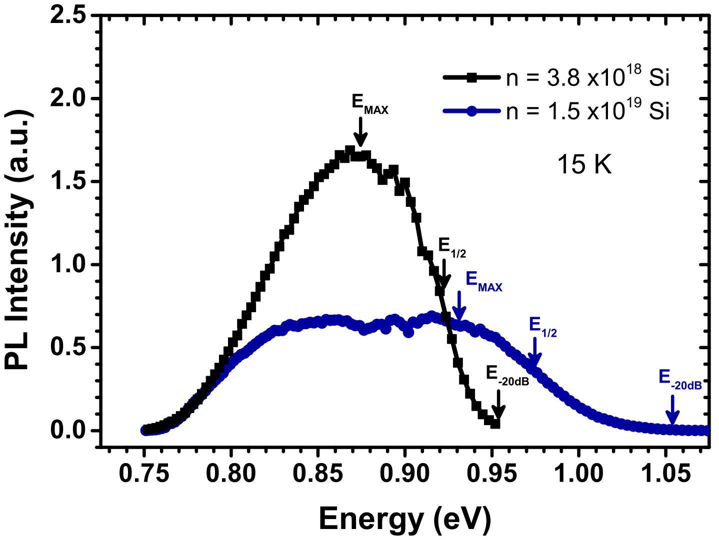

Figure 2.17: Low temperature PL spectra at 15 K for both test-structures as a function of energy. The arrows represent the energies at maximum intensity (E_{MAX}), half intensity ($E_{1/2}$), and at -20dB (E_{-20dB}), at the high energy tail of the spectra. The free-carrier concentration of both wafers is shown in the legend.

Similar observations are made as in Fig. 2.11, the PL emission broadens and shifts towards higher energies as a function of doping concentration. This observed effect has previously been associated to the MB effect. Of note is that no distinctive emission line at 797 meV is measured for both test-structures, which again confirms that the measured emission line at 797 meV, shown in Fig. 2.11, originates from the lowest doped layer, as this layer was not included in these test-structures. The asymmetric emission lineshape with a smooth and steep slope on the low energy and high-energy sides, respectively, is observed for the collector/emitter layer, indicating indirect (without k-selection) band-to-band (B-B) or band-to-acceptor (B-A) emission. B-B recombination is known to be more dominant for higher doping concentrations as the density-of-states tail at the valence band increases with doping level, which eventually overlaps with the deeper acceptor states [24][22]. B-A recombination is typically the dominant recombination process in n-type GaAs for doping concentrations below 5x10^{17} cm^{-3} with carbon impurities as the main acceptor species in MBE grown GaAs (Ea = 26.4 meV [24]), [30]. Shallow acceptors, carbon (C), silicon (Si), and zinc (Zn) have been previously identified in undoped MOCVD grown InGaAs by Goetz *et al.* assigning binding energies of 13 meV, 25 meV, and 22 meV assigned to these acceptors, respectively [7]. As these binding energies are less than the binding energy of the acceptor carbon in GaAs, and the effective mass of InGaAs is smaller than GaAs, indirect B-B recombination is tentatively assigned as the dominant recombination process for these InGaAs test-structures with doping concentrations greater than 2.2x10^{17}cm^{-3}.

Fig. 2.18 shows the low temperature spectra of the InGaAs layers with different doping concentrations plotted on a logarithmic scale. The spectrum with an approximate doping concentration of 1.5x10^{19}cm^{-3} originates from the doping uniformity test-structure (Fig.2.1(b)). The arrows represent the -20 dB points of E_{MAX} at the high energy tails of the spectra.

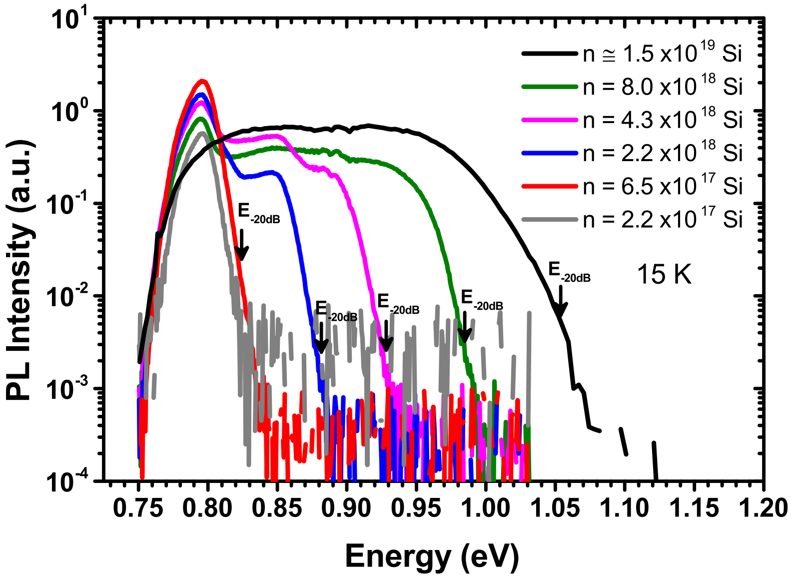

Figure 2.18: Low temperature PL spectra at 15 K from Fig. 2.11 and Fig. 2.17; plotted on a logarithmic scale as a function of energy. The legend represents the doping concentration measured by SIMS. The doping concentration of the highest doped layer (n=1.5x10^{19} cm^{-3}) was deduced from eCV measurements.

Plotting the low temperature PL spectra on a logarithmic scale highlights the blue-shifting and broadening of the PL spectra with increasing doping. An increase in linewidth with doping concentration is observed due to the MB effect. The experimentally measured FWHM linewidths were compared with the theoretical linewidths of n-doped InGaAs using a parabolic band approximation. Fig. 2.19 plots the energy half-width as a function of doping concentration, where the black line represents the calculated Fermi energy in the conduction band, and the blue square symbols represent the experimentally measured half-width linewidth.

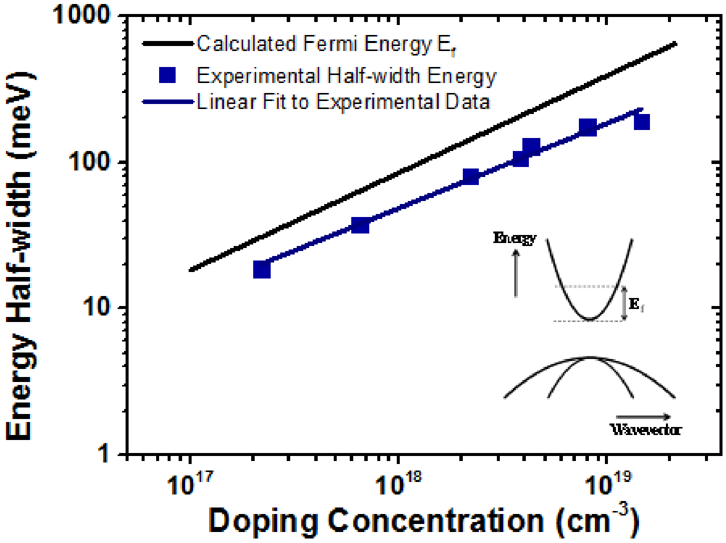

Figure 2.19: Energy half-width as a function of free-carrier/doping concentration. The black solid line follows the calculated Fermi energy as a function of free-carrier concentration, while the blue square symbols represent the experimentally measured half-width linewidth as function of doping concentration.

Good agreement is observed between the experimentally measured FWHM energy and theoretical modelling. Fig. 2.20 plots the doping concentration as a function of the measured half-width energy. From Fig. 2.20, an empirical relation is derived between ΔE and n in the form of Eq. 2.13.

$$n = 3 \times 10^{17} e^{21.6\Delta E} \tag{2.13}$$

The established fit to the experimental data can be used as a tool to determine the free-electron concentration of InGaAs with doping concentrations between ~ $1\text{x}10^{17}\text{cm}^{-3}$ and ~$2\text{x}10^{19}\text{cm}^{-3}$ by low temperature PL. Not only does the emission linewidth increase as a function of doping, a shift in the peak emission energy towards higher energies is also observed. Similarly, the blue-shift of the emission as a function of doping can be used as a tool to determine the free-electron concentration of InGaAs through low temperature PL. Fig. 2.21 shows the doping concentration plotted as a function of the measured energy at -20dB (E_{-20dB}) at the high energy tails of the PL spectra. The data is plotted at E_{-20dB} instead of E_{MAX}, as assigning the peak wavelength at E_{MAX} in Fig. 2.11(b) and 2.17 proved to be difficult due to the broadness of the PL spectra. The horizontal error bars

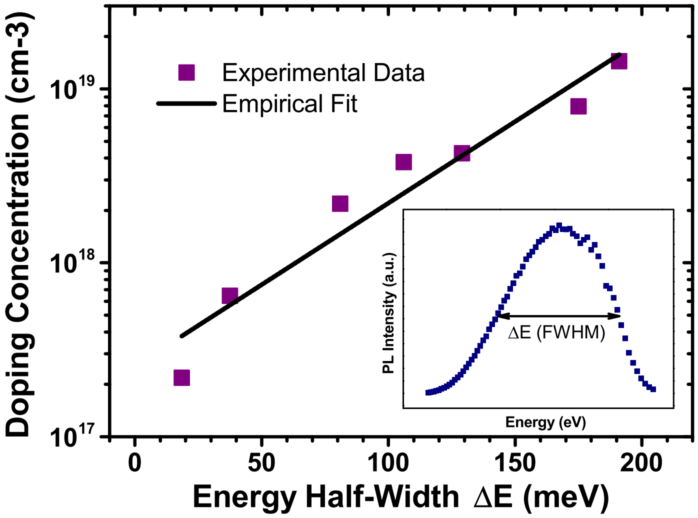

Figure 2.20: Doping concentration as a function of the measured energy half-width energy. A logarithmic fit is applied to the data. The inset schematically illustrates the measured half-width energy.

(partially covered by the symbols) represent the measured energy shift for a four order magnitude change in excitation density. The experimental data is in good agreement with the theoretical

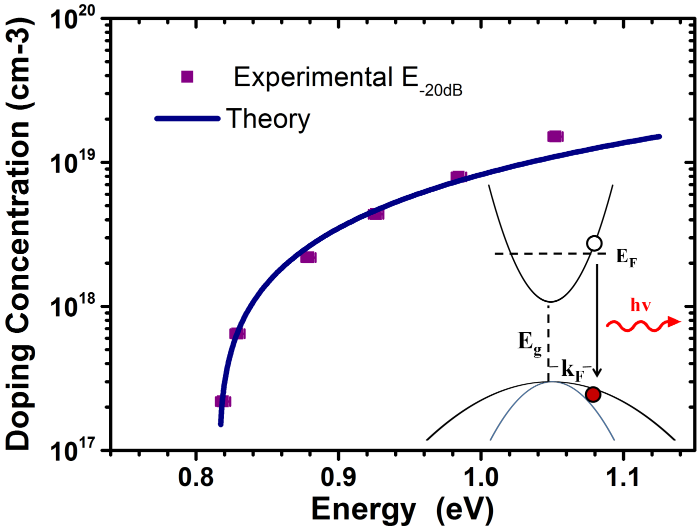

Figure 2.21: Doping concentration as a function of the energy at -20 dB at the high energy tail of the PL spectra. The inset schematically shows the recombination process. Of note, the horizontal error bars are partially covered by the symbols.

model. A third order polynomial fit was applied to the data in the form of Eq. 2.14.

$$n = 7.29 \times 10^{20} E^3 - 1.83 \times 10^{21} E^2 + 1.57 \times 10^{21} E - 4.55 \times 10^{20} \tag{2.14}$$

In addition to Eq. 2.13, this relation can also be used as a tool to non-destructively determine the absolute doping concentration of n-type InGaAs by low temperature PL.

The doping uniformity of the n^+ InGaAs layer (n $\approx$2x10^{19} cm^{-3} Si), representing the contact layer of the RTD, was first investigated over a full 2$''$ wafer at 15 K, the structure is schematically shown in Fig. 2.1(b). Fig. 2.22 plots a series of PL spectra at 15 K in 500 μm steps from the wafer edge towards the wafer center, as shown schematically in the inset. Locations "A" and "G" are measured at 500 μm and 3.5 mm from the periphery of the wafer, respectively. From the experimental data, an increase in spectral linewidth from wafer center (location "G") to periphery (location "A") of 10 meV and 1 meV is measured at -20 dB of the high and low energy tails of the spectra, respectively. At -10 dB, a broadening of 10 meV and 2 meV from the wafer center (location "G") to the periphery (location "A"), is measured at the high and low energy tails of the spectra, respectively. The broadening at the low-energy tail of the spectrum is attributed to an InGaAs alloy composition variation at the wafer edge. A 1 meV shift in PL corresponds to a 0.16 % change in indium concentration. Due to the small shift at low energy being associated to small alloy composition variations, the observed broadening at the high-energy tail of the spectrum is attributed to the MB effect. The relationship between MB shift and doping concentration, as previously investigated for n^+ InGaAs, is shown in Fig. 2.21. A measured ΔE shift of 9 meV at -20 dB translates to a 4.6 % variation in doping. This corresponds to a doping variation of 6.0x10^{17} cm^{-3}, with increasing doping towards the wafer edge.

Using the same analysis, the spatial variation of the doping concentration was non-destructively mapped by measuring the PL spectrum at different points over the wafer. Fig. 2.23(a) and (b) show doping uniformity maps of the contact and emitter/collector layers, respectively, non-destructively mapped using low temperature PL. The measurements were performed over full 2$''$ wafers with a 5 mm spatial resolution. The data points on the maps represent energy at -20 dB of I_{EMAX} at the high energy tails of the spectra. Subsequently, the emission energy at those points was converted to a corresponding doping concentration (via Fig. 2.21 and Eq. 2.14), and plotting on a gradient scale. For the n^+ InGaAs test wafer with a doping concentration equivalent to the contact layers of the RTD structure, a measured energy variation of 24 meV corresponds to a Δn of $\sim$ 2x10^{18} cm^{-3}, which correlates to a doping uniformity of ± 8 % over the full wafer.

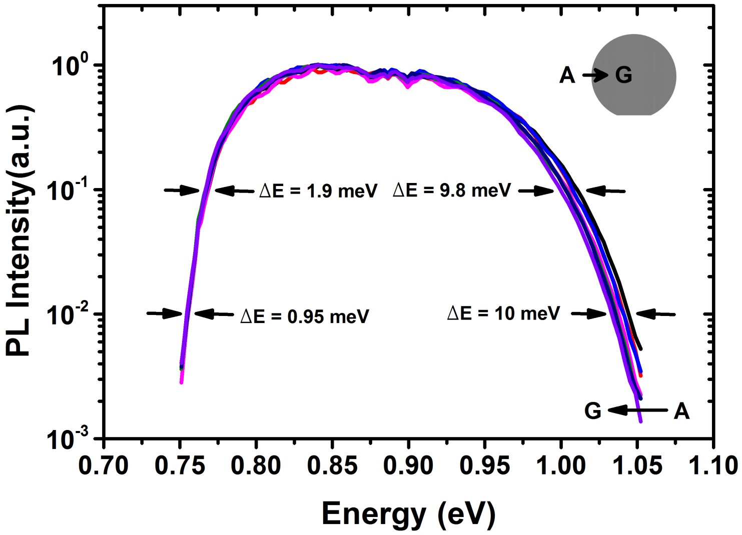

Figure 2.22: A series of photoluminescence spectra measured at 15 K from the wafer edge towards the wafer center with 500 μm steps, as shown schematically in the inset. The measured energy shift at -10 dB and -20 dB over the full line-scan are shown.

Similarly, for the n^+ InGaAs test wafer with a doping concentration equivalent to the emitter/collector layers of the RTD structure, a measured energy shift of 22 meV corresponds to a Δn of 9x10^{17} cm^{-3}, which correlates to a doping uniformity of ± 10 %. The variation in doping, measured with PL, was verified with eCV, by measuring the free-carrier concentrations on two locations. Fig. 2.23 (c) and (d) show the measured free-carrier concentrations at locations "A" and "B" up to a depth of approximately 70 nm for both maps. A difference in free-carrier concentration of approximately 1.3x10^{18} cm^{-3} to 1.9x10^{18} cm^{-3} , and 1.6x10^{17} cm^{-3} to 1.9x10^{17} cm^{-3} was measured for the maps which represent the contact and emitter/collector layers of the RTD, respectively. The error bars on the graphs indicate the measured error in free-carrier concentration as calculated from the non-linearity of the 1/C^2 curve. The cause of the observed decrease in free-carrier concentration with depth in Fig. 2.23(b) is not yet clear but might be due to non-optimal etching conditions resulting in a decrease in area, with an apparent reduction in doping as a result. For both wafers, a good correlation is found between the measured free-carrier concentrations with eCV and the doping concentrations via low temperature PL analysis.

The measurement of doping via the analysis of low temperature PL measurements is highly advantageous in not only being a rapid non-destructive measurement technique, but the measurement is also found to be more reproducible than eCV as no etching is involved during the measurement process [1][31]. With regard to the origin of the measured doping variation, Si_2H_6 was used as the

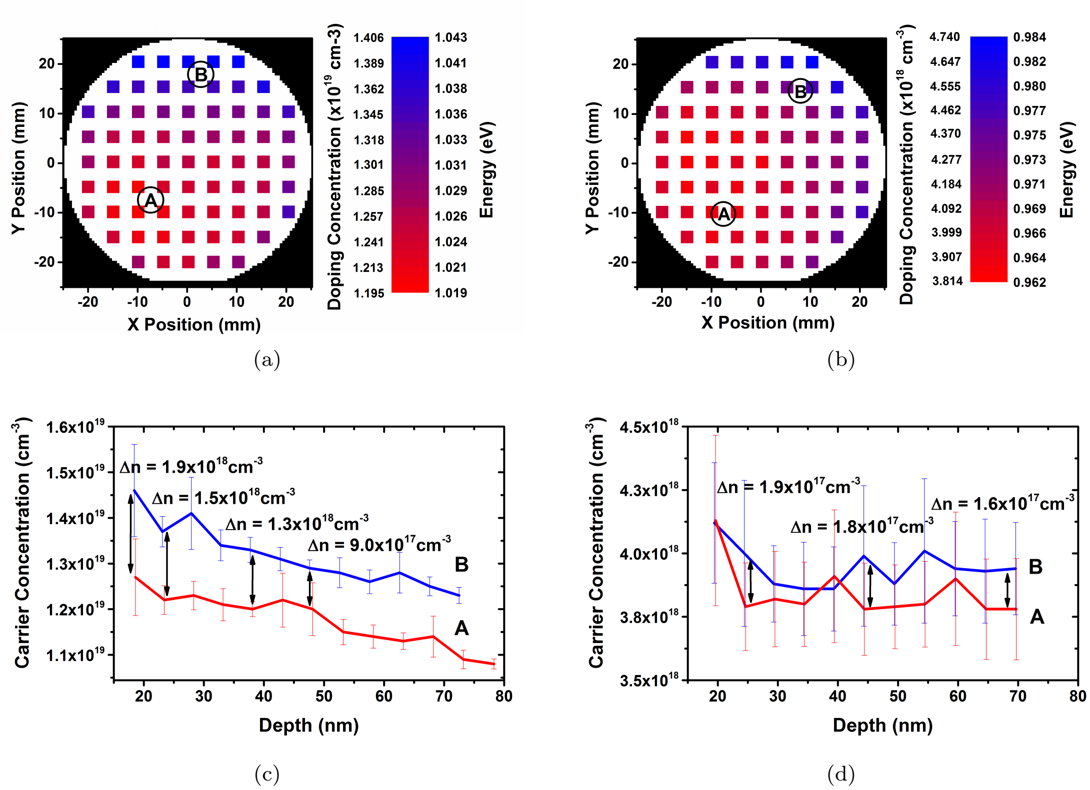

(a)

(b)

(c)

(d)

Figure 2.23: (a) (b) PL maps of doping concentration of n$^+$ InGaAs test-layers determined from PL at 15 K. The test-layers have an equivalent doping concentration of the contact and emitter/collector layers of the RTD structure, respectively. (c) (d) eCV profiles measured at 300 K, at locations "A" and "B" of the maps shown in (a) and (b), respectively, for an etch depth step of $\sim$ 5 nm.

preferred doping gas for this work, instead of silane (SiH_4), due to the higher silicon incorporation efficiency and lower temperature dependence of Si_2H_6 [32]. However, thermal effects are considered important as the dopant silicon was incorporated from the precursor disilane within the dissociation rate limited region of Si_2H_6 at a temperature of 560 °C (measured with a Laytec EpiTT pyrometer (calibrated using an Absolut probe)), and a pressure of 100 Torr [33][34]. The observed effect is not well explained by gas-phase depletion or saturation effects as both wafers show similar doping uniformities. For a depletion or saturation effect, an improvement in doping uniformity should have been observed for the wafer with a lower doping concentration, however, this effect is not observed in these measurements.

With regard to the impact on the device performance, doping uniformity is important. For the contact layers, a variation in doping will affect the contact resistance of the device, and the associated device losses, as the depletion width of a non-alloyed ohmic contact is highly dependent on the doping concentration. For the emitter/collector layers, a doping variation will have an impact on the V-I performance of the device as the tunnelling current is highly dependent on the doping concentration in the emitter region. Teranishi *et al.* reported that the current density almost doubles for a twofold increase in the emitter doping concentration for similar high current density InGaAs/AlAs/InP RTD structures [35]. For a measured emitter/collector doping uniformity of ± 10 %, a peak current density variation between 630 kA/cm^2 to 770 kA/cm^2 is expected over the full wafer for a RTD with a nominal peak current density of 700 kA/cm^2. Devices fabricated in the high doping density region (location "B" in Fig. 2.23) will have a larger peak current than devices fabricated in the lower doping density region (location"A"). Devices with a higher doping density in the emitter layer are expected to have a higher output power due to the increased ΔI (Ipeak - Ivalley) and reduced NDR. Whilst a doping uniformity of ± 10 % over the full wafer is not ideal for volume manufacture as the device variability will be large, it allows efficient research as simultaneous experiments with different process conditions can be carried out at different positions over the wafer, to explore optimum process parameters. In future work, devices will be fabricated over the full wafer to investigate the impact of the measured doping uniformity on the device performance. From literature, a ten-fold improvement in doping uniformity is expected for these structures through optimisation of the growth. On-wafer doping uniformities for MOVPE grown GaAs on 6″ GaAs wafers of 1.24 % and 1.1 % standard deviation at carrier densities of 8x10^{17} cm^{-3} and 3x10^{19} cm^{-3} for n- and p-type, respectively, were reported. [36]. Optimising the growth conditions for high wafer uniformity will also have to be investigated in future work.

2.5 Conclusions

This chapter covered optical spectroscopy of n-type InGaAs. Photoluminescence was measured as a function of doping concentration for InGaAs test-layers at low temperatures and correlated to SIMS and eCV profiling. A photoluminescence characterisation technique was developed to measure the absolute doping concentration of the highly n-doped InGaAs layers non-destructively through low temperature PL. It was shown how the emission wavelength is dominated by the Moss-Burstein effect and how correlating this shift to eCV and SIMS allows non-destructive mapping of the absolute doping concentration. n$^+$ InGaAs test-structures were grown by MOVPE to investigate the doping uniformity over the full wafer. By examining the PL spectra from different positions over the full 2″ n$^+$ InGaAs test-wafers, it was possible to deduce the absolute doping concentrations and uniformity of the highly doped collector/emitter and contact layers of the RTD structure. A ± 8 % doping variation for the contact layers, and a ± 10 % for the emitter/collector layers was measured, for 62 % of the wafer area. These results were confirmed by measuring the free-carrier concentration over the wafer by eCV. The measured variation over the wafer was attributed to thermal effects as the dopant silicon was incorporated from the precursor disilane within the dissociation rate limited region. The observed effect could not be explained by gas-phase depletion or saturation effects as both wafers showed similar doping uniformities. The optical spectroscopy of the epitaxy through PL is both time/cost effective and highly advantageous for the growth optimisation process.

With regard to the manufacturability, process variations will cause manufactured devices to have a diverse performance/quality profile. Doping variations over the wafer will have an impact on the contact resistance and operating current of the device. Devices with a larger doping density are expected to have a higher output power due to the larger tunnelling current, but will have a lower contact resistance. To manufacture the RTD THz emitter cost-effectively, good circuit design is required, to make sure that the electrical parameter tolerances are accommodated in the design to assure functionality, high yield, and high reliability. As some devices will perform better depending on the location on the wafer, profit can be maximised by selling these high quality devices for a higher price by separating them (a process called “binning) from the relatively low performance/quality devices. This performance binning can be done for various parameters, including oscillation frequency, output power, and device quality.

References

[1] P. Blood, “Capacitance-voltage profiling and the characterisation of III-V semiconductors using electrolyte barriers”, Semicond. Sci. Technol. 1 (1986), 7.

[2] W.C. Johnson, P.T. Panousis, “The Influence of Debye Length on the C-V Measurement of Doping Profiles”, IEEE Trans. Electron Devices, 18 (1971), 965.

[3] Fox, M., “Optical Properties of Solids”. 2nd ed. New York: Oxford University Press Inc.; 2010.

[4] Software Spectra, Inc (2008) *Optical Data from Sopra SA*, Available at: http://www.sspectra.com/sopra.html (Accessed: 23/09/13).

[5] D. K. Gaskill, N. Bottka, L. Aina, and M. Mattingly, “Band-gap determination by photoreflectance of InGaAs and InAlAs lattice matched to InP”, Applied Physics Letters 56, 1269 (1990)

[6] T. P. Pearsall, L. Eaves, and J. C. Portal, “Photoluminescence and Impurity Concentration in GaInAsP Lattice-matched to InP”, J. Appl. Phys. 54, 1037 (1983).

[7] K.H. Goetz, D. Bimberg, H. Jrgensen, J. Selders, A.V. Solomonov, G. F. Glinskii, M. Razeghi, “Optical and crystallographic properties and impurity incorporation of GaXln1 _xAs (0.44 <x <0.49) grown by liquid phase epitaxy, vapor phase epitaxy, and metal organic chemical vapor deposition”,J. Appl. Phys., 54 (1983), 4543.

[8] Yu-Ssu Chen and O. K. Kim, “Near band gap absorption and photoluminescence of In0.53Ga0.47As semiconductor alloy” J. Appl. Phys. 52, 7392 (1981).

[9] I. C. Bassignana, C. J. Miner, and N. Puetz, “Photoluminescence and double crystal xray study of InGaAs/InP: Effect of mismatch strain on band gap”, Journal of Applied Physics 65, 4299 (1989)

[10] E. F. Schubert and W. T. Tsang, “Photoluminescence line shape of excitons in alloy semiconductors”, Phys. Rev. B 34, 2991 (1986).

[11] Pallab K. Bhattacharya, Mulpuri V. Rao, and MingJong Tsai, “Growth and photoluminescence spectra of high-purity liquid phase epitaxial In0.53Ga0.47As”,Journal of Applied Physics 54, 5096 (1983)

[12] G. Borghs, K. Bhattacharyya, K. Deneffe, P. Van Mieghem, and R. Mertens, “Bandgap narrowing in highly doped n- and p-type GaAs studied by photoluminescence spectroscopy” Journal of Applied Physics 66, 4381 (1989)

[13] J. I. Pankove, “Cathodoluminescence of n-Type GaAs”, Journal of Applied Physics 39, 5368 (1968)

[14] Bo E. Sernelius, “Band-gap shifts in heavily p-type doped semiconductors of the zinc-blende and diamond type”, Phys. Rev. B 34, 5610 (1986)

[15] T. S. Moss, Proc. Phys. Soc. (London) B76, 775 (1954)

[16] K. F. Berggren and B. E. Sernelius, “Band-gap narrowing in heavily doped many-valley semiconductors”,Phys. Rev. B **24**, 1971 (1981)

[17] Pankove, J. I. “Optical processes in semiconductors”, Englewood Cliffs, N.J. : Prentice-Hall; 1971

[18] P.Y. Yu, M. Cardone, Fundamentals of Semiconductors: Physics and Material Properties, Springer Verlag, 2001.

[19] I. Vurgaftman, J. R. Meyer, and L. R. Ram-Mohan, “Band parameters for IIIV compound semiconductors and their alloys”, Journal of Applied Physics 89, 5815 (2001)

[20] M.K Hudait, P Modak, S.B Krupanidhi, “Si incorporation and BursteinMoss shift in n-type GaAs”, Materials Science and Engineering: B, Volume 60, Issue 1, 31 May 1999, Pages 1-11,

[21] R. M. Sieg and S. A. Ringel, “Reabsorption, band-gap narrowing, and the reconciliation of photoluminescence spectra with electrical measurements for epitaxial n-InP”, Journal of Applied Physics 80, 448 (1996)

[22] V. A. Vilkotskii, D. S. Domanevskii, R. D. Kakanakov, V. V. Krasovskii, and V. D. Tkarchev, “Burstein-Moss Effect and Near-Band-Edge Luminescence Spectrum of Highly Doped Indium Arsenide”, Phys. Status Solidi B 91, 71 (1979)

[23] H. C. Casey Jr. and Frank Stern, “Concentration-dependent absorption and spontaneous emission of heavily doped GaAs”, Journal of Applied Physics 47, 631 (1976)

[24] Jiang DeSheng, Y. Makita, K. Ploog, and H. J. Queisser, “Electrical properties and photoluminescence of Te-doped GaAs grown by molecular beam epitaxy”, Journal of Applied Physics 53, 999 (1982)

[25] Huade Yao and A. Compaan, “Plasmons, photoluminescence, and band-gap narrowing in very heavily doped n-GaAs”, Applied Physics Letters 57, 147 (1990)

[26] Martn Muoz, Fred H. Pollak, Mathias Kahn, Dan Ritter, Leeor Kronik, and Guy M. Cohen, “Burstein-Moss shift of n-doped In0.53Ga0.47As/InP”, Phys. Rev. B 63, 233302

[27] B. G. Arnaudov, V. A. Vilkotskii, D. S. Domanevskii, S. K. Evtimova, and V. D. Tkarchev, SOY. Phys. Semicond. 11,1054 (1977).

[28] Y. Fedoryshyn, M. Beck, P. Kaspar, and H. Jaeckel, “Characterization of Si volume- and delta-doped InGaAs grown by molecular beam epitaxy”, J. Appl. Phys. **107**, 093710 (2010).

[29] A. P. Levanyuk and V. V. Osipov, SOY. Phys. Semicond. 7, 721 (1973).

[30] H. Knzel and K. Ploog, “The effect of As2 and As4 molecular beam species on photoluminescence of molecular beam epitaxially grown GaAs”, Applied Physics Letters 37, 416 (1980)

[31] I. Mayes, “Accuracy and reproducibility of the electrochemical profiler” Materials Science and Engineering B, 80 (2001) 160.

[32] T. F. Kuech, B.S. Meyerson and E. Veuhoff, “Mechanism of Carbon Incorporation in MOCVD GaAs”, Appl. Phys. Lett., 44 (1984), 986.

[33] C. Blaauw, F.R. Shepherd, C.J. Miner, A.J. Springthorpe, “Silicon incorporation in InP during LP-MOCVD using disilane” J. Electron. Mater., 19 (1990), 1.

[34] M. Shimazu, K. Kamon, K. Kimura, M. Mashita, M. Mihara, M. Ishii, “Silicon doping using disilane in low-pressure OMVPE of GaAs”, Journal of Crystal Growth, Volume 83, Issue 3, June 1987, Pages 327-333

[35] A. Teranishi, S. Suzuki, H. Sugiyama, H. Yokoyama, and M. Asada, “Resonant Tunnaling Diodes with Very High Peak Current Density Using Thin Barrier and High Emitter Doping”, Device Research Conf., .VIA-3, Santa Barbara (USA), Jun., 2008.

[36] M. Christiansen, M. Luenenbuerger, B. Schineller, M. Heuken, and H. Juergensen, “Advances in MOCVD technology for research, development and mass production of compound semiconductor devices”, Opto-Electron. Rev. 10, 237 (2002).

Chapter 3

Optical Spectroscopy of Resonant Tunnelling Diode

3.1 Introduction

This chapter covers optical spectroscopy of high current density InGaAs/AlAs/InP resonant tunnelling diodes (RTDs) structures grown by metal-organic vapour phase epitaxy (MOVPE). Optical spectroscopy is known to be a powerful technique for studying the electronic properties of resonant tunnelling structures [1][2][3][4][5][6][7].

In this chapter, a range of characterisation techniques are applied to RTD structures to allow non-destructive determination of doping level, ternary alloy composition, and quantum well(QW) thickness, via a low temperature photoluminescence (PL) technique. The origin of the PL emission of these high current density RTD structures is investigated in detail, as this has not been fully clarified in the literature [8][9].

The optical properties of doped and undoped RTD structures are explored through low temperature PL, to resolve the absolute energy level position of the first electron state of the RTD. As the performance of the RTD is dictated by the position of the absolute resonant energy levels in the QW, with large voltage and current spans required in the negative differential resistance (NDR) region of the RTD for maximum power extraction, being able to accurately measure energy levels in these structures is highly advantageous for device and growth optimisation. The absolute energy levels of the RTD structures are resolved through a combination of doped and undoped structures. The analysis also allows important scattering mechanisms affecting device performance to be investigated, and provides a non-destructive monitor of the QW alloy content and thickness. PL mapping of the RTD wafer has been performed at low temperatures for the assessment of variations in InGaAs alloy composition and well-width fluctuations with high spatial uniformity in a non-destructive test.

Optical spectroscopy of the epitaxy through PL is both time/cost effective and highly advantageous for the growth optimisation process, being a non-destructive technique, compared to other techniques such as SIMS, eCV, and transmission electron microscopy (TEM). The details of the growth process are discussed and confirmed using high resolution X-ray diffraction (HR-XRD) crystallography. The rapid non-destructive characterisation and wafer mapping of these structures promises a route to future growth optimisation of such structures.

3.2 Epitaxial Material and Growth Details

The epitaxial growth of the RTD structures was carried out under the supervision of Dr. Ben Stevens from the National Centre of III-V Technologies. The growth was performed in a vertical Thomas Swan 6 x 2″ close-coupled shower head MOVPE reactor on (100) semi-insulating InP:Fe substrates with a 0.07 °offcut at a pressure of 100 Torr. The wafer was placed with the major flat towards the edge of the susceptor plate. A Laytec EpiTT pyrometer (calibrated using an Absolut probe) was used to control the growth temperature to 560 °C. The thermocouple set point to achieve this was set between 585 °C and 629 °C. The wafer was heated by three stationary resistive graphite heaters located underneath the wafer carrier which was rotated at 100 rpm in the clockwise direction. Trimethylgallium (TMG), trimethylaluminium (TMA) and trimethylindium (TMI), housed in stainless steel bubblers, were used as group-III precursors and arsine (AsH_3) and phosphine (PH_3) as the group-V source materials. The ternary InGaAs alloy was grown under a V/III ratio of 200. Hydrogen (H_2) was used as the carrier gas and purified by a palladium cell. Epison^{TM} gas phase analysers were used to accurately control the concentration of the gas phase. Disilane (Si_2H_6) diluted to 10 ppm in helium (He) was used as precursor to achieve n-doping concentrations up to $2x10^{19}$ cm^{-3}. Using disilane instead of silane (SiH_4) is often preferred due to the higher silicon incorporation efficiency and lower temperature dependence [10]. To achieve high n-doping concentrations (up to $2x10^{19}$ cm^{-3}), a comparatively low growth rate of 6 nm/min. was used to maximise the incorporation of the silicon dopant in the crystal. The growth rate was calibrated with the EpiTT system using optical reflectance interferometry.

The epitaxy of the RTD structure consisted of a 100 nm InP buffer layer, followed by 200 nm $In_{0.53}Ga_{0.47}As$, and 400 nm highly n-doped $In_{0.53}Ga_{0.47}As$ ($2x10^{19}$ cm^{-3} Si) to serve as the lower contact. A 20 nm n-doped $In_{0.53}Ga_{0.47}As$ ($3x10^{18}$ cm^{-3} Si) emitter layer was subsequently grown, followed by a 2 nm $In_{0.53}Ga_{0.47}As$ spacer layer. An $In_{0.80}Ga_{0.20}As$ quantum well was formed between two 1.1 nm AlAs barriers. At the collector side, a 20 nm $In_{0.53}Ga_{0.47}As$ spacer layer was grown with a 25 nm $In_{0.53}Ga_{0.47}As$ ($3x10^{18}$ cm^{-3} Si) collector layer. The epitaxy was terminated with 15 nm n-doped $In_{0.53}Ga_{0.47}As$ ($2x10^{19}$ cm^{-3} Si), and 8 nm $In_{0.80}Ga_{0.20}As$ ($2x10^{19}$ cm^{-3} Si) to enhance the formation of a low-resistance ohmic contact at the collector side. Fig. 3.1 schematically shows the RTD layer structure. RTD structures were grown with varying QW thicknesses of 3 nm, 3.5 nm, 4 nm, and 4.5 nm. The undoped RTD structures were grown primarily for an optical spectroscopy study, as a repeat of the doped RTD structure with a 4.5 nm QW, but without the inclusion of the precursor Si_2H_6 as the dopant gas. Fig. 3.1 also shows a transmission electron microscope (TEM) image of a RTD structure with a 4.5 nm QW. The growth appears to be of excellent quality and defect free.

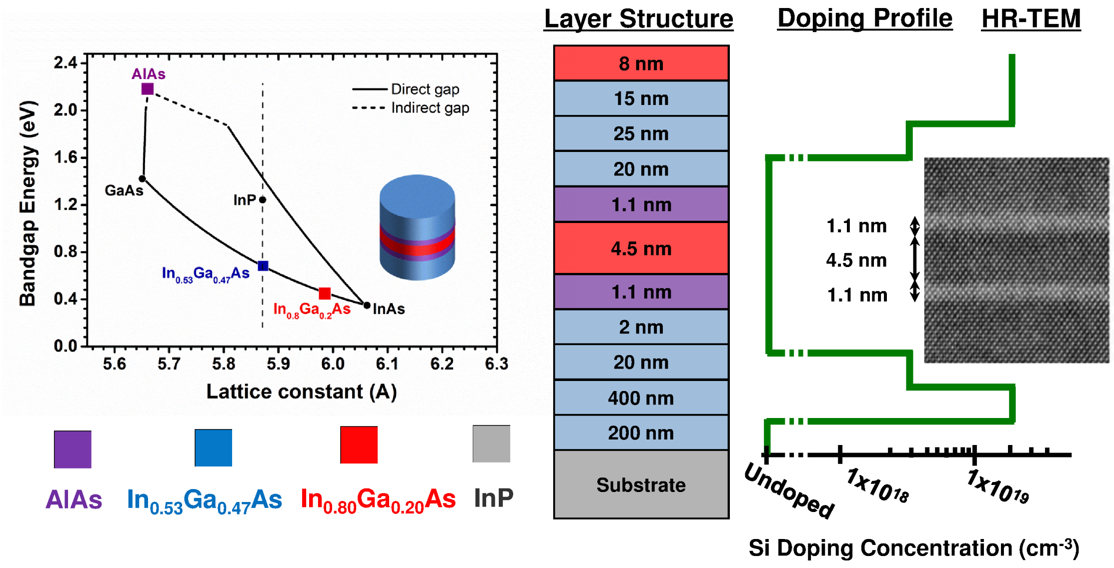

Figure 3.1: Schematic of RTD layer structure and transmission electron microscope (TEM) image of a 4.5 nm QW (TEM image courtesy of Rohm Semiconductor)

3.3 Modelling of Energy Transitions

The energy transitions of the RTD were modelled as part of the investigation. This work was carried out to ensure that the experimental measurement system was optimum for the detection of QW emission, and to compare theory against experimental results. The detectable wavelength range of our PL system is mainly governed by the wavelength ranges of the InGaAs photodetector (0.73 - 1.55 eV) and the double-grating monochromator. The resonant states of the undoped InGaAs/AlAs RTD structure were calculated without an applied external electric field for the conduction and valence bands. The transmission coefficients of the RTD structure, in Fig. 3.2, were calculated through a finite square-well model with open boundary conditions applied to the structure [11]. The programming language MATLAB was used to model the InGaAs/AlAs/InP RTD. A basic transfer matrix algorithm was adapted from R. Petersen [12] and used as a platform for the development of the model. Worthy of mention is that the model is only based on global coherent tunnelling, no phase-decoherence scattering events are considered in this investigation.

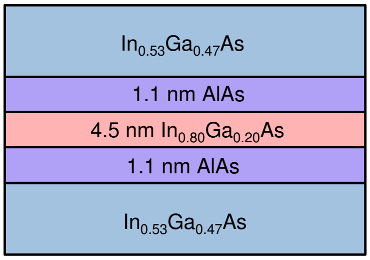

Figure 3.2: Layer structure used for modelling the energy transitions of the RTD

The transfer matrix method was first proposed by Tsu and Esaki in 1973 [11] for the numerical calculation of the transmission probability function of the RTD. This method is based on solving the 1D Schrdinger equation with scattering boundaries on the wave function. Considering the 1D time-independent Schrdinger equation 3.1

$$\frac{\hbar^2}{2}\frac{\partial}{\partial z}\left(\frac{1}{m^*(z)}\frac{\partial}{\partial z}\right)\psi(z) + V(z)\psi(z) = E_z\psi(z) \tag{3.1}$$

The wave function in each section (i.e. barriers and well) of the RTD (simplified band structure diagram shown in Fig. 3.3) are expressed in plane waveform following Eq. 3.2

$$\psi_i(z) = A_i e^{jk_i z} + B_i e^{-jk_i z} \tag{3.2}$$

where k_i is the complex wave number (Eq. 3.3)

$$k_i = \frac{\sqrt{2m_i^*(E_z - V_i)}}{\hbar} \tag{3.3}$$

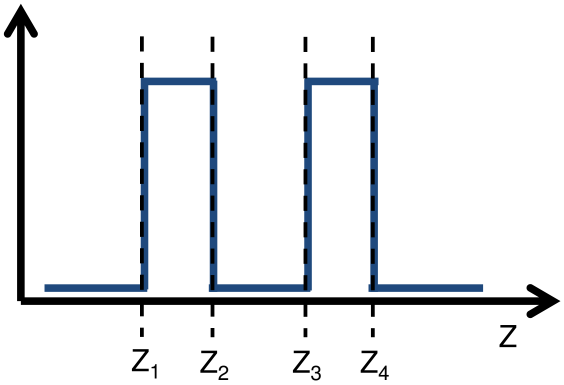

Figure 3.3: Simplified band diagram of a double barrier RTD

At each boundary, two conditions on the wave functions must hold (Eq. 3.4 Eq. 3.5)

$$\psi_i(z_i) = \psi_{i+1}(z+1) \tag{3.4}$$

$$\left.\frac{1}{m_i^*}\frac{\partial\psi_i(z)}{\partial(z)}\right|_{z=z_{i+1}} = \left.\frac{1}{m_{i+1}^*}\frac{\partial\psi_{i+1}(z)}{\partial(z)}\right|_{z=z_{i+1}} \tag{3.5}$$

The coefficients A & B in the adjacent sections are then related to each other as follows (Eq. 3.6)

$$\begin{bmatrix}\frac{A_{i+1}}{B_{i+1}}\end{bmatrix} = T_i \begin{bmatrix}\frac{A_i}{B_i}\end{bmatrix} \tag{3.6}$$

where T_i is defined as the transfer matrix between two sections (Eq. 3.7)

$$T_i = \frac{1}{2}\begin{bmatrix} 1+\frac{m_{i+1}^*}{m_i^*}\frac{k_i}{k_{i+1}}e^{j(k_i-k_{i+1})z_{i+1}} & 1-\frac{m_{i+1}^*}{m_i^*}\frac{k_i}{k_{i+1}}e^{-j(k_i+k_{i+1})z_{i+1}} \\ 1-\frac{m_{i+1}^*}{m_i^*}\frac{k_i}{k_{i+1}}e^{j(k_i+k_{i+1})z_{i+1}} & 1+\frac{m_{i+1}^*}{m_i^*}\frac{k_i}{k_{i+1}}e^{-j(k_i-k_{i+1})z_{i+1}} \end{bmatrix} \tag{3.7}$$

The A & B coefficients of the collector and emitter can be related to each other following Eq. 3.8 and Eq. 3.9

$$\begin{bmatrix}\frac{A_{E_z}^L}{B_{E_z}^L}\end{bmatrix} = T \begin{bmatrix}\frac{A_{E_z}^R}{B_{E_z}^R}\end{bmatrix} \tag{3.8}$$

$$T = T_i T_{i-1} T_{i-2} ... T_1 \tag{3.9}$$

By using scattering conditions for the emitter (Eq. 3.10)and collector (Eq. 3.11).

$$(A_{E_z}^L, B_{E_z}^R) = (1,0) \tag{3.10}$$

$$(A_{E_z}^L, B_{E_z}^R) = (0,1) \tag{3.11}$$

The transmission probability $T(E_z)$ is expressed by Eq. 3.12

$$T(E_z) = \frac{m^{*L}}{m^{*R}} \frac{k^R}{k^L} \frac{\left|A^R_{E_z}\right|^2}{\left|A^L_{E_z}\right|^2} \tag{3.12}$$

Table 3.1 lists the semiconductor material parameters that were used to calculate the energy levels of the RTD structure.

Layer	**$In_{0.53}Ga_{0.47}As$**	**$In_{0.80}Ga_{0.20}As$**	**AlAs**
a_0(A)	5.867	5.976	5.659
$\alpha_{th}(10^{-6}/C)$	5.857	5.463	5.2
Eg(eV)	0.811	0.556	3.13
C11(10^{11}dyn/cm^2)	9.99	9.04	12.5
C12(10^{11}dyn/cm^2)	4.93	4.70	5.3
a_c(eV)	-6.058	-5.498	-5.64
a_v(eV)	1.075	1.032	2.74
b(eV)	-1.753	-1.779	-1.5
m^*_c/m_0	0.0436	0.0318	0.13
m^*_{hh}/m_0	0.609	0.604	0.44

Table 3.1: Parameters used to calculate the resonant energy levels of the RTD. The parameters values are taken from [13][14][15]

The band structure of the RTD structure was modelled using model-solid theory, a theory first proposed by Chris Van de Walle [16]. This method relates the energy levels in bulk semiconductors from self-consistent *ab initio* band structure calculations to a common reference level. This reference level is chosen to be the average electrostatic potential in a semi-infinite "model-solid" built up from a superposition of neutral atoms to mimic the bulk electron density. Fig. 3.4 shows the modelled energy band diagram of an undoped InGaAs/AlAs RTD structure.

The black and orange lines represent the band structure with and without the inclusion of strain, respectively. The tunnelling barriers of the RTD are under tensile strain, as the lattice constant of AlAs is smaller than lattice matched InGaAs to InP, which reduces the band-gap energy of AlAs. The tensile strain shifts and splits the degenerate valence bands at the Γ points, effectively rising the light hole band above the heavy hole band, which has a larger effective mass. The opposite occurs for the compressively strained $In_{0.8}Ga_{0.2}As$ well, as the band-gap energy increases due to compressive strain and the heavy-hole band rises above the light hole band.

Fig. 3.5 (a) and (b) show the modelled transmission coefficients as a function of incident-electron energy for the conduction and valence bands at 15 K, respectively, for the band structure shown in Fig. 3.2.

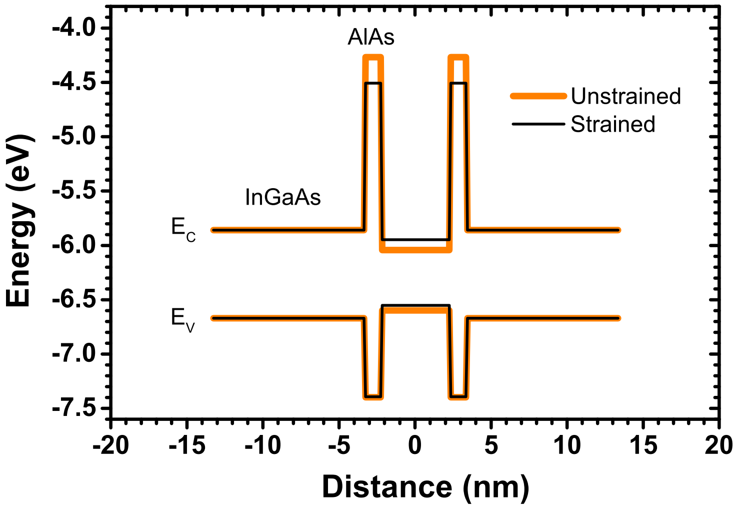

Figure 3.4: Modelled band structure of InGaAs/AlAs RTD with (orange line) and without strain (black line) at 15 K.

The peaks in the transmission spectra correspond to the discrete energy states in the QW along the growth direction. Unity transmission is observed at the resonant energy levels as the transmission coefficients are calculated for a symmetrical structure. The observed increase in energy separation between adjacent transmission peaks is explained by the parabolic energy dispersion for the in-plane momentum of carriers in the QW. The transmission coefficients are only calculated for the heavy holes in the valence band as the $\mathrm{In_{0.8}Ga_{0.2}As}$ quantum well is compressively strained. A smaller energy spacing between resonances in the valence band is calculated, due to the larger effective mass of the holes. Furthermore, the resonance width of the electronic states in the conduction band is larger than for the hole states in the valence band, which is also associated to the difference in effective mass between electrons and holes. Fig. 3.6 shows the modelled band diagram of the InGaAs/AlAs RTD with the first and second energy states of the conduction and heavy-hole bands. Two resonant states are calculated in the conduction band for energies less than the conduction band edge of AlAs with a measured energy separation of 0.71 eV. As observed in Fig. 3.6, these resonant energies are quasi-bound states as the AlAs barriers have a finite width of 1.1 nm. For the valence band, the first heavy-hole state is a bound state, as the quantisation energy of the resonant state is less than the valence band energy edge of $\mathrm{In_{0.53}Ga_{0.47}As}$. The smaller quantisation energy in the valence band is associated with the higher effective mass of the holes. The strain dependence of the effective mass is not considered in these calculations.

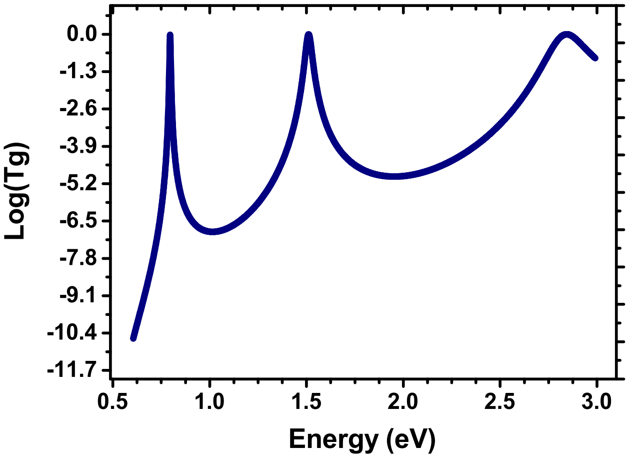

(a)

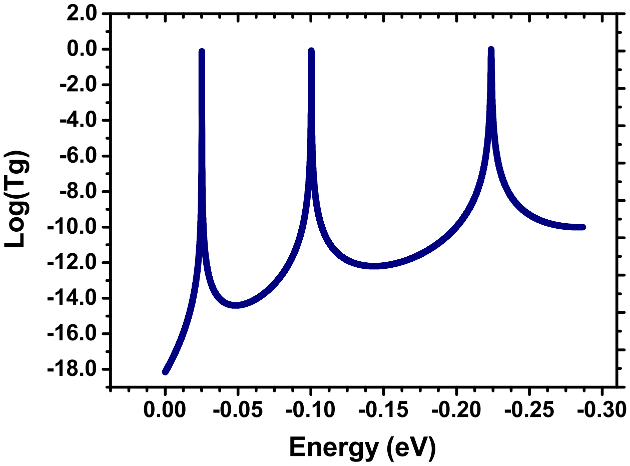

(b)

Figure 3.5: Modelled transmission coefficients for (a) the conduction band, and (b) the valence band.

The electron 1-heavy hole 1 (e1hh1) transition is calculated as the sum of the bandgap-energy of the strained $In_{0.8}Ga_{0.2}As$ well and the lowest energy states of the conduction and heavy hole bands, following Eq. 3.13.

$$E_1HH_1 = E_{well} + E_{C1} + E_{HH1} \tag{3.13}$$

A transition energy of 827 meV is calculated for e1hh1. This transition energy is 16 meV larger than the low temperature band-gap energy of lattice matched InGaAs ($Eg_{2K} = 811$ meV) [15].

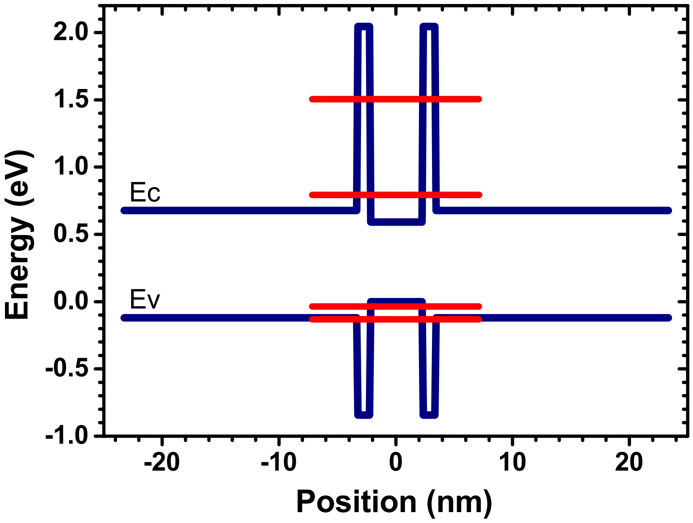

Figure 3.6: Energy band diagram of an undoped InGaAs/AlAs based RTD structure. The horizontal lines represent the first two resonant energy levels in the conduction and valence bands.

Fig. 3.7 shows the effect of the layer thickness of the AlAs barriers, the compressively strained quantum well (QW), and the indium content of the $In_{0.80}Ga_{0.20}As$ QW on the confinement energy of the first electron and heavy-hole states.

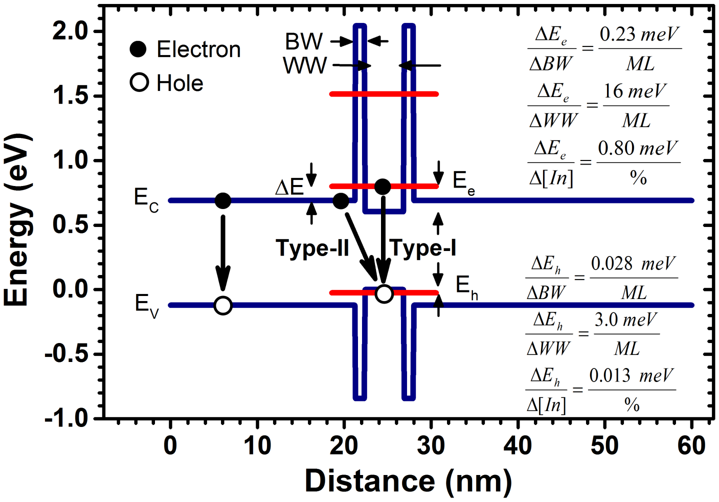

Figure 3.7: Band-structure of a typical InGaAs/AlAs/InP based RTD. The possible luminescence transitions which may occur in the RTD structure are indicated by arrows. The horizontal red lines indicate the first and second electron states and first heavy-hole state. The effect of monolayer (ML) fluctuations in barrier width (BW), and well width (WW), and indium [In] concentration on the resonant energy levels are included.

From calculations, it follows that the confinement energy of the electrons in the QW is a strong function of the quantum well width (WW) and the indium content [In], but is significantly less sensitive to variations in barrier width (BW). For holes, as expected for a significant increase in mass (from $0.03\mathrm{m}_0$ to $0.60\mathrm{m}_0$), there is a considerable reduction in the sensitivity of the confinement energy to all parameters. To a first approximation, the energy of the type-II transition indicated in Fig. 3.7 is determined by the indium composition of the QW and the band-offset. The first electron state in the QW can be deduced if all the energetic transitions of the structure shown in Fig. 3.7 are measurable. The carrier lifetime in the QW, known as the dwell time, τ_d, was also considered theoretically using the finite square-well model. The decay rate of the resonant state for completely coherent transmission is given by Eq. 3.14.

$$\frac{1}{\tau_d} = \frac{\Gamma}{\hbar} \tag{3.14}$$

where τ_d is the elastic decay rate, $\hbar$ the reduced Planck's constant, and Γ the elastic width of the resonant level. The elastic width of the resonant state is approximated to the FWHM of the resonant state calculated from the transmission coefficient spectrum using the transfer-matrix method. Fig. 3.8 shows the FWHM linewidth of the the first resonant energy state in the conduction band as a function of barrier thickness for RTD structures with well widths ranging between 3.0-4.5 nm. An exponential relationship between barrier thickness and the resonance width is observed with broad and narrow resonances for thin and thick potential barriers, respectively. By increasing the barrier thickness, the confinement in the well becomes stronger, with a concomitant increase in the lifetime of the carriers at resonance. An increase in the resonance width is also observed for thinner QWs. By decreasing the well width, the electron confinement energy increases, which reduces the resonance lifetime due to the lower potential barrier height. A FWHM of 3.2 meV is calculated for a 4.5 nm QW with 1.1 nm barriers. Through Eq. 3.14 and Fig. 3.8, the electron dwell time was calculated for the structure. Fig. 3.9. shows the dwell time as a function of barrier and well thickness. The inset schematically illustrates the multiple-reflection process of the electron in the quantum well. As observed in Fig. 3.9, the electron dwell time in the quantum well is inversely proportional to the resonance width, with a short dwell time associated to a broad resonance. The dwell time becomes longer for thicker barrier and well thicknesses, as the multiple reflection time becomes longer. An electron escape time of 58 fs was calculated for a 4.5 nm $\mathrm{In}_{0.8}\mathrm{Ga}_{0.2}\mathrm{As}$ QW confined by 1.1 nm AlAs barriers and $\mathrm{In}_{0.53}\mathrm{Ga}_{0.47}\mathrm{As}$ spacer layers. As the speed of operation of the RTD is mainly governed by tunnelling probability of the electron through the structure, with short

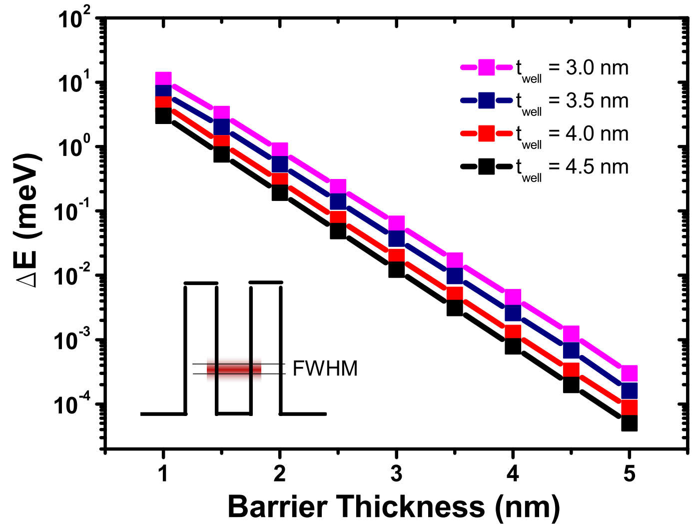

Figure 3.8: Resonance width as a function of barrier thickness for different QW widths.The inset pictographically shows the energy-band diagram indicating the FWHM linewidth of the first resonant energy level

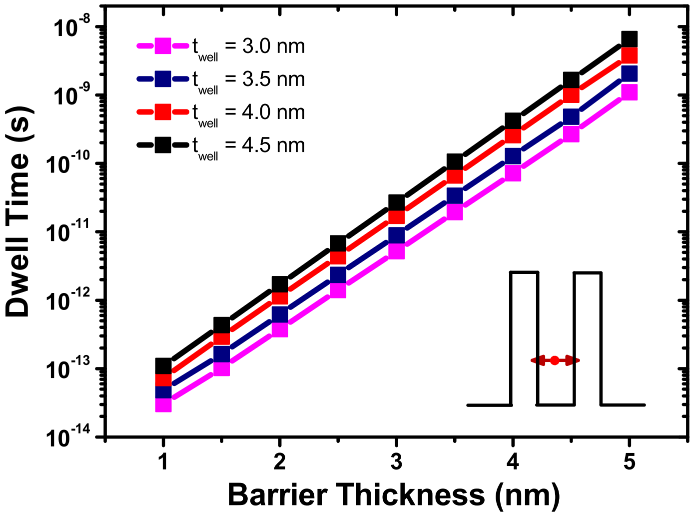

Figure 3.9: Electron dwell time as a function of barrier thickness for different well widths. The inset pictographically shows the energy-band diagram illustrating the multiple-reflection process of an electron.

dwell times being required, the RTD is able to operate at very high frequencies, as compared to many other electronic devices where the speed of operating is governed by a conventional transit-time [17].

3.4 Photoluminescence Spectroscopy of Resonant Tunnelling Diode

PL experiments were performed over a temperature range from 15 to 300 K in a closed cycle helium cryostat. Nd:YVO$_4$ laser excitation at 532 nm, chopped at 20 Hz, was used to excite the samples. A Bentham DMc150 double monochromator was used to disperse and analyse the PL. The signal was detected by an InGaAs transimpedance amplified photodetector coupled to a EG&G 5208 two-phase lock-in analyser. PL experiments were performed with an excitation power of 15 mW focused to a spot of $\sim$ 75 µm in diameter. High-resolution X-ray diffractometry (HR-XRD) was applied on the (004) reflection to characterise the crystal, including layer composition and strain.

3.4.1 Low Temperature Photoluminescence Spectroscopy

Fig. 3.10 shows temperature dependent PL spectra of the 4.5 nm QW RTD structure (shown schematically in Fig. 3.1) at the wafer center from 15 K to 300 K. A broad emission spectrum is observed at 300 K, which resolves into two distinctive emission features at 789 meV and 834 meV when the sample is cooled below 50 K. A FWHM linewidth of 43 meV is estimated of the broad emission feature at 834 meV from the half-width at half maximum (HWHM) linewidth at the high energy end of the spectrum, as indicated in Fig. 3.10. A weak signal is measured at room temperature, which is associated to the reduction in bulk non-radiative recombination lifetime and increase in surface recombination velocity with temperature. Low temperature PL spectroscopy has previously been shown to be useful in studying the characteristics of the resonant tunnelling process. Young *et al.*[2], Skolnick *et al.* [3], and Buckle *et al.* [1] applied PL to determine the charge accumulation in resonant tunneling structures as a function of bias.

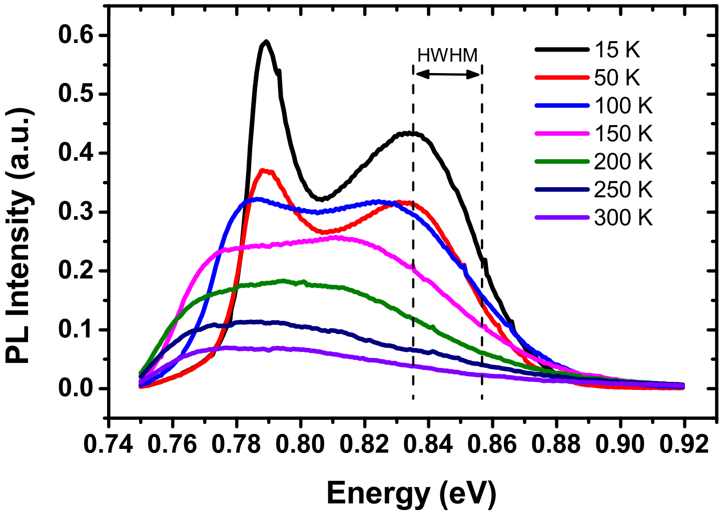

Figure 3.10: Temperature dependent PL spectra of the full RTD structure from 15 K to 300 K.

3.4.2 Origin of the Photoluminescence Emission

The eCV profiler was used as a selective etch tool to explore the origin of the observed emission. Fig. 3.11 shows the measured free-carrier concentration of the RTD structure as a function of depth through eCV. The solid line represents the designed doping profile. Good agreement is observed between the designed and measured free-carrier/doping profiles. The good agreement between both profiles highlights the use of eCV as a highly accurate selective etch tool. This technique was used to create a PL sample with several craters of different etch depths within a few millimetres of each other. For these thin, highly doped structures, an etch step of $\sim$ 2 nm was used.

Fig. 3.12 shows 15 K PL spectra for different etch depths. For the first sample, etching was halted at the highly doped collector layer located above the QW, as shown in the inset of Fig. 3.12(a). The red line on the eCV profile represents the location of the double barrier structure and the blue dotted line represents the measured free-carrier concentration. Etching was halted within an approximate distance of 25 nm above the QW. As in the case of the unetched sample (Fig. 3.10), two features are observed at 789 and 834 meV at 15 K. For the second sample, etching was carried out through the QW, as shown in Fig. 3.12(b)'s inset, and halted on the highly doped emitter layer, within an approximate distance of 16 nm below the QW. In this case, only emission at 789 meV remains detectable. For the third sample, the etch continued through the highly doped emitter layer to the undoped InGaAs buffer layer. The third etch was carried out using a H_3PO_4:H_2O_2:H_2O (1:1:38) wet etchant with an approximate etch rate of 100 nm/min. at room temperature. As

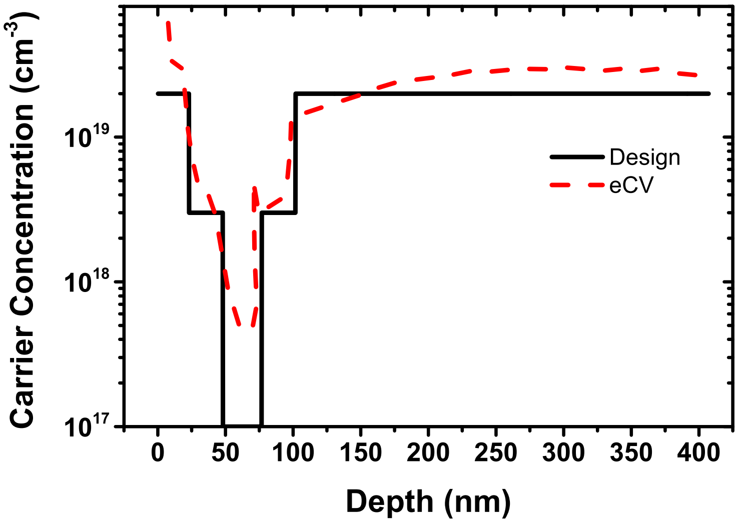

Figure 3.11: Free-carrier concentration as a function of depth of the RTD structure measured by eCV. The dashed line represents the measured free-carrier concentration and the solid line represents the required doping profile.

only emission at 789 meV remains detectable for the second sample, the emission as 834 meV can therefore be attributed to the QW. As the PL emission at 789 meV remains detectable for the other two samples, this emission line is attributed to bulk InGaAs. A 3 meV broadening of the InGaAs emission linewidth is also measured between Fig. 3.12(b) and Fig. 3.12(c). The origin of this observation is not yet clear, but it is maybe caused by re-absorption of the undoped InGaAs emission through the n^+ InGaAs layer.

To further explore the origin of the low temperature PL features in Fig. 3.10, a line-scan was carried out along the edge of the wafer, as schematically illustrated in Fig. 3.13(a). This technique allows a partially quantitative PL map with higher resolution than can be obtained using standard positioning of the stages due to the shallow angle used. Previous selective etch measurements were not able to unambiguously identify the origin of the bulk InGaAs peak observed at 789 meV [18]. Fig. 3.13(b) shows the PL intensity as a function of energy for 103 scans measured along the edge of the wafer in the epitaxial direction with a 10 micron step size, as indicated. Due to the finite spot size of the excitation light, approximately 75 μm in diameter, the PL emission from the 4.5 nm QW was spread across multiple spectra. Assuming a spread of ± 10 scans for the QW and bulk InGaAs layer, which is reasonable as the well is only 4.5 nm thick, the separation of the QW and undoped InGaAs buffer layer is in good agreement with the designed 400 nm n^+ InGaAs layer. As no emission is observed at the band-gap energy of InGaAs for the undoped InGaAs

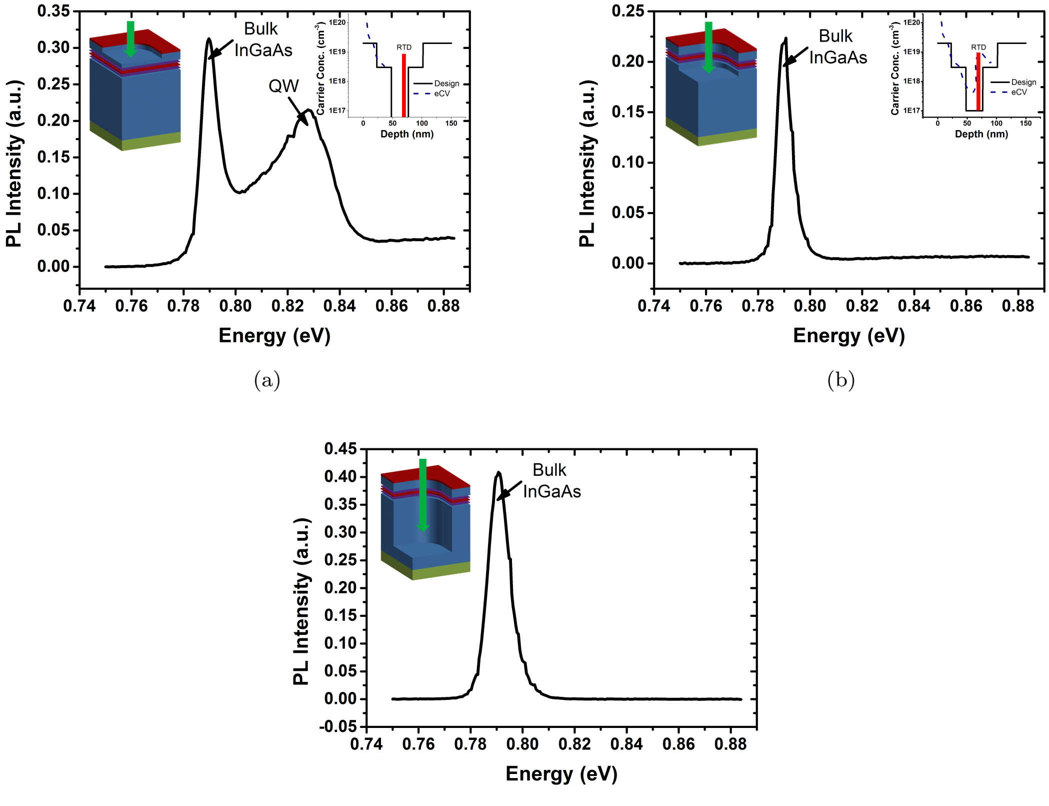

(a)

(b)

(c)

Figure 3.12: PL spectra at 15 K for different etch depths. In (a) etching was halted at the highly doped collector layer located above the QW, in (b), etching halted on the highly doped emitter layer below the QW, in (c), etching was halted on the undoped InGaAs buffer layer. The eCV profiles of etches (a) and (b) are shown in the insets, with free carrier concentrations plotted as a function of depth. The red line on the eCV profile represents the location of the double barrier structure and the blue dotted line represents the measured free-carrier concentration.

spacer layers in Fig. 3.13(b), the emission line at 789 meV is attributed to the 200 nm undoped InGaAs buffer layer. This suggests that the photogenerated carriers tunnel rapidly in the QW, and the electrostatic potential profile associated with the doped RTD spatially separates the carriers, preventing radiative recombination within the undoped spacer layers closest to the QW.

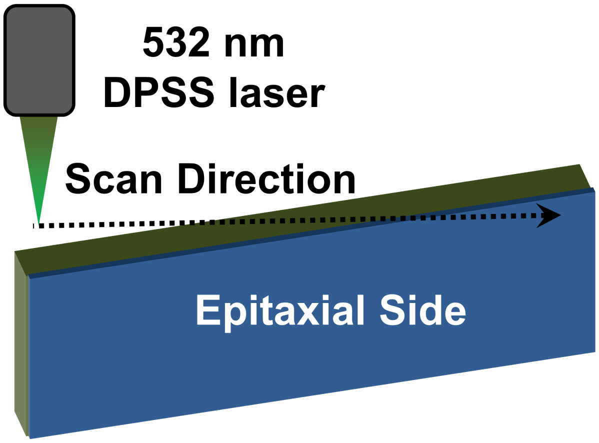

(a)

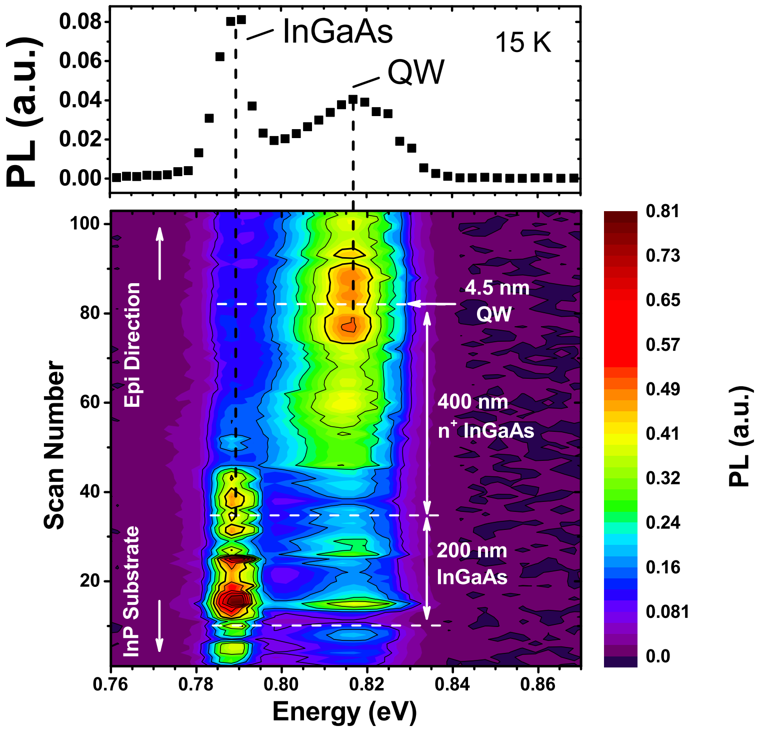

(b)

Figure 3.13: (a) Schematic diagram of the PL linescan technique along the edge of the wafer performed with a diode-pumped solid-state (DPSS) laser (b) PL emission measured at 15 K as a function of energy measured along the scan direction as indicated in (a)

3.4.3 Photoluminescence Spectroscopy of Undoped/n$^+$ InGaAs

Fig. 3.14 shows temperature dependent PL spectra of the etched sample with the highly doped emitter layer on the surface (Fig.3.12 (b)). The inset shows the same data plotted on a logarithmic scale. In addition to the emission feature at 789 meV, a broad emission extending to $\sim$ 1.1 eV is measured. PL emission as a function of doping in InGaAs was investigated in Chapter 2, where a broad PL emission extending towards higher energies is observed due to the Moss-Burstein effect. The emission at 789 meV from the deeper undoped InGaAs buffer layer is measured as a stronger signal than the emission from the highly doped InGaAs layer, even though this layer is more deeply burried in the layer stack. This shows that the radiative recombination efficiency of the undoped InGaAs layer is greater than the recombination efficiency of the highly n-doped InGaAs. The low radiative recombination efficiency of the highly doped InGaAs layer can be associated to a short non-radiative recombination time due to increased Auger recombination [19][20].

An Auger process involves three carriers, where the energy released by the recombination of an electron and hole is transferred to another nearby carrier instead of creating a photon. This electron then thermalises back down to the conduction band edge. The total recombination lifetime τ can be represented by the parametric equation Eq. 3.15

$$\tau = [\tau_{SRH}^{-1} + Bn + Cn^2]^{-1} \tag{3.15}$$

where the three terms on the right-hand side represent the Shockley-Read-Hall (SRH, A coefficient), radiative, and Auger recombination contributions, respectively. n is the free-electron concentration, and B and C are the radiative and Auger recombination coefficients. Henry *et al.* have shown from measurements performed on InGaAs over a doping concentration range of 3x10^{17}cm^{-3} to 1x10^{19} cm^{-3} that the recombination lifetime decreases with doping concentration due to a combination of radiative and Auger recombination [21]. Ahrenkiel and co-workers have found that in the doping range from 10^{16} to 10^{18} cm^{-3}, the radiative lifetime varies as 1/n, with n being defined as the majority carrier doping concentration [22]. This behavior was indicative that radiative recombination is the dominant mechanism in the doping range from 10^{16} to 10^{18} cm^{-3}, were a “B” coefficient of 1.43x10^{-10} cm^{-3}s^{-1} was measured, which was also in strong agreement with the observation of InGaAs as a strong light emitter. They have also shown that the SRH lifetime is on the order of a microsecond for undoped InGaAs samples, and for doping densities greater than 5x10^{18} cm^{-3} Auger recombination becomes the dominant recombination mechanism as the Auger recombination lifetime is inversely proportional to the square of the majority carrier concentration.

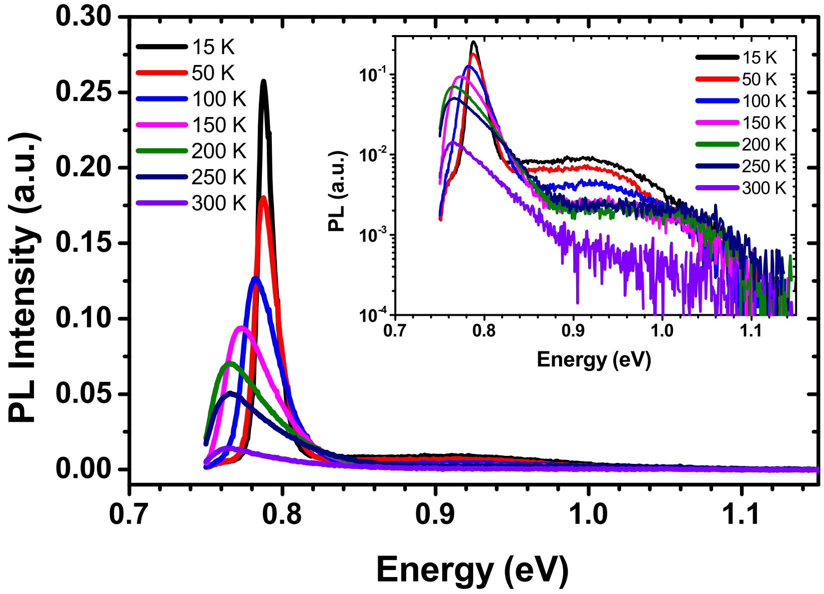

Figure 3.14: Temperature dependent PL spectra on the second etch sample (Fig.3.12(b)) with the highly doped emitter layer (n = 2x10^{19} cm^{-3}) exposed from 15 300 K. The inset shows the spectra plotted on a logarithmic scale.

For an Auger recombination constant of 8.1x10^{-29} cm^{6}/s [22], a recombination lifetime of 31 picoseconds is calculated for the highly doped emitter/collector layers with a doping concentration of 2x10^{19} cm^{-3}. Indeed, the Auger recombination lifetime is approximately ten times shorter than the radiative recombination lifetime for a doping concentration of 2x10^{19}cm^{-3}, which is in good agreement with the observations made in Fig. 3.14. From the low temperature PL emission spectra shown in Fig. 3.14, it was also possible to deduce the absolute free carrier concentration of the 400 nm n^{+} InGaAs layer. The measured energy at -20 dB of I_{EMAX} at the high energy tail of the spectrum (E_{-20dB} = 1.11 eV) corresponds to a free carrier concentration of 3.1x10^{19}cm^{-3}, which is in very good agreement with the measured free-carrier concentration of 3x10^{19}cm^{-3} shown in Fig. 3.11.

Aside from HR-XRD, PL spectroscopy is also a powerful technique which can be applied to determine the crystal quality. The PL emission linewidth generally gives a good measure of the material quality with narrow linewidths commonly being a characteristic of high quality material. At low temperatures, the PL linewidth of bound excitons can be less than 0.1 meV in binary III-V semiconductors [23]. The linewidth of ternaries and quarternaries is typically larger. Low temperature PL excitonic linewidths with a FWHM of less than 2 meV have been reported for high quality

MOVPE grown $In_{0.53}Ga_{0.47}As$ by a number of workers [15][24][25][26]. An excitonic PL linewidth of 1.2 meV was measured by Schubert *et al.* for $In_{0.53}Ga_{0.47}As$ grown by chemical-beam epitaxy (CBE) [23][27]. The broader linewidths of ternary and quaternary semiconductors are commonly attributed to compositional inhomogeneities and to alloy clustering [28][29]. Schubert *et al.* showed good agreement between experimental and theoretical data by developing a quantitative model describing the broadening of the linewidths of the exciton and the band-to-acceptor recombinations due to alloy broadening [23]. A FWHM PL emission linewidth of 6.9 meV was measured at 15 K for the emission line at 789 meV. From the position of the peak emission energy, the InGaAs emission at 789 meV could not be associated to a free exciton, or exciton bound to a shallow acceptor as the low temperature PL emission is 17 meV red-shifted from the nominal band-gap energy of $In_{0.538}Ga_{0.462}As$ (806 meV for a 200 ppm positive lattice mismatch). Binding energies up to 4.5 meV have been assigned for the aforementioned near band-gap excitonic emission lines by Goetz *et al.* [15]. The same group have also assigned binding energies of 13 meV ± 1 meV, 25 meV ± 1 meV, and 22 meV ± 1 meV for the shallow acceptors, carbon (C), silicon (Si), and zinc (Zn), respectively, in undoped MOCVD grown InGaAs [15]. Of note, temperature dependent PL spectroscopy can also be used to determine the activation energies of impurities in the crystal. A donor-to-acceptor pair (DAP) recombination process between a donor and acceptor is unlikely as other exciton emission lines are typically observed along with DAP emission lines [15][30][25][31][32][24][23]. In this work, only a single emission line is observed. Similar observations were made by Bass *et al.* for low temperature MOVPE grown undoped InGaAs at 620 °C [25]. They showed that at high growth temperatures (>636 °C), the PL spectrum typically consists of a near band edge exciton line and an electron-to-acceptor (e-A0) or a donor-acceptor pair line. However, at low growth temperatures, the PL spectrum is dominated by e-A0 recombination due to exciton ionization caused by strongly fluctuating local potentials in the crystal. An e-A0 optical transition involves an electron in the conduction band recombining with a hole trapped on an acceptor level.

The Maxwell-Boltzmann lineshape of the e-A0 luminescence for a direct bandgap semiconductor can be described by Eq.3.16, assuming a hole effective mass m_{hole} ->infinite, which is a valid approximation as the hole bound to an acceptor can be treated as an immobile particle with an effective mass m_{hole} ->infinite (i.e. zero curvature) [33].

$$I_{SP}^{(e-A^0)} \approx [hv-(E_g-E_A)]^{1/2} exp(-\frac{hv-(E_g-E_A)}{k_B T}) \tag{3.16}$$

Fig. 3.15 shows the theoretical emission line shape for temperatures from 20-100 K. The inset of the figure schematically illustrates the e-A0 recombination mechanism. The lineshape of an e-A0 transition has a characteristic asymmetric lineshape with a minimum FWHM of approximately 1.80 k_BT, and peak emission at (E_C-E_A) + kT/2, assuming a defect-free semiconductor. As observed in Fig. 3.15, the linewidth of an e-A0 transition is highly dependent on the crystal temperature. From Fig. 3.15, an e-A0 transition at 15 K has a minimum FWHM of approximately 2.25 meV. The linewidth discrepancy of 4.7 meV between theory and the measured FWHM can be associated to a combination of alloy broadening and some thermal broadening, due to self-heating of the semiconductor from the laser excitation light and non-optimal cooling conditions of the sample in the cryostat. Whereas self-heating effects can be minimised by using very short excitation pulses, the experimental setup was not equipped to perform such experiments. Further, carbon is selected as a good candidate for the acceptor level as the measured energy shift of the PL spectra (17 meV) is in good agreement with the binding energy of carbon (13 meV).

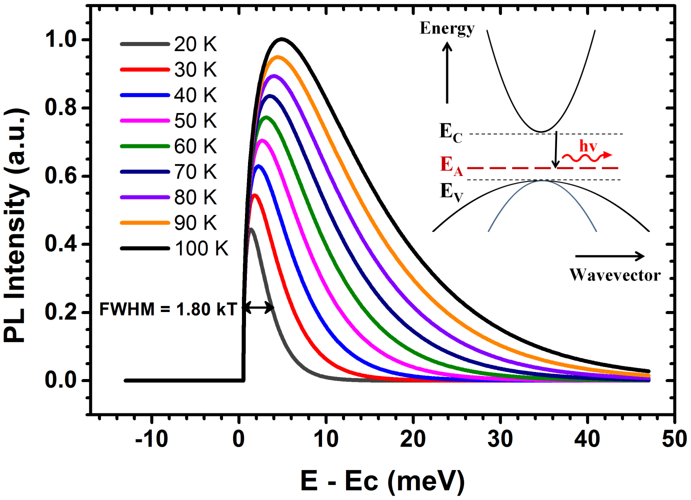

Figure 3.15: Lineshape function for a band-to-acceptor (e-A0) recombination in bulk InGaAs from 20-100 K. The inset schematically illustrates the e-A0 recombination mechanism.

Hydrogen and carbon impurities are difficult to avoid in MOVPE growth, as they are byproducts of the precursor breakdown [34]. Fry *et al.* [32] found a dramatic improvement in the PL properties for InGaAs samples grown by MOVPE at 650 °C compared to lower growth temperatures, which was attributed to a reduction in carbon contamination. The growth temperature and V-III ratio are important parameters which influence the impurity incorporation and, thus, mobility of the material. The effects of the V/III ratio on the electronic and optical properties of InGaAs layers grown by MOVPE were investigated by Kamada *et al.* [24]. They found that the donor and acceptor concentrations increase almost linearly in the high V-III ratio, measuring an acceptor impurity concentration of $\sim$ 8x10^{15}cm^{-3} for a V-III ratio of 300. In this work, a carbon impurity concentration of 3x10^{15} atoms/cm^{3} was measured by SIMS for a V-III ratio of 400, which is in-line with the results reported by Kamada *et al.* A reduction in background impurity concentration is expected by future growth optimisation.

3.4.4 Photoluminescence Spectroscopy of Doped/Undoped RTD Structures

Fig. 3.16 shows the electronic band structure and charge density profile of the RTD (with doped emitter/collector) at 15 K. The first and second electron states and first heavy-hole state are indicated by horizontal red lines. NEMO5, a simulation tool based on the non-equilibrium Green's functions (NEGFs) formalism, was used to calculate the band structure [35]. A Hartree model was used to solve the quantum charge self-consistently with the electrostatic potential. As observed in Fig. 3.16, the electrostatic potential is raised on the collector side, with respect to the emitter due to the asymmetry of the RTD structure as the undoped collector and emitter spacer layers are 20 nm and 2 nm, respectively. An electron density of $\sim$ 1x10^{18} cm^{-3} is calculated within the well without a bias applied to the structure. This quantum well charge originates from the diffusion of carriers from the dopant atoms of the highly doped emitter and collector layers. Type-I recombination between the first electron and heavy-hole states is observed in this type of structure as the doping induced electrons in the QW recombine with captured photo-generated holes.

Fig. 3.17 shows excitation power dependent PL spectra of the doped RTD sample measured at 15 K. The feature at 789 meV has previously been assigned to e-A recombination in bulk InGaAs using a selective etch technique based on electrochemical capacitance-voltage profiling (eCV) (section 3.4.2), whereas the feature at 826 meV is attributed to an e1hh1 recombination within the QW, being in excellent agreement with the modelled energetic transition at 827 meV (section 3.3). The absolute position and linewidth of these two emission lines provide valuable information about the alloy composition and broadening of the bulk InGaAs layers, and the QW perfection and first electron-heavy-hole transition energy, respectively. A full-width at half-maximum (FWHM) linewidth of 35 meV is measured for the e1hh1 transition, which appears to consist of two emission lines, as indicated by the two gaussian lineshapes which are fitted to the spectrum, as shown in Fig. 3.17.

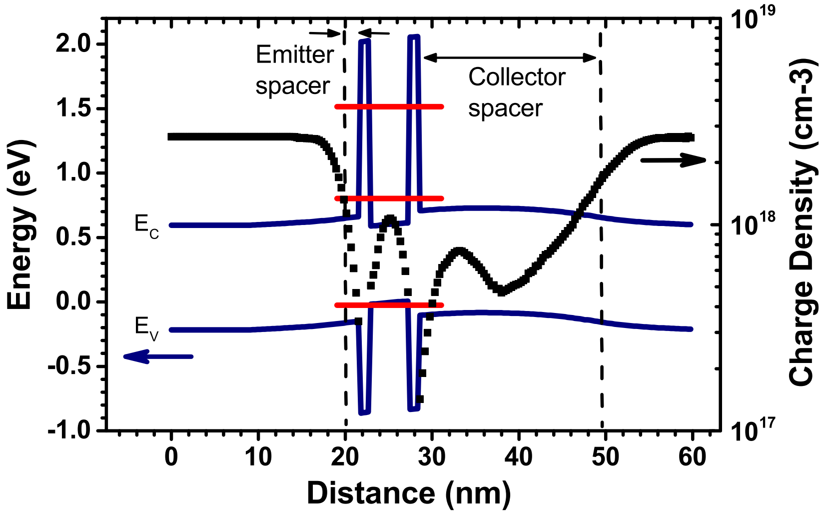

Figure 3.16: Modelled band structure and charge density profile of the doped RTD at 15 K. The horizontal red lines indicate the first and second electron states and first heavy-hole state. The boundary of the emitter and collector spacer layers is defined by the vertical dashed lines.

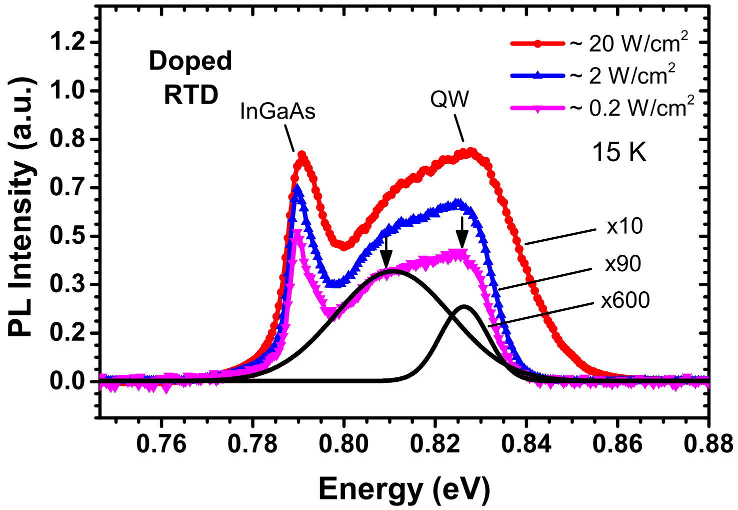

Figure 3.17: Excitation power dependent PL spectra of the doped RTD structure at 15 K. The two black curves are Gaussian fits to the QW emission feature

If the band-offsets of such a structure are well known, the first resonant energy level above the conduction-band of the emitter, ΔE, can be deduced from the measured e1hh1 transition. In order to engineer higher current density/frequency devices and reproducibly manufacture these devices, a precise knowledge of this energetic position is required. However, the use of band-offsets has been highlighted as being inaccurate in the simulation of the absolute energies of particular bound-states from optical transitions in similar structures [36][37][38]. At the lowest excitation density of 0.2 W/cm^2, PL linewidths of 5 meV and $\sim$ 35 meV are measured for the bulk InGaAs and QW emission lines, respectively. For the bulk InGaAs, the origin of broadening is assumed to be due to compositional inhomogeneities (alloy broadening) [28]. The measured value of 5 meV is in line with other reports [39][29]. Assuming a theoretical FWHM emission linewidth of 2.3 meV for a conduction-band-to-acceptor transition for ternary InGaAs at 15 K, 4.4 meV of the measured linewidth of this transition is assigned to alloy and thermal broadening [29]. For the QW, in addition to alloy broadening (reduced as compared to lattice-matched ternary due to higher indium composition), well width fluctuations, barrier width fluctuations, and lifetime broadening of the states will come into play [40]. Of note is that the feature attributed to the QW appears to be a doublet with separation $\sim$ 20 meV, which is in excellent agreement with a calculated value of 19 meV for a ML fluctuation of the QW (Fig. 3.7). Power dependent measurements shown in Fig. 3.17 do not indicate strong saturation effects for these two transitions, suggesting that they have a similar density of states.

With regard to the broadening mechanisms for recombination from such ML fluctuations, as the indium concentration in the QW approaches the binary compound InAs, alloy broadening in the QW is expected to be less pronounced as compared to the case for lattice-matched ternary InGaAs which is close to a 50/50 ratio. Whilst the effect of ML fluctuations of the barrier thickness will have a small effect on the confinement energies, they may have a significant role in modifying lifetime broadening of the transition. Calculation of the electron dwell time gives 58 fs for this structure (1.1 nm barrier), corresponding to a lifetime broadening of 3.2 meV. If a 0.8 nm barrier is considered this value rises to 6.0 meV. These values appear to be in-line with the measured linewidth of the QW transition.

Fig. 3.18 shows a low temperature PL spectrum of a nominally identical undoped RTD sample with a 4.5 nm QW measured at 15 K. Features at 805 meV and 769 meV are measured with FWHM linewidths of 4.8 meV and 13 meV, respectively. The emission at 805 meV, 13 meV red-shifted from the low temperature band-gap energy of $In_{0.526}Ga_{0.474}As$ (818 meV for a 400 ppm negative lattice mismatch), is once again a strong indication of an e-A0 recombination with carbon as acceptor level. The slight shift in energy between the doped and undoped sample is due to campaign-to-campaign variations in lattice-matching which is described later. The inset of the figure shows the calculated e-A0 lineshape at 15 K for $In_{0.526}Ga_{0.474}As$ with a binding energy of 13 meV assigned to carbon. The experimental emission band shows good agreement with the theoretical lineshape of the e-A0

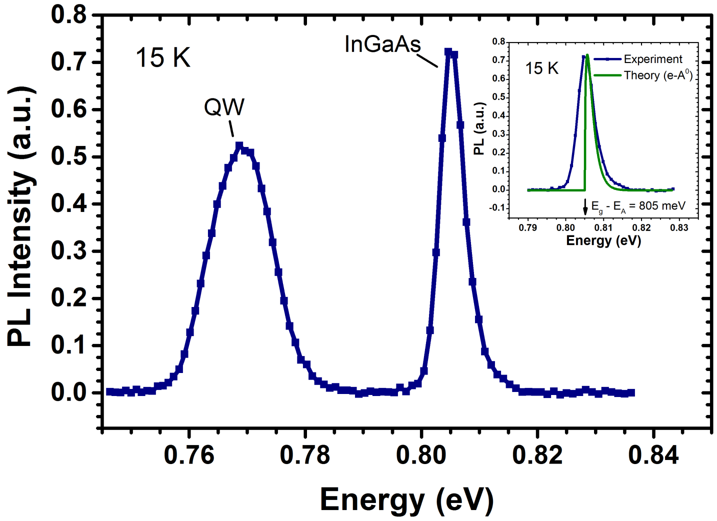

Figure 3.18: Low temperature PL spectrum of the undoped RTD structure measured at 15 K. The inset shows the experimental data and theoretical lineshape for an e-A0 transition in InGaAs.

transition. As the e-A0 transition at 15 K has a minimum FWHM of approximately 2.25 meV, a 4.2 meV linewidth broadening is attributed to alloy broadening. The emission band at 769 meV, 36 meV below the InGaAs emission line, is attributed to the QW, as this emission does not remain observable when the experiment is repeated with the QW etched off (as described in section 3.4.2). Fig. 3.19 shows power dependent low temperature PL spectra at 15 K. Compared to the RTD structure (with doping), the PL emission of the undoped RTD is clearly below the band-gap energy of bulk InGaAs, which is strongly suggestive of a type-II transition. With increasing PL excitation power density, a blue-shift of the PL peak is observed, which confirms type-II QW recombination. A type-II band alignment occurs when the band-gaps of two materials show a partial overlap. An example of such a type-II staggered band alignment is GaAs/GaSb. The radiative states in type-II GaSb/GaAs quantum wells and quantum dots (QDs) have been studied by a number of workers [41][42]. As the tunnel barriers of the RTD are very thin, the photo-generated minority carriers become spatially separated as the electrons can tunnel out of the QW into the surrounding undoped InGaAs layers due to short dwell time, and the holes remain captured in the QW due to the large valence band discontinuity of the $In_{0.8}Ga_{0.2}As$ well and lattice matched InGaAs layers. Due to the low kinetic energy at low temperatures (kT = 1.25 meV at 15 K), and the large valence band discontinuity ($\sim$ 120 meV), the holes are prevented escape from the QW into the surrounding InGaAs layers. Then, radiative recombination takes place between the electrons confined in the InGaAs layers and the holes in the quantum well.

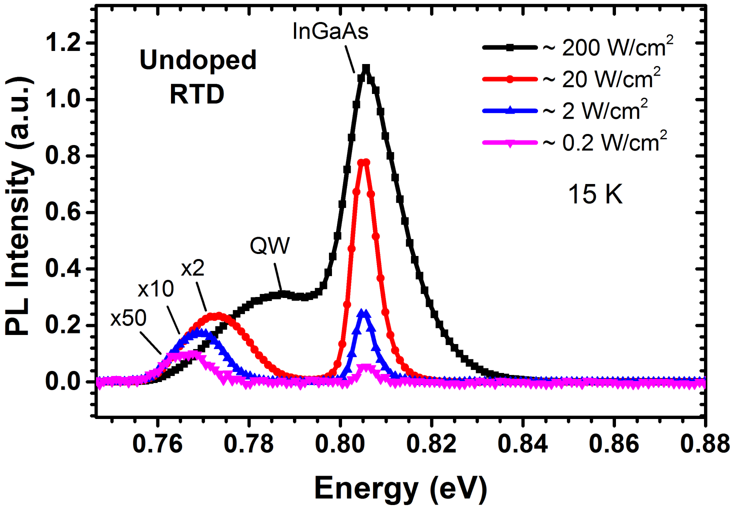

Figure 3.19: Excitation power dependent PL spectra of the undoped RTD structure at 15 K

For a type-II recombination, the strongly localised holes in the QW create an electrostatic well (triangular) in the conduction band for the electrons in the surrounding layers with an electric-field strength given by Eq. 3.17.

$$\epsilon = \frac{2\pi e n_w}{\epsilon_0} \propto \sqrt{I} \tag{3.17}$$

where ϵ is the electric field strength, e the electron charge, n_w the steady-state sheet electron concentration, ϵ_0 the dielectric constant of the cladding layer, and I the photon flux. The ground electron state, E_e, in the triangular well is given by Eq. 3.18

$$E_e \equiv bI^{1/3} \tag{3.18}$$

with Eq. 3.19

$$b = \left[\frac{9\pi}{8}\right]^{2/3} \left[\frac{\hbar}{2m_e}\right]^{1/3} \left[\frac{2\pi e^2}{\epsilon_0}\right]^{2/3} \left[\frac{\alpha(L+l)^2}{\gamma}\right]^{1/3} \tag{3.19}$$

where m_e is the cladding effective electron mass, α the absorption coefficient, L the width of the quantum well, l the cladding layer thickness, and γ the radiative recombination coefficient. An increase in excitation density raises the steepness of the confining potential, with a concomitant increase in the quantisation energy of the electron [42]. Eq. 3.18 clearly shows that the quantisation energy of the electrons follows the third root of the excitation density, a characteristic of a type-II recombination process. In addition to a blue-shift, the excitation power dependent PL exhibits a broadening of the type-II QW emission linewidth as a function of excitation density. As the electrostatically induced triangular QW due to the Coulomb attraction between the electrons and trapped holes become more pronounced as a function of excitation density, the effect of ML barrier fluctuations are expected to become more significant due to the increased electron wave function overlap with the barriers, broadening the electronic states. In the low excitation power limit, a linewidth of 10 meV is found for the type-II QW transition. For the QW hole states contributing to the emission, lifetime broadening is negligible, and the sensitivity of the emission energy to structural parameters is very weak. If a linewidth of 5 meV is assumed for the electrons in the ternary, then the holes confined within the QW contribute around 7 meV to the linewidth broadening. It is noted that the type-I QW transition has a total linewidth of $\sim$ 35 meV, and that the ratios of these broadenings are similar to the ratio of effective masses of the electrons and holes. Fig. 3.20 shows the measured peak emission energy as a function of the third root of the excitation power density for both structures. For the undoped RTD structure, the sub band-gap emission feature strongly follows the third root of the excitation density, whereas the bulk InGaAs emission does not follow this trend and remains constant, which is clear evidence of a type-II QW recombination [42]. This trend is not observed for the doped RTD structure showing type-I QW recombination. The difference in energy of the e-A transition of the undoped ternary is explained by campaign-to-campaign variation in the epitaxial process.

The structural quality of the epitaxy was evaluated by HR-XRD. For the doped RTD, the InGaAs layers were determined to be lattice-matched, whilst a negative lattice mismatch of 95 arcsec was measured for the undoped RTD structure. This corresponds to a mismatch of 400 ppm between the InGaAs layers and the InP substrate, or $In_{0.526}Ga_{0.474}As$ (as opposed to $In_{0.532}Ga_{0.468}As$ for lattice matched). This small compositional variation results in the different peak emission energy of bulk InGaAs between both samples. The inset of Fig. 3.20 schematically shows the type-I and type-II QW recombination of the doped and undoped structures, respectively, and illustrates the principle of deducing the energy of the first resonant energy level above the conduction band of the emitter. Due to the campaign-to-campaign variation in the composition of the lattice-matched InGaAs, the first resonant energy level is approximated to ΔE = E1 + E2 (shown in inset). To minimise the effect of band-bending due to the photogenerated charge carriers in the analysis, the peak emission energies are extrapolated to zero excitation density. A value for ΔE of 75 meV (to the dominant transition observed in PL as it is assumed to have the higher density of states) is obtained. The standard band-offsets used in Fig. 3.6 yielded a modelled value of ΔE of 110 meV. A more accurate measurement of this energy level is expected by growing both structures in a single

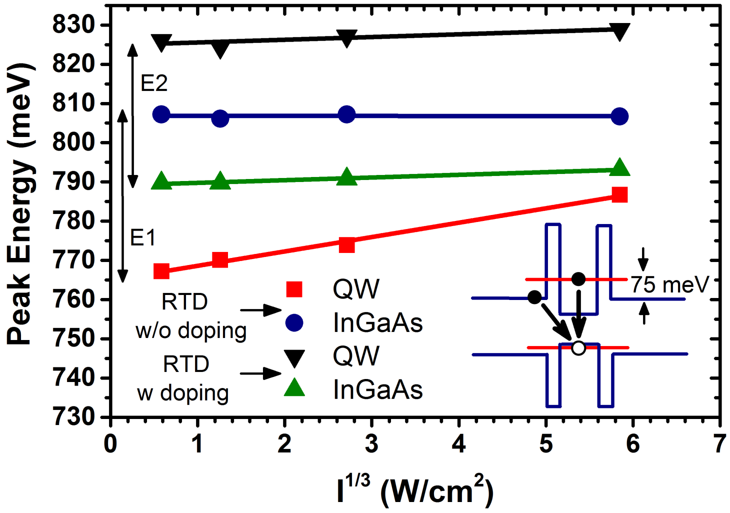

Figure 3.20: Peak emission energy as a function of excitation power density for both structures. The inset shows a schematic diagram of the recombination processes in both structures illustrating how the first resonant energy level, ΔE, is deduced.

run to ensure that identical growth conditions are applied to both structures. The technique is powerful as no prior knowledge of the band-offset of this highly strained heterostructure is required to determine ΔE. Further, this technique does not only allow the measurement of ΔE, but by comparing the position of the type-I and type-II QW emission, the alloy concentration and QW thickness can be non-destructively and separately characterised and monitored.

3.4.5 Quantum Well Width Dependent Photoluminescence

PL spectroscopy was carried out of RTD structures with different well widths ranging between 3.0 - 4.5 nm. Fig. 3.21 shows low temperature PL spectra measured at 15 K for structures with different well widths. Of note is that the PL emission intensity is normalised to the peak PL signal of the InGaAs buffer layer. Blue-shifted QW emission is observed for RTDs with reducing well widths, as expected from the solutions of the time-independent Schrodinger's equation for an infinite well, given in Eq. 3.20.

$$E_n = \frac{\hbar^2\pi^2n^2}{2ml_w^2} \tag{3.20}$$

where l_w is defined as the quantum well width. Fig.3.22 shows the experimentally measured and theoretically calculated e1hh1 QW peak transition energy as a function of well width at 15 K, using the full Schrodinger solver presented in Section 3.3. Superlinear relationships are observed for the

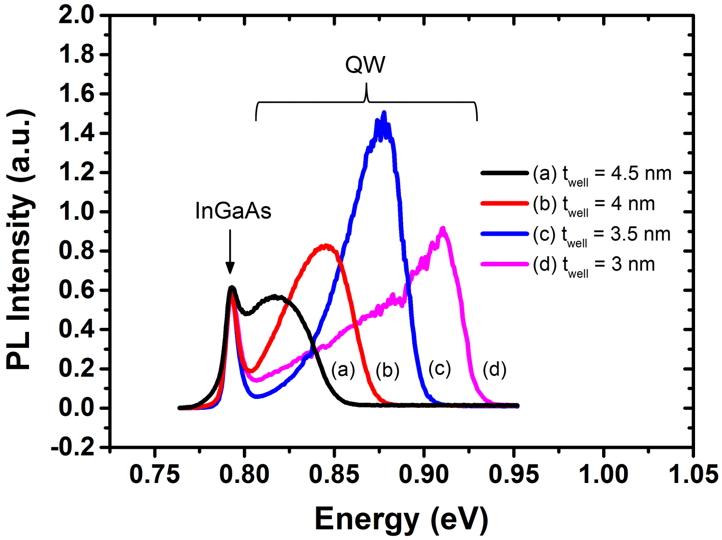

Figure 3.21: Low temperature PL at 15 K from RTDs with well-widths from 3 nm to 4.5 nm.

experimentally measured PL energy and the theoretical energy transitions. The error between experiment and theory is greatest for the 3.0 nm well. The observed discrepancy between theory and experiment can unlikely be attributed to a miscalibrated growth rate, as the measured error decreases with increasing well width. If a change in growth rate would have been responsible for the measured discrepancy, the measured emission of the thinnest QW should have shown better agreement with the theoretical data. A possible explanation is the non-parabolic nature of the electronic band-structure of InGaAs which is not included in this model. As the effective mass of electrons tends to increase in the conduction band of InGaAs, a decrease in e1hh1 transition energy is expected for higher transition energies. Overall, good agreement is observed between theory and experiment.

Fig. 3.23 shows PL spectra measured at 300 K for the same RTD structures. Similar to the low temperature PL spectra shown in Fig. 3.21, the peak emission energy shifts towards higher energies for a reduction in well width. These results indicate that both room temperature and low temperature PL can be used to detect monolayer well width fluctuations over the wafer due to the strong dependency between QW emission and well width. From a manufacturing perspective, performing these measurements at room temperature is very attractive as room temperature PL mapping tools are readily available commercially without the need for a custom-built cryostat.

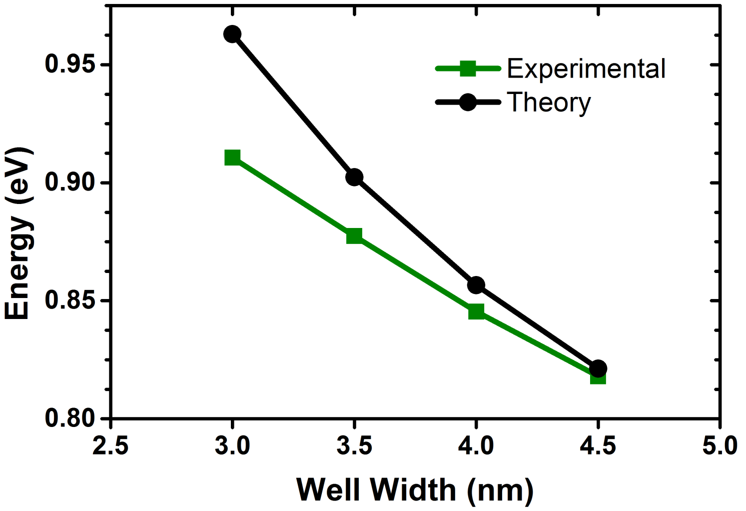

Figure 3.22: QW emission energy as a function of well width at 15 K. The round and square symbols represent the theoretical and experimental results, respectively. The theoretical transition energies were calculated using the full Schrodinger solver presented in Section 3.3.

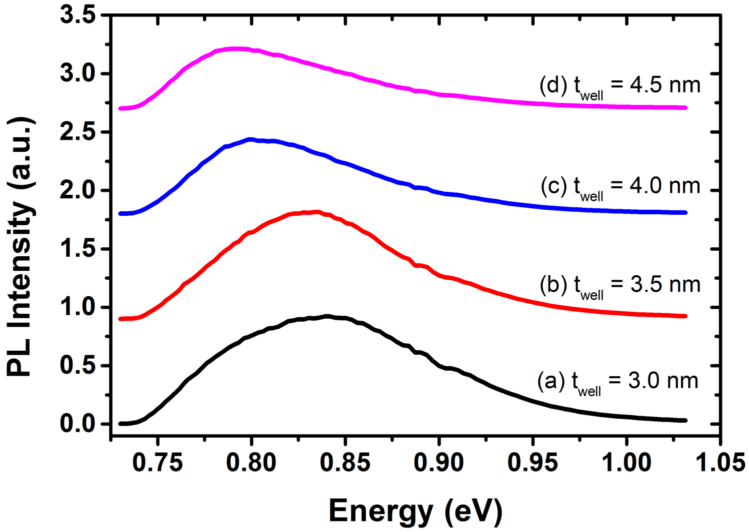

Figure 3.23: Room temperature PL spectra of RTDs with well widths between 3.0-4.5 nm. The PL spectra are displaced vertically for clarity.

3.4.6 Wafer Level Composition and Thickness Uniformity

From a manufacturing perspective, high yield of high performance RTDs requires not only a uniform doping concentration, but also uniformity of the layer thicknesses and alloy composition of the QW. A rapid, non-destructive assessment of the epitaxial material is valuable in the optimisation and monitoring of the growth process, which in turn allows the maximisation of device yield. Full wafer optical characterisation of high performance RTD structures is so far relatively unexplored. Photoluminescence excitation spectroscopy has previously already been applied to triple barrier GaAs/AlGaAs structures and allowed the variation in quantum well width to be deduced from a line-scan across the wafer [43]. For the RTD sample discussed previously, the uniformity of bulk InGaAs layers and the QW were investigated by PL mapping a 2″ wafer. Fig. 3.24 shows a wafer map measured over a full 2″ RTD wafer with a 5 mm resolution (68 points) at 15 K. The differences in peak energies ΔE, with respect to the wafer center, for both the InGaAs layers and QW emission are plotted as a function of position. Figs. 3.24(a) and (b) show the peak energy of the InGaAs emission line for the leading-to-trailing and outer-to-inner directions, respectively, and the peak energy of the QW emission line is shown in Figs. 3.24(c) and (d). The emission process of the InGaAs peak has previously been identified to originate from free-to-bound recombination process from the undoped bulk InGaAs. The QW emission at 828 meV is attributed to the e1hh1 transition. By measuring PL at low temperatures, thermal broadening effects are minimised, allowing both the QW and InGaAs emission lines to be investigated in detail. A dish-shaped profile is observed in most of the curves of Fig. 3.24 for both bulk InGaAs emission from the bulk InGaAs and QW emission, with a greater change for the QW (8-9 meV) as compared to bulk InGaAs (∼ 4 meV). Furthermore, the change in QW emission shows differences from leading-to-trailing and outer-to-inner. Low temperature PL performed on the emission peak of bulk InGaAs suggested that the observed ΔE profile of the bulk InGaAs emission peak is caused by an alloy non-uniformity over the wafer as no quantisation is present in the bulk InGaAs layers. The observed blue-shift at the wafer edge is explained by the InGaAs alloy being tensile strained (i.e. higher Ga to In ratio). Strain can also lead to lattice relaxation with the formation of dislocations. This can pose a major reliability issue and affect device performance.

According to Vegard's law, the change in composition corresponding to a + 4.0 meV shift corresponds to a ∼+ 0.03 % lattice mismatch strain. The critical thickness of InGaAs on InP with a 0.03 % strain was theoretically considered. Fig. 3.25 shows the critical layer thicknesses of InGaAs on InP calculated using the mechanical force balance model of Matthews and Blakeslee (M&B) [44], and the energy balance model first proposed by Frank-van der Merwe [46] and later extended by People and Bean (P&B) [45]. It is generally known that the experimental critical layer thickness of InGaAs on InP lies between both models [47]. Critical thicknesses of 0.78 μm and 150 μm are calculated for the M&B's and P&B's models, respectively, suggesting pseudomorphic growth for the RTD structures of 800 nm in thickness over the mapped region of the wafer. This

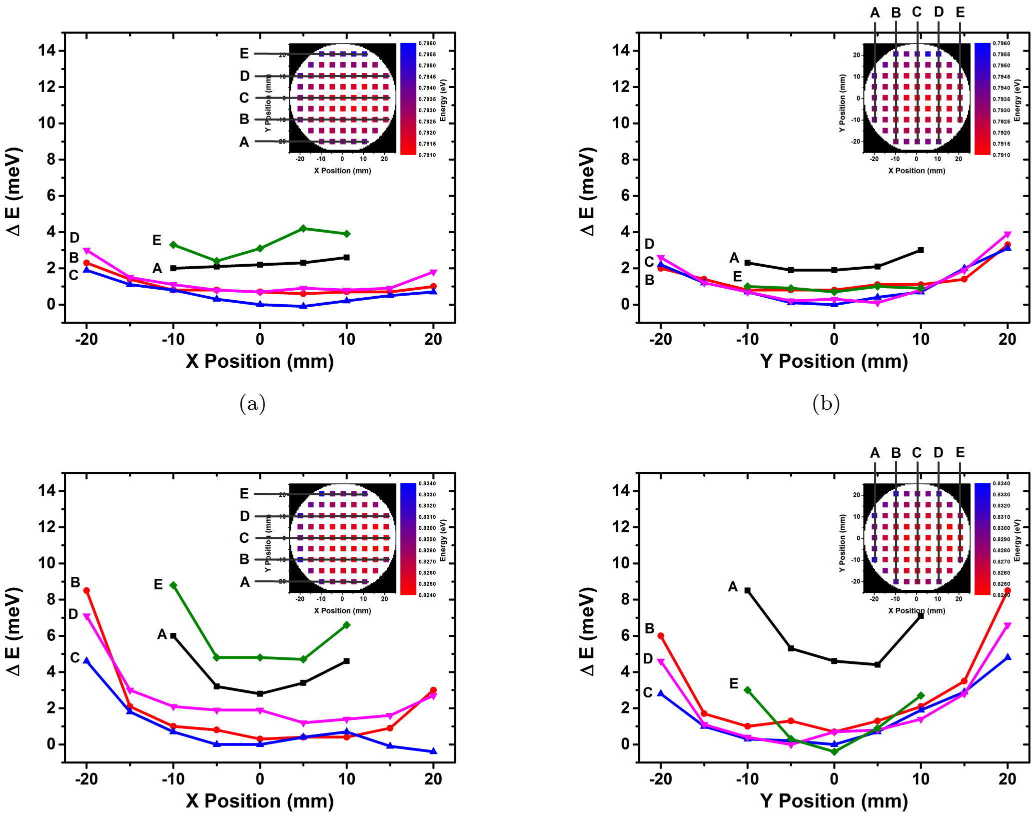

(a) (b) (c) (d)

Figure 3.24: (a) (c) leading-to-trailing and (b) (d) outer-to-inner line-scans of the InGaAs, and QW peak energy shifts, respectively, as determined by PL at 15 K. Insets show origin of line-scans with regard to the wafer map.

corresponds to a radius of 20 mm from the wafer center (62 % wafer real-estate) that is lattice matched and pseudomorphic, for an alloy composition variation of 0.6 % from $In_{0.532}Ga_{0.472}As$ to $In_{0.526}Ga_{0.478}As$. The larger measured energy shift for the QW is attributed to a change in the quantum confinement of the charge carriers. If the same alloy composition variation of 0.6 % is considered for the $In_{0.8}Ga_{0.2}As$ of the QW, the QW becomes less compressively strained at the wafer edge, as the lattice matched n^+ InGaAs becomes tensile strained. Using this alloy composition in the model, a 8.0 meV shift of the e1hh1 transition is calculated. This is in good agreement with the measured shift of 8.5 meV. Furthermore, the composition of the group-III sublattice is essentially mass-transfer controlled [48]. As a consequence, a change of alloy composition has a concomitant change in growth rate and hence layer thickness. From experimental low temperature PL data and theoretical modelling, the QW thickness uniformity is estimated to be within ∼ 0.5 % for the results shown in Fig. 3.24. This is in good agreement with a predicted 0.65 % growth rate reduction from

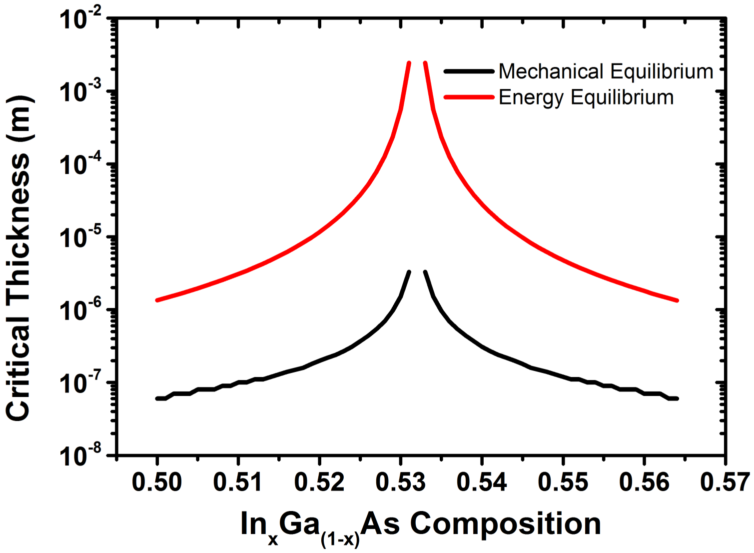

Figure 3.25: Critical thicknesses of InGaAs on InP modelled using the Matthews and Blakeslee's mechanical equilibrium and People and Bean's energy balance models.

the relative change in composition of the alloy assuming a constant gallium supply (i.e. the alloy is indium deficient at the edge).

HR-XRD was applied to investigate the material quality at the wafer edge in greater detail. Fig. 3.26 shows HR-XRD spectra measured with a 500 µm spatial resolution from the edge towards the wafer center on the (004) reflection. The spectra are displaced vertically for clarity. From Fig. 3.26, tensile strain of the nominally lattice-matched InGaAs layer is clearly observed at the wafer edge. The lattice matched condition is met at a distance of ∼ 3.5 mm from the wafer edge. Within 500 µm from the edge, a 1.25x10$^{-1\circ}$peak splitting is measured between InP and InGaAs, which corresponds to a tensile strain of 0.19 %. The physical origin of this change in alloy composition (i.e. indium deficient, gallium rich) requires further investigation as it will also impact upon epitaxial layer thicknesses in this region. It is noted that an effect of phosphorus incorporation originating from the polycrystalline material on the susceptor, effectively increasing the band-gap of the quaternary InGaAsP compound, could also have contributed to the overall observed effect; however, a very low phosphorus concentration (3x10^{14} atoms/cm^{-3}) was measured with SIMS, suggesting that this is an unlikely cause for the band-gap shift. For a tensile strain of 0.19 % critical thicknesses of 80 nm and 2 µm are calculated using M&B's and P&B's models, respectively. According to M&B's model, the epitaxy relaxes whereas P&B's model suggests pseudomorphic growth.

Reciprocal space mapping (RSM) was carried out to quantify the relaxation at this point, 500 µm from the edge. Fig. 3.27 shows a reciprocal space map measured on the asymmetric (224)

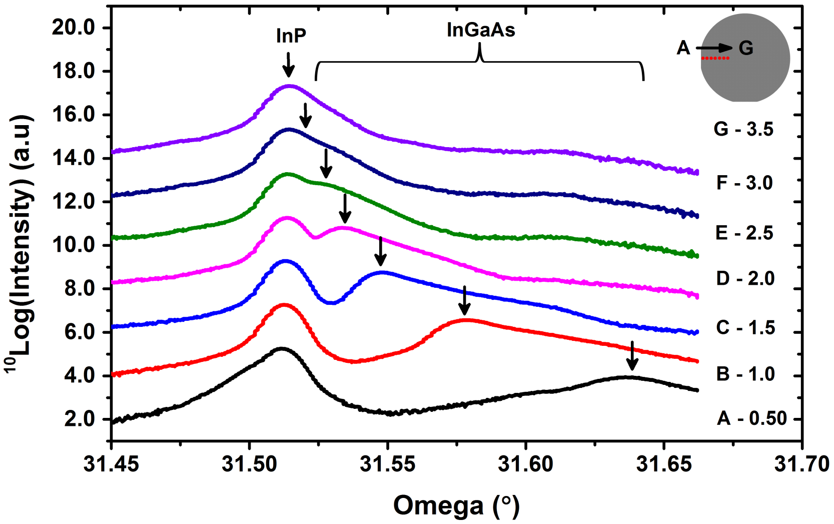

Figure 3.26: HR-XRD spectra from the wafer edge towards the wafer center with 500 μm steps, as shown schematically in the inset. The (004) InGaAs Bragg reflections are shown by down pointing arrows and guide to the eye to indicate the lattice mismatch to the InP substrate. The spectra plotted logarithmically are displaced vertically for clarity.

reflection. The red dot on the figure's inset indicates the location of the RSM, within 500 μm from the wafer edge. The in-plane reciprocal lattice constant (q_X) of InP is marked as a black line to

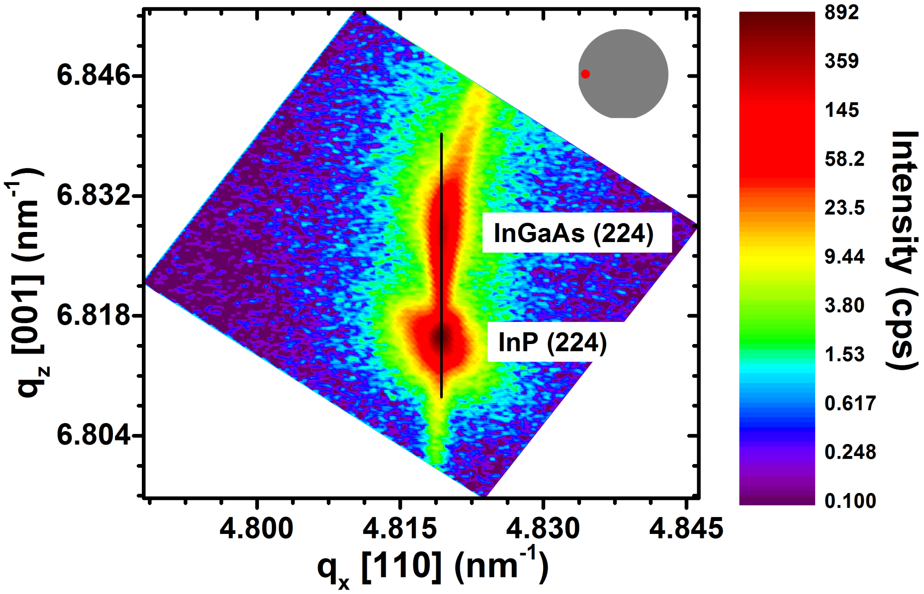

Figure 3.27: Reciprocal space map on the asymmetric (224) positive reflection. The location of the map on the wafer is indicated by a red dot on the figure's inset, 500 μm in from the edge. The in-plane reciprocal lattice constant (q_X) of InP is marked as a black line to guide the eye.

guide the eye. For pseudomorphic growth, whilst the lattice constant normal to the growth plane is modified by the Poisson ratio, the in-plane lattice constant of the InGaAs layer should be equal to that of the InP matrix. The observed deviation of the InGaAs reflection from the in-plane lattice constant evidences partial relaxation of the InGaAs layer. A 7 % partial relaxation of this InGaAs layer is estimated within 500 μm from the wafer edge. The observed broadening of the InGaAs peak in q_Z is attributed to the non-uniform strain at the wafer edge. This suggests that optimum performance and reliability for devices fabricated within a region of 3.5 mm to the wafer edge may be affected.

3.5 Conclusions

In this chapter, the optical spectroscopic characterisation of MOVPE grown, high current density (~ 700 kA/cm^2) InGaAs/AlAs/InP based diodes RTDs was reported. The origin of the PL emission from the RTD structure was investigated with a high spatial resolution, confirming emission from the bulk InGaAs buffer layer and QW. The optical properties of nominally identical doped and undoped RTD structures were investigated in detail, with type-I and type-II QW recombination determined for both structures, respectively. A technique was proposed and demonstrated to resolve the absolute first electron resonant energy level of a RTD by non-destructive low temperature PL spectroscopy. This allowed the absolute position of the first resonant energy level to be deduced without prior knowledge of the band offsets. It was shown that this technique can be used to monitor the well width and indium concentration of the RTD, which is attractive for process control in a manufacturing environment. With regard to the wafer uniformity mapping, both alloy and QW uniformity and perfection were non-destructively mapped over a full wafer, and conclusions were confirmed with HR-XRD. InGaAs alloy composition fluctuations of less than 0.6 % and a QW thickness variation of less than 0.5 % were deduced from this non-destructive mapping technique for 62 % of the wafer area.

References

[1] P.D. Buckle, P.Dawson, C.Y. Kuo, A.H. Roberts, W.S. Truscott, M. Lynch, M. Missous, “Charge accumulation in GaAs/AlGaAs triple barrier resonant tunneling structures”,J. Appl. Phys., 83 (1998), 882.

[2] J.F. Young, B.M. Wood, G.C. Aers, R.L.S. Devine, H.C. Liu, D. Landheer, M. Buchanan, A.J. Springthorpe, P. Mandeville, “Effect of circuit oscillations on the dc currentvoltage characteristics of double barrier resonant tunneling structures” , Phys. Rev. Lett., 60 (1988), 2085.

[3] M.S. Skolnick, D.G. Hayes, P.E. Simmonds, A.W. Higgs, G.W. Smith, H.J. Hutchinson, C.R. Whitehouse, L. Eaves, M. Henini, O.H. Hughes, M.L. Leadbeater, and D.P. Halliday, “Electronic processes in double-barrier resonant-tunneling structures studied by photoluminescence spectroscopy in zero and finite magnetic fields”, Phys. Rev. B, 41 (1990), 10754.

[4] J.W. Cockburn, P.D. Buckle, M.S. Skolnick, D.M. Whittaker, W.I.E. Tagg, R. Grey, G. Hill, M.A. Pate, “Investigation of electroluminescence from excited state carrier populations in double barrier resonant tunnelling structures” ,Superlattices and Microstructures, Volume 12, Issue 3, 1992, Pages 413-417

[5] O. Kuhn, D.K. Maude, J.C. Portal, M. Henini, L. Eaves, G. Hill, M.A. Pate, “Electroluminescence in p-i-n doublebarrier resonant tunnelling structures”, Microelectronics Journal, Volume 25, Issue 8, November 1994, Pages 741-746,

[6] C. R. H. White, H. B. Evans, L. Eaves, P. M. Martin, M. Henini, G. Hill, and M. A. Pate, “Electroluminescence investigations of electron and hole resonant tunneling in p-i-n double-barrier structure”,Phys. Rev. B 45, 9513(R) (1992)

[7] C.-Y. Kuo, M.A. Lynch, A.H. Roberts, P.D. Buckle, P. Dawson, M. Missous, W.S. Truscott, Physica E, “An electrical and optical study of electrons in triple barrier structures”, Low-dimensional Systems and Nanostructures, Volume 2, Issues 14, (1998)

[8] W.Z. Shen, S.C. Shen, Y. Chang, W.G. Tang, Y. Lu, A.Z. Li, “Photoluminescence studies of InAs/InGaAs/AlAs strained single quantum well structures”, Appl. Phys. Lett. 68 (1996), 78.

[9] Y. Zhang, M. Guan, X. Liu, Y. Zeng, Dependence of the electrical and optical properties on growth interruption in AlAs/ In0.53Ga0.47As/InAs resonant tunneling diodes, Nanoscale Res. Lett., 6 (2011), 603.

[10] T. F. Kuech, B.S. Meyerson and E. Veuhoff, “Mechanism of Carbon Incorporation in MOCVD GaAs”, Appl. Phys. Lett., 44 (1984), 986.

[11] R. Tsu and L. Esaki, “Tunneling in a Finite Superlattice,” Appl. Phys. Lett., 22, No. 11, pp. 562564, 1973.

[12] R. Petersen, Theoretical Investigation of the Resonant Tunneling Phenomena and its Applications in Resonant Tunneling Diodes, Mini-project, 2007.

[13] S. Adachi, “Material parameters of In1x Ga x As y P1y and related binaries”,Journal of Applied Physics 53, 8775 (1982)

[14] M. P. C. M. Krijn, “Heterojunction band offsets and effective masses in III-V quaternary alloys”, Semicond. Sci. Technol. 6, 27 1991

[15] K.H. Goetz, D. Bimberg, H. Jrgensen, J. Selders, A.V. Solomonov, G. F. Glinskii, M. Razeghi, “Optical and crystallographic properties and impurity incorporation of GaX ln1-xAs (0.44 <x <0.49) grown by liquid phase epitaxy, vapor phase epitaxy, and metal organic chemical vapor deposition”,J. Appl. Phys., 54 (1983), 4543.

[16] C.G. Van de Walle, “Band lineups and deformation potentials in the model-solid theory”, Phys. Rev. B, 39 (1989), 1871.

[17] S. M. Sze, Physics of Semiconductor Devices (Wiley, New York, 2007) 3rd ed., pp. 417-465.

[18] K.J.P. Jacobs, B.J. Stevens, T. Mukai, D. Ohnishi, R.A. Hogg, “Non-destructive mapping of doping and structural composition of MOVPE-grown high current density resonant tunnelling diodes through photoluminescence spectroscopy”,Journal of Crystal Growth, Volume 418, 15 May 2015, Pages 102-110

[19] P. T. Landsberg, Recombination in Semiconductors, Cambridge University Press, Cambridge, 1991, p. 220.

[20] Metzger, W. K. and Wanlass, M. W. and Ellingson, R. J. and Ahrenkiel, R. K. and Carapella, J. J., “Auger recombination in low-band-gap n-type InGaAs”, Applied Physics Letters, 79, 3272-3274 (2001),

[21] C. H. Henry, R. A. Logan, F. R. Merrit, and C. G. Betha, Radiative and nonradiative lifetimes in n-type and p-type 1.6 um InGaAs, Electron. Lett. 20, 358 (1984).

[22] Ahrenkiel, R. K. and Ellingson, R. and Johnston, S. and Wanlass, M., “Recombination lifetime of In0.53Ga0.47As as a function of doping density”,Applied Physics Letters, 72, 3470-3472 (1998)

[23] E. F. Schubert and W. T. Tsang, “Photoluminescence line shape of excitons in alloy semiconductors”, Phys. Rev. B 34, 2991 (1986).

[24] M. Kamada, H. Ishikaw, “Effects of V/II ratio on electronic and optical properties of GaInAs layers grown by MOCVD”, Journal of Crystal Growth 94 (1989) 849-856

[25] S.J. Bass, S.J. Barnett, G.T. Brown, N.G. Chew, A.G. Cullis, A.D. Pitt, M.S. Skolnick, “Effect of growth temperature on the optical, electrical and crystallographic properties of epitaxial indium gallium arsenide grown by MOCVD in an atmospheric pressure reactor”,Journal of Crystal Growth, Volume 79, Issues 13, 2 December 1986, Pages 378-385

[26] I. C. Bassignana, C. J. Miner, and N. Puetz, “Photoluminescence and double-crystal x-ray study of InGaAs/InP: Effect of mismatch strain on band gap”, Journal of Applied Physics 65, 4299 (1989)

[27] W. T. Tsang, A. H. Dayem, T. H. Chiu, J. E. Cunningham, E. F. Schubert, J. A. Ditzenberger, J. Shah, J. L. Zyskind, and N. Tabatabaie, “Chemical beam epitaxial growth of extremely high quality InGaAs on InP”, Applied Physics Letters 49, 170 (1986)

[28] Pikhtin, A.N. Sov. Phys. Semicond. 11 245, 1977.

[29] C. Charreaux, G. Guillot, and A. Nouailhat, “Alloy broadening in photoluminescence spectra of Ga0.47In0.53As”, Journal of Applied Physics 60, 768 (1986)

[30] Pallab K. Bhattacharya, Mulpuri V. Rao, and MingJong Tsai, “Growth and photoluminescence spectra of highpurity liquid phase epitaxial In0.53Ga0.47As”,Journal of Applied Physics 54, 5096 (1983)

[31] S.J. Bass, M.S. Skolnick, H. Chudzynska, L. Smith, "MOCVD of indium phosphide and indium gallium arsenide using trimethylindium-trimethylamine adducts",Journal of Crystal Growth, Volume 75, Issue 2, 2 May 1986

[32] K. L. Fry, C. P. Kuo, R. M. Cohen, and G. B. Stringfellow, "Photoluminescence of organometallic vapor phase epitaxial GaInAs",Applied Physics Letters 46, 955 (1985)

[33] I. Pelant, J. Valenta, Luminescence Spectroscopy of Semiconductors, Oxford University Press, 2012, p.133

[34] T.F. Kuech, G.J. Scilla, F.Cardone, "The influence of hydrocarbons in MOVPE GaAs growth: Improved detection of carbon by secondary ion mass spectroscopy",J. Cryst. Growth, 95 (1988), 550.

[35] Steiger, S., Povolotskyi, M., Park, H.H., Kubis, T., Klimeck, G.: Nemo5: a parallel multiscale nanoelectronics modeling tool. IEEE Trans. Nanotechnol. 10 (6), 14641474 (2011)

[36] H. A. P. Tudury, M. K. K. Nakaema, F. Iikawa, J. A. Brum, E. Ribeiro, W. Carvalho Jr., A. A. Bernussi, A. L. Gobbi, Strain-dependent optical emission in In1xGaxAs/InP quantum wells, Physical Review B - PHYS REV B , vol. 64, no. 15, 153301, 2001

[37] D. Gershoni, H. Temkin M. B. Panish and R. A. Hamm, "Excitonic Transitions in Strained-layer InxGa1-xAs/InP Quantum Wells", Phys. Rev. B39, 5531-5534 (1989).Rapid Communications

[38] Nag, B. R. ; Mukhopadhyay, Sanghamitra, "Band offset in InP/Ga0.47In0.53As heterostructures",Applied Physics Letters, 58 (10). pp. 1056-1058 (1991)

[39] J. Hellara, F. Hassen, H. Maaref, H. Dumont, V. Souliere, Y. Monteil, "Alloy broadening effect on optical properties of InGaAs grown by MOCVD with TMAs precursor",Microelectronics Journal, Volume 35, Issue 2, February 2004, Pages 207-212

[40] M.S. Skolnick, P.R. Tapster, S.J. Bass, A.D. Pitt, A. Apsley, S.P. Aldred, "Investigation of InGaAs-InP quantum wells by optical spectroscopy",Semicond. Sci. Technol., 1 (1986), 29.

[41] K. Suzuki, R. A. Hogg, and Y. Arakawa, "Structural and optical properties of type II GaSb/GaAs self-assembled quantum dots grown by molecular beam epitaxy",Journal of Applied Physics 85, 8349 (1999)

[42] N.N. Ledentsov, J. Bhrer, M. Beer, F. Heinrichsdorff, M. Grundmann, D. Bimberg, S.V. Ivanov, B.Ya. Meltser, S.V. Shaposhnikov, I.N. Yassievich, P.S. Kopev, Z.I. Alferov, “Radiative states in type-II GaSb/GaAs quantum wells”,Phys. Rev., B 52 (1995), 14058.

[43] P. D. Buckle, P. Dawson, M. Missous, and W. S. Truscott, “Full wafer optical characterisation of resonant tunnelling structures using photoluminescence excitation spectroscopy,” J. Cryst. Growth 175/176, 1299 (1997)

[44] J.W. Matthews and A.E. Blakeslee, “Defects in epitaxial multilayers. I. Misfit dislocations”,J. Cryst. Growth, 27 (1974),118.

[45] R. People, J.C. Bean, “Calculation of critical layer thickness versus lattice mismatch for Ge x Si1x /Si strained layer heterostructures”, Appl. Phys. Lett., 47 (1985), 322.

[46] J. H. Van der Merwe, “Crystal Interfaces. Part II. Finite Overgrowths”,J. Appl. Phys. 34,123 (1962)

[47] H. Temkin, D. G. Gershoni, S. N. G. Chu, J. M. Vandenberg, R. A. Hamm, and M. B. Panish, “Critical layer thickness in strained Ga1x In x As/InP quantum wells”,Applied Physics Letters 55, 1668 (1989)

[48] W.L. Holstein, “Design and modeling of chemical vapor deposition reactors”,Prog. Cryst. Growth Charact. Mater., 24 (1992), 111.

Chapter 4

Design of Terahertz Emitter

4.1 Introduction

Research onto millimetre and submillimetre waves covering a frequency range from 100 GHz to 30 THz has recently received great interest, as this band of frequencies can offer ultra-broadband wireless communications, imaging applications, and is well suited for spectroscopic sensing [1]. There is demand to develop emitters in this frequency range, as emerging applications are mainly limited by a lack of solid-state emitters, rather than detectors [2]. THz emitters operating at ambient room temperature are attractive, as no cooling is required which constrains device practicability.

Significant difficulties are posed on the design and physical realisation to develop such devices. Due to the short wavelength of these frequencies, compared to microwaves, on-chip transmission line structures can enable a variety of options for system level integration such as on-chip antennas and beam steering. These technologies have been so far only applied on high-end military systems. In addition, the materials and technologies available from the semiconductor industry are attractive for the realisation of such devices as they can provide a route to volume manufacture with cost scalability.

In this chapter, the design procedure of a submilimeter-wave antenna monolithically integrated with a RTD is described. The THz oscillator is designed to emit at the lower end of the THz spectrum, in the 300 GHz band, as the atmospheric attenuation is relatively low ($\sim$10dB/km) in this frequency range, compared to the higher frequencies (>1000dB/km), and to minimise the complexity of the device fabrication.

4.2 Background

RTDs can operate at very high frequencies with cut-off frequencies in the terahertz range. At the time of writing, the RTD is recognised as the fastest electronic device with emission at a fundamental oscillation of 1.55 THz being reported in 2014 [3]. The RTD is fast due to the very short tunnelling time through the structure, which leads to very high cut-off frequencies. Compared to conventional electronic devices, the speed of operation of the RTD is mainly governed by the tunnelling probability of the electron through the structure, instead of a conventional transit-time [4].

The observation of negative differential conductance of resonant tunnelling devices at terahertz frequencies was first reported by Sollner *et al.* in 1983 [5]. The RTD is well suited for oscillator operation, due to the negative conductance characteristic of the device. Fig. 4.1 shows the small-signal equivalent circuit of the RTD after Brown *et al.* [6]. The series resistance, Rs, includes parasitic resistances such as: contact resistance, spreading resistance, and resistance of the emitter and collector regions. The parallel space charge capacitance, $\mathrm{C_D}$, represents the charging and discharging effect of electrons at the semiconductor depletion regions. Compared to the Esaki tunnel diode, the RTD model includes an element of inductance, known as the quantum inductance, $\mathrm{L_{QW}}$. This inductance represents the temporal delay of the RTD current with respect to the applied voltage due to the finite electron tunnelling time required through the structure [6]. The magnitude of this inductance is determined by the lifetime of the quasi-bound state through Eq. 4.1,

$$L_{QW} = \frac{\tau_n}{G} \tag{4.1}$$

where $\mathrm{L_{QW}}$ is the QW inductance, τ_n the lifetime of the quasi-bound state, and G the negative differential conductance. The frequency dependent impedance of the RTD is given by Eq. 4.2.

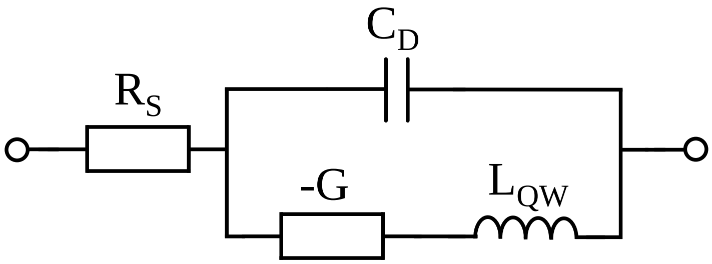

Figure 4.1: Small-signal equivalent circuit of an ideal RTD (i.e. no surface leakage current) after Brown *et al.* [6]

$$Z(f) = R(f) + jX(f) \tag{4.2}$$

The impedance of the RTD is complex as the parasitic space charge capacitance and quantum inductance are reactive. Due to the negative differential conductance, the RTD can supply power to an external circuit (e.g. antenna) for frequencies where the real part, R(f), of the circuit is positive. The RTD is therefore very suitable for oscillator operation. The maximum oscillation frequency of the RTD, $\mathrm{f_{MAX}}$, is defined as the frequency where R(f) becomes zero, as given by Eq. 4.3 [7].

$$f_{MAX} = \frac{1}{2\pi}\sqrt{\frac{1}{2L_{QW}^2 C_D}}\sqrt{\left\{2L_{QW} - \frac{C_D}{G^2} + \sqrt{\left[\left(\frac{C_D}{G^2} - 2L_{QW}\right)^2 - \frac{4L_{QW}(1+R_SG)}{R_SG}\right]}\right\}} \tag{4.3}$$

Eq. 4.3 simplifies to Eq. 4.4 when Lq is assumed to be negligibly small.

$$f_{MAX} = \frac{1}{2\pi C_D}\sqrt{\frac{-G}{R_S} - G^2} \tag{4.4}$$

Maximum power transfer occurs between the RTD and the load when the load conductance matches the average negative conductance of the RTD under steady-state. This condition is met for $\mathrm{G_{load}}$ = Gn/2 [8]. For a RTD with a static V-I characteristic represented by a cubic polynomial, the maximum output power from the RTD reduces to Eq. 4.5

$$P_{MAX} = \frac{3}{16}\Delta V \Delta I \tag{4.5}$$

where ΔV is defined as the difference between the valley and peak voltage and ΔI the difference between the peak and valley current [8][10][9]. Both ΔV and ΔI are important parameters for a high output power. The maximum output power of the RTD reduces with increasing frequency due to the intrinsic delay of the electrons travelling through the structure (i.e. tunnelling time through the double barriers and transit-time in the depletion layer of the collector), which degrades Gn. The frequency dependent maximum output power of the RTD is given by Eq.4.6 [11]

$$P_{MAX} = \frac{3}{16}cos(\omega\tau)\Delta V \Delta I \tag{4.6}$$

where ω is defined as the angular frequency and τ as the intrinsic delay , which consists of the tunnelling time across the double barriers and the transit time in the collector depletion region.

4.3 Design of Terahertz Antenna

4.3.1 Slot Antenna

Submm-wave antennas were designed to couple the electromagnetic energy generated by the RTD into the atmosphere. The slot antenna is selected as the preferred antenna to minimise the complexity of design, fabrication, and monolithical integration of the RTD on the InP substrate. Fig. 4.2 pictographically shows a basic half-wavelength slot antenna with associated voltage and current distributions. A basic slot antenna consists out of a metallic ground plane with a slot cut-out. A signal feed is located within the slot and electrical contacts are made between the slot and the feed.

The voltage distribution across the slot is maximum at the feed, which reduces towards zero at both ends of the slot. The voltage and current distribution are 90°out of phase, as the incident wave is fully reflected towards the source at both ends of the slot.

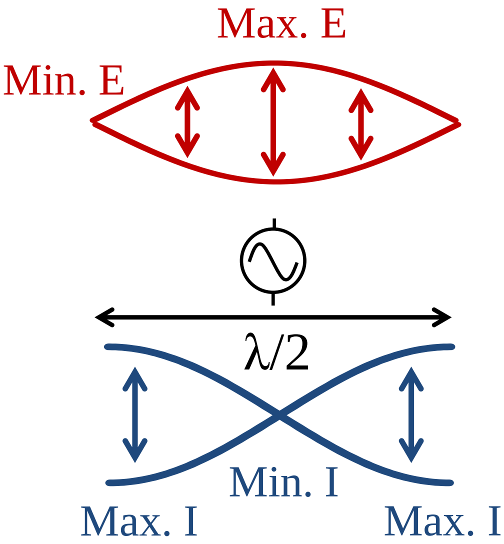

Figure 4.2: Center-fed half-wavelength slot antenna. The voltage and current distributions are shown along the length of the slot in red and blue, respectively.

The equivalent circuit of the slot antenna is drawn as a parallel RLC circuit, with R representing the radiation resistance. Resonance occurs when the inductive and capacitive reactances are equal in magnitude. At resonance, a standing wave of the electromagnetic field is formed within the slot, and the radiation impedance is purely resistive. The frequency of oscillation is governed by the length of the slot. Electrical energy is continuously supplied to the slot antenna by the RTD to negate the radiation loss of the antenna. To sustain the oscillation, the absolute value of the NDC should exceed the radiation loss of the antenna.

The Babinet-Booker duality relationship was used to estimate the radiation conductance of the slot antenna [12]. The duality principle relates the radiated fields and impedance to that of a dual antenna, which is a linear dipole antenna in the case for the slot antenna. Fig. 4.3 shows the dual of the slot antenna by interchanging the conductive material and air of a dipole antenna.

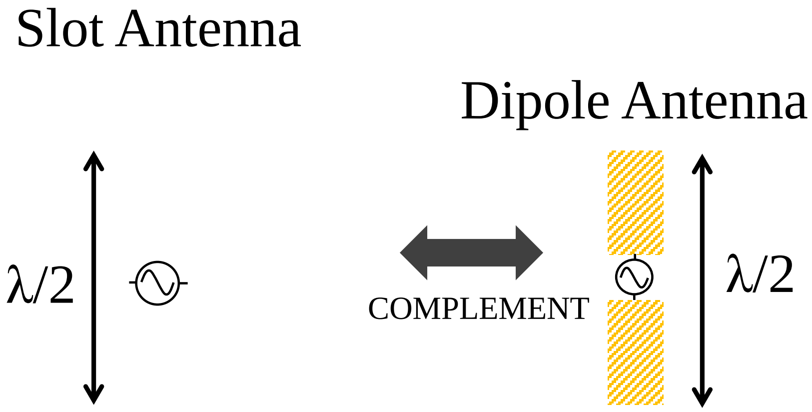

Figure 4.3: Dual antennas - the half-wavelength slot antenna and dipole antenna

The relationship between the impedance of the slot antenna and the impedance of the linear dipole antenna is given by Eq. 4.7

$$Z_{dipole}Z_{slot} = \frac{\eta^2}{4}\left(\eta = \sqrt{\frac{\mu_0}{\epsilon_0}}\right) \tag{4.7}$$

where Z_{slot} is the slot antenna impedance, Z_{dipole} the dual linear antenna impedance,η the characteristic impedance, μ_0 the magnetic constant, and ϵ_0 the electric constant of free space. The characteristic wave impedance of free space is approximately 376.7 ohms. A radiation resistance of 486 ohms is calculated for the slot antenna at resonance using the Babinet-Booker relationship for a dual dipole antenna with a typical radiation resistance of 73 ohms at resonance. This prediction is only valid for antennas which are suspended in free space ($\epsilon_{\mathrm{r}} = 1$). For a slot antenna fabricated on an infinite dielectric, the Booker relationship is satisfied by using the mean dielectic constant ($\epsilon = (\epsilon + 1)/2$) between the atmosphere and substrate [13]. For a slot antenna on a InP substrate with a static dielectric constant of 12.9 [14], a radiation resistance of 184 ohms is calculated at resonance in the thick substrate approximation, following Eq. 4.8 [15].

$$Z = \frac{486\Omega}{\sqrt{\frac{1+\epsilon_{rsub}}{2}}} \tag{4.8}$$

For a 350 µm thick semi-insulating InP:Fe antenna substrate positioned on a 16 mm thick high-resistivity float-zone silicon lens with a relative permittivity comparable to InP ($\epsilon_{\mathrm{r}} = 11.7$ [16]), this approximation remains valid as the emission wavelength at THz frequencies is much smaller than the total thickness of the dielectric substrate. The slot antenna radiates when the physical length of the slot is equal to the guide wavelength. For a slot antenna suspended in free space, the guide wavelength is equivalent to the free space wavelength. The guide wavelength for a slot antenna on a dielectric substrate is given by Eq. 4.9

$$\lambda_m = \frac{\lambda_0}{\sqrt{\epsilon_r}} \tag{4.9}$$

where λ_m is the guide wavelength, λ_0 the free space wavelength, and ϵ_r the mean dielectric constant [13]. Fig. 4.4 shows a graph with the calculated slot length of the antenna on InP for a guide velocity of $c/(\sqrt{7.45})$, where c is defined as the speed of light. The photon energy is plotted as a function of the oscillation frequency. The inverse variation in Fig. 4.4 shows that the slot length of the antenna decreases as a function of oscillation frequency. An oscillation frequency of 350 GHz requires a slot length of 163 µm.

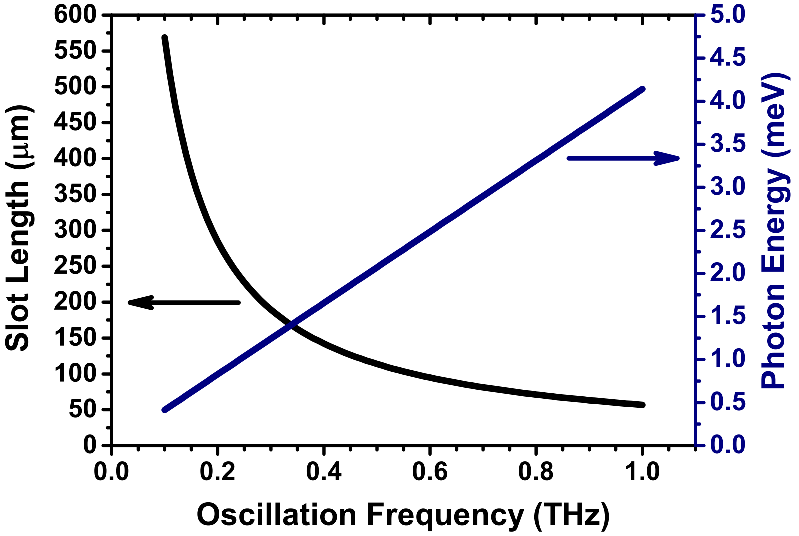

Figure 4.4: Slot length as a function of oscillation frequency

Electrical isolation between the emitter and collector electrodes of the slot antenna is created by capacitively coupling both sides of the slot antenna to provide a low impedance path at the oscillation frequency, while maintaining electrical isolation at DC. This configuration is shown in Fig. 4.5. A high capacitance C_{RF} is used to achieve a low capacitive reactance to maximise the DC-to-RF conversion efficiency by minimising the loading effect on the RTD. These RF capacitors, C_{RF}, are known as metal-insulator-metal (MIM) reflectors.

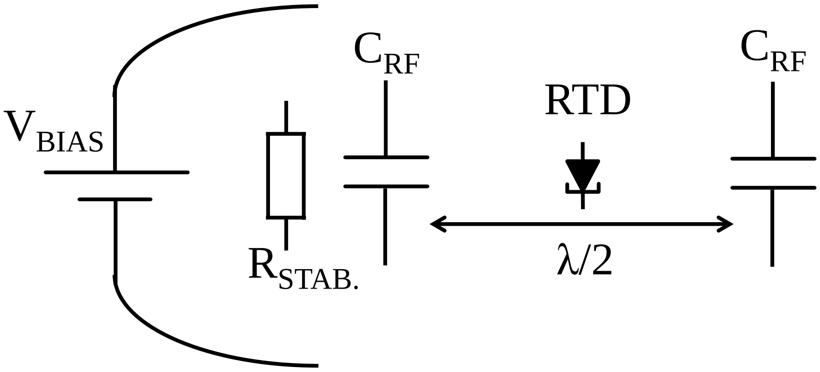

Figure 4.5: Schematic diagram of a RTD oscillator with a half-wavelength slot antenna coupled to a RTD oscillator, including MIM reflectors in the form of RF capacitors and a bias stabilisation resistor.

4.3.2 Metal-Insulator-Metal Reflectors

Metal-insulator-metal (MIM) reflectors were designed with a capacitive reactance of less than 0.5 ohm at the oscillation frequency. The capacitance of a parallel plate capacitor is given by Eq. 4.10

$$C = \frac{A\epsilon_0\epsilon_r}{d} \tag{4.10}$$

where C is the capacitance, A the surface area, ϵ_0 the free-space permittivity, ϵ_r the relative permittivity, and d the parallel plate separation. To maximise the capacitance density of the MIM structure, a small plate separation and a dielectric material with a high relative permittivity are required. Fig. 4.6 shows the calculated area of the MIM structure for different Si_3N_4 plate separations for a capacitive reactance of less than 0.5 ohm. Silicon nitride is preferred above silicon dioxide as the dielectric material, due to the higher electric permittivity of silicon nitride,

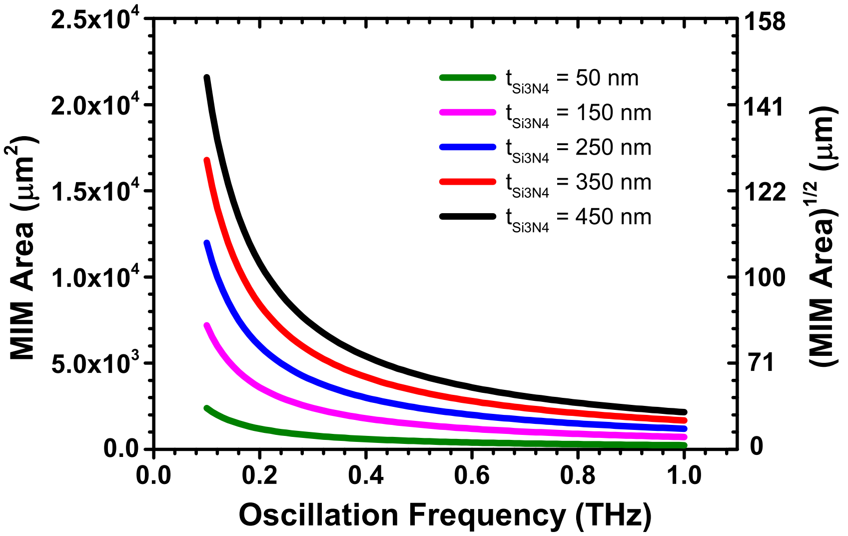

Figure 4.6: MIM area as a function of oscillation frequencies using silicon nitride as dielectric material.

to achieve a higher capacitance density. A dielectric film thickness of 150 nm Si_3N_4 was chosen for the fabrication of the MIM reflectors. While thinner silicon nitride results in a higher capacitance per chip area, it sets the bar higher for the manufacturability and long term reliability, as pinholes and electrically active defects in thin dielectric films can greatly reduce the breakdown voltage of the device, or worse, lead to a short between conducting layers making the device inoperable.

4.3.3 Bias Stabilisation

Bias stabilisation is required for the RTD to eliminate low frequency parasitic oscillations below the target oscillation frequency, as the RTD exhibits NDR from DC to f_{MAX}. A common stabilisation technique for tunnel diodes is a shunt regulator in the form of an external resistance connected in parallel with the NDR of the RTD [8][10][9]. The tunnel diode is stabilised when the combined V-I characteristic of the tunnel diode and resistor has a positive slope throughout. This condition is set by Eq. 4.11.

$$\frac{1}{R_{stab}} > G_n \tag{4.11}$$

The stabilisation resistance has to be small enough for the RTD to provide sufficient stabilisation, but large enough to minimise the DC power loss within the resistor. As the bias stabiliser degrades the oscillator DC-to-RF conversion efficiency, Dansky *et al.* [17] and Reddy *et al.* [8] demonstrated solutions based on non-linear (diode) resistors, and Schottky diodes, respectively, to reduce power loss within the stabiliser and maximise the device efficiency. To lower the current consumption, the turn on voltage of the stabilisers is set just below the peak voltage of the RTD. To lower the overall complexity of the THz emitter, simple surface mount thick film resistors were selected for bias stabilisation in this project. Small SMD film resistors are attractive as they can be easily integrated on the THz chip, and have good high-frequency performance due to their low parasitic inductance.

4.3.4 Output Coupling of Terahertz Radiation

It is characteristic for a planar antenna on a dielectric substrate to radiate most of its power into the substrate. This is due to the difference in electric permittivity between the dielectric substrate ($\epsilon_{\mathrm{InP}} = 12.4$) and the atmosphere ($\epsilon_{\mathrm{air}} \approx 1$). The radiated power into the dielectric has a factor of $\epsilon_{\mathrm{InP}}^{3/2}$ over the power radiated into the atmosphere [13]. For a slot antenna on a semi-infinite dielectric InP substrate, this equates to ~ 98 % of the total power being emitted through the substrate. Unfortunately, due to total internal reflection at the interface between the substrate and air, a large portion of radiated energy is trapped in the substrate and coupled to substrate modes. This is pictographically illustrated in Fig. 4.7. A critical angle of $\theta_c \approx 16°$ is calculated for a slot antenna on InP.

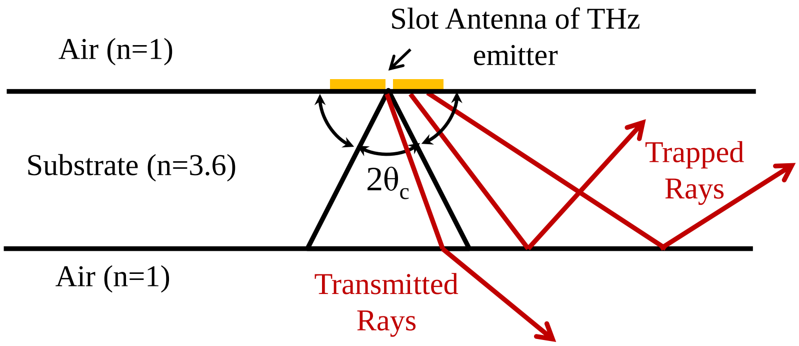

Figure 4.7: A hyper-hemispherial silicon lens combined with the InP substrate to maximise the coupling of electromagnetic radiation from the device into the atmosphere.

To maximise the coupling between the antenna substrate and air, a hyper-hemispherical lens made of high resistivity silicon ($\epsilon_{\mathrm{Si}} = 11.7$) is attached to the substrate. This is schematically illustrated in Fig. 4.8. High resistivity silicon is used as the lens material as the refractive index matches well with the InP substrate, and the absorption is very low at THz frequencies [18]. The hyper-hemispherical lens has the added advantage that it sharpens the radiation pattern of the

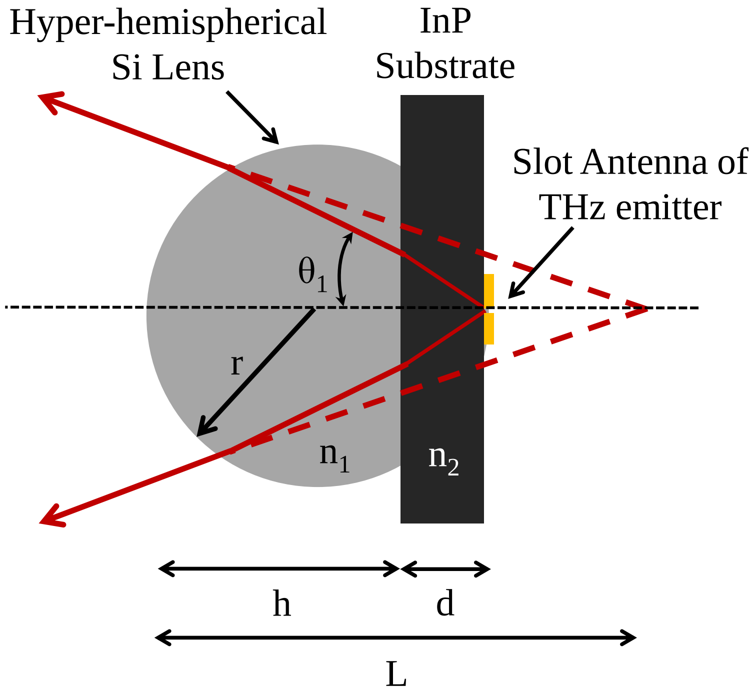

Figure 4.8: A hyper-hemispherial silicon lens combined with the InP substrate to maximise the coupling of electromagnetic radiation from the device into the atmosphere.

integrated antenna and therefore increases the gain by a factor of ∼ 12 in case of a Si lens [13]. The effective focal length, defined by L in Fig. 4.8, was calculated with MATLAB to ∼ 89 mm ($\theta_1 \approx 50°$) for a hyper-hemispherical lens with a height of 16 mm and a diameter of 25 mm. Of note, the gap between the lens and the substrate must be significantly less that one wavelength, to allow optical tunnelling between the substrate and lens. Using a thin layer of glue with a low loss tangent at the operating frequency between the lens and substrate can be used to enhance the coupling. No glue was used in this work as multiple devices were tested using the same lens.

4.4 Conclusions

In this chapter, the basic operation and the design requirements of a RTD based THz oscillator were described and discussed. Important parameters of the RTD such as the maximum operating frequency and output power were introduced. The design specifications of a RTD based THz emitter for operation in the 300 GHz band were discussed, including a slot antenna, MIM reflector design, bias stabilisation techniques and output coupling of the THz emission through the dielectric substrate.

References

[1] T. Nagatsuma "Generating millimeter and terahertz waves", IEEE Microw. Mag., vol. 10, p.64 , 2009.

[2] Mann, C., "Practical Challenges for the Commercialisation of Terahertz Electronics," Microwave Symposium, 2007. IEEE/MTT-S International , vol., no., pp.1705,1708, 2007

[3] S. Suzuki & M. Asada, 46st International Conference on Solid State Devices and Materials, Tsukuba, 2014

[4] S. M. Sze & Kwok K. NG, Tunnel Devices, in Physics of Semiconductor Devices, 3rd ed. New York: Wiley, 2007, pp. 417-465.

[5] T. C. L. G. Sollner, W. D. Goodhue, P. E. Tannenwald, C. D. Parker, D. O. Peck, "Resonant tunneling through quantum wells at frequencies up to 2.5 THz", Appl. Phys. Lett. 43, 588 (1983)

[6] E. R. Brown, T. C. L. G. Sollner, C. D. Parker, W. D. Goodhue, and C. L. Chen, "Oscillations up to 420 GHz in GaAs/AlAs resonant tunnelling diodes," Appl. Physics Lett., vol. 55, no. 23, pp. 1777-1719, 1989.

[7] T. C. L. G. Sollner, E. R. Brown, C. D. Parker and W. D. Goodhue, Highfrequency applications of resonant-tunneling diodes, Electronic Properties of Multilayers and Low-dimensional Semiconductor Structures, edited by J. M. Chamberlain et al (Plenum Press, New York, 1990), pp. 283-96.

[8] M. Reddy, M J. Mondry, M. J. W. Rodwell, S. C. Martin, R. E. Muller, R. P. Smith, D. H. Chow, and J. N. Schulman, "Fabrication and dc, microwave characteristics of submicron Schottkycollector AlAs/In0.53Ga0.47As/InP resonant tunneling diodes", Journal of Applied Physics 77, 4819 (1995)

[9] Kim, C.S.; Brandli, A., "High-Frequency High-Power Operation of Tunnel Diodes," Circuit Theory, IRE Transactions on , vol.8, no.4, pp.416,425, Dec 1961

[10] Trambarulo, R., "Some X-band microwave Esaki-diode circuits," Solid-State Circuits Conference. Digest of Technical Papers. 1961 IEEE International , vol.IV, no., pp.18,19, 15-17 Feb. 1961

[11] S. Suzuki, M. Shiraishi, H. Shibayama, and M. Asada, "High-Power Operation of Terahertz Oscillators with Resonant Tunneling Diodes Using Impedance-Matched Antennas and Array Configuration", IEEE J. Selected Topics Quantum Electron., vol. 19, no. 1, 8500108, Feb. 2013.

[12] Booker, H.G., "Slot aerials and their relation to complementary wire aerials (Babinet's principle)," Electrical Engineers - Part IIIA: Radiolocation, Journal of the Institution of , vol.93, no.4, pp.620,626, 1946

[13] Rebeiz, G.M., "Millimeter-wave and terahertz integrated circuit antennas," Proceedings of the IEEE , vol.80, no.11, pp.1748,1770, Nov 1992

[14] S. Kasap, P. Capper, Springer Handbook of Electronic and Photonic Materials Springer US, p.748; 2006

[15] Kominami, M.; Pozar, David M.; Schaubert, D.H., "Dipole and slot elements and arrays on semi-infinite substrates," Antennas and Propagation, IEEE Transactions on , vol.33, no.6, pp.600,607, Jun 1985

[16] D. Grischkowsky, S. Keiding, M. van Exter, and C. Fattinger, "Far-infrared time-domain spectroscopy with terahertz beams of dielectrics and semiconductors," J. Opt. Soc. Am. B 7, 2006-2015 (1990).

[17] Wallmark, J.T.; Dansky, A.H., "Nonlinear Biasing Resistors for Microwave Tunnel-Diode Oscillators (Correspondence)," Microwave Theory and Techniques, IEEE Transactions on , vol.11, no.4, pp.260,262, Jul 1963

[18] Lee, Yun-Shik, "Principles of Terahertz Science and Technology", Springer US, p. 67; 2009

Chapter 5

Device Fabrication Development

5.1 Introduction

This chapter covers the development work and the fabrication process of the micron scale RTD THz emitter. As device dimensions are reduced and current densities increased, low resistance ohmic contacts are required to minimise dc voltage drops and resistive-capacitive (RC) time constants to access the higher oscillation frequencies. An investigation is carried out for low resistance non-alloyed ohmic contacts to InGaAs. This is followed by the development work for the fabrication of the air-bridge structure, including an investigation in the wet etching characteristics of InGaAs to optimise the etching of the air-bridge. For the RTD THz emitter, the fabrication process consists out of two main stages: the RTD fabrication and the antenna integration. In this work, the RTD is monolithically integrated on the InP substrate with a slot antenna using metal-insulator-metal (MIM) technology.

5.2 Development of Low Resistance Ohmic Contacts

High-speed electronic devices, including the RTD, require low resistance metal-semiconductor contacts to minimise the resistive-capacitive delay, or RC delay, which sets the fundamental limit on the speed of the device. Low RC delays are of major interest to the semiconductor industry [1][2]. To minimise the parasitic capacitance of the RTD, a small device size and a high current density are required. This leads to the requirement of low resistance ohmic contacts to obtain a low RC time constant. Low resistance contacts also reduce self-heating effects in the device, which is advantageous for optimum device performance and long-term reliability. Linear transfer length measurement (LTLM) test-structures [3][4] were fabricated to investigate the contact resistance of titanium(Ti)/gold(Au) based non-alloyed ohmic contacts to highly doped $\mathrm{In_{0.53}Ga_{0.47}As}$ ($\mathrm{Si: 2x10^{19}cm^{-3}}$). A photolithography mask was designed using L-Edit (Tanner Tools) and manufactured by Compugraphics UK. A number of reviews of ohmic contact development to III-V compound semiconductors are available from [5][6][7].

In 2007, Crook *et al.* [8] reported on ultra-low non-alloyed ohmic contacts with a specific contact resistivity of less than 1 $\Omega.\mu\mathrm{m}^2$ to high indium content MBE grown $\mathrm{In_xGa_{1-x}As}$. E-beam evaporation was used to deposit a Ti(20 nm)/Pd(40 nm)/Au(200 nm) metal contact stack. Crook *et al.* found that the attained particular resistivity has a strong dependence on the procedures used to remove surface oxides prior to contact deposition. Their surface preparation procedure consisted of a 10 min. long UV-ozone treatment, followed by a 10 s ammonium hydroxide predeposition soak, after which the sample was blown dry using N_2. Annealing the contacts at a temperature of 300 °C reduced the specific contact resistivity from $\sim$0.9 $\Omega.\mu\mathrm{m}^2$ to $\sim$0.5 $\Omega.\mu\mathrm{m}^2$. Thermally evaporated Ti/Au based contacts on MOVPE grown InGaAs were developed in this work. The effect of ozone treatment, ammonium hydroxide predepositon soak, and post-metallisation anneal on the specific contact resistivity were investigated.

The LTLM test-structures were fabricated on an InGaAs calibration wafer which consisted of a single 400 nm n^+ InGaAs (n = $2\mathrm{x}10^{19}\mathrm{cm}^{-3}$) latticed matched layer on a semi-insulating InP substrate. Fig. 5.1 shows a single LTLM test-structure with a contact gap spacing of 1 µm. These test-structures were fabricated by patterning the sample with i-line photolithography, followed by a Ti(20nm)/Au(200nm) deposition and a metal lift-off process. Each test pattern was subsequently electrically isolated by photolithography and wet etching to the semi-insulating InP substrate. The electrical isolation ensures uniform current flow perpendicular between the metal contacts. The etching was carried out using a $\mathrm{H_3PO_4{:}H_2O_2{:}H_2O}$ based etchant with a volumetric ratio of 1:1:38, respectively, for an etch rate of approximately 100 nm/min. at room temperature. Due to the etch selectivity between InP and InGaAs, the underlying InP substrate was not attacked. The specific contact resistivity ρ_c (ohm-cm^2) was determined by measuring the resistance between various contact gaps from 1 µm to 45 µm.

The four-probe technique is used for an accurate measurement of the LTLM gap resistance, by excluding parasitic resistance in the circuit from the measurement, and the measurement is rendered independent of the probe placement. This technique is required for measuring low resistance ohmic contacts, as the parasitic series resistance in the circuit can be comparable to the resistance of the LTLM gap.

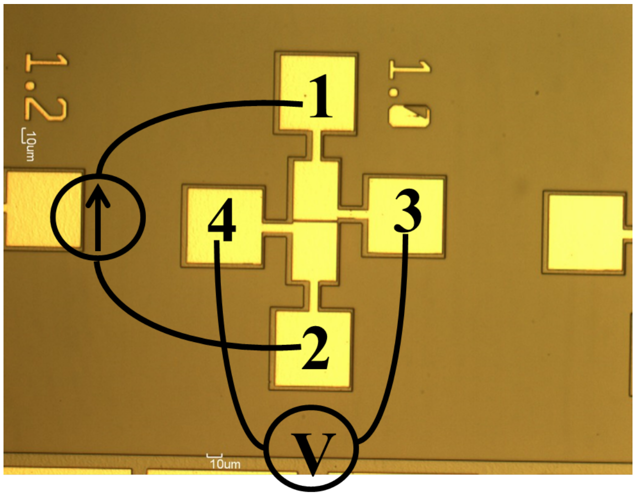

Figure 5.1: LTLM test-structure with a gap spacing of 1.0 μm. The voltage and current probes connections are shown on the figure.

Fig. 5.1 shows an optical microscope image of a single LTLM test-structure with a 1 μm gap width. Two probes, represented by "1" & "2" on Fig. 5.2, are used to supply a uniform current flow across the full width of the gap. Two other probes, represented by "3" & "4", sense the voltage across the gap. Fig. 5.2 shows the measured total measured resistance (Rt) plotted as a function of gap spacing for a constant contact width (W) of 30 μm.

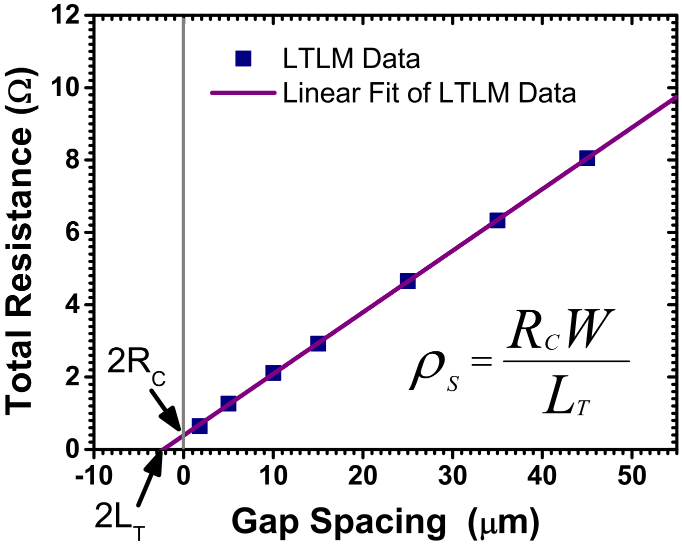

Figure 5.2: LTLM resistance as a function of gap spacing for Ti(20 nm)/Au(200 nm) contacts on $In_{0.53}Ga_{0.47}As$ (Si:$2x10^{19}cm^{-3}$). The width (W) of the LTLM patterns is 30 μm.

The transfer length, L_T, sets the effective contact area and represents the distance on the graph at which the voltage underneath the contact dropped to 1/e (37 %). The specific contact resistivity of a metal contact is calculated through Eq. 5.1

$$\rho_c = L_T^2 \rho_s \tag{5.1}$$

where ρ_c is the specific contact resistivity, L_T the transfer length, and ρ_s the sheet resistivity. The results and discussions on the effect of ozone treatment, ammonium hydroxide predeposition soak, and post-metallisation anneal on the specific contact resistivity are presented in the following sections.

5.2.1 UV/Ozone Treatment

Ozone (O_3) is a very powerful oxidiser which is commonly used in the semiconductor manufacturing industry for cleaning semiconductor surfaces. Ozone reacts with hydrocarbon residues by releasing diatomic oxygen and an oxygen radical which reacts with the hydrocarbon to form carbon oxides and other organic molecules such as alcohols and ketones [9]. This technique is very useful for the removal of stubborn submonolayer hydrocarbon. UV-ozone can also be used to passivate defective surface layers, often associated with native oxides, as it oxidizes most inorganic compounds to their final oxidative state [10], and to restore the stoichiometric composition at the semiconductor surface [11].

Ultraviolet (UV) light generated ozone is an alternative surface preparation technique to oxygen plasma etching with the added advantage that no atomic displacement damage is produced at the surface during the treatment [9]. A clean semiconductor surface prior to ohmic contact deposition is important as remaining hydrocarbon deposits can block the interface reactions and alter the work function of the surface. An investigation was carried out to study the effect of ozone on Ti/Au based contacts on InGaAs. As our semiconductor fabrication facility was not equipped with a UV-Ozone cleaning system, a homemade UV-ozone generator was built for this investigation. A similar UV-ozone generator was built by Vig *et al.* [12] to investigate the UV-ozone cleaning effect of surfaces. A corona discharge was used to generate ozone through the ionization of diatomic oxygen. A high voltage transformer with an output voltage of 3 kV was used to ionise atmospheric oxygen. The reaction of atomic oxygen and other diatomic oxygen molecules produces ozone according to Eq. 5.2.

$$3O_2 + Energy \rightarrow 2O_3 \quad (5.2)$$

Fig. 5.3(a) shows a photograph of the ozone generator. A violet ionized-air glow is clearly observed which indicates that the system is operating correctly. To enhance the oxidation process, atomic oxygen is also produced at the surface of the sample. This is easily achieved through the use of low-pressure mercury discharge tubes emitting at 253.7 nm. Ozone has a strong absorption at 253.7 nm. Fig. 5.3(b) shows a photograph of the ozone generator including the UV lamps.

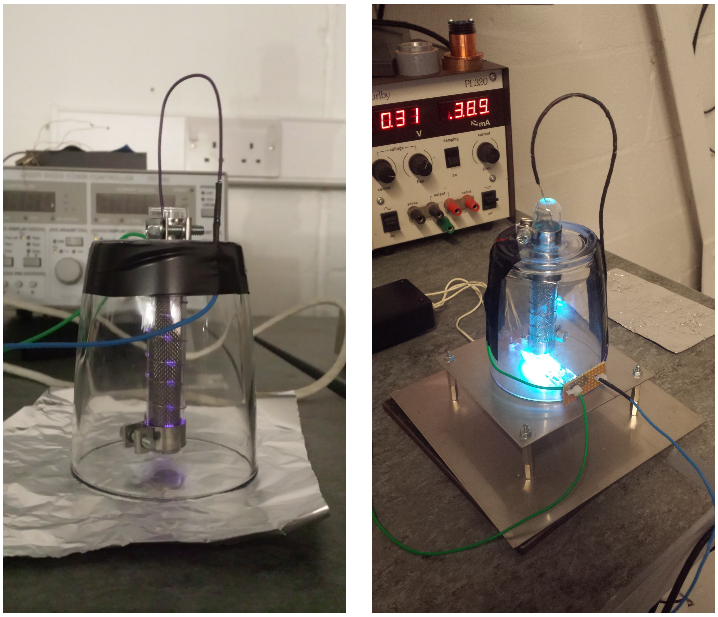

(a) (b)

Figure 5.3: (a) Vertical tube ozonator (b) Complete apparatus for UV/ozone treatment experiments

The effectiveness of the ozone cleaning process was evaluated through a wettability test. The hydrophilicity of a glass coverslip was assessed by measuring the contact angle of water on a glass surface. Clean glass has a contact angle of less than 10 °[13]. Fig. 5.4 shows the experimental results. Droplets “A” and “B” were deposited on an untreated and treated cover slip, respectively. Both surfaces were first cleaned with isopropyl alcohol, followed by a 10 min. ozone exposure for glass “B” prior the deposition of the deionised water droplets. Contact angles, represented by α on Fig. 5.4, of ~ 45 °and ~ 5 °are measured for glass slides “A” and “B”, respectively. This test confirms that the ozone apparatus functions correctly with test results comparable to commercial apparatus [14][13][15]. Three samples were prepared to investigate the effect of ozone on Ti/Au non-alloyed ohmic contacts on InGaAs. Two samples were treated with ozone for exposure times of 10 and 30 minutes. The native oxide on all three samples was removed after the exposure using a NH_4OH:H_2O

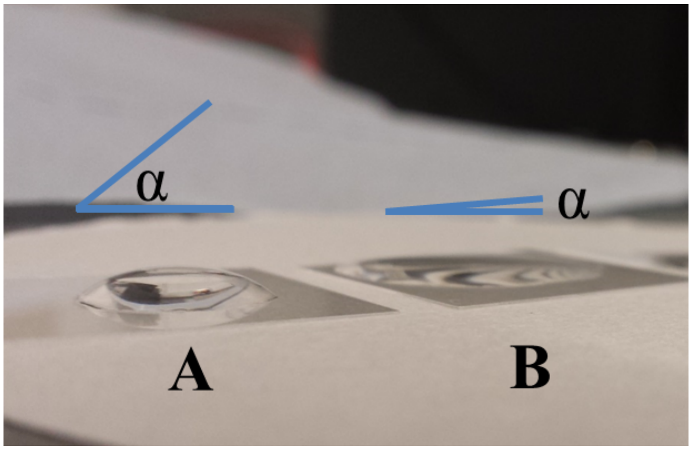

Figure 5.4: Water droplet on a (a) unprocessed and (b) processed glass slide (10 min. UV/Ozone exposure)

1:19 solution and blown dry with N_2 before the samples were loaded into the metal evaporator. Fig. 5.5 shows the measured specific contact resistivity for different surface preparations. The specific contact resistivity decreases from 18 $\Omega.\mu m^2$ to 15 $\Omega.\mu m^2$ for the samples which underwent a minimum of 10 min. ozone treatment. A similar reduction effect of specific contact resistivity for surface preparations including a UV-ozone treatment was observed by [8][16][17][18].

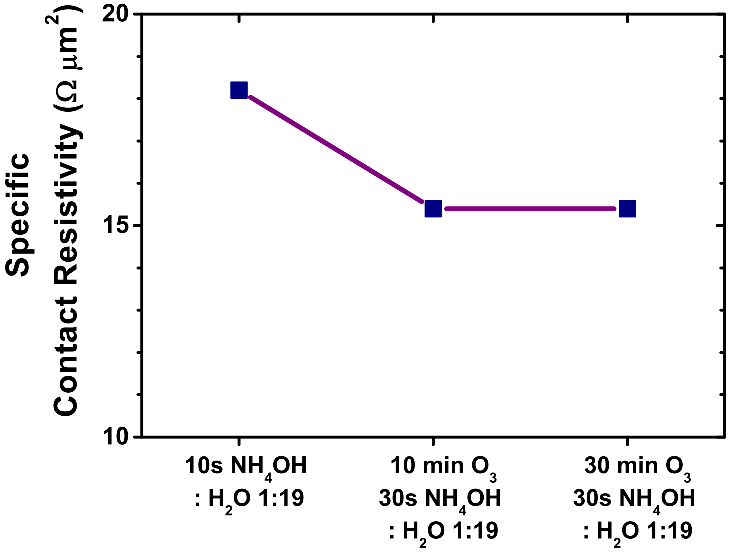

Figure 5.5: Specific contact resistivity as a function of UV/ozone treatment time

5.2.2 Native Oxide Removal

The native oxide on the semiconductor sample is usually removed prior the metal deposition, as native oxides are known to inhibit interface reactions between a semiconductor-ohmic contact. A basic solution of ammonium hydroxide (NH_4OH) was used to remove the native oxide on the InGaAs test samples. NH_4OH is attractive as it does not only dissolve the native oxide but it will also remove any metal-ion contaminants [9]. After the removal of the native oxide, the samples were blown dry using N_2. To avoid the native oxide regrowing, the samples were loaded into the deposition system within a time span of five minutes. Fig. 5.6 shows the specific contact resistivity as a function of NH_4OH concentration for different predeposition soaks. A reduction in specific contact resistivity from 24 $\Omega.\mu m^2$ to 15 $\Omega.\mu m^2$ is measured for the samples which underwent a concentrated NH_4OH predeposition soak. This shows that aqueous NH_4OH solutions with a low pH is not as effective as undiluted NH_4OH with a normality of 14.5 to remove the surface oxides [17].

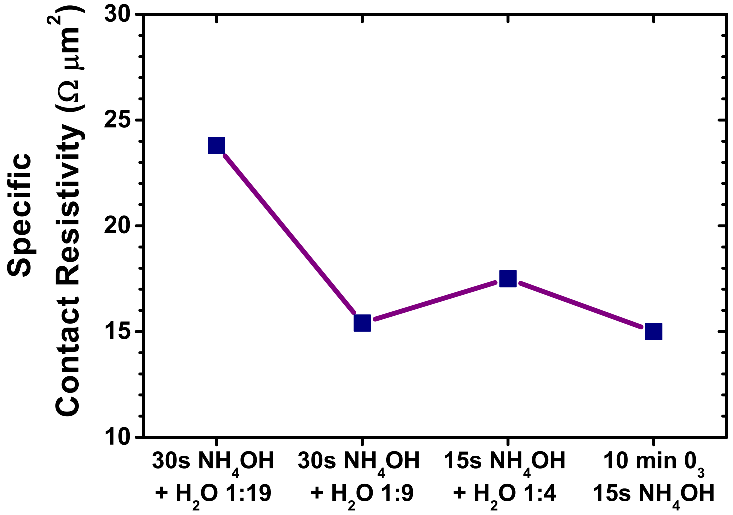

Figure 5.6: Specific contact resistivity as a function of the concentration of the NH_4OH predeposition soak

5.2.3 Post-Metallisation Anneal

The metal-semiconductor contacts were annealed to investigate the effect of heat treatment on the specific contact resistivity. A hot plate in atmospheric pressure was used for the annealing process. Prior to metal deposition, the sample under test was prepared by a 10 min. O_3 exposure followed by a 15 s dip in a 14.5N NH_4OH solution, after which the sample was blown dry using N_2. Fig. 5.7 shows the specific contact resistivity as a function of post-metallisation anneal time and temperature. To reduce experimental error, a single sample was used to explore the optimum annealing temperature and time. This was achieved by increasing the temperature and time while measuring the contact resistance between successive anneals. A specific contact resistivity of ~ 15 $\Omega.\mu m^2$ was measured for the unannealed sample.

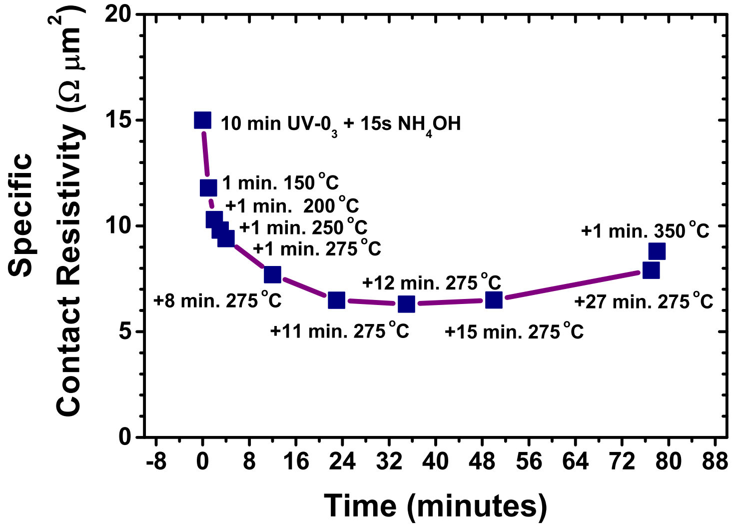

Figure 5.7: Specific contact resistivity as a function of the concentration of the NH_4OH predeposition soak.

Annealing the sample for ~ 35 min. at 275 °C reduces the specific contact resistivity from ~ 15 $\Omega.\mu m^2$ to ~ 6.3 $\Omega.\mu m^2$. The reduction in the specific contact resistivity with temperature can be associated to a thermally induced interfacial reaction between the semiconductor and the metal. An increase in contact resistance is measured for anneal times longer than ~ 35 min. The observed degradation of the Ti/Au contact for a longer anneal time can be attributed to indium outdiffusion from the InGaAs into the metal stack [8].

In conclusion, a specific contact resistivity of ~ 6.3 $\Omega.\mu m^2$ was obtained for a Ti(20 nm)/Au(200 nm) non-alloyed ohmic contact on $In_{0.53}Ga_{0.47}As$ (Si:2x10^{19} cm^{-3}). The surface preparation procedure for the optimum contact consisted of a 10 min. O_3 treatment followed by a 15 s dip in 14.5N NH_4OH after which the sample was blown dry using N_2. A Ti(20 nm)/Au(200 nm) metal stack was deposited onto the samples in a metal evaporator. After the deposition, a post-metallisation anneal at 275 °C was carried out for the duration of ~ 35 min. to obtain a specific contact resistivity of ~ 6.3 $\Omega\mu m^2$.

5.3 Development of Air-bridge Structure

To maximise the bandwidth of the RTD, a small device area is required for a low device capacitance. Air-bridge interconnection technology is widely used for high frequency devices to reduce device capacitance, and was implemented for the fabrication of the micron scale RTD.

The wet etching characteristics of InGaAs were explored and the structural design requirements for the realisation of the metallic air-bridge were investigated. Fig. 5.8(a) shows an optical microscope image of an air-bridge test-structure fabricated to investigate the maximum length:width ratio of a 1 μm thick gold air-bridge. These inverted LTLM air-bridge structures were fabricated using the LTLM photolithography mask on a n^+ InGaAs wafer. Metallic strips with dimensions equivalent to the LTLM contact gaps from 1 μm to 45 μm were fabricated by a metal evaporation and lift-off process. Etching of InGaAs and InP was subsequently carried out with H_3PO_4:H_2O_2:H_2O (1:1:18) and HCl, respectively, to create "tunnels" below the 36 μm long metallic stripes. Fig.5.8(b) shows a SEM image of a 1.2 μm wide bridge with a length:width ratio of 30. From this investigation, a design rule with a maximum length:width ratio of 30 was set for the air-bridge, as a low yield was observed for bridge widths of less than 1.2 μm.

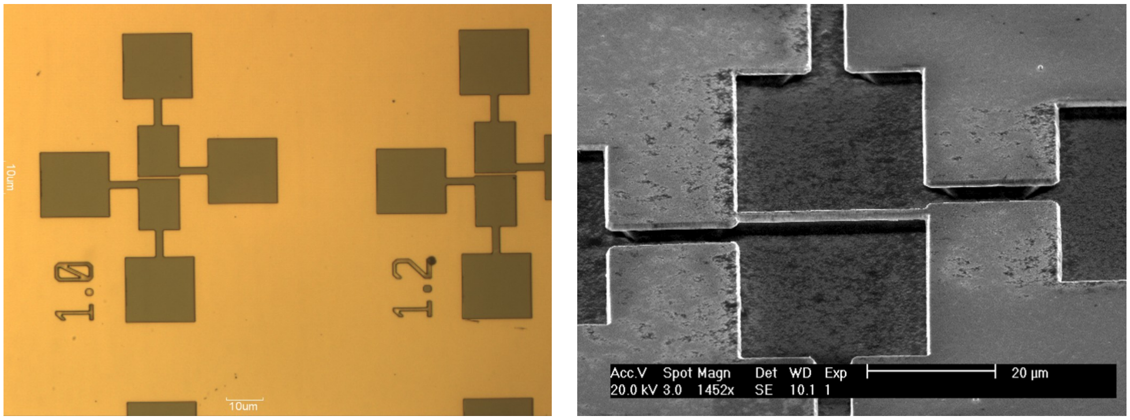

(a) (b)

Figure 5.8: (a) optical (b) electron microscope image of the air-bridge test-structure.

The wet etching characteristics of InGaAs were also investigated to find the optimum etching conditions for the fabrication of the air-bridge. The etching profile and the lateral etch rate of InGaAs is highly dependent on the crystallographic direction [22][21][19][20]. The etch rate into a particular crystallographic orientation is greatly determined by the relative orientation of the slow-etching (111)A plane [9]. The (111)A plane etches slower as all three bonding electrons of the group-III surface atoms of the plane are bonded to the lattice. The (111)A plane is therefore less reactive to the etchant than the fast etching (111)B plane which has two unbounded electrons on the group-V surface atoms. A photoresist etch pattern was fabricated on a 400 nm InGaAs layer to investigate the etch profiles along different crystallographic directions. Fig. 5.9 shows SEM images of the etch profiles obtained for the different crystallographic orientations. V-shaped, dovetail, and nearly vertical etch profiles are obtained for mask patterns aligned in the [01-1], [011], and [010] directions, respectively. A nearly vertical etch profile is observed for etching along the [010] and [001] crystallographic directions, as etching is not impeded by the slow etching (111)A plane [22]. Kim [21] found that the lateral etch rate of InGaAs, using a reaction rate controlled H_3PO_4:H_2O_2:H_2O etchant, in the [010] direction is approximately twice as fast as in other crystallographic directions. In this work, the RTD devices were fabricated with the air-bridge aligned along the [001] direction to benefit from the faster lateral etch rate in the [010] direction.

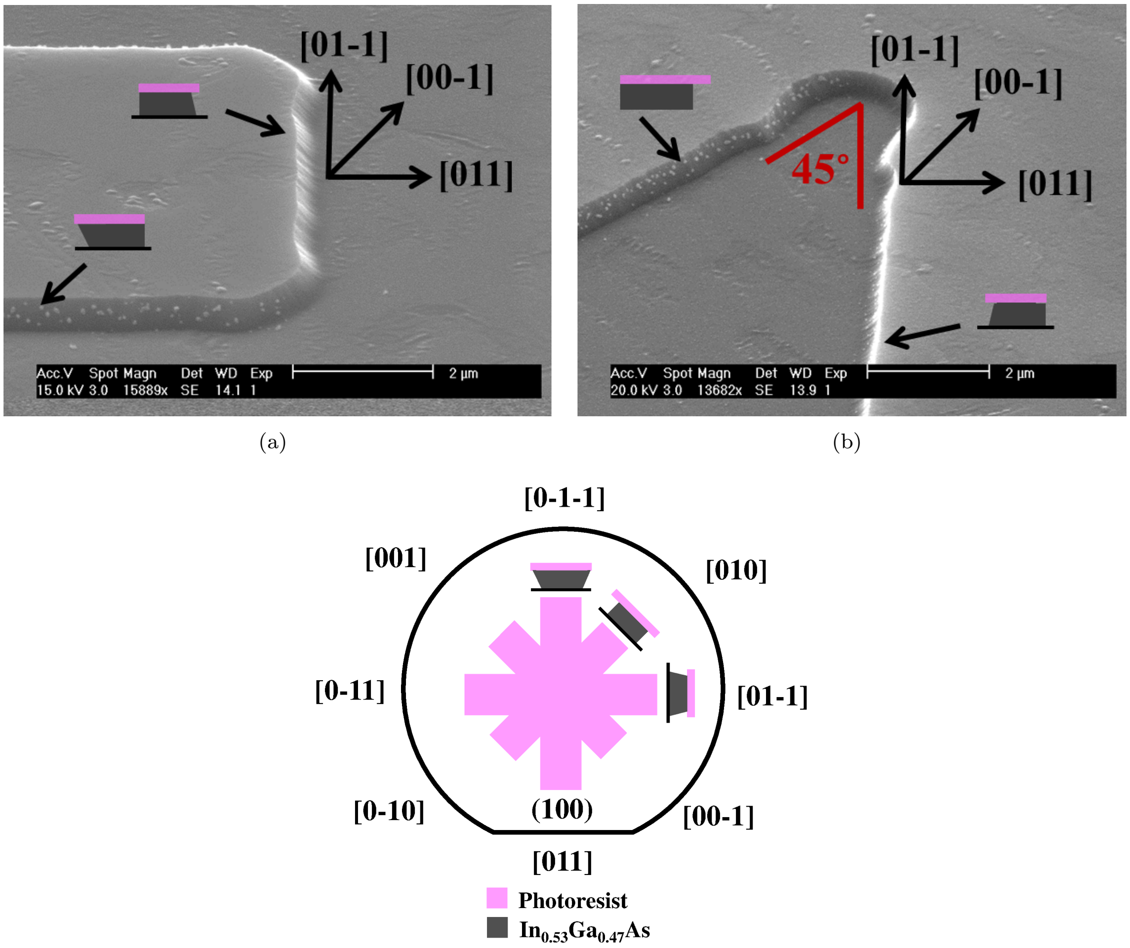

(a)

(b)

(c)

Figure 5.9: (a-c)Etching profiles of InGaAs according to the crystallographic orientations on a European-Japanese (EJ) oriented InP substrate.

5.4 Device Fabrication Process

This section covers the step-by-step fabrication of the RTD based THz emitter. The fabrication process consists out of two main stages:

1. **RTD fabrication**
    (a) Metallisation
    (b) Wet etch
2. **Antenna Integration**
    (a) Metal-insulator-metal (MIM) fabrication

Fig. 5.10 pictographically shows the main fabrication stages for the RTD based THz emitter. The fabrication process is based on air-bridge technology, standard i-line photolithography, and wet chemical etching.

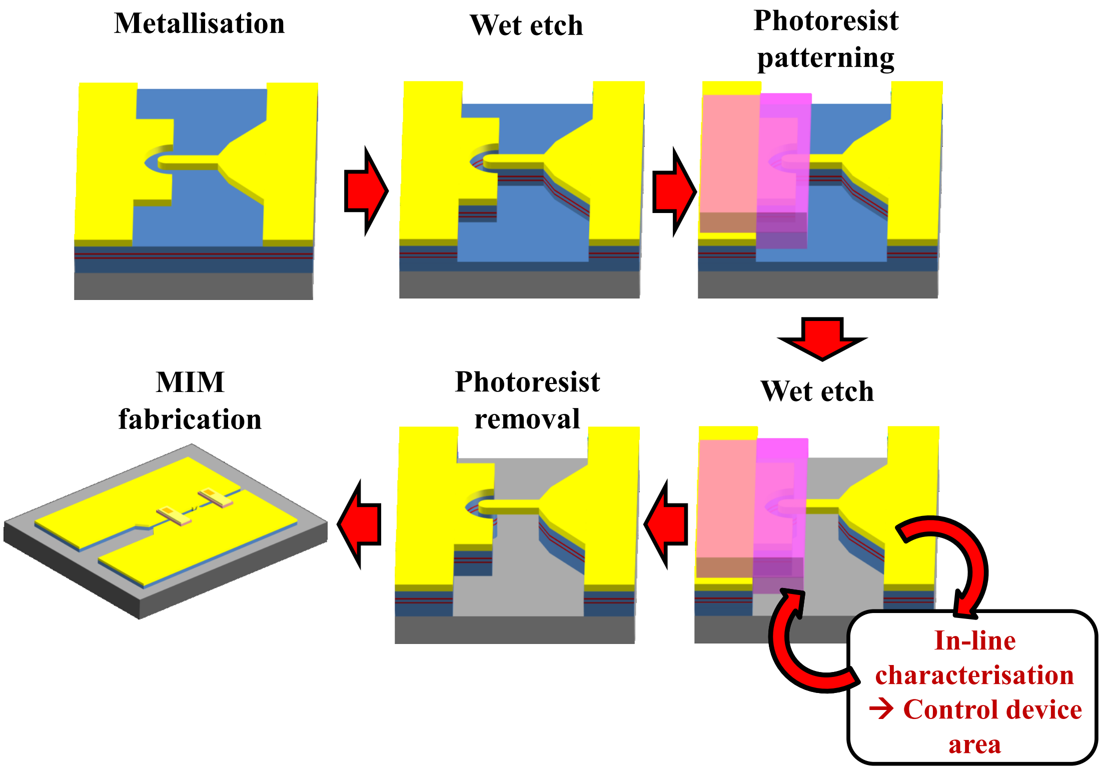

Figure 5.10: Fabrication process flow of the RTD based THz emitter.

5.4.1 Metallisation Stage

Fig. 5.11 schematically shows the process flow of the metallisation stage. The fabrication starts by cleaving a 15 mm by 15 mm sample from the RTD wafer using a scribe and break system. This is followed by cleaning the sample thoroughly through a 3-stage clean process with boiling n-butyl acetate, acetone, and isopropyl alcohol. The sample is dried using nitrogen (N_2) to avoid drying stains, and inspected under an optical microscope. This process is repeated until less than one piece of dirt per field of view is observed at 100x optical magnification. To obtain ultra-low resistance contacts, the metal contacts are deposited on the as-grown sample at the start of the fabrication process. This is required to minimise the exposure to dirty deposits and possible damage to the highly doped surface layer during future processing steps. The sample is loaded into the evaporator following a 10 min. UV/O_3 exposure, 15 s 14.5N NH_4OH pre-deposition soak, and a N_2 blow dry. A thin metal seed layer of Ti(20 nm)/Au(20 nm) is deposited by a metal evaporation process to fabricate the metal-semiconductor contacts. The thickness of the metal film is monitored during the evaporation process using a thin-film thickness monitor.

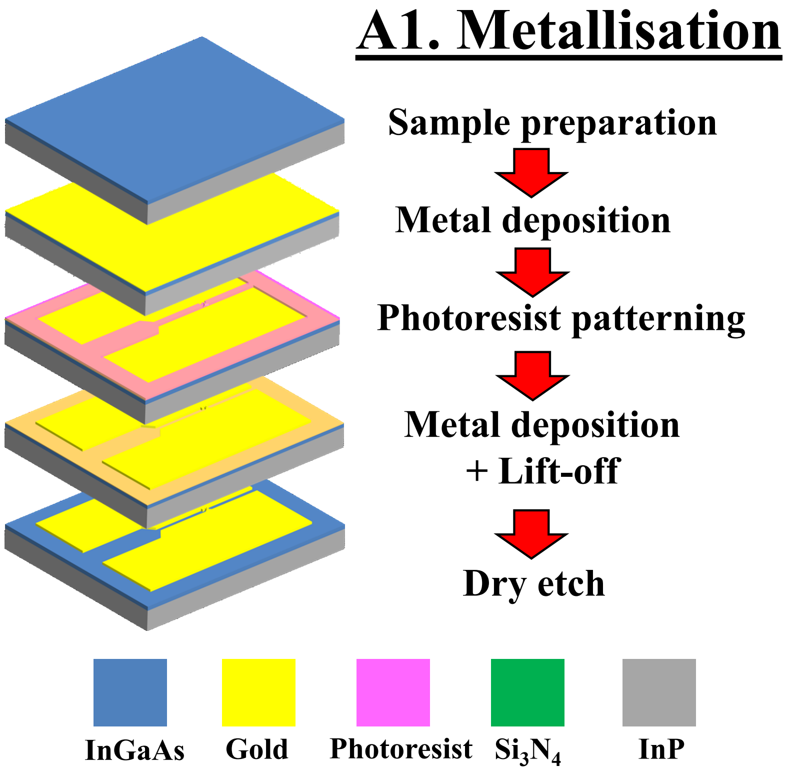

Figure 5.11: Process flow of the metallisation stage. The coloured squares in the legend represent the layers of the RTD structure and materials used during the fabrication.

Following the metal deposition, the sample has negative photoresist spun on. A negative resist is chosen to attain a suitable undercut profile for the following metallisation and lift-off step. The optimal exposure dose and development time parameters for the metal lift-off were first determined on a test sample. Fig. 5.12 shows SEM images of photoresist patterns fabricated with a constant exposure dose for development times from 50 s to 75 s. It is known that a low exposure dose and long development time for negative photoresist results in a more pronounced undercut profile [23]. The undercut profile from the negative resist eases the metal lift-off process as it prevents the resist sidewalls from being coated with metal. Fig. 5.12 shows that a more pronounced undercut profile is obtained for longer development times. An optimal development time of 65 s is determined from this experiment as the metal lift-off was clean, and the widening of the photoresist pattern during the development is minimal.

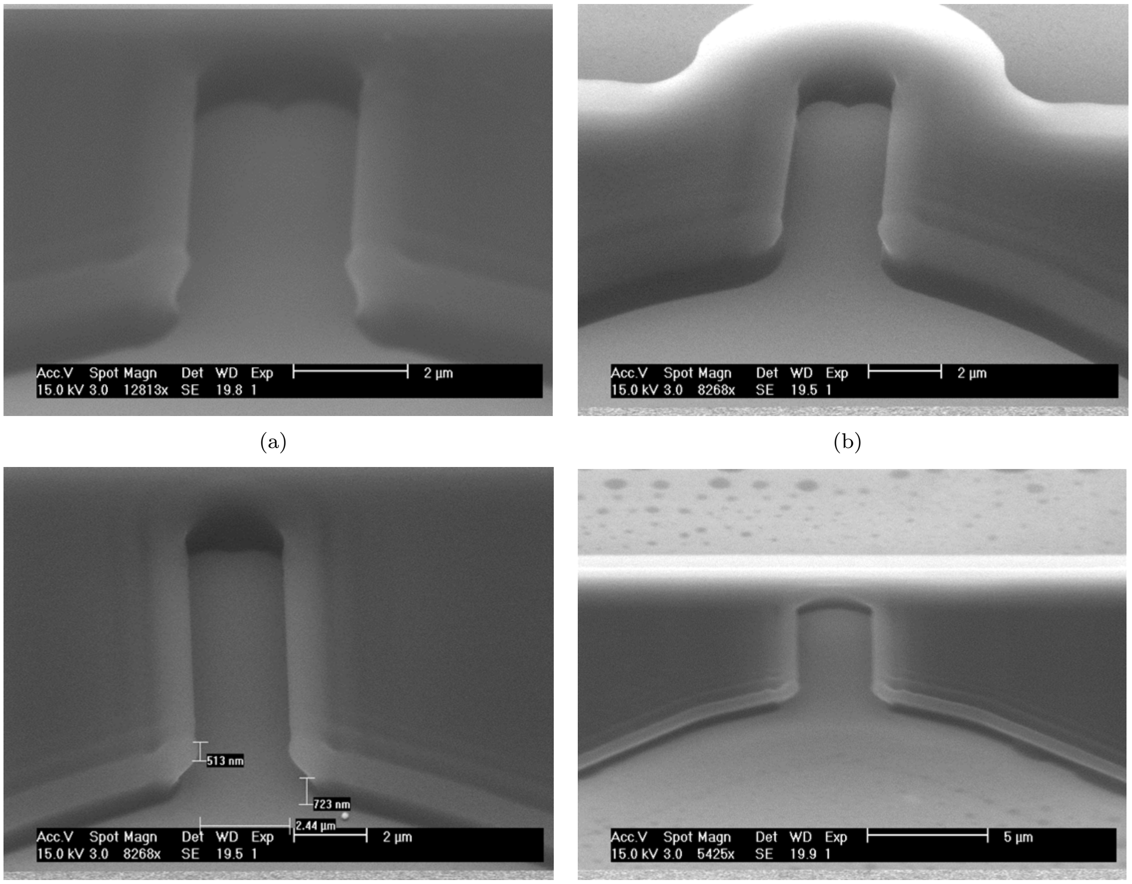

(a) (b)

(c) (d)

Figure 5.12: Undercut profiles of negative resist for various development times (a) 50 s (b) 55 s (c) 65 s (d) 75 s

The fabrication continues with a one micron gold deposition by a metal evaporation process to fabricate the electrodes of the slot antenna and RTD. Fig. 5.13(a) shows a SEM image of the deposited metal on the patterned sample. The undercut profile of the negative resist ensures that no resist sidewalls are coated with evaporated metal, which leads to a clean metal lift-off as shown in Fig.5.13 (b). The metal seed layer is removed using a reactive ion etch with gas compositions of $SiCl_4$+Ar and CHF_3+O_2 for the selective etching of gold and titanium, respectively.

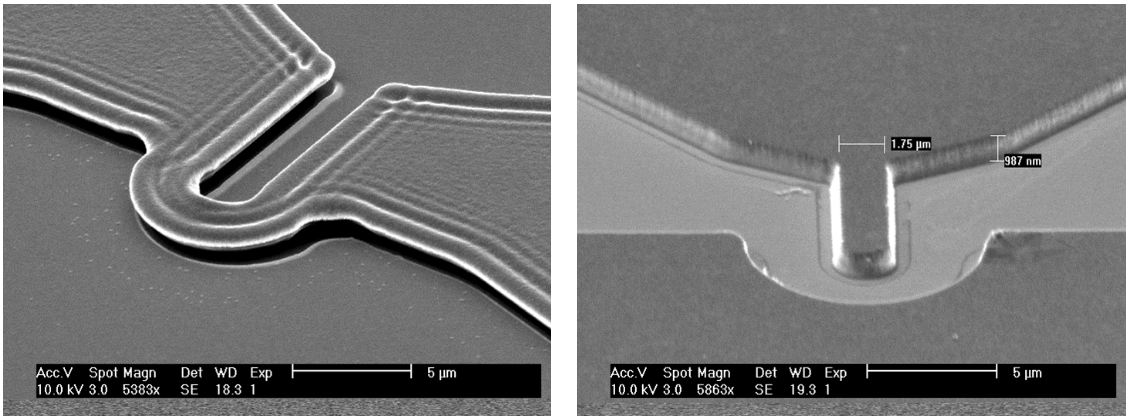

(a)

(b)

Figure 5.13: SEM images of deposited metal (a) prior and (b) post metal lift-off

5.4.2 Wet Etching Stage

After the metallisation stage, the RTD and air-bridge are fabricated, and the slot antenna is isolated. Fig. 5.14 schematically shows the process flow. A controlled shallow wet etch (H_3PO_4:H_2O_2:H_2O = 1:1:38, etch rate of 100 nm/min. at room temperature) of 150 nm is carried out down to the highly doped emitter layer located below the double-barrier heterostructure. The sample is patterned before the etch process with photoresist to provide a good step coverage for the dielectric and the metal of the MIM reflectors. Fig. 5.15 shows a SEM image of the photoresist pattern which indicates that the metal electrodes are protected at the edges with photoresist within the slot. After the photoresist removal, new photoresist is spun onto the sample and patterned to define the RTD mesa before the second wet etch. Fig. 5.16 shows a SEM image of the photoresist pattern. The edges of the metal electrodes for the MIM reflectors are protected again to obtain good coverage of the dielectric and metal interconnects.

The Au air-bridge contact is fabricated by wet etching the exposed InGaAs to produce a "tunnel" below the exposed Au stripe and provide electrical isolation between the emitter and collector electrodes. The metallic air-bridge structure electrically separates the bonding pad region of the collector electrode from the active tunnelling area, whilst providing an effective reduction in parasitic capacitance. A low interconnect capacitance is obtained between the emitter and collector

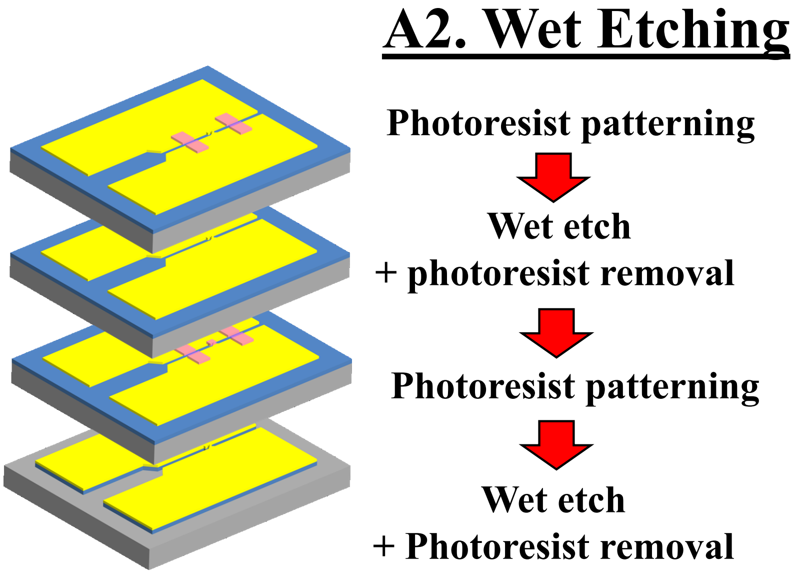

Figure 5.14: Process flow of the wet etching stage

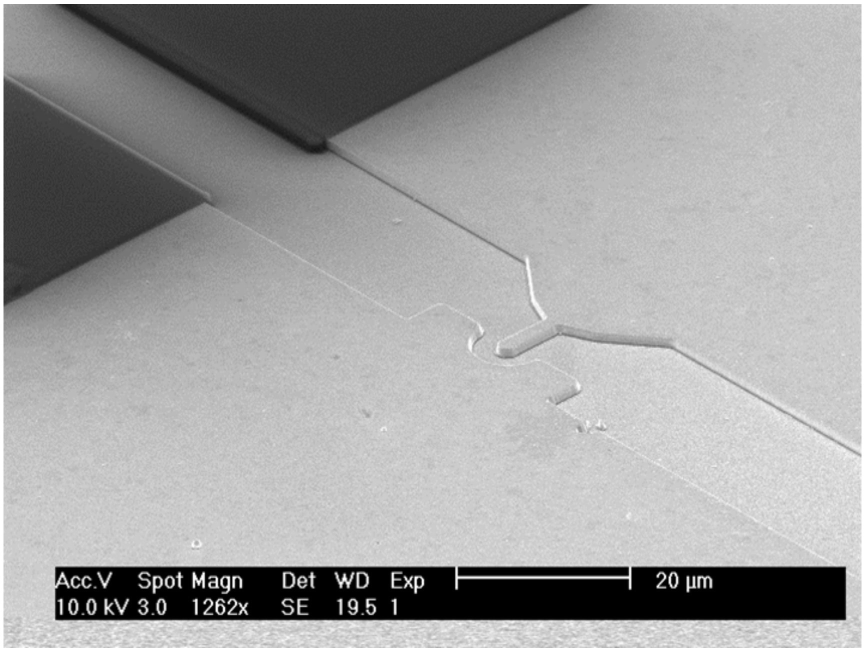

Figure 5.15: SEM image of the photoresist pattern for the fabrication of the MIM reflectors.

electrodes due to air having a dielectric constant of essentially 1. The InP layer underneath the highly doped emitter contact layers acts as an etch stop layer due to the selectivity of the phosphoric based wet etchant, which enhances the lateral etching underneath the air-bridge. Test-structures

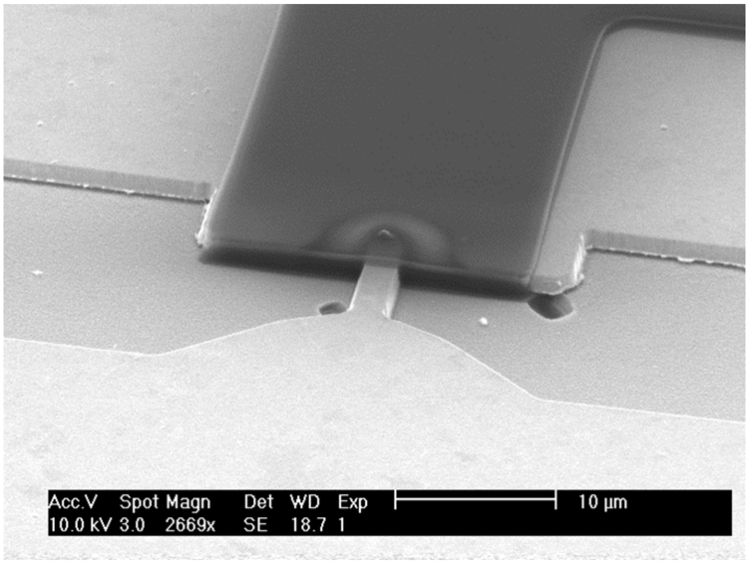

Figure 5.16: SEM image of the patterned photoresist for the fabrication of the RTD.

on the wafer are used to measure the undercut progress during the wet etch process.

Fig. 5.17(a) shows a SEM image of such test-structures, where the smallest features were already etched off during the wet etch process. Through this technique, it is possible to monitor the etch progress of the tunnel below the exposed Au stripe. Fig. 5.17(b) shows a SEM image of the fabricated RTD with the air-bridge structure.

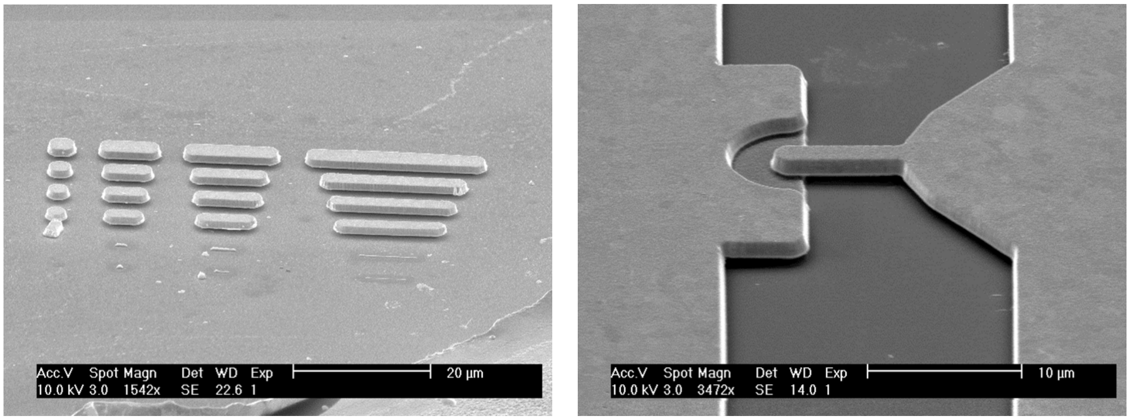

(a) (b)

Figure 5.17: (a) SEM image of the test structure used for controlling the wet etch process of the air-bridge fabrication (b) SEM image of fully fabricated $\sim 3.3\ \mu\text{m}^2$ RTD with the air-bridge structure.

As both electrodes are deposited during the single metal evaporation process, the emitter current is guided through the full RTD structure by a second contact electrode on the collector side. Due to the high current density through the RTD, a very low resistance path is created between the collector and emitter for such a contacting arrangement. Eliminating a second contact metallisation to the emitter layer by guiding the emitter current through the full RTD structure also allows the voltage-current (V-I) characteristic of the RTD to be measured during the etch process. Fig. 5.18 shows an annotated SEM image and a schematic cross section of the RTD device.

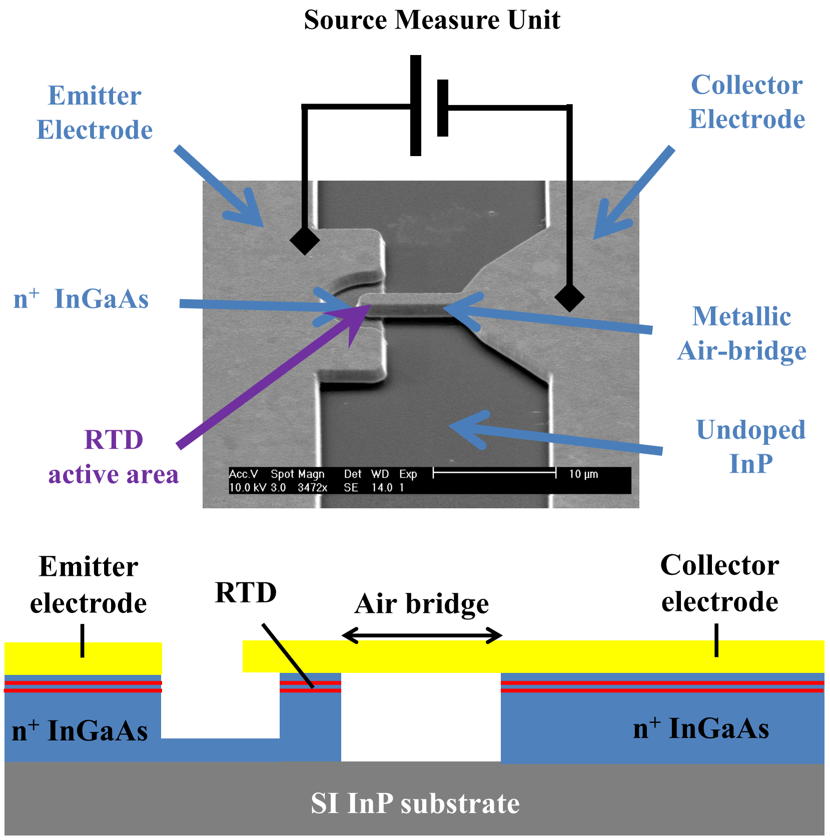

Figure 5.18: SEM image and schematic cross section of the RTD

The V-I measurements were carried out in third quadrant operation (negative bias applied to the collector), as the current density is lower in this operation mode as the thicker undoped spacer layer is now on the emitter side. By operating in this scheme, the peak current density and voltage is lower compared to first quadrant operation, which consequently minimises catastrophic failure due to self-heating. Accurate control over the final mesa area was demonstrated through this method. Fig. 5.19 shows a graph of such RTD V-I characteristics for etches of duration 540 s to 690 s with 30 s steps. A reduction in peak current and peak voltage is clearly observed with increasing etch time. The observed reduction in peak current is associated with a reduction in mesa size, as the total tunnelling current is directly proportional to the mesa area. The corresponding mesa area for each V-I characteristic is deduced from the current density through the RTD as indicated in the Fig. 5.19. The current density was deduced from a second fabrication based on EBL and dry etching techniques, which allowed for an accurate measurement of the mesa area. The fabrication and characterisation of this control sample was carried out by Rohm Semiconductor. From Fig. 5.19, an areal etch rate of approximately 2.33x10^{-2} $\mu m^2/s$ is deduced, which corresponds to a RTD peak current reduction rate of 160 $\mu A/s$. Based on an etch time resolution of 1 second, this results in an areal etch accuracy of $\sim$ 0.7 % for a single device based on a final area of 3.3 μm^2.

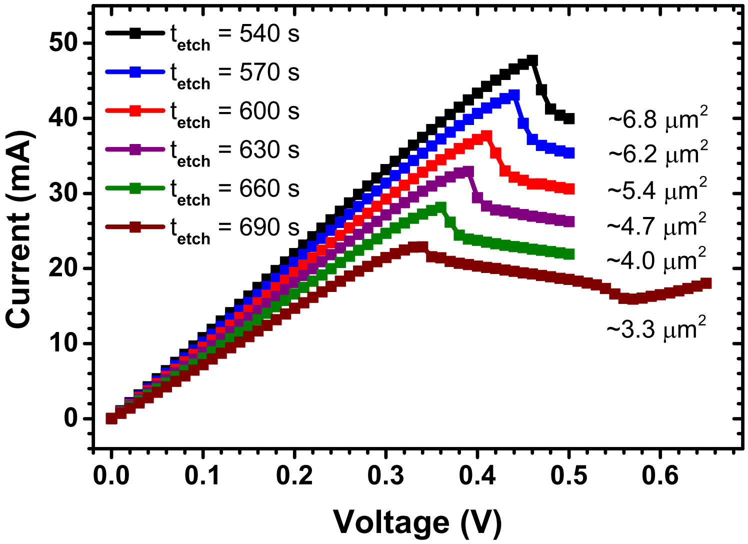

Figure 5.19: V-I characteristics of the RTD measured during the fabrication process. The etch time for each V-I characteristic is shown in the legend. The device area shown in μm^2 represents the total RTD area as calculated from the peak current density measured from a second sample.

A greater etch area accuracy is expected by using a more diluted etchant and a source-measure unit (SMU) with higher accuracy and resolution.

A phosphoric based etchant with a low concentration of peroxide was selected for the etch process to avoid bubble formation on the wafer surface, which is known to mask and degrade the surface quality during the etching procedure. To obtain uniform, reproducible etch results, pre-cleaning with a dilute NH_4OH solution (NH_4OH:H_2O = 1:19) was carried out to remove the native oxide. This ensures a uniform surface for the etchant to attack, since a variation in initial etch rate at different places on the wafer can produce undesired differences in etch depths across the wafer, which is important as small quantities of the structure are to be removed for ultra-fine control of the final device area. Whilst wet etch processes may be considered to be highly variable in research laboratories, careful environmental control, control of the etch chemicals, agitation, stirring, or the use of spray etching methods in an industrial environment can produce highly reproducible results. The manufacture of micron scale InGaAs-InP HBTs using an all-wet-etch process was recently shown to have high uniformity across the whole of a 3″ wafer and high reproducibility from wafer to wafer [24]. The avoidance of plasma processes, and the elimination of the risk of damage to the electrical properties of the device due to bombardment of the surface with energetic ions during dry etching are also seen as a benefit. The effect and influence of dry plasma etching processes of Si/SiGe resonant interband tunnel diodes (RITDs) was investigated by Park *et al.* [25], where a ~ 40 % enhancement in PVCR for the HBr plasma etched RITD (70 μm mesa diameter, Jpeak $= 32\text{A/cm}^2$) was measured compared to the wet etched RITD. The mechanism involved for the improved PVCR was attributed to hydrogen passivation, which is responsible for passivating ionised centres, and reducing the bulk defect state densities, thereby lowering the measured valley current density [26]. However, greater surface damage was measured on the plasma-etched sample. Whereas dry etch damage might be less significant for devices with a large diameter, the damage (up to 100 nm deep [27]) can have a large impact on the performance of micron and sub-micron scale devices, as the size of the device approaches the dimension to the damaged region. The effect of dry and wet etching on the RTD performance will have to be explored in future work. Further discussion on the measurement of the V-I characteristics is included in Chapter 6.

5.4.3 MIM Fabrication

The THz emitter was completed with the fabrication of the MIM reflectors to capacitive couple the slot antenna electrodes as these capacitors behave like short circuits at high frequency. Bias stabilisation was provided to the THz emitter with a SMD resistor. Fig. 5.20 schematically shows the process flow. The process starts with a deposition of 150 nm silicon nitride by plasma-enhanced chemical vapour deposition (PECVD). The deposition rate of the PECVD system was calibrated by depositing 100 nm of Si_3N_4 on a silicon test sample and measuring the dielectric thickness with an ellipsometer. The patterned dielectric of the MIM reflectors is fabricated using a reactive ion etching process with a gas composition of trifluoromethane (CHF_3) and oxygen (O_2). Photoresist is used to define the pattern during the etch process. Fig. 5.21 shows a SEM image and cross section of the MIM structure. To maximise the capacitance of the MIM reflectors, a rectangular cut-out is created on one side of the MIM dielectric to interconnect the metal of the slot antenna

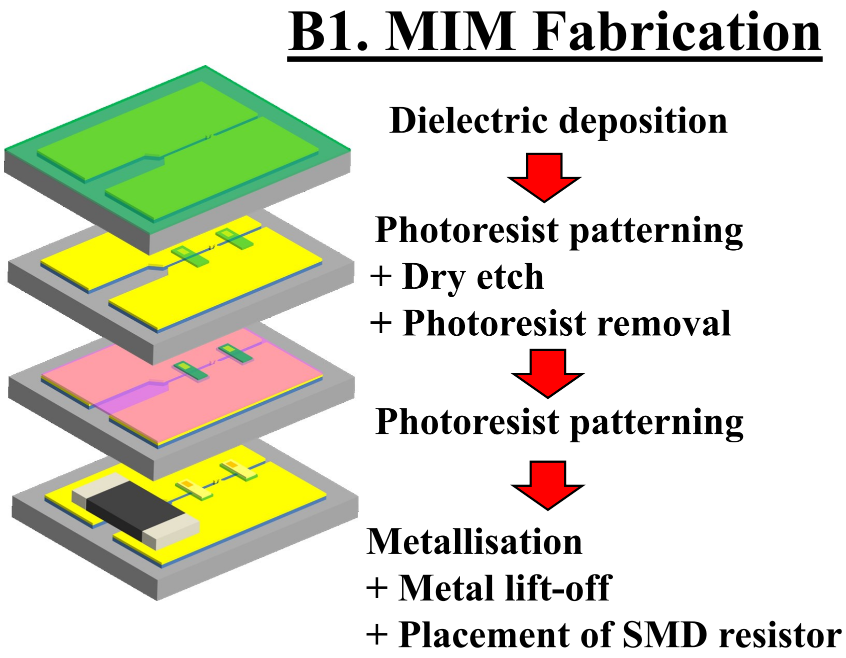

B1. MIM Fabrication

Dielectric deposition

Photoresist patterning
+ Dry etch
+ Photoresist removal

Photoresist patterning

Metallisation
+ Metal lift-off
+ Placement of SMD resistor

Figure 5.20: MIM fabrication process flow

and MIM reflector. After the dry etch process, the photoresist is removed and a new photoresist is spun onto the sample and patterned for the MIM reflector metallisation. A Ti(20 nm)/Au(150 nm) metallisation is deposited through a sputtering process. Sputtering is preferred over metal evaporation to improve the metal step coverage on the dielectric film. Fig. 5.22 shows the step coverage of the dielectric and metal film within the slot after the metal lift-off. Good step coverage is obtained through this process.

At the end of the fabrication, a SMD resistor is placed on the chip across the electrodes to provide bias stabilisation for the RTD. Fig. 5.23 shows a schematic of the completed RTD based THz transmitter. The fabricated device is placed upon a hyper-hemispherical lens to couple the emission out of the chip.

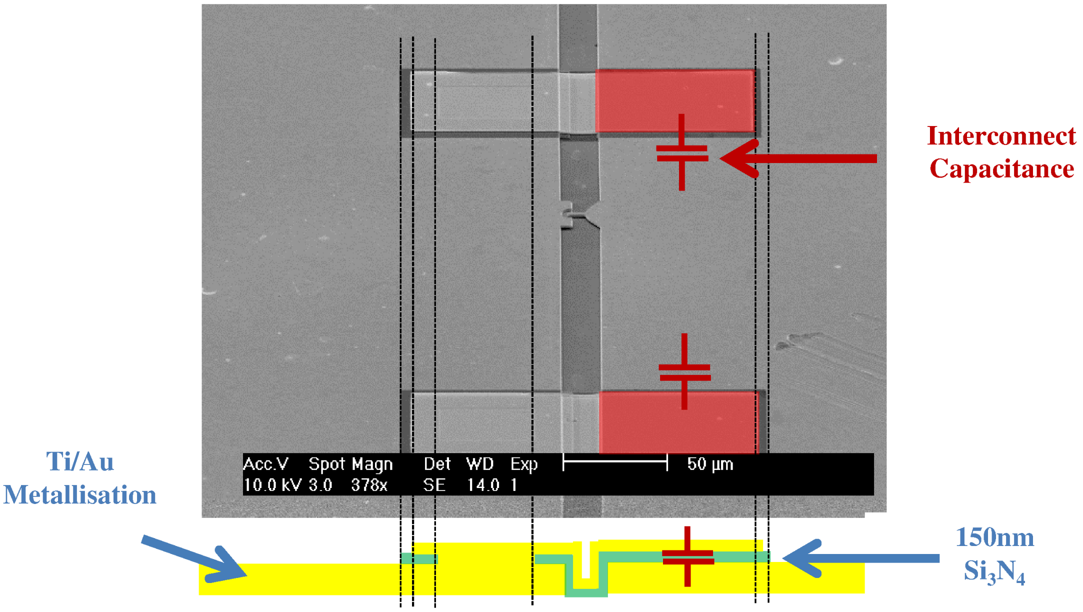

Figure 5.21: SEM image of the fabricated THz emitter. The cross section shows the metallisation and dielectric structure of the MIM reflectors. The interconnect capacitance of the MIM reflectors is shown in red.

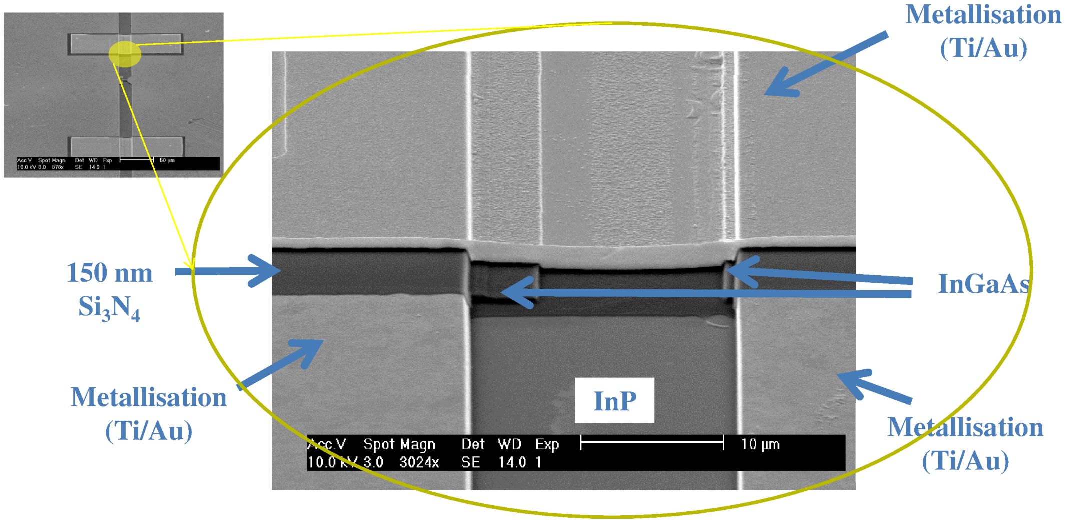

Figure 5.22: SEM image of the MIM reflector showing the step coverage of the dielectric and metal film within the slot after the metal lift-off.

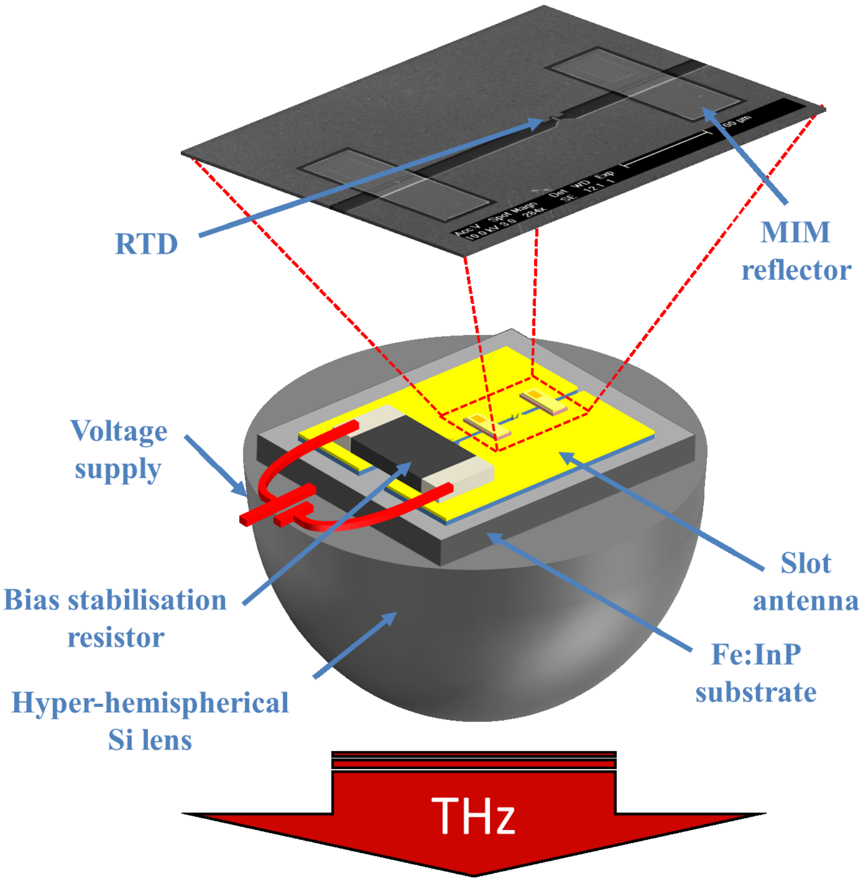

Figure 5.23: Schematic of the RTD based THz emitter

5.5 Conclusions

In this chapter, an EBL free processing technique for the fabrication of micron scale, high current density RTDs for THz applications based on air-bridge technology, standard i-line photolithography, and wet chemical etching was developed. To minimise the contact resistance of the RTD, an investigation was carried out to determine the optimum conditions for the fabrication of the metal-semiconductor contacts. A specific contact resistivity of $\sim 6.3\ \Omega\mu\text{m}^2$ was obtained. The RTD was successfully integrated monolithically with a slot antenna for the realisation of the THz emitter.

References

[1] International Technology Roadmap for Semiconductors 2013 version, URL: http://www.itrs.net/Links/2013ITRS/Summary2013.htm (2013)

[2] Plummer, James D.; Griffin, Peter B., “Material and process limits in silicon VLSI technology,” Proceedings of the IEEE , vol.89, no.3, pp.240,258, Mar 2001

[3] Gregory S. Marlow, Mukunda B. Das, “The effects of contact size and non-zero metal resistance on the determination of specific contact resistance”, Solid-State Electronics, Volume 25, Issue 2, February 1982, Pages 91-94

[4] Schroder, Dieter K. Semiconductor Material and Device Characterization. 3rd Ed. John Wiley and Sons, Inc. Hoboken, New Jersey, 2006.

[5] A.G Baca, F Ren, J.C Zolper, R.D Briggs, S.J Pearton, “A survey of ohmic contacts to III-V compound semiconductors”, Thin Solid Films, Volumes 308309, 31 October 1997, Pages 599-606

[6] V.L. Rideout, “A review of the theory and technology for ohmic contacts to group IIIV compound semiconductors”, Solid-State Electronics, Volume 18, Issue 6, June 1975, Pages 541-550,

[7] G. Stareev, H. Knzel and G. Dortmann, “A controllable mechanism of forming extremely low-resistance nonalloyed ohmic contacts to group III-V compound semiconductors”, J. Appl. Phys. 74, 7344 (1993)

[8] A. M. Crook, et al., “Low resistance, nonalloyed Ohmic contacts to InGaAs,” Appl. Phys., vol. 91, no. 19, pp. 192114-192114-3, Nov. 2007.

[9] Baca, A. G, and Carol Iris Hill Ashby. Fabrication of GaAs Devices. London: Institution of Electrical Engineers, 2005.

[10] Reinhardt, Karen A & Kern, Werner. Handbook of Semiconductor Wafer Cleaning Technology - Science, Technology, and Applications. 2nd Ed. William Andrew Inc, Norwich ,NY, 2008.

[11] Driad, R.; Lu, Z-H; Laframboise, S.; Scansen, D.; McKinnon, W.R.; McAlister, S.P., “Surface passivation of InGaAs/InP beterostructures using UV-irradiation and ozone”, Indium Phosphide and Related Materials, 1998 International Conference on , vol., no., pp.459,462, 11-15 May 1998

[12] J. R. Vig, J. Vac. Sci. Technol. A 3, 1027 (1985).

[13] http://www.senlights.com/gijyuu/drycleaning/drycleaning.html

[14] http://www.techvision.co.jp/english/products/uvo_landing01.htm

[15] http://www.novascan.com/products/psd_uvozone.php

[16] R. Dormaier and S. E. Mohney, Factors controlling the resistance of Ohmic contacts to n-InGaAs, J. Vac. Sci. Technol. B, vol. 30, no. 3, p. 031209, Apr. 2012

[17] Jain, V.; Baraskar, A.K.; Wistey, Mark A.; Singisetti, U.; Griffith, Z.; Lobisser, E.; Thibeault, Brian J.; Gossard, A.C.; Rodwell, Mark J.W., “Effect of surface preparations on contact resistivity of TiW to highly doped n-InGaAs,” Indium Phosphide & Related Materials, 2009. IPRM ’09. IEEE International Conference on , vol., no., pp.358,361, 10-14 May 2009

[18] Eunjung Cha Development of Ni-based Ohmic contacts to InAs and InGaAs, 2013

[19] M. Tong, K. Nummila, A. A. Ketterson, Selective Wet Etching Characteristics of Lattice-Matched InGaAs/InAIAs/InP, J. Electrochem. Soc., Vol. 139, No. 10, October 1992, The Electrochemical Society, Inc. L93 (page)

[20] Tarui, Y., Y. Komiya, and Y. Harada, 1971, “Preferential Etching and Etched GaAs Profile,” J. Electrochem. Soc. Jpn. 118, 118

[21] Moonjung Kim, InGaAs/InP p-i-n Photodiode with an Extrinsic Pad Isolation Structure, Journal of the Korean Physical Society, Vol. 51, No. 4, October 2007, pp. 14091412

[22] Pasquariello, D.; Bjorlin, E.S.; Lasaosa, Daniel; Chiu, Yi.-J.; Piprek, Joachim; Bowers, J.E., “Selective undercut etching of InGaAs and InGaAsP quantum wells for improved performance of long-wavelength optoelectronic devices,” Lightwave Technology, Journal of , vol.24, no.3, pp.1470,1477, March 2006

[23] http://www.microchemicals.com/technical_information/lift_off_photoresist.pdf

[24] Yanagisawa, Masaki; Kotani, K.; Kawasaki, T.; Yamabi, R.; Yaegassi, S.; Yano, H., "A robust all-wet-etching process for mesa formation of InGaAs-InP HBT featuring high uniformity and high reproducibility," Electron Devices, IEEE Transactions on , vol.51, no.8, pp.1234,1240, Aug. 2004

[25] Park, S.-Y.; Chung, S.-Y.; Berger, P.R.; Yu, R.; Thompson, P.E., "Low sidewall damage plasma etching using ICP-RIE with HBr chemistry of Si/SiGe resonant interband tunnel diodes," Electronics Letters , vol.42, no.12, pp.719,721, 8 June 2006

[26] Raghavan, M.N.V., and Venkataraman, V.: "Enhanced room temperature mobilities and reduced parallel conduction in hydrogen passivated Si=SiGe heterostructures", Semicond. Sci. Technol., 1998, 13, pp. 13171321

[27] C.D. W. Wilkinson, L. Deng and M. Rahman, "Issues in Etching Compound and Si-based Devices," Jpn. J. Appl. Phys. 41, 4261 (2002)

Chapter 6

Device Characterisation

6.1 Introduction

This chapter reports on electrical and optical characterisation of the RTD THz emitter. As discussed in Chapter 3, the volume manufacturable fabrication method for micron scale high current density RTDs provides accurate control over the final device area (and hence characteristics) by measuring the V-I characteristic of the RTD during the fabrication process. Further details about this characterisation technique are included in this chapter. By measuring the RTD V-I characteristic in-line with the fabrication process, important information about the RTD performance are extracted, such as RTD peak voltage and specific contact resistivity. Extracting these characteristics during the fabrication process without the need of additional complex test structures is advantageous from a manufacturing point of view, and provides a route for further device optimisation. To bring the RTD into oscillation mode, a bias in the NDR region is required to convert DC electrical power into high frequency oscillations. It is noted that the output power of the device is dependent on the voltage and current spans in the NDR region, which also highlights to need for a large peak-to-valley current ratio (PVCR). The electronic properties of the RTD, such as PVCR, are sensitive to structural variations such as barrier and well thickness, material composition, doping, and interface roughness. The valley current of the RTD is investigated, including temperature dependent V-I characterisation.

6.2 Device Characterisation

The RTD devices were measured on the wafer at room temperature using probes from Cascade Microtech. The DC characteristics of the devices were measured with a Keithley 2400 general-purpose sourcemeter as a voltage source. The shields of the coaxial cables connecting the test probes to the sourcemeter were earthed to reduce noise coupling into the system. A LabVIEW program was written to measure the V-I characteristic of the device. As covered in Chapter 5, the final device area of the RTD was controlled by measuring the V-I characteristic of the RTD during the fabrication process. Fig. 5.19 does not only show a reduction in the RTD peak current with increasing etch time, but a reduction in the RTD peak voltage is also observed. The reduction in the peak voltage is associated with the voltage drop across the emitter contact, the source resistance, and the air-bridge, as the IR voltage drop reduces with decreasing mesa size (i.e. reduction in tunnelling current). Extrapolating the peak voltage and current as a function of mesa area provides important information about the RTD as parasitic elements are excluded from the measurement.

Fig. 6.1 shows the RTD peak voltage and current as a function of etch time.

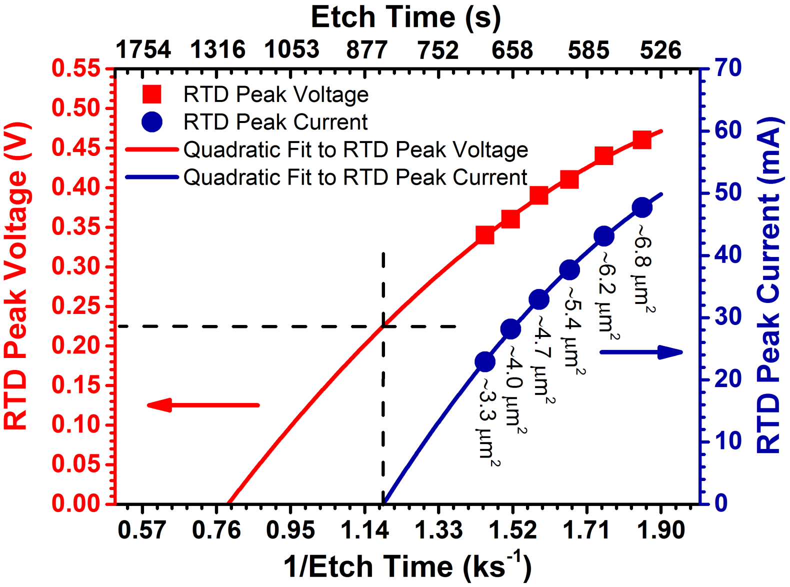

Figure 6.1: RTD peak voltage and peak current as a function of etch time. The black dotted lines guides the eye to the intercept point on the curve of the extrapolated quadratic fit to the RTD peak voltage in the limit of zero current. The approximate mesa area is displayed for the etched devices, as calculated from the current density and the RTD peak current.

A minimum peak voltage of $\sim$ 225 mV is determined in the limit of zero peak current by extrapolating the quadratic fit to the peak voltage as a function of etch time. In the limit of zero current, the peak voltage consists out of the voltage drops across the collector contact and between the emitter and collector layers of the RTD at resonance. In this limit, the voltage drops across the aforementioned parasitic elements are excluded, and a parasitic series resistance of ~5.0 ohms is deduced. The bias between the emitter and collector layers of the RTD at resonance is also extracted by subtracting the collector contact voltage from the peak voltage of the RTD. The voltage across the collector is deduced from linear transfer length method (LTLM) measurements which were performed on test-structures fabricated alongside the RTDs on the same sample. A specific contact resistivity of 8 $\Omega.\mu m^2$ was measured for the collector contact. The resistance of the emitter contact, which includes the contact resistance and the low resistance path between the collector and emitter of the RTD, is estimated to be less than ~1 Ω, as the total contact area of the emitter is much larger than the mesa area of the RTD. For a collector contact with a specific contact resistivity of 8 $\Omega.\mu m^2$, a peak voltage of 168 mV between the emitter to the collector layers of the RTD is deduced from Fig. 6.1. If the bias at resonance of the RTD is known from modelling, this fabrication method also allows a measurement of the contact resistance without the need of TLM structures. A resistive cut-off frequency of ~1 THz is estimated for a RTD with an active area of 3.3 μm^2, following Eq. 4.4 in Chapter 4.

6.3 Valley Current Characteristics

To gain a greater understanding into the valley current of the RTD, room temperature V-I characterisation was carried out for RTD devices with different perimeter/area ratios to quantify surface leakage current around the perimeter of the mesa. Temperature dependent V-I characterisation from 20 K to 300 K was also carried out to investigate the mechanism responsible for the valley current.

Fig. 6.2 shows the RTD V-I characteristics measured at 300 K during the fabrication process for etch durations from 420 s to 780 s with etch steps of 60 s. The inset of the figure shows a scanning electron microscope (SEM) image of the final device. Areal etch rates of $\sim 5.2\text{x}10^{-3}\mu m^2/s$ and $\sim 12.4\text{x}10^{-3}\mu m^2/s$ are deduced for peak current reduction rates of 36 μA/s and 85 μA/s for etch durations of 420 s and 780 s, respectively. Based on an etch time resolution of 1 second, this results in an etch accuracy of ~ 0.3 % for a final area of 3.8 μm^2. A negative differential resistance characteristic is observed in Fig. 6.2, which indicates that the total series resistance between the bias supply and the RTD is less than the measured negative differential resistance of the RTD. The observed “plateaulike” characteristic in the NDR region of the V-I characteristics is attributed to the oscillating nature of the circuit while measuring the V-I characteristic of these devices [1].

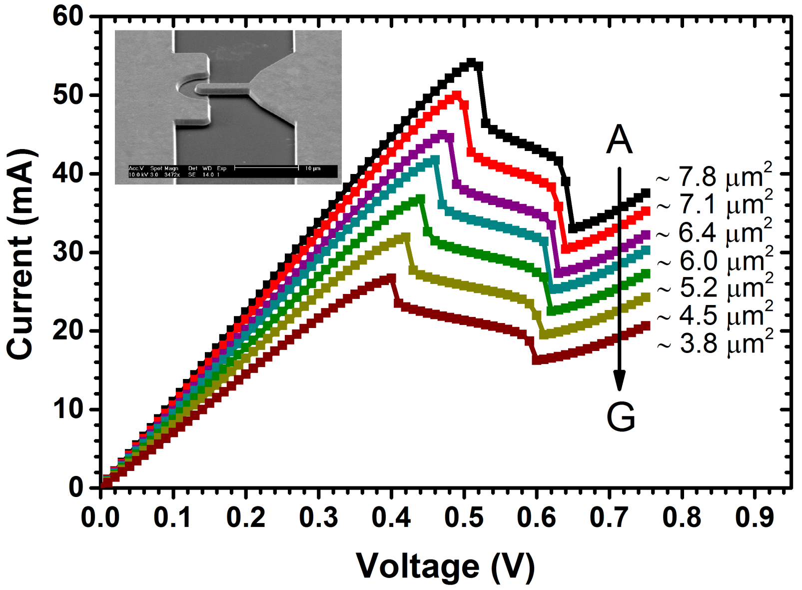

Figure 6.2: V-I characteristics of a single RTD measured in-line with the fabrication process for etch durations from 420 s (A) to 780 s (G) with 60 s etch steps. The approximate mesa area is displayed for the etched devices, as calculated from the current density and the RTD peak current. The inset shows a SEM image of the fabricated RTD.

Fig. 6.3 shows the measured RTD peak voltage and valley current as a function of peak current for the V-I characteristics shown in Fig. 6.2. In the limit of zero peak current, a minimum peak voltage of ∼ 289 mV is deduced. The inset of Fig. 6.3 shows the measured PVCR of the RTD during the etch process. No degradation in PVCR is observed for a reduction in mesa size. The RTD diameter dependence on the PVCR has been theoretically investigated by Ternent *et al.* [2], and experimentally investigated by Nomoto *et al.* [3] for ultra-small AlSb-InAs RTDs with mesa diameters down to 10 nm. Both showed that the PVCR of small RTDs degrades for a reduction in mesa diameter. They attributed the reduced PVCR to surface leakage current which increases the valley current. The RTD surface current is determined by the surface generation velocity and surface states at the perimeter surface of the mesa. In this work, no such degradation mechanism is observed due to the strong linear dependence between the valley and peak currents of the RTD, as shown in Fig. 6.3. The valley current of this RTD can therefore be attributed to the tunnelling area of the RTD, not to a leakage surface current around mesa perimeter. This is confirmed in Fig. 6.4 for the peak current and valley current plotted as a function of mesa radius for a circular device. The black solid line represents the calculated valley current for surface leakage current around the perimeter of the mesa, while the blue and green solid lines represent the calculated peak and valley

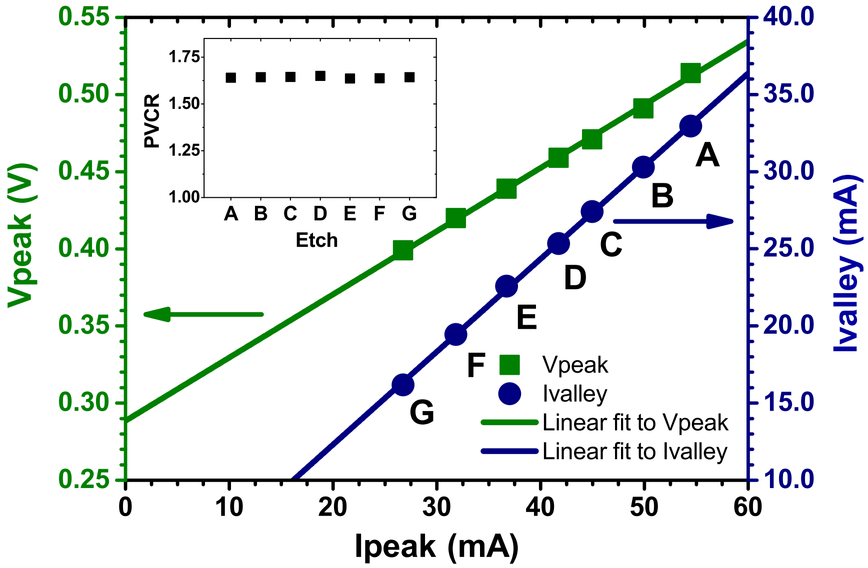

Figure 6.3: RTD peak voltage and valley current as a function of peak tunnelling current for etches A-G. Linear fits are applied to the data. The inset shows the measured PVCR for the mesa etches A-G.

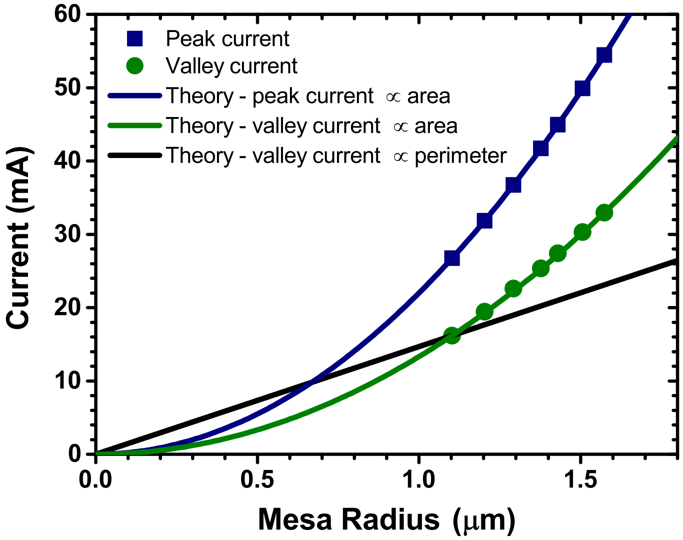

Figure 6.4: Experimental and theoretical RTD peak and valley current as a function of mesa radius for a circular device

current with no surface leakage current. These results confirm that the peak and valley current are proportional to the mesa area, as they do not scale with the perimeter of the mesa. This also indicates that high quality mesa sidewalls were fabricated using the wet etch process, as no surface leakage current is measureable. This further eliminates the requirement for mesa-sidewall passivation of the RTDs which are fabricated using this process, as very little improvement in device performance is expected.

Temperature dependent measurements were carried out to investigate the thermal dependence of the RTD V-I characteristics. The RTD devices were bonded with indium to an aluminium oxide tile and mounted on a copper heat sink in a closed-cycle helium (He) cryostat. The operating temperature was controlled by a resistive heating element attached the copper heat sink. Fig. 6.5 shows the V-I characteristic of a RTD measured as a function of temperature from 20 K to 300 K. The temperature dependence of the peak and the valley current is shown in the inset.

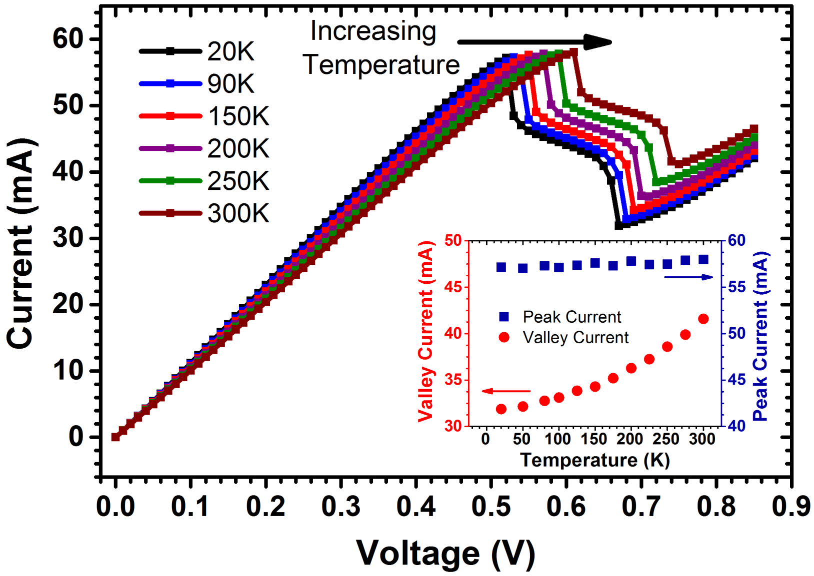

Figure 6.5: Temperature dependent RTD V-I characteristics from 20 K to 300 K. The inset shows the measured valley current as a function of temperature.

The peak current is essentially unchanged, but the valley current increases when the temperature is raised from 20 K to 300 K. As the valley current increases more rapidly than the peak current, the PVCR reduces from 1.8 to 1.4. The valley current of the RTD is known to be dependent on elastic and inelastic electron scattering processes, such as interface roughness, impurity scattering, phonon scattering, and thermal assisted tunnelling through higher resonant states [4][5]. The contribution of each mechanism to the valley current depends on the structural composition of the RTD. Lake *et al.* [6] reported that the valley current for GaAs/AlAs RTD is dominated by phonon scattering, whereas interface roughness scattering is dominant for InGaAs/AlAs based RTD with an InAs subwell [7]. The thermal dependence of optical phonon scattering was theoretically investigated by Roblin *et al.* [8] and Chevoir and Vinter [9], showing that the peak current reduces and valley current increases with temperature due to enlarged phonon scattering which degrades the peak tunnelling current and broadens the resonant transmission probability. The small increase in peak current density, measured in Fig. 6.5, as a function of temperature is most likely attributed to thermally assisted electron tunnelling through higher resonant energy levels. This observation is in good agreement with previous work reported by De Saint Pol *et al.* [10] and Klimeck *et al.* [11] on temperature dependent transmission probabilities of GaAs/AlGaAs based heterostructures. A RTD valley current of ~ 32 mA is extrapolated in the limit of zero temperature. The excess RTD current in this limit is tentatively attributed to interface roughness (IR) scattering [7]. Monolayer thickness variations in barrier thickness are expected to have a large effect on the tunnelling properties of these devices, as the 1.1 nm AlAs barriers are very thin and have a high confining potential. These observations are in good agreement with the results from the photoluminescence investigation shown in Chapter 3, and Roblin *et al.* [8] attributing IR scattering as the dominant scattering mechanism in InGaAs/AlAs based RTDs with an InAs subwell. The measured peak voltage shift with temperature is attributed to a temperature dependent increase in series resistance of the external circuit. Similar observations were reported by Li *et al.* [12] for GaN/AlGaN RTDs.

Fig. 6.6 shows the NDR and the maximum power (approximately) of the RTD as a function of temperature. A reduction in maximum power and an increase in NDR are observed as a function of temperature. The increasing valley current with temperature reduces the voltage and current spans in the NDR region which lowers the extractable output power of the RTD. These results show that device performance is optimum at low temperatures, which highlights the need for good thermal design.

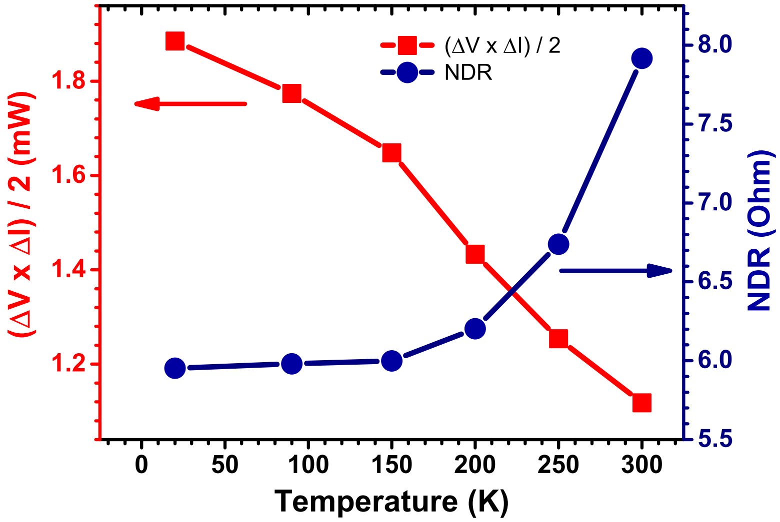

Figure 6.6: NDR and maximum extractable power (approximately) of the RTD as a function of temperature.

6.4 Measurement of Terahertz Radiation

This section describes the development of the experimental detecting apparatus and characterisation of the THz emitter. The radiated energy of the THz emitter was collected through the substrate using a silicon hyper-hemispherical lens. Fig. 6.7 shows a diagram of the THz measurement system, a photograph of the corresponding optical set-up for detecting the sub-mm electromagnetic waves is shown in Fig. 6.8. A room temperature pyroelectric detector from Gentec [13] was used for the detection of the THz radiation. This pyroelectric detector is based on a permanently poled, $LiTaO_3$ ferroelectric crystal. The detector senses the absorbed incident radiation as the instantaneous polarization of the ferroelectric crystal is a function of the rate of temperature change of the crystal [14]. The induced electrical charge due to the change in polarisation is converted into a voltage by a transimpedance amplifier. The pyroelectric detector with a 4 mm^2 active area has a noise equivalent power (NEP) of $4.0\text{x}10^{-10}\text{W}/(\text{Hz})^{1/2}$, a sensitivity of 140 kV/W [13], and a predicted absorption efficiency of ∼ 10 % [15]. A TPX (Rexolite) window with a spectral range from 50 - 2000 μm and a ∼ 90 % transmission between 400 - 2000 μm was placed in front of the detector to block out stray electromagnetic radiation [16].

As the instantaneous polarization of the pyroelectric detector changes with a rate of temperature change, source modulation was required to heat and cool down the detector crystal. This was achieved by pulsating the RTD electrically with a square waveform at a frequency of 20 Hz and a

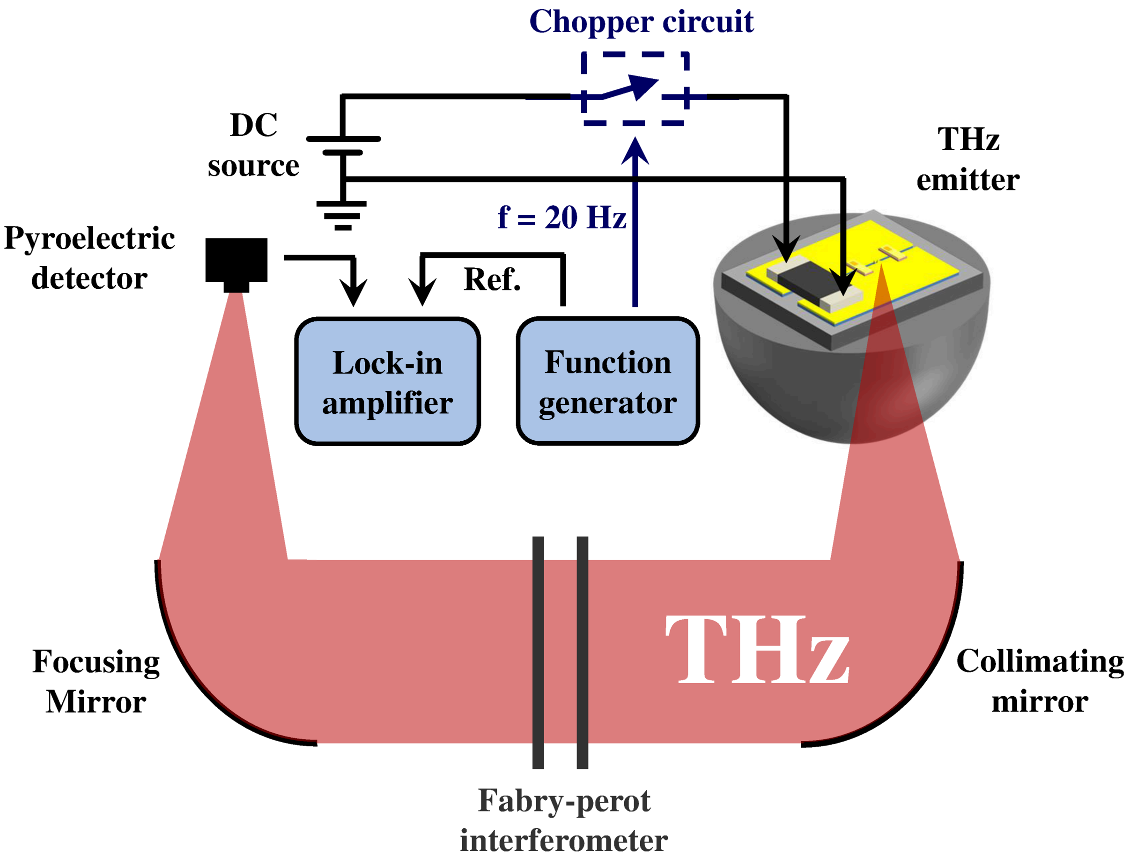

Figure 6.7: Measurement system for detecting sub-mm electromagnetic waves

duty cycle of 50 %. As most function generators are calibrated for a 50 ohm load to minimise ringing, the low impedance RTD could not be driven directly from the output of a function generator. A chopper circuit was designed and built to pulsate the RTD electrically at a voltage in the NDR region. Fig. 6.9 schematically shows a diagram of the chopper circuit. The output signal of a function generator was used to modulate the gate voltage of two enhancement-mode n-channel MOSFETs. Power MOSFETS with a low static drain-source on-resistance of 65 mΩ were selected for this circuit to minimise loading in the circuit. Due to the intrinsic body diode of the power MOSFET, two back-to-back MOSFETs are used in series for bipolar measurements.

A 50 ohm gate impedance is connected in parallel with the gates of the MOSFETs to match the input impedance the MOSFETs to the output impedance of the function generator. A gate-source voltage of 10 V was applied to saturate the MOSFET channels for a low static drain-source on resistance of 65 mΩ (gate threshold voltage of MOSFET = 1.8 V). A Keithley 2400 source-measure unit (SMU) was used as a low impedance voltage source to supply the RTD bias voltage.

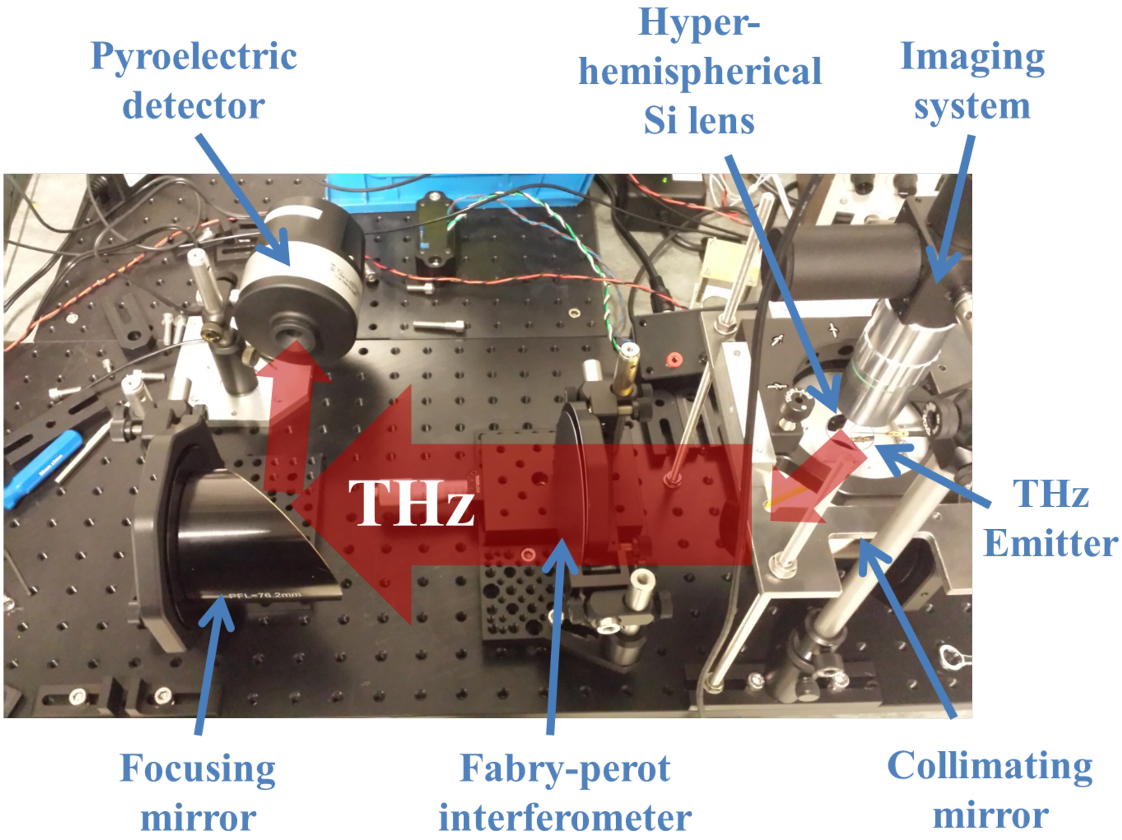

Figure 6.8: Photograph of the optical setup for detecting sub-mm electromagnetic waves

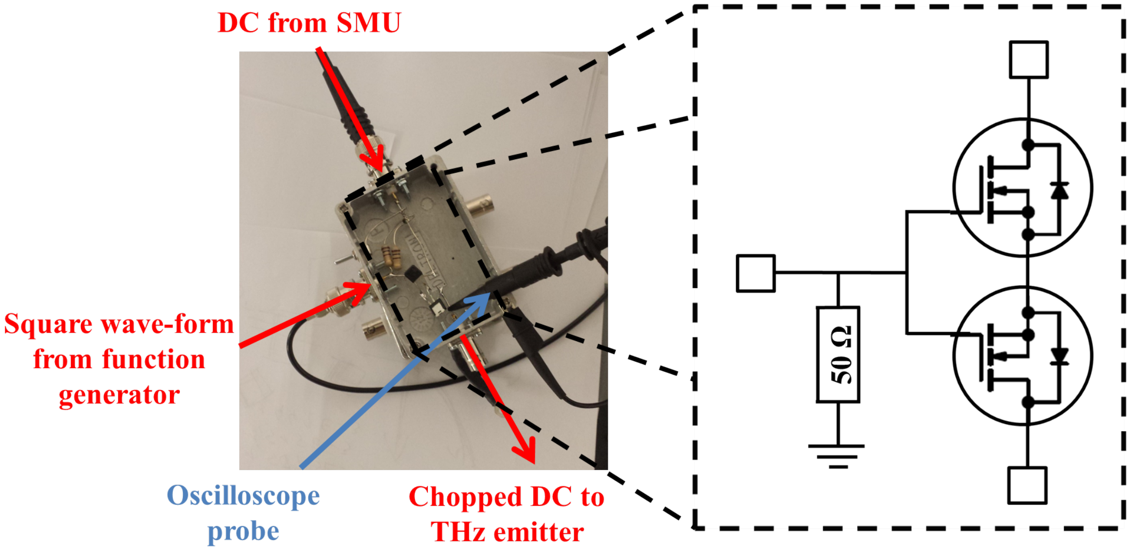

Figure 6.9: Electronic chopper circuit for pulsed measurements

A lock-in amplifier (LIA) was used to filter out the unmodulated disturbing background radiation from the measurement. A LIA acts as a synchronous demodulator followed by a low-pass filter, whereby noise signals at frequencies other than the reference frequency are rejected, and the signal-to-noise ratio is consequently improved.

The radiated energy from the THz emitter was collimated by a parabolic mirror and subsequently focused onto the detector element through another parabolic mirror. Two gold-coated 90° off-axis parabolic mirrors with a diameter of $3''$ and a focal length of 154 mm were used. The frequency measurement of the THz emitter was carried out using a simple Fabry-Perot interferometer. To measure the output power of the THz chip, the Fabry-Perot interferometer was excluded from the optical path to maximise the detected signal. To bring the RTD into the oscillation mode, the device was biased in the NDR region.

Fig. 6.10 shows the V-I characteristics of the same RTD measured with and without bias stabilisation, and the detected THz output signal as a function of the supply voltage. The V-I characteristic of the non-stabilised RTD shows the typical NDR characteristic with a measured negative resistance of $\sim$ 11 ohms. To eliminate any low frequency parasitic oscillations over the bias lines, the RTD was stabilised with an external resistance of 8.2 ohms connected in parallel with the NDR. The combined V-I characteristic of the stabilised RTD has a positive slope throughout, confirming that the stabilisation condition is met as the dynamic resistance of the stabiliser is less than half the tunnel diode's negative differential resistance. A voltage shift of 0.1 V is measured between the stabilised and non-stabilised RTD V-I characteristics. The voltage shift between the stabilised and non-stabilised RTD is attributed to the voltage drop across the finite resistance between the voltage source and the RTD. For a measured shift in voltage and current of 0.1 V and 37 mA, respectively, a source resistance of $\sim$2.7 ohms is calculated. This resistance consists of the output impedance of the SMU, resistance of the supply lines, interface resistance between the probes and the contact metallisation of the THz chip. This voltage shift can be further reduced in future work by using a 4-terminal probe method instead of two probes to supply the bias voltage to the RTD. As the RTD is only allowed to oscillate when biased in the NDR region, no emission from the chip is expected for a bias voltage smaller or higher than the peak and valley voltages, respectively. A RTD biased outside the NDR region has no gain available to negate the resistive and radiative losses in the circuit. This is in excellent agreement with the experimental data as no emission is observed for bias voltages below and above $\sim$ 0.48 V and $\sim$ 0.62 V, respectively, as shown in Fig. 6.10. Maximum power extraction of the RTD occurs when the device is biased at the mid-point of the NDR region to maximise the voltage and current excursions. Maximum output power is measured from the THz emitter when the RTD is biased at the mid-point of the NDR region (Vbias = 0.54 V). A wall-plug efficiency of ~ 7 ppm is deduced for the THz emitter with a measured output power of ~ 100 nW.

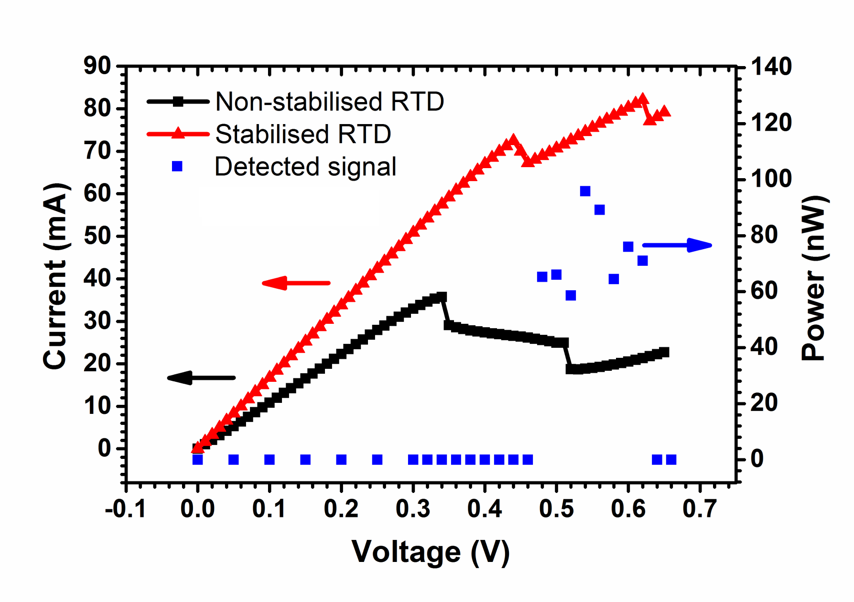

Figure 6.10: V-I characteristics of the same RTD measured with and without bias stabilisation. The detected output power is shown as a function of the supply voltage.

A simple Fabry-Perot interferometer was built to measure the emission frequency of the THz chip. Two 4″ semi-insulating Si wafers were used as the partially reflecting mirrors of the interferometer. One wafer was mounted on a translation stage to control the cavity length (i.e. the separation between the two partially reflecting surfaces) between both wafers. The transmittance function of a Fabry-Perot etalon is given by Eq. 6.1

$$T = \frac{1}{1 + F\sin^2(\delta/2)} \tag{6.1}$$

where T is the transmittance, R the reflectance, F the finesse, and δ the phase difference between each successive transmitted pair. δ at normal incidence is given by Eq. 6.2

$$\delta = \frac{4\pi cl}{f} \tag{6.2}$$

where c is the speed of light, f the frequency, l the etalon thickness, and n the refractive index of the material between the reflecting surfaces. The coefficient of finesse of the interferometer is determined by the reflectivity of the surfaces and is given by Eq. 6.3.

$$F = \frac{4R}{(1-R)^2} \tag{6.3}$$

The transmission function of the etalon originates from constructive and destructive interference effects between the two reflecting surfaces. Maximum transmission occurs when the optical path length difference between the incident and reflected waves is an integer multiple of half the wavelength. Fig. 6.11 shows transmission as a function of the frequency for different mirror reflectivities. The free spectral range (FSR) is defined as the frequency separation between adjacent transmission peaks, and is related to the full-width half-maximum by Eq. 6.4.

$$FSR = F \times FWHM \tag{6.4}$$

As shown in Fig. 6.11, etalons with a high finesse show sharp resonances with a small FWHM linewidth. The Fabry-Perot etalon was made out of semi-insulating silicon, as large polished semi-insulating 4″ Si substrates and readily available and silicon has a low imaginary part of the refractive index (i.e. the absorption) at THz frequencies (<0.05 cm^{-1} up to 1.5 THz)[17]. The black line in Fig. 6.11 shows the transmission function of the Si Fabry-Perot interferometer as calculated from

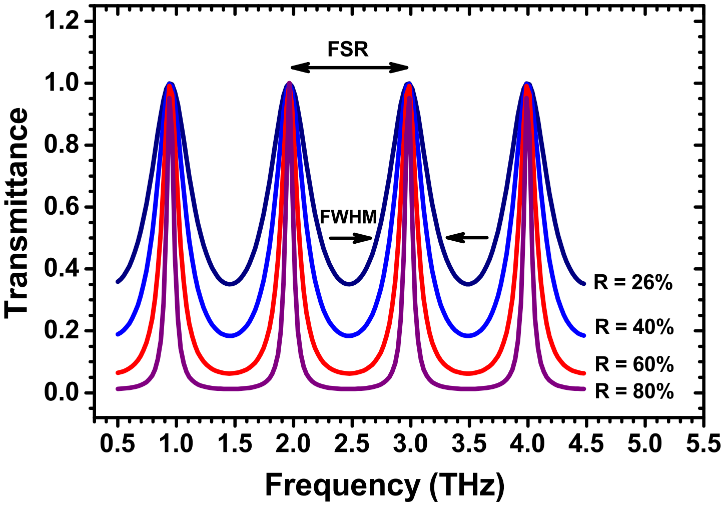

Figure 6.11: Transmission spectra of Fabry-Perot etalons with different coefficients of finesse

the normal reflectance coefficient, given by Eq. 6.5.

$$R = \left(\frac{n_2 - n_1}{n_2 + n_1}\right)^2 \tag{6.5}$$

where *n1* and *n2* are defined as the refractive index of air and silicon, respectively. For Si with a refractive index of 3.4, a reflectance of 26 % is calculated at normal incidence. Fig. 6.12 shows the detected signal, for the THz emitter shown in Fig. 6.10, as a function of translation stage position, for the etalon located at normal incidence in the collimated optical beam path. Transmission peaks are observed for repeats of ∼ 420 µm is mirror displacement, confirming emission at ∼ 350 GHz from the clear fundamental frequency Fabry-Perot oscillations. Good agreement is observed between the experimental data and theory in Fig. 6.12. There is no evidence of higher order oscillations but these are not expected due to the low power. Fig. 6.12 provides little information about the linewidth of this THz emitter as the interferometer has a low finesse. From the linewidth of the etalon, it is shown that the linewidth of the emitter is less than 186 GHz.

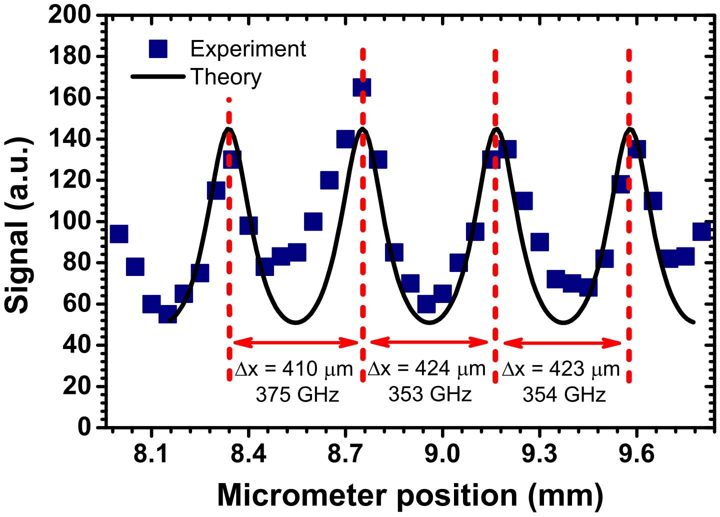

Figure 6.12: Theory and measured signal as a function of Fabry-Perot mirror displacement

6.5 Conclusions

This chapter described the electrical and optical characterisation of the RTD THz emitter, and development of the experimental characterisation setup. Important device parameters were extracted by measuring the RTD V-I characteristic during the etch process, such as RTD peak voltage (Vp = 168 mV), specific contact resistivity ($\rho_c = 8\Omega.\mu m^2$), and an estimation of the resistive cutoff frequency ($f_{MAX} = \sim 1$ THz). Extracting these characteristics in-line with the fabrication process without the need of additional complex test structures is advantageous from a manufacturing point of view, and provides a route for further device optimisation. The measured excess current, also known as the valley current, of the RTD was tentatively attributed due to interface roughness scattering, and tunnelling through higher electronic states, which can be further improved on by future growth optimisation. Finally, coherent THz emission at 350 GHz was demonstrated.

References

[1] Young, Jeff F. and Wood, B. M. and Liu, H. C. and Buchanan, M. and Landheer, D. and SpringThorpe, A. J. and Mandeville, P., “Effect of circuit oscillations on the dc currentvoltage characteristics of double barrier resonant tunneling structures”, Applied Physics Letters, 52, 1398-1400 (1988)

[2] G. Ternent and D.J. Paul, “SPICE modelling of the scaling of resonant tunnelling diodes and the effects of sidewall leakage” IEEE Transactions on Electron Devices 59(12), 3555 (2012)

[3] K. Nomoto, K. Taira, T. Suzuki, I. Hase, H. Hiroshima, and M. Komuro, “Diameter dependence of currentvoltage characteristics of ultrasmall area AlSbInAs resonant tunneling diodes with diameters down to 20 nm”, Applied Physics Letters 70, 2025 (1997)

[4] P. Johansson, “Effects of interface-roughness scattering on resonant tunneling”, Phys. Rev. B 46, 12865(R) (1992)

[5] G. Klimeck, R. Lake, and D. K. Blanks, “Role of interface roughness scattering in self-consistent resonant-tunneling-diode simulations”, Phys. Rev. B 58, 7279 (1998)

[6] R. Lake, G. Klimeck, R. C. Bowen, C. Fernando, M. Leng, T. Moise, and Y. C. Kao, “Interface roughness, polar optical phonons, and the valley current of a resonant tunneling diode”, Superlattices Microstruct. 20, 279 (1996).

[7] Patrick Roblin, Robert C. Potter, and Ayub Fathimulla, “Interface roughness scattering in AlAs/InGaAs resonant tunneling diodes with an InAs subwell”, Journal of Applied Physics 79, 2502 (1996)

[8] P. Roblin and W. R. Liou, “Three-dimensional scattering-assisted tunneling in resonant-tunneling diodes”, Phys. Rev. B 47, 2146 (1993) .

[9] F. Chevoir and B. Vinter, “Calculation of phononassisted tunneling and valley current in a doublebarrier diode”, Applied Physics Letters 55, 1859 (1989);

[10] L. de Saint Pol, O. Vanbsien and D. Lippens, “Estimation of temperature limit for negative differential resistance using resonant tunnelling”, Electronic Letters 26:342 (1990)

[11] G. Klimeck, R. Lake, R. C. Bowen, W. R. Frensley, and D. Blanks, “NanoElectronic MOdeling (NEMO)”, 53rd Annual Device Research Conference Digest, pp.52 -53 1995 :IEEE Press

[12] D Li and J Shao and L Tang and C Edmunds and G Gardner and M J Manfra and O Malis. “Temperature-dependence of negative differential resistance in GaN/AlGaN resonant tunneling structures”, Semicond. Sci. Technol. 28 074024 (2013)

[13] http://gentec-eo.com/Content/downloads/specifications-sheet/THZ-I-BNC_2014_V2.0.pdf

[14] http://gentec-eo.com/Content/downloads/application-note/AN_201924_THz_R1.pdf

[15] http://gentec-eo.com/Content/downloads/absorption-curves/Curves_THz_2014_V2.0.pdf

[16] http://gentec-eo.com/Content/downloads/application-note/AN_202192_IR_Windows.pdf

[17] D. Grischkowsky, S. Keiding, M. van Exter, and C. Fattinger, “Far-infrared time-domain spectroscopy with terahertz beams of dielectrics and semiconductors,” J. Opt. Soc. Am. B 7, 2006-2015 (1990).

Chapter 7

Summary and Future Work

7.1 Summary

This thesis focused on the design, fabrication, and characterisation of high current density InGaAs/AlAs/InP RTD THz emitters grown by MOVPE for THz applications. The RTD structures were grown by MOVPE to meet the large scale, high throughput needs of the growing high technology market. Low-cost manufacturing of the RTD THz emitter will require high wafer uniformity, high yield, and high throughput epitaxy. Process control is very important for high yield in volume manufacturing, as feature sizes become increasingly small. To manufacture the RTD THz emitter cost-effectively, good circuit design is also required, as electrical parameter tolerances have to accommodated for to assure functionality, high yield, and high reliability.

In Chapter 2, the optical properties of InGaAs were explored. PL emission was measured as a function of doping concentration on InGaAs test-layers at low temperatures and correlated to SIMS and eCV profiling to provide non-destructive mapping of the doping concentration over the wafer. A low temperature PL mapping tool was developed for this work. InGaAs test-structures equivalent to the contact and emitter/collector layers were used to measure the doping uniformity of the RTD wafers. By measuring the Moss-Burstein shift at different locations over the full wafer, a ± 8 % doping uniformity for the contact layers, and a ± 10 % for the emitter/collector layers was deduced for 62 % of the wafer area. These results were confirmed by measuring the free-carrier concentration over the wafer with an eCV profiler. The measured variation over the wafer was attributed to thermal effects as the dopant silicon was incorporated from the precursor disilane within the dissociation rate limited region. The observed effect is not well explained by gas-phase depletion or saturation effects as both wafers showed similar doping uniformities. Doping uniformity is important, as a variation in doping will affect the contact resistance of the device, the associated device losses, and the V-I performance as the tunnelling current is highly dependent on the doping concentration. Whilst a doping uniformity of ± 10 % over the full wafer is not ideal for volume manufacture, it is good for research to explore the optimum process parameters, as simultaneous experiments with different process conditions can be carried out at different positions over the wafer. Furthermore, no InGaAs test-structures are likely to be needed in future work to map the doping uniformity non-destructively, as PL emission was observed from the highly doped contact layer of the full RTD structure.

The optical properties of the RTD structure were explored in Chapter 3. It was shown that the low temperature PL emission from the RTD structure predominantly originates from the QW and the undoped InGaAs buffer layer. Good agreement was observed between the experimental results and the developed theoretical model. Type-I and type-II QW recombination was determined for nominally identical doped and undoped RTD structures. A technique was developed to allow the absolute position of the first resonant energy level ($\sim$ 75 meV) to be deduced without prior knowledge of the band-offsets, and monitor the well width and indium concentration of the RTD, through low temperature PL spectroscopy. Using the low temperature PL mapping tool, both alloy and QW uniformity and perfection were non-destructively mapped over a full wafer. InGaAs alloy composition fluctuations of less than 0.6 % and a QW thickness variation of less than 0.5 % were deduced from this non-destructive mapping technique for 62 % of the wafer area. The rapid non-destructive characterisation and wafer mapping of these structures allows a route to future growth optimisation. Monolayer well-width fluctuations were also detected at room temperature. From a manufacturing perspective, performing these measurements at room temperature is very attractive as room temperature PL mapping tools are readily available commercially without the need for a custom-built cryostat. This will have to be further investigated in future work.

Chapter 4 covered the design procedure of a RTD based THz oscillator, monolithically integrated on the InP substrate. The design specifications for operation in the 300 GHz band were discussed, including metal-insulator-metal (MIM) structures, slot antenna design, bias stabilisation techniques and output coupling of the THz emission through the dielectric substrate.

Chapter 5 covered the development of an EBL free fabrication process for the fabrication of a RTD THz emitter based on standard i-line photolithography, wet chemical etching, and air-bridge technology. A specific contact resistivity of $\sim 6.3\ \Omega\mu\text{m}^2$ was achieved for non-alloyed Ti/Au based ohmic contacts. A UV-Ozone cleaning apparatus was developed to achieve low resistance ohmic contacts. The developed fabrication process is not only simple and manufacturable, but also provides ultra-fine control of the final device area (and hence characteristics) by measuring the V-I characteristic of the RTD during the fabrication process. The requirement for a second contact metallisation to the emitter layer was also eliminated by guiding the emitter current through the full RTD structure by a second contact electrode on the collector side, simplifying the overall device fabrication process.

The fabricated devices were characterised in Chapter 6. By measuring the RTD V-I characteristics during the etch process, the RTD peak voltage (Vp = 168 mV), and specific contact resistivity ($\rho_C = 8\ \Omega\mu\text{m}^2$) were deduced. Extracting these characteristics in-line with the fabrication process without the need of additional complex test structures is advantageous from a manufacturing point of view, and provides a route for further device optimisation. The measured excess current, also known as the valley current, of the RTD was tentatively attributed to interface roughness scattering, and tunnelling through higher electronic states. Finally, coherent THz emission at 350 GHz was demonstrated.

7.2 Future Work

7.2.1 Optical Characterisation

In Chapter 3, a technique was developed to deduce the absolute position of the first resonant energy level, ΔE , by a combination of type-I and type-II QW recombination. Due to the campaign-to-campaign variation in the composition of the lattice-matched InGaAs, ΔE was approximated to ∼ 75 meV. A more accurate measurement of this energy level is expected by growing both structures (doped and undoped RTD) in a single run to ensure identical growth conditions to both structures. Fig. 7.1(a) shows the proposed layer structure, where an undoped RTD is included in the undoped InGaAs buffer layer. Of note is that an AlInAs buffer layer is also included in the layer structure to act as a getter for unintentional contamination prior to the growth of the first AlAs barrier. As aluminium has a high oxygen affinity, the first AlAs barrier may be affected by a small amount of residual contamination which remains within the reactor. The thick AlInAs buffer layer is included to "clean" the reactor prior to the growth of the double barrier heterostructure to ensure that the RTD is protected from any unintentional contamination. As for the undoped RTD in the buffer region, impact on device performance of the RTD is expected to be minimal. Previous TEM samples were grown with stacks of 4xQWs which did not show any structural problems. This should allow for a very nice chracterisation technique for future RTDs, if everything goes well, and a nice PL spectrum (type-I and type-II) is obtained, plus no change in device characteristics.

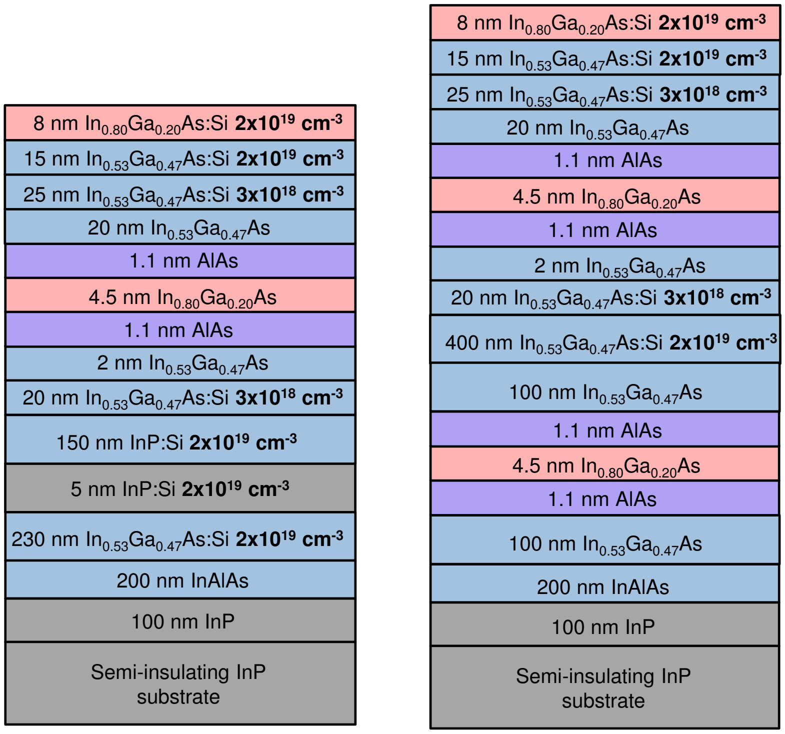

(a) (b)

Figure 7.1: Proposed layer structures including (a) an InP etch stop layer (b) undoped RTD test structure for PL characterisation.

7.2.2 Sub-µm^2 Resonant Tunnelling Diode

To access the higher frequencies (f >1 THz), the device area has to be reduced to sub-µm^2 dimensions to lower the parasitic capacitance of the RTD. The RTD area is limited by the current mask-set to approximately 3.3 µm^2. The mask design has to be improved to allow the fabrication of narrower air-bridges. Furthermore, incorporating a highly doped InP etch-stop layer in the 400 nm n$^+$ InGaAs emitter contact layer can provide a route to additional lateral etching to further reduce the RTD mesa area to sub-µm^2 dimensions. The proposed RTD layer structure is shown in Fig. 7.1(b). The etching will be performed before the air-bridge is created, as illustrated in Fig. 7.2. Test-structures on the wafer will be used to measure the undercut progress during the wet etch process. The effect of the highly doped InP layer on the device performance will have to be investigated as well. The proposed device fabrication flow is shown in Fig.7.3.

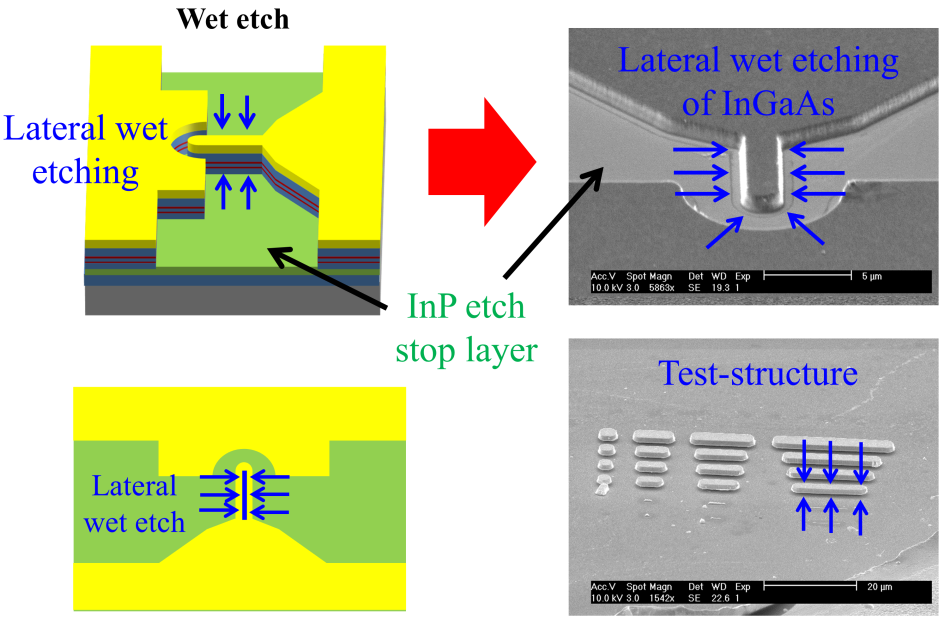

Figure 7.2: Lateral wet etching by using a InP etch stop layer (shown in green). Test-structures are used to monitor the etch progress.

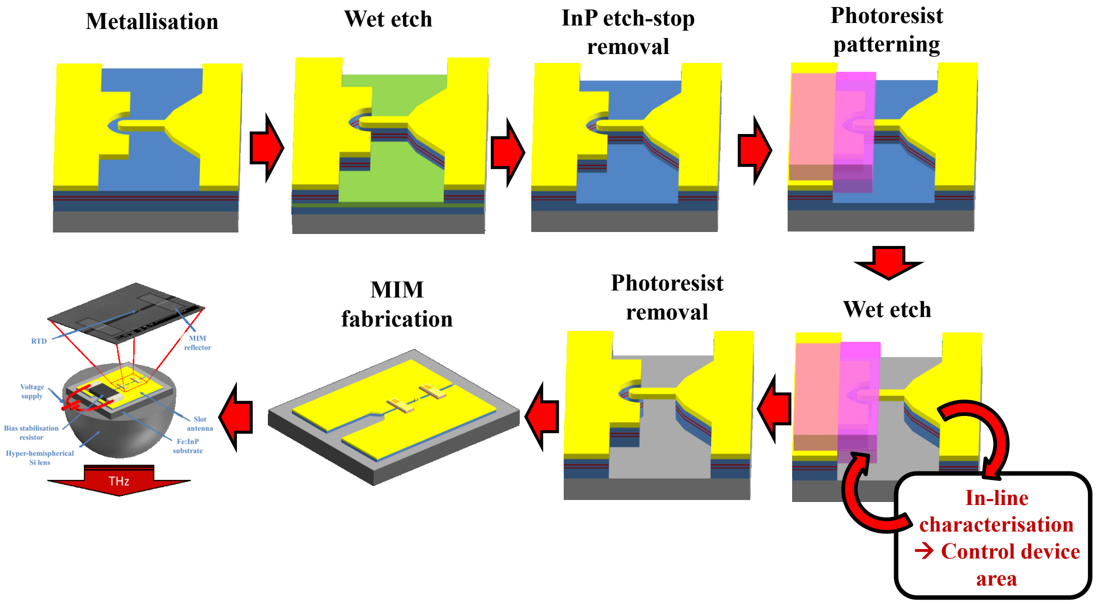

Figure 7.3: Proposed fabrication process flow for the sub-µm^2 RTD THz emitter.

At the moment, the output power of the THz emitter (∼100 nW) is mainly limited by the antenna (P_{MAX} RTD $\sim$ 0.5 mW). Future antenna design will allow the output power of the THz emitter to increase to the $\sim$ mW level.